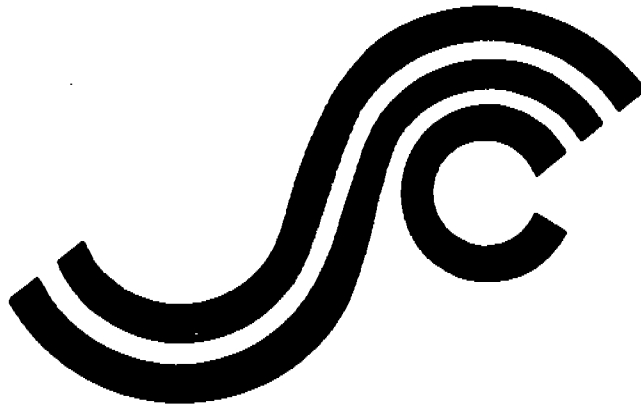


SSC-366

**THRESHOLD CORROSION
FATIGUE OF WELDED
SHIPBUILDING STEELS**



This document has been approved
for public release and sale; its
distribution is unlimited

SHIP STRUCTURE COMMITTEE

1992

SSC-366 Threshold Corrosion Fatigue of Welded Shipbuilding Steels Ship Structure Committee 1992

SHIP STRUCTURE COMMITTEE

The SHIP STRUCTURE COMMITTEE is constituted to prosecute a research program to improve the hull structures of ships and other marine structures by an extension of knowledge pertaining to design, materials, and methods of construction.

RADM A. E. Henn, USCG (Chairman)
Chief, Office of Marine Safety, Security
and Environmental Protection
U. S. Coast Guard

Mr. Alexander Malakhoff
Director, Structural Integrity
Subgroup (SEA 55Y)
Naval Sea Systems Command

Dr. Donald Liu
Senior Vice President
American Bureau of Shipping

Mr. H. T. Haller
Associate Administrator for Ship-
building and Ship Operations
Maritime Administration

Mr. Thomas W. Allen
Engineering Officer (N7)
Military Sealift Command

CDR Michael K. Parmelee, USCG
Executive Director
Ship Structure Committee
U. S. Coast Guard

CONTRACTING OFFICER TECHNICAL REPRESENTATIVE

Mr. William J. Siekierka
SEA 55Y3
Naval Sea Systems Command

SHIP STRUCTURE SUBCOMMITTEE

The SHIP STRUCTURE SUBCOMMITTEE acts for the Ship Structure Committee on technical matters by providing technical coordination for determining the goals and objectives of the program and by evaluating and interpreting the results in terms of structural design, construction, and operation.

AMERICAN BUREAU OF SHIPPING

Mr. Stephen G. Arntson (Chairman)
Mr. John F. Conlon
Dr. John S. Spencer
Mr. Glenn M. Ashe

NAVAL SEA SYSTEMS COMMAND

Dr. Robert A. Sielski
Mr. Charles L. Null
Mr. W. Thomas Packard
Mr. Allen H. Engle

MILITARY SEALIFT COMMAND

Mr. Robert E. Van Jones
Mr. Rickard A. Anderson
Mr. Michael W. Touma
Mr. Jeffrey E. Beach

MARITIME ADMINISTRATION

Mr. Frederick Seibold
Mr. Norman O. Hammer
Mr. Chao H. Lin
Dr. Walter M. Maclean

U. S. COAST GUARD

CAPT T. E. Thompson
CAPT W. E. Colburn, Jr.
CDR Mark E. Noll
Mr. H. Paul Cojeen

SHIP STRUCTURE SUBCOMMITTEE LIAISON MEMBERS

U. S. COAST GUARD ACADEMY

LCDR Bruce R. Mustain

U. S. MERCHANT MARINE ACADEMY

Dr. C. B. Kim

U. S. NAVAL ACADEMY

Dr. Ramswar Bhattacharyya

STATE UNIVERSITY OF NEW YORK MARITIME COLLEGE

Dr. W. R. Porter

SOCIETY OF NAVAL ARCHITECTS AND MARINE ENGINEERS

Dr. William Sandberg

NATIONAL ACADEMY OF SCIENCES - MARINE BOARD

Mr. Alexander B. Stavovy

NATIONAL ACADEMY OF SCIENCES - COMMITTEE ON MARINE STRUCTURES

Mr. Peter M. Palermo

WELDING RESEARCH COUNCIL

Dr. Martin Prager

AMERICAN IRON AND STEEL INSTITUTE

Mr. Alexander D. Wilson

DEPARTMENT OF NATIONAL DEFENCE - CANADA

Dr. Neil G. Pegg

Member Agencies:

*United States Coast Guard
Naval Sea Systems Command
Maritime Administration
American Bureau of Shipping
Military Sealift Command*



**Ship
Structure
Committee**

An Interagency Advisory Committee

Address Correspondence to:

Executive Director
Ship Structure Committee
U. S. Coast Guard (G-MIR)
2100 Second Street, S.W.
Washington, D.C. 20593-0001
PH: (202) 267-0003
FAX: (202) 267-4839

June 18, 1992

SSC-366
SR-1319

**THRESHOLD CORROSION FATIGUE OF
WELDED SHIPBUILDING STEELS**

This report presents the development of the near-threshold corrosion fatigue test methodology for welded high strength, low alloy (HSLA) shipbuilding steels. The tests which were developed under this Small Business Innovative Research (SBIR) project will permit the direct evaluation of corrosion fatigue resistance of the weld metal, heat affected zone, and base metal regions. Special filler metals were developed for this project and used to assess the influence of various weld metal constituents on mechanical properties. This report includes descriptions of the preparation and evaluation of the microstructure and mechanical properties for baseline weldments. The development of the partial hydrogen embrittlement method to accelerate the collection of near-threshold corrosion fatigue data is particularly interesting and worthy of further exploration.

A handwritten signature in black ink, reading 'A. E. HENN'. The letters are cursive and somewhat stylized, with a large 'H' and 'N'.

A. E. HENN
Rear Admiral, U.S. Coast Guard
Chairman, Ship Structure Committee

1. Report No. SSC-366		2. Government Accession No.		3. Recipient's Catalog No.	
4. Title and Subtitle Threshold Corrosion Fatigue of Welded Shipbuilding Steels				5. Report Date January 1992	
				6. Performing Organization Code	
7. Author(s) G.H. Reynolds and J.A. Todd				8. Performing Organization Report No. SR-1319	
9. Performing Organization Name and Address MNSW, Inc. P.O. Box 865 San Marcos, CA				10. Work Unit No. (TRAIS)	
				11. Contract or Grant No. DTCG23-86-C-20050	
12. Sponsoring Agency Name and Address Commandant (G-M) U.S. Coast Guard 2100 Second Street, SW Washington, DC 20593				13. Type of Report and Period Covered Final Report	
				14. Sponsoring Agency Code G-M	
15. Supplementary Notes Sponsored by the Ship Structure Committee and its member agencies. Funded by the U.S. Navy Small Business Innovative Research Program.					
16. Abstract This report provides an overview of the development and verification of a test methodology for near-threshold corrosion fatigue of welded high strength, low alloy (HSLA) shipbuilding steels. The method permits the direct evaluation of the corrosion fatigue resistance of weld metal, heat-affected zone (HAZ), and base metal regions. Experimental powder-cored electrode filler metals were prepared to evaluate the effect of weld metal carbon and copper contents on weldment mechanical properties in the as-welded condition. Welded joint geometries used in this study were developed in the first phase of this project. This report incorporates findings from phases one and two. The study concludes with recommendations concerning the further development of the partial hydrogen embrittlement method to accelerate the collection of near threshold corrosion fatigue data.					
17. Key Words Corrosion Fatigue Threshold Corrosion Fatigue Hydrogen Embrittlement Fatigue Resistance Mechanical Properties			18. Distribution Statement Available from: Nat'l Technical Information Service Port Royal Road Springfield, VA 22161		
19. Security Classif. (of this report) Unclassified		20. Security Classif. (of this page) Unclassified		21. No. of Pages 228	22. Price

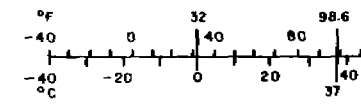
METRIC CONVERSION FACTORS

Approximate Conversions to Metric Measures

Symbol	When You Know	Multiply by	To Find	Symbol
LENGTH				
in	inches	*2.5	centimeters	cm
ft	feet	30	centimeters	cm
yd	yards	0.9	meters	m
mi	miles	1.6	kilometers	km
AREA				
in ²	square inches	6.5	square centimeters	cm ²
ft ²	square feet	0.09	square meters	m ²
yd ²	square yards	0.8	square meters	m ²
mi ²	square miles	2.6	square kilometers	km ²
	acres	0.4	hectares	ha
MASS (weight)				
oz	ounces	28	grams	g
lb	pounds	0.45	kilograms	kg
	short tons (2000 lb)	0.9	tonnes	t
VOLUME				
tsp	teaspoons	5	milliliters	ml
Tbsp	tablespoons	15	milliliters	ml
fl oz	fluid ounces	30	milliliters	ml
c	cups	0.24	liters	l
pt	pints	0.47	liters	l
qt	quarts	0.95	liters	l
gal	gallons	3.8	liters	l
ft ³	cubic feet	0.03	cubic meters	m ³
yd ³	cubic yards	0.76	cubic meters	m ³
TEMPERATURE (exact)				
°F	Fahrenheit temperature	5/9 (after subtracting 32)	Celsius temperature	°C

Approximate Conversions from

Symbol	When You Know	Multiply by
LENGTH		
mm	millimeters	0.04
cm	centimeters	0.4
m	meters	3.3
m	meters	1.1
km	kilometers	0.6
AREA		
cm ²	square centimeters	0.16
m ²	square meters	1.2
km ²	square kilometers	0.4
ha	hectares (10,000 m ²)	2.5
MASS (weight)		
g	grams	0.035
kg	kilograms	2.2
t	tonnes (1000 kg)	1.1
VOLUME		
ml	milliliters	0.03
l	liters	2.1
l	liters	1.06
l	liters	0.26
m ³	cubic meters	35
m ³	cubic meters	1.3
TEMPERATURE (exact)		
°C	Celsius temperature	9/5 (then add 32)



* 1 in = 2.54 (exact). For other exact conversions and more detailed tables, see NBS Mon. Publ. 250, Units of Weights and Measures, Price \$2.25, SD Catalog No. C11 10 286.

TABLE OF CONTENTS

INTRODUCTION 1

PHASE II TECHNICAL OBJECTIVES 1

EXPERIMENTAL RESULTS 2

 Preparation of Baseline Welds 2

 Materials 2

 Welding Procedure Development 3

 Preparation of Welds with Varying Cu, C Contents 3

CONCLUSIONS FROM WELDING PROCEDURE AND FILLER METAL
COMPOSITON DEVELOPMENT STUDIES 7

APPENDIX: DEVELOPMENT OF THRESHOLD CORROSION FATIGUE
TESTING TECHNIQUES A-1

THRESHOLD CORROSION FATIGUE OF WELDED SHIPBUILDING STEELS - PHASE II

INTRODUCTION

The primary objective of this SBIR Phase II project was the development and verification of a test methodology for near-threshold corrosion fatigue of welded HSLA shipbuilding steels which would permit direct evaluation of the corrosion fatigue resistance of weld metal, heat affected zone (HAZ) and base metal regions. A secondary objective was the evaluation of experimental filler metal compositions for submerged arc welding of MIL S-24645 structural steels. Welded joint geometries were developed in Phase I which were expected to permit direct evaluation of the corrosion fatigue performance of weld metal and HAZ microstructures. In this phase, experimental powder-cored electrode filler metals were prepared to evaluate the effect of weld metal carbon and copper contents on weldment mechanical properties in the as-welded condition, particularly low temperature impact toughness, for the developed joint geometries. The first section of this report describes the preparation and evaluation of the microstructure and mechanical properties of baseline weldments prepared with solid electrodes and experimental weldments prepared with powder-cored electrodes. Baseline weldments were used for preparation of compact tension specimens for near-threshold corrosion fatigue tests. Development of the near-threshold corrosion fatigue test methodology and a variety of supporting studies are described in Appendix A.

PHASE II TECHNICAL OBJECTIVES

The Phase II project had the following specific technical objectives:

1. To demonstrate techniques for producing and evaluating experimental weld metal compositions in developmental shipbuilding steels such as MIL S-24645 Class 3 using the submerged arc welding process. In particular the effects of weld metal copper content on as-welded microstructure, strength, and toughness were to be examined in detail for selection of optimum weld metal composition(s).
2. To prepare and evaluate, through detailed microstructural and mechanical property testing, welded test plates suitable for corrosion fatigue crack growth rate testing of isostructural base metal, weld metal, and HAZ test specimens.
3. To further develop an accelerated test technique for determining the threshold stress intensity range and the near-threshold corrosion fatigue crack growth rates at 10 Hz, 20°C, in (a) MIL

S-24645 (HSLA 80) and (b) a 50 ksi yield strength steel such as DH36 (HSS/HTS).

4. To investigate the effects of lower frequency on MIL S-24645 by selecting a value, x Hz, in the range 0.2-1 Hz chosen for comparison with data from offshore steels.
5. To conduct tests on base plate MIL S-24645 steel and DH36 at 10 Hz and a second frequency (either 2 Hz or x Hz, depending on the outcome of objective #4) in air and seawater at both the free corrosion potential and -1.0V (SCE) cathodic protection.
6. Optional tests (depending on the outcome of objective #5) to be conducted on a 30 ksi yield strength steel such as Grade E at either 2 Hz or x Hz in air and seawater at both the free corrosion potential and -1.0V (SCE) cathodic protection.
7. To conduct tests on submerged arc weld metal and heat affected zone (HAZ) microstructures of MIL S-24645 Class 3 steel at 20°C, 10 Hz and either 2 Hz or x Hz in air and ASTM seawater at the free corrosion potential and -1.0V (SCE) cathodic protection.
8. To characterize the base metal, weld metal, and HAZ microstructures, corrosion products, and crack propagation paths after testing under the above conditions.
9. To obtain potentiodynamic polarization curves for the weld metal and, if possible, HAZ microstructures.
10. To initiate a basic study to identify how the externally applied potential relates to the level of cathodic protection at the highly stressed crack tip.
11. To initiate an alloy design study aimed at optimizing the mechanical properties of MIL S-24645 steel.
12. To prepare, and submit for Ship Structures Committee approval, a detailed procedure for near-threshold corrosion fatigue crack growth rate testing in seawater environments with or without the application of cathodic protection.

EXPERIMENTAL RESULTS

Preparation of Baseline Welds

Materials

Additional 0.75 in. thick MIL S-24645 plate was obtained from Lukens Steel. This plate was from the same heat as used for the Phase I experiments.

Welding Procedure Development

Baseline welds were prepared using procedures identical to those employed in Phase I. Initially, four identical SAW welds were prepared in 30.0 in. long MIL S-24645 plate. Table 1 shows the SAW welding process parameters. These procedures were replicated when additional compact tension (CT) specimens were required later in the project.

Three plates were used for destructive testing to assure reproducibility of as-welded properties and for preparation of CT corrosion fatigue test specimens. The fourth was used for preparation of additional CT specimens.

Figures 1-3 show metallographic cross sections through the three welds destructively tested. Table 2 summarizes the weld metal chemical analyses for the three welds, which are seen to be virtually identical.

Table 3 shows the all-weld-metal and transverse tensile properties of each of the three welds. Table 4 summarizes the RT, 0, -60°, and -120°F CVN impact toughnesses measured for each weld and also for the base metal. Results for all welds are in reasonable agreement. CT specimens were machined with the notch at the weld metal centerline and HAZ (fusion line + 2mm) locations for corrosion fatigue testing. Double cantilever beam (constant K) specimens were machined from the base metal for possible use in electrochemical studies of corrosion fatigue crack growth.

Preparation of Welds with Varying Cu, C Contents

To permit an evaluation of experimental submerged arc weld metal compositions, in particular the effect of weld metal Cu content on as-welded microstructure, strength, and impact toughness (objective No. 1), a series of five metal powder-cored electrode compositions was fabricated at Rankin Industries, San Diego. Each was fabricated from low S, P sheath material in 100 lb quantities. Wire diameter was 0.093 in.

Table 5 shows the composition range for the baseline L-TEC 95 solid electrode. Experimental composition F8901 is an attempt to hit the midpoints of the L-TEC 95 compositional range with a powder-cored electrode to compare the performance of powder-cored vs. solid electrode baseline compositions. Experimental composition F8902 separates the effect of low C content on the baseline composition. Experimental compositions F8903-5 introduce varying Cu levels into the low-C filler metal composition to approach base metal Cu content.

The five powder-cored electrode compositions shown in Table 5 were used for submerged arc welding trials. Most initial experiments were performed with the F8901 electrode composition, which is

the powder-cored analog of the L-TEC 95 solid electrode. The electrodes were baked out at 475°F for 16 hours prior to use.

Initial welding conditions used for the F8901 powder-cored electrode duplicated those used previously for the L-TEC 95 solid electrode (shown in Table 1). These conditions were found to result in high levels of weld metal porosity. Higher heat input conditions were established as shown in Table 6. These conditions led to elimination of weld metal porosity but did not completely eliminate intermittent fusion line porosity. Welds satisfactory for initial mechanical testing were nevertheless produced.

Table 7 shows the weld metal chemical analyses for the powder-cored electrode weld. These should be compared with the solid electrode welds shown previously (Table 2). The powder-cored electrode weld exhibits slightly higher C, Mn, Cr, and Ni levels, and apparently lower O₂ levels, than the solid electrode welds.

Tensile property data (Table 8) for the powder-cored and solid electrode welds show slightly higher yield strength levels for the powder-cored electrode weld with other properties virtually identical to those of the solid electrode welds. CVN impact toughness values for the powder-cored electrode weld are shown in Table 9 and should be compared with Table 4 for corresponding solid electrode weld values. Weld metal impact toughnesses for the powder-cored electrode welds are significantly lower than for the solid electrode weld. HAZ toughnesses are higher for the powder-cored electrode weldments due presumably to a lower effective heat input for these welds.

Two replicate welded test plates were prepared with the low-C F8902 powder-cored electrode. The plates are identified as 12-890920 and 13-890921. Welding procedures used, which are identical to those used previously for the F8901 electrode, are shown in Table 10. The welded test plates were found acceptable in radiographic examination. (Subsequently, minor lack of fusion on the vertical side of the weld metal was detected during machining which, because of its orientation, was not visible in radiography.)

Weld metal chemical analyses for both plates are shown in Table 11, where the compositions are seen to be quite similar. Both exhibit the desired low C levels. Destructive testing was performed on one plate. Table 12 compares the tensile properties obtained for the low-C F8902 powder-cored electrode with results for higher-C solid and powder-cored electrodes, where the only possibly significant difference for the low-C electrode weld may be a slightly higher weld metal yield strength.

Table 13 shows the impact toughness test results. These should be compared with those shown in Table 9 for the higher-C F8901 powder-cored electrode. The lower carbon weld metal produced

by the low-C F8902 powder-cored electrode shows lower weld metal toughness. Somewhat higher HAZ impact toughnesses are observed.

Additional test plates were welded using a vacuum baked version of the powder-cored high electrode composition F8901. The electrodes were vacuum baked at 700°F for 2 hours and are designated F8901-2. Welding process parameters are shown in Table 14. For a constant electrode feed rate, the vacuum baked electrode was found to draw approximately 15% more welding current than the original F8901 electrode (see Table 6). Travel speed was increased slightly to partially compensate for the increased heat input which resulted.

One as-welded test plate (18-900705) was used for destructive testing. Table 15 shows the weld metal chemical analysis for this weld. It is similar to that obtained for the F8901 electrode. Table 16 shows a comparison of the tensile properties obtained with the F8901 and F8901-2 electrodes. Higher all-weld-metal tensile strength was observed for the vacuum baked electrode. Table 17 shows a comparison of the impact toughness of weldments prepared with the F8901 and F8901-2 electrodes. HAZ toughnesses are similar as expected. Weld metal toughness appears significantly better for the weld prepared with the vacuum baked electrode, particularly at -60°F, and approaches that of the baseline weld.

One weld was prepared with the vacuum baked version of the F8902 electrode. Welding process parameters are shown in Table 18. Two welds were prepared with the non-vacuum baked versions of the high-Cu-content F8903 and F8904 electrodes. Welding process parameters are shown in Tables 19 and 20. Weld metal chemical analyses for these latter two welds are shown in Table 21.

Destructive test results were obtained for the additional weld prepared with the vacuum baked version of the F8902 electrode. Weld metal chemical analysis is shown in Table 22 and compared with earlier welds prepared with the non-vacuum baked version of this electrode. A metallographic cross section of weld No. 19-900904 is shown in Figure 4.

Table 23 shows the comparative tensile properties of the non-vacuum baked and vacuum baked versions of welds prepared with the F8902 low-C electrode. The only obvious difference is lower all-weld metal yield strength for the weld prepared with the vacuum baked electrode. Table 24 shows a comparison of the impact toughness properties. With respect to weld metal toughness, the vacuum baked electrode weld shows significantly higher toughness only at 0°F, the results for other temperatures being virtually identical to those of the non-vacuum baked electrode weld. HAZ toughness values are similar for both weldments.

The two welds prepared with non-vacuum baked versions of the higher-Cu-content, low-C electrodes were also destructively tested.

Table 25 shows the tensile properties of the welds prepared with non-vacuum baked versions of the F8903 and F8904 electrodes and contrasts them with other powder-cored electrodes of lower Cu contents. The sequentially increasing Cu content of the low-C F8902, 3, 4 electrode series has no apparent effect on tensile properties.

Impact toughness properties of the weldments produced with the F8903 and F8904 electrodes compared with the low-Cu F8902 electrode are shown in Table 26. At the higher test temperature, the toughness values for the higher-Cu-content weld metals are inferior to those of the low-Cu F8902 electrode, at least in the non-vacuum baked condition.

Metallographic cross sections of the welds prepared with the F8903 and F8904 electrodes are shown in Figures 5 and 6.

Two welds were prepared with the vacuum baked versions of high-Cu-content powder-cored electrodes F8903-2 and F8904-2 and destructively tested for comparison with results on non-vacuum baked electrodes. Welding process parameters used to prepare these two welds are shown in Tables 27 and 28.

Weld metal chemical analyses for each weld are shown in Table 29. These results are similar to those shown previously for welds prepared with the same electrodes but in the as-received, rather than vacuum baked, condition.

Tensile test results are shown in Table 30 and compared with those for the high-Cu-content non-vacuum baked electrodes. The all-weld-metal yield strengths for both vacuum baked electrode welds were noticeably higher than for their non-vacuum baked counterparts. For the highest Cu-content weld, the all-weld-metal elongation was sharply reduced for the weld prepared with the vacuum baked electrode.

Table 31 summarizes the impact toughness values measured for these welds compared with the non-vacuum baked versions. Weld metal values are similar for vacuum baked and non-vacuum baked electrode welds and both are inferior to those of the lower-Cu-content welds reported previously. HAZ toughness values are similar to those of other welds of similar heat input prepared during the project.

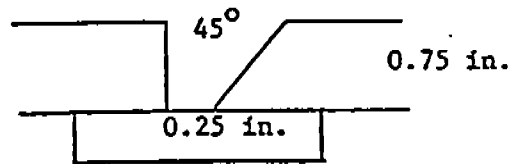
CONCLUSIONS FROM WELDING PROCEDURE AND FILLER METAL COMPOSITON DEVELOPMENT STUDIES

1. Baseline welding procedures with the L-TEC 95 solid electrode gave consistent and reproducible results. A number of weld metal and HAZ CT test specimens were prepared from replicate welds for use in corrosion fatigue test methodology development.
2. Powder-cored electrodes of a deposit composition equivalent to the L-TEC 95 solid electrode produced welds of similar tensile properties but of lower weld metal impact toughness, particularly at the lower test temperatures. HAZ impact toughnesses were higher for the powder-cored electrode welds.
3. Weld metal impact toughness for welds produced with the powder-cored electrode of a deposit composition equivalent to the L-TEC 95 solid electrode was improved significantly by vaccuum baking the electrode prior to welding and was nearly equal to that obtained with the solid electrode.
4. A lower-C-content version of the same powder-cored electrode composition produced equivalent tensile properties but reduced weld metal impact toughness. Vacuum baking prior to welding provided no significant improvement in weld metal impact toughness.
5. Sequential increases in the Cu content of the low-C-content powder-cored electrode composition had no apparent effect on weldment tensile strength and did not improve weld metal impact toughness. Vacuum baking the electrodes prior to welding increased weld metal tensile strength but reduced weld metal ductility. Weld metal impact toughness was inferior to that obtained with lower-Cu-content weld metal compositions.

Table 1. Submerged Arc Weld Procedures

Base Plate: 0.75 in. thick, MIL S-24645

Joint Configuration:



Weld Length: 26.0 in.

Electrode: 0.093 in. D., Linde 95 MIL 100S-1

Electrode Extension: 1.50 in.

Flux: Oerlikon OP 121TT

Flux Depth: 0.75 in.

Preheat: None

Interpass Temperature: 200°F

Voltage: 33V DCRP

Amperage: 350A

Travel Speed: 12.8

Heat Input: 53,600 J/in.

No. Passes: 10

Plate I.D. Nos. 01-890131
02-890201
03-890201
04-890303

Table 2. Weld Metal Chemical Analyses (wt %)

<u>Element</u>	<u>01-890131</u>	<u>02-890201</u>	<u>03-890201</u>
C	0.03	0.03	0.03
Mn	1.40	1.41	1.40
Si	0.39	0.39	0.39
P	0.013	0.014	0.013
S	0.011	0.012	0.011
Cr	0.15	0.12	0.14
Ni	1.70	1.76	1.77
Mo	0.33	0.34	0.33
Cu	0.17	0.11	0.15
O ₂	230 ppm	242 ppm	271 ppm
Fe	Bal.	Bal.	Bal.

Table 3. Tensile Test Results

	Yield Strength (psi)	Tensile Strength (psi)	Elonga- tion(%)	Reduc- tion in Area(%)	Frac- ture Location
Plate #					
01-890131					
All Weld	85900	109000	27	67	*
Transverse	83200	95700	21	79	BM
Plate #					
02-890201					
All Weld	85900	110000	25	78	*
Transverse	83900	96000	22	79	BM
Plate #					
03-890201					
All Weld	85900	112000	25	69	*
Transverse	84300	95500	23	78	BM

Table 4. Charpy Vee Notch Impact Toughness Test Results

	<u>Impact Strength (ft-lb)</u>	<u>Lateral Deformation (mils)</u>	<u>% Shear Area</u>
Plate #01-890131 Weld			
RT			
1	112.0	0.073	100
2	120.0	0.069	100
3	107.5	0.070	100
Average	113.2		
0°F			
1	87.0	0.051	80
2	88.0	0.061	80
3	90.5	0.050	90
Average	88.5		
-60°F			
1	43.5	0.031	40
2	42.5	0.028	40
3	55.0	0.035	40
Average	47.0		
-120°F			
1	18.5	0.010	20
2	30.0	0.017	20
3	36.5	0.024	20
Average	28.3		
Plate #01-890131 HAZ - 2mm from F.L.			
RT			
1	138.0	0.086	100
2	137.0	0.083	100
3	141.0	0.083	100
Average	138.7		
0°F			
1	125.0	0.080	100
2	114.0	0.071	100
3	127.0	0.079	100
Average	122.0		

Table 4. (Continued)

	<u>Impact Strength (ft-lb)</u>	<u>Lateral Deformation (mils)</u>	<u>% Shear Area</u>
-60°F			
1	60.0	0.042	60
2	99.0	0.067	60
3	74.0	0.050	60
Average	77.7		
-120°F			
1	43.5	0.032	20
2	34.0	0.020	10
3	26.0	0.022	20
Average	34.5		
Plate #02-890201			
Weld			
RT			
1	126.0	0.076	100
2	120.0	0.083	100
3	119.0	0.080	100
Average	121.7		
-60°F			
1	104.5	0.055	90
2	96.0	0.056	90
3	88.5	0.060	90
Average	96.3		
-60°F			
1	62.5	0.049	70
2	60.0	0.042	70
3	64.0	0.041	70
Average	62.2		
-120°F			
1	20.0	0.014	40
2	20.5	0.014	40
3	30.0	0.020	40
Average	23.5		

Table 4. (Continued)

	<u>Impact Strength (ft-lb)</u>	<u>Lateral Deformation (mils)</u>	<u>% Shear Area</u>
Plate #02-890201			
HAZ - 2mm from FL			
RT			
1	141.0	0.082	100
2	143.0	0.087	100
3	137.0	0.091	100
Average	140.3		
0°F			
1	144.0	0.088	100
2	128.5	0.083	100
3	144.5	0.086	100
Average	139.0		
-60°F			
1	102.0	0.068	70
2	93.5	0.058	70
3	83.5	0.056	60
Average	93.5		
-120°F			
1	55.0	0.039	40
2	26.0	0.022	10
3	37.0	0.027	40
Average	39.3		
Plate #03-890201			
Weld			
RT			
1	125.5	0.082	100
2	126.0	0.082	100
3	130.0	0.080	100
Average	127.2		
0°F			
1	99.5	0.060	100
2	91.0	0.060	100
3	100.5	0.063	100
Average	97.0		

Table 4. (Continued)

	<u>Impact Strength (ft-lb)</u>	<u>Lateral Deformation (mils)</u>	<u>% Shear Area</u>
-60°F			
1	61.0	0.037	70
2	63.0	0.040	60
3	37.5	0.026	50
Average	53.8		
-120°F			
1	20.0	0.011	20
2	22.5	0.013	20
3	33.5	0.026	40
Average	25.3		
Plate #03-890201			
HAZ - 2mm from F.L.			
RT			
1	134.0	0.083	100
2	132.0	0.078	100
3	146.0	0.088	100
Average	137.3		
0°F			
1	135.0	0.078	100
2	128.5	0.075	100
3	137.0	0.080	100
Average	132.8		
-60°F			
1	110.0	0.071	80
2	109.0	0.069	70
3	116.5	0.077	80
Average	111.8		
-120°F			
1	40.0	0.044	30
2	32.0	0.022	20
3	36.0	0.027	20
Average	36.0		

Table 4. (Continued)

	<u>Impact Strength (ft-lb)</u>	<u>Lateral Deformation (mils)</u>	<u>% Shear Area</u>
Plate #01-890131			
Base Metal			
RT			
1	204.0	0.089	100
2	211.5	0.094	100
3	213.0	0.093	100
Average	209.5		
0°F			
1	186.0	0.091	100
2	187.5	0.092	100
3	220.0	0.085	100
Average	197.8		
-60°F			
1	147.5	0.086	100
2	196.0	0.091	100
3	146.0	0.085	100
Average	163.2		
-120°F			
1	147.0	0.085	100
2	63.0	0.023	10
3	124.0	0.078	100
Average	111.3		

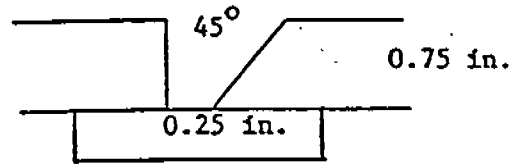
Table 5. Target Filler Metal Compositions (wt %, Balance Fe)

<u>Electrode</u>	<u>C</u>	<u>Mn</u>	<u>Si</u>	<u>Mo</u>	<u>Ni</u>	<u>Cr</u>	<u>P</u>	<u>S</u>	<u>Cu</u>
L-TEC 95 Min.	0.03		1.45	0.25	0.30	1.60	0.05	-	-
Solid Electrode 0.008 Max.	0.09 -		1.75	0.40	0.40	1.95	0.16	0.010	
<u>Powder-Cored Compositions</u>									
F8901 0.010	0.06 -		1.62	0.32	0.35	1.76	0.10	0.010	
F8902 0.010	0.02 -		1.62	0.32	0.35	1.76	0.10	0.010	
F8903 0.010	0.02 0.40		1.62	0.32	0.35	1.76	0.10	0.010	
F8904 0.010	0.02 0.80		1.62	0.32	0.35	1.76	0.10	0.010	
F8905 0.010	0.02 1.20		1.62	0.32	0.35	1.76	0.10	0.010	

Table 6. Submerged Arc Weld Procedures - Powder-Cored Electrode

Base Plate: 0.75 in. thick, MIL S-24645

Joint Configuration:



Weld Length:

26.0 in.

Electrode:

0.093 in. D., F8901

Electrode Extension:

1.50 in.

Flux:

Oerlikon OP 121TT

Flux Depth:

0.75 in.

Preheat:

None

Interpass Temperature:

200°F

Voltage:

35V DCRP

Amperage:

360A

Travel Speed:

13.0 in./min

Heat Input:

58,200 J/in.

No. Passes:

7

Plate I.D. Nos.

08-890907
09-890914
10-890915

Table 7. Weld Metal Chemical Analyses of Powder-Cored Electrode (F8901)
Weld (wt %)

<u>Element</u>	<u>08-890907</u>
C	0.06
Mn	1.50
Si	0.29
P	0.11
S	0.11
Cr	0.22
Ni	1.83
Mo	0.37
Cu	0.10
O ₂	0.006
Fe	Bal.

Table 8. Comparison of Tensile Test Results for Solid and Powder-Cored Electrodes

Solid Electrode (L-TEC 95)	Yield Strength (psi)	Tensile Strength (psi)	Reduc- Elonga- tion (%)	tion in Area (%)	Frac- ture Location
Plate # 01-890131					
All Weld	85900	109000	27	67	*
Transverse	83200	95700	21	79	BM
Plate # 02-890201					
All Weld	85900	110000	25	78	*
Transverse	83900	96000	22	79	BM
Plate # 03-890201					
All Weld	85900	112000	25	69	*
Transverse	84300	95500	23	78	BM
Powder-Cored Electrode (F8901)					
Plate # 09,10					
All Weld	87000	110000	23	70	*
Transverse	87700	98700	23.5	75	BM

Table 9. Charpy Vee Notch Impact Toughness Test Results - Powder-Cored Electrode (F8901)

	Impact Strength (ft-lb)	Lateral Deformation (mils)	Shear Area (%)
Plate 09, 10 Weld			
RT			
1	90.5	0.066	100
2	94.0	0.063	100
3	86.0	0.055	100
Average	90.2		
0°F			
1	72.0	0.51	80
2	75.0	0.50	80
3	72.5	0.50	80
Average	73.2		
-60°F			
1	32.0	0.021	30
2	26.0	0.019	30
3	28.5	0.020	25
Average	28.8		
-120°F			
1	20.0	0.011	10
2	16.0	0.008	5
3	16.0	0.008	5
Average	17.3		
Plate 09, 10 HAZ - 2mm from F.L.			
RT			
1	159.5	0.091	90
2	144.5	0.091	90
3	149.0	0.093	90
Average	151.0		
0°F			
1	158.0	0.097	90
2	151.0	0.095	90
3	159.5	0.096	90
Average	156.2		

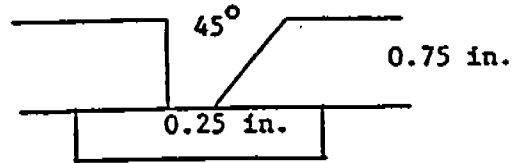
Table 9. (Continued)

	<u>Impact Strength (ft-lb)</u>	<u>Lateral Deformation (mils)</u>	<u>Shear Area (%)</u>
-60°F			
1	121.5	0.080	60
2	117.0	0.078	50
3	128.0	0.082	60
Average	122.2		
-120°F			
1	39.5	0.029	15
2	69.0	0.049	20
3	80.5	0.057	20
Average	63.0		

Table 10. Submerged Arc Weld Procedures - Powder-Cored Electrode

Base Plate: 0.75 in. thick, MIL S-24645

Joint Configuration:



Weld Length: 26.0 in.

Electrode: 0.093 in. D., F8902

Electrode Extension: 1.50 in.

Flux: Oerlikon OP 121TT

Flux Depth: 0.75 in.

Preheat: None

Interpass Temperature: 200°F

Voltage: 35V DCRP

Amperage: 360A

Travel Speed: 13.0 in./min

Heat Input: 58,200 J/in.

No. Passes: 7

Plate I.D. Nos. 12-890920
13-890921

Table 11. Weld Metal Chemical Analyses for Low-C Powder-Cored Electrode (F8902) Welds (wt %)

<u>Element</u>	<u>12-890920</u>	<u>13-890921</u>
C	0.04	0.04
Mn	1.49	1.50
Si	0.35	0.35
P	0.012	0.013
S	0.011	0.014
Cr	0.25	0.28
Ni	1.79	1.97
Mo	0.33	0.34
Cu	0.09	0.12
O	398 ppm	455 ppm
Fe	Bal.	Bal.

Table 12. Comparison of Tensile Test Results for Solid and Powder-Cored Electrodes

Solid Electrode (L-TEC 95)	Yield Strength (psi)	Tensile Strength (psi)	Elonga- tion (%)	Reduc- tion in Area (%)	Frac- ture Location
Plate # 01-890131					
All Weld	85900	109000	27	67	*
Transverse	83200	95700	21	79	BM
Plate # 02-890201					
All Weld	85900	110000	25	78	*
Transverse	83900	96000	22	79	BM
Plate # 03-890201					
All Weld	85900	112000	25	69	*
Transverse	84300	95500	23	78	BM
<u>Powder-Cored Electrode (F8901)</u>					
Plate # 09,10					
All Weld	87000	110000	23	70	*
Transverse	87700	98700	23.5	75	BM
<u>Low-C Powder-Cored Electrode (F8902)</u>					
Plate # 13-890921					
All Weld	93000	104000	20	69	*
Transverse	84700	96200	24	79	BM

Table 13. Charpy Vee Notch Impact Toughness Test Results - Powder-Cored Electrode (F8902)

	Impact Strength (ft-lb)	Lateral Deformation (mils)	Shear Area (%)
Plate 13 Weld			
RT			
1	71.0	0.055	95
2	74.5	0.056	95
3	74.0	0.059	90
Average	73.2		
0°F			
1	46.0	0.035	40
2	34.0	0.029	50
3	47.0	0.037	60
Average	42.3		
-60°F			
1	27.5	0.019	20
2	20.0	0.013	20
3	30.0	0.022	20
Average	25.8		
-120°F			
1	8.5	0.005	5
2	8.0	0.005	5
3	7.5	0.004	5
Average	8.0		
Plate 13 HAZ - 2mm from F.L.			
RT			
1	190.5	0.095	No break
2	172.0	0.097	No break
3	167.0	0.093	No break
Average	176.5		
0°F			
1	148.0	0.092	No break
2	148.0	0.099	No break
3	162.5	0.091	No break
Average	152.8		

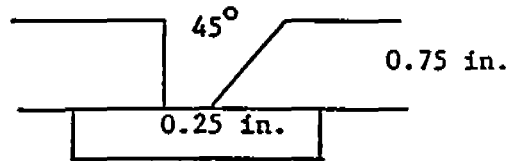
Table 13. (Continued)

	<u>Impact Strength (ft-lb)</u>	<u>Lateral Deformation (mils)</u>	<u>Shear Area (%)</u>
-60°F			
1	144.0	0.087	No break
2	125.0	0.081	No break
3	132.5	0.080	No break
Average	152.8		
-120°F			
1	100.0	0.068	20
2	13.0	0.008	10
3	123.0	0.082	30
Average	78.7		

Table 14. Submerged Arc Weld Procedures - Powder-Cored Electrode

Base Plate: 0.75 in. thick, MIL S-24645

Joint Configuration:



Weld Length:

26.0 in.

Electrode:

0.093 in. D., F8901-2, vacuum baked

Electrode Extension:

1.50 in.

Flux:

Oerlikon OP 121TT

Flux Depth:

0.75 in.

Preheat:

None

Interpass Temperature:

200°F

Voltage:

37V DCRP

Amperage:

420A

Travel Speed:

15.0 in./min

Heat Input:

62,160 J/in.

No. Passes:

7

Plate I.D. No.

18-900705

Table 15. Weld Metal Chemical Analysis of Vacuum Baked Powder-Cored Electrode (F8901-2) Weld (wt %)

<u>Element</u>	<u>18-900705</u>
C	0.06
Mn	1.44
Si	0.39
P	0.012
S	0.013
Cr	0.28
Ni	1.85
Mo	0.39
Cu	0.17
O ₂	510 ppm
Fe	Bal.

Table 16. Comparison of Tensile Test Results for Powder-Cored and Vacuum Baked Powder-Cored Electrodes

Powder-Cored Electrode	Yield Strength (psi)	Tensile Strength (psi)	Elongation (%)	Reduction in Area (%)	Fracture Location
<u>Powder-Cored Electrode (F8901)</u>					
Plate #					
09,10					
All Weld	87000	110000	23	70	*
Transverse	87700	98700	23.5	75	BM
<u>Vacuum Baked Powder-Cored Electrode (F8901-2)</u>					
Plate #					
18					
All Weld	95600	121000	21	40	*
Transverse	87700	99200	21.5	77	BM

Table 17. Comparison of Charpy Vee Notch Impact Toughness Test Results - Powder-Cored Electrode (F8901) and Vacuum Baked Powder-Cored Electrode (F8901-2)

	<u>Impact Strength (ft-lb)</u>	<u>Lateral Deformation (mils)</u>	<u>Shear Area (%)</u>
Plate 09, 10 Weld			
RT			
1	90.5	0.066	100
2	94.0	0.063	100
3	86.0	0.055	100
Average	90.2		
0°F			
1	72.0	0.51	80
2	75.0	0.50	80
3	72.5	0.50	80
Average	73.2		
-60°F			
1	32.0	0.021	30
2	26.0	0.019	30
3	28.5	0.020	25
Average	28.8		
-120°F			
1	20.0	0.011	10
2	16.0	0.008	5
3	16.0	0.008	5
Average	17.3		
Plate 09, 10 HAZ - 2mm from F.L.			
RT			
1	159.5	0.091	90
2	144.5	0.091	90
3	149.0	0.093	90
Average	151.0		
0°F			
1	158.0	0.097	90
2	151.0	0.095	90
3	159.5	0.096	90
Average	156.2		

Table 17. (Continued)

	<u>Impact Strength (ft-lb)</u>	<u>Lateral Deformation (mils)</u>	<u>Shear Area (%)</u>
-60°F			
1	121.5	0.080	60
2	117.0	0.078	50
3	128.0	0.082	60
Average	122.2		
-120°F			
1	39.5	0.029	15
2	69.0	0.049	20
3	80.5	0.057	20
Average	63.0		
Plate 18 Weld			
RT			
1	96.5	0.067	100
2	97.5	0.065	100
3	96.0	0.065	100
Average	96.7		
0°F			
1	79.5	0.050	90
2	80.0	0.055	90
3	89.5	0.057	95
Average	83.0		
-60°F			
1	62.0	0.308	40
2	62.5	0.040	40
3	57.0	0.036	30
Average	60.5		
-120°F			
1	11.0	0.005	5
2	20.0	0.010	10
3	29.0	0.018	10
Average	20.0		
Plate 18			
HAZ - 2mm from F.L.			
RT			
1	162.5	0.098	90
2	157.0	0.093	90
3	155.0	0.093	90
Average	158.2		

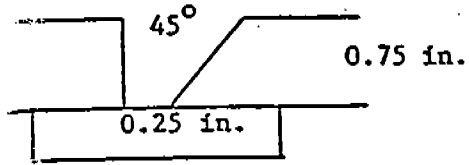
Table 17. (Continued)

	<u>Impact Strength (ft-lbs)</u>	<u>Lateral Deformation (mils)</u>	<u>Shear Area (%)</u>
Plate 18			
HAZ - 2mm from F.L.			
0°F			
1	167.5	0.099	90
2	167.0	0.095	90
3	164.5	0.080	90
Average	166.3		
-60°F			
1	146.0	0.090	89
2	116.0	0.074	50
3	118.5	0.093	60
Average	126.3		
-120°F			
1	127.0	0.079	60
2	55.0	0.039	25
3	90.0	0.061	40
Average	90.7		

1 Procedures - Powder-Cored Electrode

Base Plate: 1/8 in. thick, MIL S-24645

Joint Configuration:



Electrode: 1/8 in.

Electrode Diameter: 3/32 in. D., F8902-2, vacuum baked

Shielding Gas: Argon

Flux: Nikon OP 121TT

Flux Depth: 1/8 in.

Preheat: None

Interpass Temperature: 100°F

Voltage: 20 V DCRP

Amperage: 100 A

Travel Speed: 10 in./min

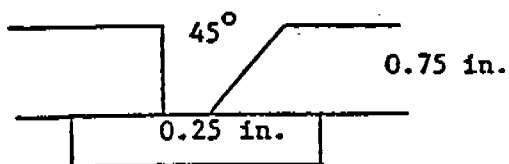
Heat Input: 160 J/in.

900904

Table 19. Submerged Arc Weld Procedures - Powder-Cored Electrode

Base Plate: 0.75 in. thick, MIL S-24645

Joint Configuration:



Weld Length:

20.0 in.

Electrode:

0.093 in. D., F8903-1, vacuum baked

Electrode Extension:

1.50 in.

Flux:

Oerlikon OP 121TT

Flux Depth:

1.0 in.

Preheat:

None

Interpass Temperature:

200°F

Voltage:

37V DCRP

Amperage:

390A

Travel Speed:

15.0 in./min

Heat Input:

57,720 J/in.

No. Passes:

6

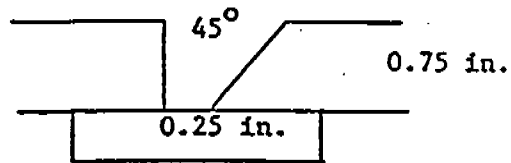
Plate I.D. No.

16-900330

Table 20. Submerged Arc Weld Procedures - Powder-Cored Electrode

Base Plate: 0.75 in. thick, MIL S-24645

Joint Configuration:



Weld Length: 20.0 in.

Electrode: 0.093 in. D., F8904-1, vacuum baked

Electrode Extension: 1.50 in.

Flux: Oerlikon OP 121TT

Flux Depth: 1.0 in.

Preheat: None

Interpass Temperature: 200°F

Voltage: 37V DCRP

Amperage: 390A

Travel Speed: 15.0 in./min

Heat Input: 57,720 J/in.

No. Passes: 7

Plate I.D. No. 17-900602

Table 21. Weld Metal Chemical Analysis of Powder-Cored Electrode
(F8903-1, F8904-1) Welds (wt %)

<u>Element</u>	<u>16-900330</u>	<u>17-900602</u>
C	0.02	0.01
Mn	1.34	1.63
Si	0.27	0.27
P	0.013	0.013
S	0.013	0.013
Cr	0.21	0.21
Ni	1.94	1.78
Mo	0.34	0.37
Cu	0.51	0.73
O ₂	0.051	0.051
Fe	Bal.	Bal.

Table 22. Weld Metal Chemical Analyses of Powder-Cored Electrode (F8902) Welds (wt %)

<u>Element</u>	<u>12-890920*</u>	<u>13-890921*</u>	<u>19-900904**</u>
C	0.04	0.04	0.04
Mn	1.49	1.50	1.30
Si	0.35	0.35	0.30
P	0.012	0.013	0.012
S	0.011	0.014	0.013
Cr	0.25	0.28	0.27
Ni	1.79	1.97	1.84
Mo	0.33	0.34	0.35
Cu	0.09	0.12	0.16
O	398 ppm	455 ppm	413 ppm
Fe	Bal.	Bal.	Bal.

*Non-vacuum baked.

**Vacuum baked.

Table 23. Comparison of Tensile Test Results for Vacuum Baked and Non-Vacuum Baked Low-Carbon F8902 Powder-Cored Electrodes

Low-C Powder-Cored Electrode (F8902)	Yield Strength (psi)	Tensile Strength (psi)	Elongation (%)	Reduction in Area (%)	Fracture Location
Plate # 13-890921					
All Weld	93000	104000	20	69	*
Transverse (Non-vacuum baked)	84700	96200	24	79	BM
Plate # 19-900904					
All Weld	82200	108000	25	62	*
Transverse (Vacuum baked)	85600	96600	23.5	79	BM

Table 24. Charpy Vee Notch Impact Toughness Test Results for Non-Vacuum Baked and Vacuum Baked Low-Carbon Powder-Cored Electrode (F8902)

	Impact Strength <u>(ft-lb)</u>	Lateral Deformation <u>(mils)</u>	Shear Area <u>(%)</u>
Plate 13 Weld (Non-vacuum baked)			
RT			
1	71.0	0.055	95
2	74.5	0.056	95
3	74.0	0.059	90
Average	73.2		
0°F			
1	46.0	0.035	40
2	34.0	0.029	50
3	47.0	0.037	60
Average	42.3		
-60°F			
1	27.5	0.019	20
2	20.0	0.013	20
3	30.0	0.022	20
Average	25.8		
-120°F			
1	8.5	0.005	5
2	8.0	0.005	5
3	7.5	0.004	5
Average	8.0		
Plate 13 HAZ - 2 mm from F.L.			
RT			
1	190.5	0.095	No break
2	172.0	0.097	No break
3	167.0	0.093	No break
Average	176.5		
0°F			
1	148.0	0.092	No break
2	148.0	0.099	No break
3	162.5	0.091	No break
Average	152.8		

Table 24. (Continued)

	<u>Impact Strength (ft-lb)</u>	<u>Lateral Deformation (mils)</u>	<u>Shear Area (%)</u>
-60°F			
1	144.0	0.087	No break
2	125.0	0.081	No break
3	132.5	0.080	No break
Average	152.8		
-120°F			
1	100.0	0.068	20
2	13.0	0.008	10
3	123.0	0.082	30
Average	78.7		
Plate 19 Weld (Vacuum baked)			
RT			
1	68.5	0.050	80
2	75.0	0.051	90
3	70.0	0.047	90
Average	71.2		
0°F			
1	83.5	0.059	80
2	61.0	0.040	60
3	49.5	0.036	50
Average	64.7		
-60°F			
1	25.0	0.018	15
2	25.0	0.018	20
3	21.0	0.015	15
Average	23.7		
-120°F			
1	9.5	0.006	10
2	9.5	0.006	10
3	7.5	0.004	5
Average	8.8		

Table 24. (Continued)

	<u>Impact Strength (ft-lb)</u>	<u>Lateral Deformation (mils)</u>	<u>Shear Area (%)</u>
Plate 19 (HAZ - 2 mm from F.L.)			
RT			
1	155.5	0.094	90
2	159.0	0.094	90
3	154.0	0.090	90
Average	156.2		
0°F			
1	174.0	0.088	90
2	139.5	0.085	90
3	177.0	0.089	90
Average	163.5		
-60°F			
1	145.0	0.082	90
2	124.5	0.078	90
3	136.0	0.086	90
Average	135.2		
-120°F			
1	58.0	0.041	30
2	35.0	0.025	20
3	95.0	0.062	30
Average	62.7		

Table 25. Comparison of Tensile Test Results for Non-Vacuum Baked Powder-Cored Electrodes

Electrode	Yield Strength (psi)	Tensile Strength (psi)	Elongation (%)	Reduction in Area (%)	Fracture Location
F8901					
All Weld	87000	110000	23	70	*
Transverse	87700	98700	23.5	75	BM
F8902					
All Weld	93000	104000	20	69	*
Transverse	84700	96200	24	79	BM
F8903					
All Weld	84400	101000	25	71	*
Transverse	87400	97400	22.5	81.8	BM
F8904					
All Weld	91900	103000	20	64	*
Transverse	84100	96400	22.5	81.5	BM

Table 26. Charpy Vee Notch Impact Toughness Test Results - Low-Carbon Powder-Cored Electrodes

	<u>Impact Strength (ft-lb)</u>	<u>Lateral Deformation (mils)</u>	<u>Shear Area (%)</u>
Plate 13 Weld (F8902)			
RT			
1	71.0	0.055	95
2	74.5	0.056	95
3	74.0	0.059	90
Average	73.2		
0°F			
1	46.0	0.035	40
2	34.0	0.029	50
3	47.0	0.037	60
Average	42.3		
-60°F			
1	27.5	0.019	20
2	20.0	0.013	20
3	30.0	0.022	20
Average	25.8		
-120°F			
1	8.5	0.005	5
2	8.0	0.005	5
3	7.5	0.004	5
Average	8.0		
Plate 13 HAZ - 2 mm from F.L.			
RT			
1	190.5	0.095	No break
2	172.0	0.097	No break
3	167.0	0.093	No break
Average	176.5		
0°F			
1	148.0	0.092	No break
2	148.0	0.099	No break
3	162.5	0.091	No break
Average	152.8		

Table 26. (Continued)

	Impact Strength (ft-lb)	Lateral Deformation (mils)	Shear Area (%)
-60°F			
1	144.0	0.087	No break
2	125.0	0.081	No break
3	132.5	0.080	No break
Average	152.8		
-120°F			
1	100.0	0.068	20
2	13.0	0.008	10
3	123.0	0.082	30
Average	78.7		
Plate 16 Weld (F8903)			
RT			
1	64.0	0.046	90
2	65.0	0.049	90
3	61.0	0.046	80
Average	63.3		
0°F			
1	46.0	0.030	50
2	50.0	0.035	50
Average	48.0*		
-60°F			
1	23.5	0.011	25
2	22.5	0.016	20
Average	23.0*		
-120°F			
1	7.0	0.002	5
2	7.5	0.005	5
3	8.5	0.005	5
Average	7.7		
Plate 16			
HAZ - 2 mm from F.L.			
RT			
1	159.5	0.095	90
2	157.0	0.093	90
3	175.5	0.094	90
Average	164.0		

Table 26 (Continued)

	<u>Impact Strength (ft-lb)</u>	<u>Lateral Deformation (mils)</u>	<u>Shear Area (%)</u>
0°F			
1	144.5	0.082	90
2	130.5	0.080	90
Average	137.5*		
-60°F			
1	122.0	0.077	80
2	108.0	0.068	70
Average	115.0*		
-120°F			
1	56.5	0.039	20
2	71.0	0.047	30
3	68.5	0.045	30
Average	65.3		
Plate 17 Weld (F8904)			
RT			
1	58.5	0.046	30
2	62.0	0.048	40
3	62.0	0.049	40
Average	60.8		
0°F			
1	26.0	0.021	15
2	27.0	0.022	15
3	42.0	0.030	20
Average	31.7		
-60°F			
1	15.5	0.014	10
2	13.0	0.010	10
3	17.0	0.014	10
Average	15.2		
-120°F			
1	10.0	0.008	5
2	6.0	0.004	5
3	7.0	0.005	5
Average	7.7		

Table 26 (Continued)

	<u>Impact Strength (ft-lb)</u>	<u>Lateral Deformation (mils)</u>	<u>Shear Area (%)</u>
Plate 17			
HAZ - 2 mm from F.L.			
RT			
1	170.5	0.094	90
2	160.5	0.091	90
3	165.0	0.093	90
Average	165.3		
0°F			
1	164.0	0.095	90
2	158.5	0.091	90
3	165.5	0.091	90
Average	162.7		
-60°F			
1	121.0	0.079	80
2	106.5	0.071	80
3	127.0	0.085	90
Average	118.2		
-120°F			
1	44.5	0.035	20
2	106.5	0.065	50
3	115.0	0.077	50
Average	88.7		

*Insufficient material for third specimen.

Table 27. Submerged Arc Weld Procedure - Powder-Cored Electrode

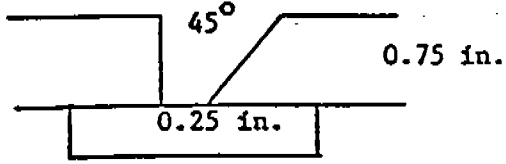
Base Plate:	0.75 in. thick, MIL S-24645
Joint Configuration:	
Weld Length:	24.0 in.
Electrode:	0.093 in. D., F8903-2, vacuum baked
Electrode Extension:	1.50 in.
Flux:	Oerlikon OP 121TT
Flux Depth:	1.0 in.
Preheat:	None
Interpass Temperature:	200°F
Voltage:	37 V DCRP
Amperage:	420 A
Travel Speed:	15.0 in./min
Heat Input:	62,160 J/in.
No. Passes:	7
Plate I.D. No.	20-901211

Table 28. Submerged Arc Weld Procedure - Powder-Cored Electrode

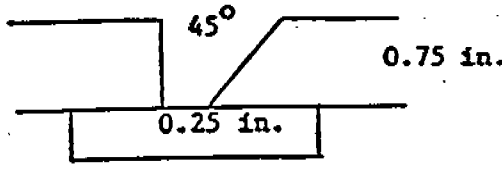
Base Plate:	0.75 in. thick, MIL S-24645
Joint Configuration:	
Weld Length:	24.0 in.
Electrode:	0.093 in. D., F8904-2, vacuum baked
Electrode Extension:	1.50 in.
Flux:	Oerlikon OP 121TT
Flux Depth:	1.0 in.
Preheat:	None
Interpass Temperature:	200°F
Voltage:	37 V DCRP
Amperage:	420 A
Travel Speed:	15.0 in./min
Heat Input:	62,160 J/in.
No. Passes:	7
Plate I.D. No.	21-901212

Table 29. Weld Metal Chemical Analysis of Vacuum Baked Powder-Cored Electrode (F8903-2, F8904-2) Welds (wt %)

<u>Element</u>	<u>20-901211</u>	<u>21-901212</u>
C	0.02	0.02
Mn	1.52	1.74
Si	0.34	0.36
P	0.012	0.012
S	0.012	0.013
Cr	0.23	0.22
Ni	2.14	1.90
Mo	0.39	0.41
Cu	0.57	0.70
O ₂	0.050	0.051
Fe	Bal.	Bal.

Table 30. Comparison of Tensile Test Results for Vacuum Baked and Non-Vacuum Baked High-Cu-Content Powder-Cored Electrodes

Electrode	Yield Strength (psi)	Tensile Strength (psi)	Elongation (%)	Reduction in Area (%)	Fracture Location
F8903					
All Weld	84400	101000	25	71	*
Transverse	87400	97400	22.5	81.8	BM
F8904					
All Weld	91900	103000	20	64	*
Transverse	84100	96400	22.5	81.5	BM
F8903-2 ^(a)					
All Weld	97600	106000	25.0	68	*
Transverse	86600	103000	22.0	76	BM
F8904-4 ^(a)					
All Weld	106000	110000	16.0	37	*
Transverse	85700	95800	22.5	76	BM

^(a) Vacuum baked

Table 31. Charpy Vee Notch Impact Toughness Test Results for Non-Vacuum Baked and Vacuum Baked High-Cu-Content Powder-Cored Electrodes

	<u>Impact Strength (ft-lb)</u>	<u>Lateral Deformation (mils)</u>	<u>Shear Area (%)</u>
Plate 16 Weld (F8903)			
RT			
1	64.0	0.046	90
2	65.0	0.049	90
3	61.0	0.046	80
Average	63.3		
0°F			
1	46.0	0.030	50
2	50.0	0.035	50
Average	48.0*		
-60°F			
1	23.5	0.011	25
2	22.5	0.016	20
Average	23.0*		
-120°F			
1	7.0	0.002	5
2	7.5	0.005	5
3	8.5	0.005	5
Average	7.7		
Plate 16 HAZ - 2 mm from F.L.			
RT			
1	159.5	0.095	90
2	157.0	0.093	90
3	175.5	0.094	90
Average	164.0		
0°F			
1	144.5	0.082	90
2	130.5	0.080	90
Average	137.5*		
-60°F			
1	122.0	0.077	80
2	108.0	0.068	70
Average	115.0*		

Table 31. (Continued)

	<u>Impact Strength (ft-lb)</u>	<u>Lateral Deformation (mils)</u>	<u>Shear Area (%)</u>
-120°F			
1	56.5	0.039	20
2	71.0	0.047	30
3	68.5	0.045	30
Average	65.3		

Plate 17 Weld (F8904)

RT			
1	58.5	0.046	30
2	62.0	0.048	40
3	62.0	0.049	40
Average	60.8		

0°F			
1	26.0	0.021	15
2	27.0	0.022	15
3	42.0	0.030	20
Average	31.7		

-60°F			
1	15.5	0.014	10
2	13.0	0.010	10
3	17.0	0.014	10
Average	15.2		

-120°F			
1	10.0	0.008	5
2	6.0	0.004	5
3	7.0	0.005	5
Average	7.7		

Plate 17
HAZ - 2 mm from F.L.

RT			
1	170.5	0.094	90
2	160.5	0.091	90
3	165.0	0.093	90
Average	165.3		

Table 31. (Continued)

	Impact Strength (ft-lb)	Lateral Deformation (mils)	Shear Area (%)
0°F			
1	164.0	0.095	90
2	158.5	0.091	90
3	165.5	0.091	90
Average	162.7		
-60°F			
1	121.0	0.079	80
2	106.5	0.071	80
3	127.0	0.085	90
Average	118.2		
-120°F			
1	44.5	0.035	20
2	106.5	0.065	50
3	115.0	0.077	50
Average	88.7		
Plate 20 Weld (F8903-2) Vacuum Baked			
RT			
1	70.5	0.055	90
2	63.0	0.051	85
3	62.5	0.049	80
Average	65.3		
0°F			
1	43.0	0.035	60
2	51.5	0.039	60
3	50.0	0.041	65
Average	48.2		
-60°F			
1	28.0	0.020	40
2	23.0	0.020	30
3	27.0	0.020	20
Average	26.0		
-120°F			
1	9.5	0.008	5
2	9.5	0.007	5
3	8.0	0.008	5
Average	9.0		

Table 31. (Continued)

	<u>Impact Strength (ft-lb)</u>	<u>Lateral Deformation (mils)</u>	<u>Shear Area (%)</u>
Plate 20			
HAZ - 2 mm from F.L.			
RT			
1	158.0	0.087	90
2	170.0	0.087	90
3	159.5	0.085	90
Average	162.3		
0°F			
1	128.0	0.082	80
2	129.0	0.077	80
3	131.0	0.082	80
Average	129.3		
-60°F			
1	127.0	0.081	80
2	123.0	0.078	80
3	133.0	0.078	80
Average	127.8		
-120°F			
1	113.0	0.072	50
2	108.0	0.072	50
3	99.5	0.067	40
Average	106.8		
Plate 21 Weld (F8903-2)			
Vacuum Baked			
RT			
1	47.0	0.037	50
2	62.0	0.050	50
3	50.0	0.037	50
Average	53.0		
0°F			
1	29.5	0.024	25
2	15.0	0.016	25
3	14.5	0.011	20
Average	19.7		

Table 31. (Continued)

	<u>Impact Strength (ft-lb)</u>	<u>Lateral Deformation (mils)</u>	<u>Shear Area (%)</u>
-60°F			
1	8.5	0.006	10
2	10.0	0.008	10
3	14.0	0.012	10
Average	10.8		
-120°F			
1	4.0	0.002	5
2	5.0	0.002	5
3	6.0	0.004	5
Average	5.0		
Plate 21 HAZ - 2 mm from F.L.			
RT			
1	155.0	0.090	90
2	179.5	0.084	90
3	167.0	0.093	90
Average	167.2		
0°F			
1	136.0	0.086	90
2	175.0	0.087	80
3	137.5	0.087	90
Average	149.5		
-60°F			
1	111.0	0.072	80
2	128.0	0.080	80
3	127.5	0.077	70
Average	122.2		
-120°F			
1	99.5	0.069	50
2	124.5	0.081	80
3	96.5	0.070	50
Average	106.8		

*Insufficient material for third specimen.

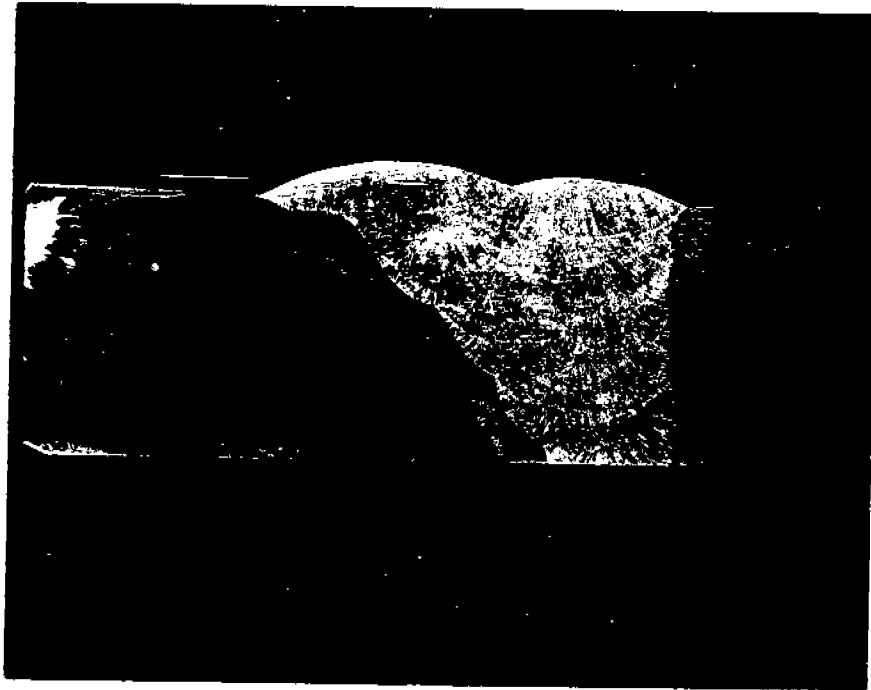


Figure 1. Metallographic cross section, weld No. 01-890131.

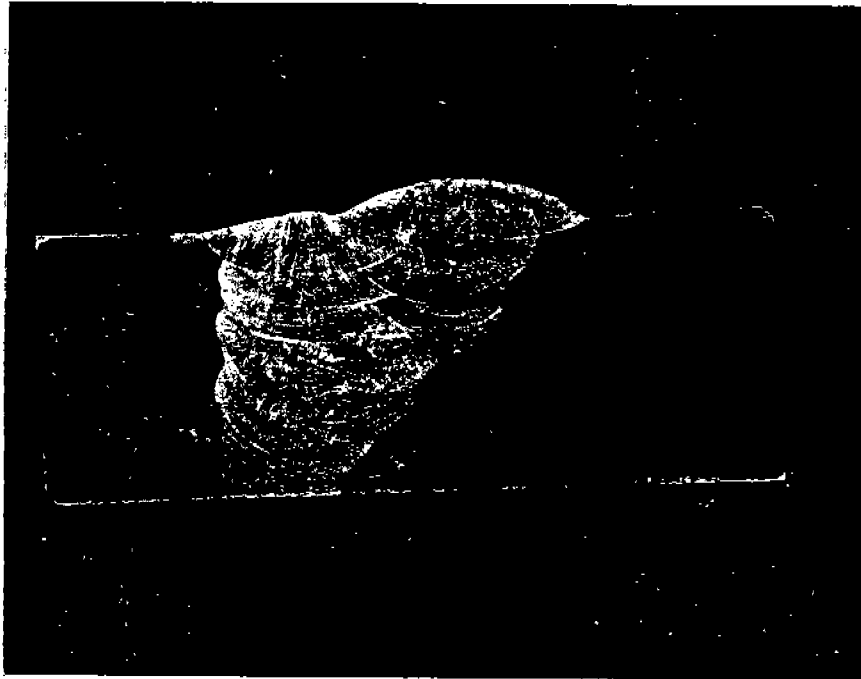


Figure 2. Metallographic cross section, weld No. 02-890201.



Figure 3. Metallographic cross section, weld No. 03-890201.

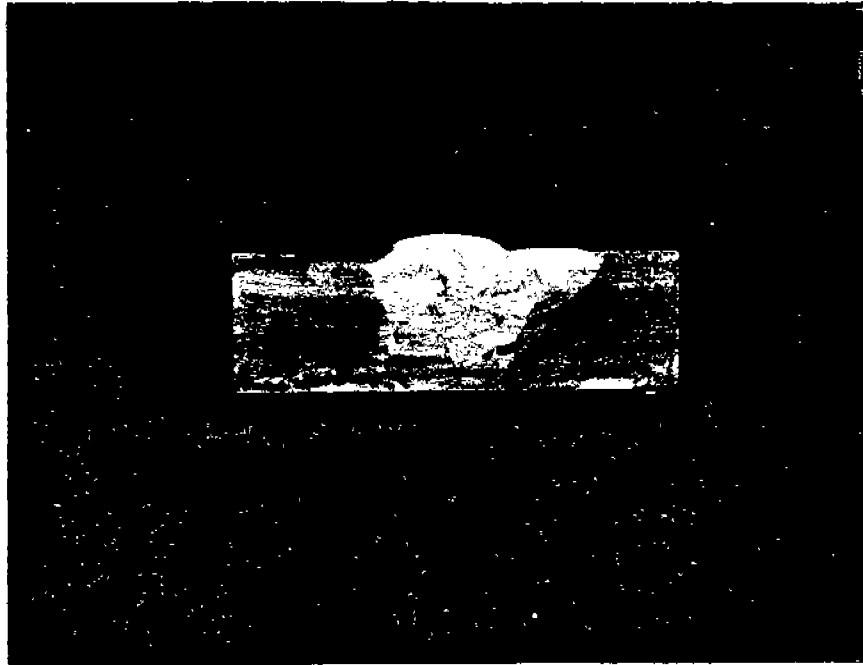


Figure 4. Metallographic cross section, weld No. 19-900904.
Actual size.

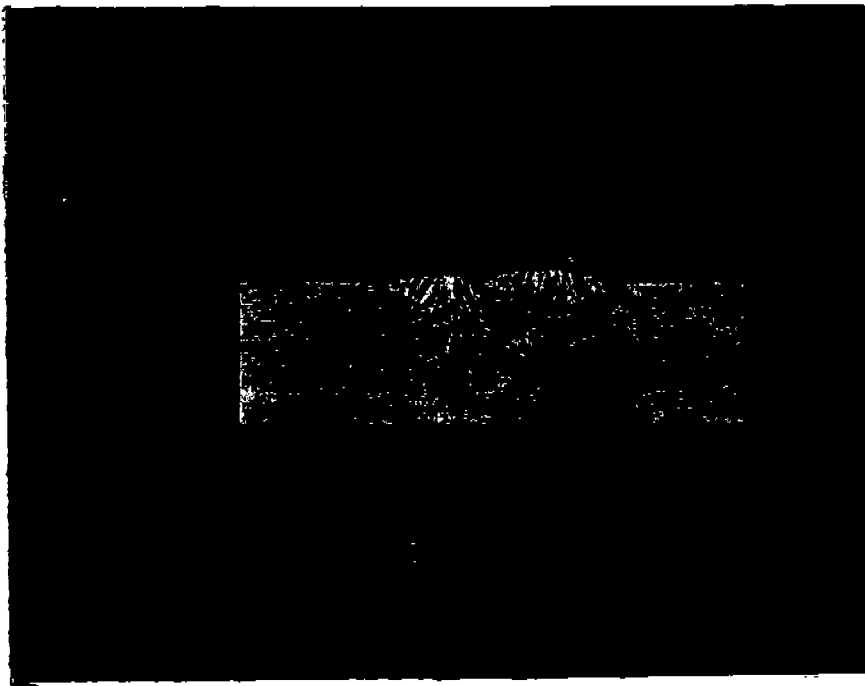


Figure 5. Metallographic cross section, weld No. 16-900330.
Actual size.

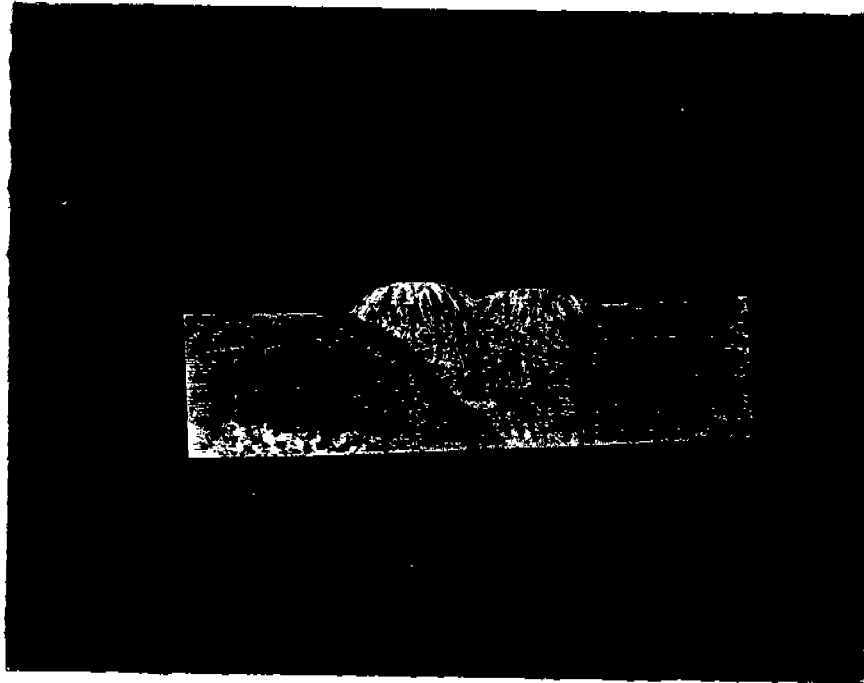


Figure 6. Metallographic cross section, weld No. 117-900602.
Actual size.

APPENDIX A

**DEVELOPMENT OF THRESHOLD CORROSION
FATIGUE TESTING TECHNIQUES**

**Dr. Judith A. Todd
Associate Professor
Department of Metallurgical and Materials Engineering
Illinois Institute of Technology
Chicago, IL 60616**

TABLE OF CONTENTS

	page
SUMMARY OF RESULTS	A-4
1. INTRODUCTION	A-5
2. IDENTIFICATION AND SIGNIFICANCE OF THE PROBLEM	A-5
3. PHASE II TECHNICAL OBJECTIVES	A-5
4. WORK PLAN	A-7
5. EXPERIMENTAL PROCEDURES	A-7
5.1 Materials	A-7
5.2 Near-threshold Corrosion Fatigue Crack Propagation Tests	A-7
5.3 Microstructural Studies	A-9
5.4 Polarization Curves	A-9
5.5 Impedance Measurements	A-9
5.6 Accelerated Test Procedures	A-10
5.6.1 Frequency Shifting	A-10
5.6.2 Partial Hydrogen Embrittlement	A-10
5.7 Alloy Design Study	A-10
6. RESULTS	A-11
6.1 Fatigue Crack Propagation Data	A-11
6.1.1 MIL S-24645 Base Metal - 10 Hz	A-11
6.1.2 ASTM A710 Base Metal - 2 Hz	A-11
6.1.3 MIL S-24645 Base Metal - 0.2 Hz	A-12
6.1.4 Frequency Effect	A-13
6.1.5 Weld Metal	A-13
6.1.6 Comparison Between MIL S-24645 Base and Weld Metals	A-14
6.1.7 MIL S-24645 HAZ	A-14
6.2 Microstructural Studies	A-15
6.2.1 MIL S-24645 and ASTM A710 Base Metals	A-15
6.2.2 ASTM A710 Tested at 2 Hz	A-15
6.2.3 MIL S-24645 Base Metal	A-16
6.2.4 MIL S-24645 Weld Metal	A-16
6.2.5 MIL S-24645 "HAZ"	A-17

TABLE OF CONTENTS

	page
6.3 Polarization Curves	A-18
6.3.1 Test Series I	A-18
6.3.2 Test Series II	A-19
6.4 Impedance Measurements	A-19
6.5 Accelerated Test Procedures	A-20
6.5.1 Frequency Shifting	A-20
6.5.2 Partial Hydrogen Embrittlement	A-21
7. CONCLUSIONS	A-22
8. FUTURE RESEARCH	A-24
9. REFERENCES	A-24
TABLES	A-26
FIGURES	A-33
APPENDIX I	

THRESHOLD CORROSION FATIGUE OF WELDED SHIPBUILDING STEELS PHASE II

SUMMARY OF RESULTS

Near-threshold corrosion fatigue crack propagation data have been collected for MIL-S24645 HSLA steel, a compatible strength weld metal and its HAZ in air, ASTM seawater at the free corrosion potential and ASTM seawater at -0.8V and -1.0 V (SCE) cathodic protection as a function of frequency (10, 2 and 0.2 Hz). Based on these results, frequency shifting between 10 and 0.2 Hz was explored as a method of accelerating the collection of near-threshold data and has been found to depend on the prior history of the specimen. Threshold data collected at 0.2 Hz were adequately reproduced when specimens were load shed at 10 Hz to threshold and then the frequency shifted to 0.2 Hz with no change in load. However, when specimens were load shed at 0.2 Hz and shifted to 10 Hz at threshold, significantly higher values of ΔK_{th} and ΔK_{eff} were obtained compared to the values from a single test at 10 Hz.

The most significant result to arise from this program was the development of the partial hydrogen embrittlement method to accelerate the collection of near-threshold data. This procedure offers the potential for clearly defining the threshold and reducing the time required for collection of threshold data by either conventional load shedding or "increasing R-ratio" techniques by at least a factor of two at 0.2 Hz. This method may prove to be a generic test method applicable not only to ferrous materials but also to non-ferrous materials which are embrittled by hydrogen. This method merits further investigation and offers the potential for development as an ASTM standard procedure.

1. INTRODUCTION

This report summarizes the near-threshold corrosion fatigue crack propagation data collected for MIL S-24645 steel, a compatible strength weld metal and its HAZ, as a function of frequency. The report begins with a statement of the problem, the Phase II technical objectives and the original work plan. Section 5 describes the experimental procedures adopted in this study. The results and discussion are presented in section 6 in the order: 6.1 - fatigue crack propagation data; 6.2 - microstructural studies; 6.3 - polarization data; 6.4 - impedance data; 6.5 accelerated test procedures; 6.6 - alloy design study. The conclusions are presented in section 7 and suggestions for future work in section 8. A paper submitted to the ASME Offshore Mechanics and Arctic Engineering Conference is included as Appendix I.

2. IDENTIFICATION AND SIGNIFICANCE OF THE PROBLEM

High strength low alloy steels, when subjected to cyclic stresses in the marine environment, exhibit more rapid nucleation and propagation of corrosion fatigue cracks than comparable steels tested in air. The critical areas in fatigue performance of shipbuilding and marine structural steels are the welded joints, which may be submerged fully in sea water and which must be protected by cathodic polarization. Relatively few studies exist of corrosion fatigue of weldments in the marine environment, particularly for the low frequencies (0.1 - 0.2 Hz) associated with marine structures.¹⁻¹⁰ The mechanisms of corrosion fatigue crack propagation and the roles of metal dissolution at the crack tip, corrosion debris, cathodic hydrogen and weld residual stresses are not well defined for natural sea water environments.¹¹⁻¹³ There is critical need for long term corrosion fatigue crack propagation studies in the slow growth regime (10^{-6} to 10^{-5} mm/cycle), which marks the transition from threshold behavior, below which flaws are non-propagating, to the mid growth (10^{-5} to 10^{-3} mm/cycle) where the effects of mean stress, microstructure and environment are no longer dominant. This is particularly true for cathodically protected structures, where the relationships between the electrochemical, mechanical and microstructural conditions within a corrosion fatigue crack are not well established.

A fundamental fracture mechanics study has been conducted to develop near-threshold corrosion fatigue crack propagation test techniques for shipbuilding steels and their weldments in marine environments, at both the free corrosion potential and under cathodic protection. This report contains the results of the Phase II near-threshold corrosion fatigue crack propagation tests, corrosion tests and microstructural investigations of MIL S-24645 Class 3 steel.

3. PHASE II TECHNICAL OBJECTIVES

1. To demonstrate techniques for producing and evaluating experimental weld metal compositions in developmental shipbuilding steels such as MIL S-24645 Class 3 using the submerged arc welding process. In particular, the effects of weld metal copper

content on as-welded microstructures, strength and toughness are to be examined in detail for selection of optimum weld metal composition(s).

2. To prepare and evaluate, through detailed microstructural and mechanical property testing, welded test plates suitable for corrosion fatigue crack growth rate testing of isostructural base metal, weld metal and HAZ test specimens.
3. To further develop an accelerated test technique for determining the threshold stress intensity range and the near-threshold corrosion fatigue crack growth rates at 10 Hz, 20 C, in (a) MIL S-24645 (HSLA 80), and (b) a 50 ksi yield strength steel such as DH36 (HSS/HTS).
4. To investigate the effects of lower frequency on MIL S-24645 by selecting a value, X Hz in the range 0.2 - 1 Hz chosen for comparison with data from offshore steels.
5. To conduct tests on base plate MIL S-24645 steel and DH36 at 10 Hz and a second frequency (either 2 Hz or X Hz, depending on the outcome of objective #4) in air and seawater at both the free corrosion potential and -1.0 V (SCE) cathodic protection.
6. Optional tests (depending on the outcome of objective #5) may be conducted on a 30 ksi yield strength steel such as Grade E at either 2 Hz or X Hz in air and seawater at both the free corrosion potential and -1.0 V (SCE) cathodic protection.
7. To conduct tests on submerged arc weld metal and heat affected zone microstructures (HAZ) of MIL S-24645 Class 3 steel at 20 C, 10 Hz and either 2 Hz or X Hz in air and ASTM seawater at the free corrosion potential and -1.0 V (SCE) cathodic protection.
8. To characterize the base metal, weld metal and HAZ microstructures, corrosion products and crack propagation paths after testing under the above conditions.
9. To obtain potentiodynamic polarization curves for the weld metal and, if possible, HAZ microstructures.
10. To initiate a basic study to identify how the externally applied potential relates to the level of cathodic protection at the highly stressed crack tip.
11. To initiate an alloy design study aimed at optimizing the mechanical properties of MIL S-24645 steel.
12. To prepare and submit for ship structures committee approval, a detailed procedure for near-threshold corrosion fatigue crack growth rate testing in seawater environments with or without the application of cathodic protection.

4. WORK PLAN

The original work plan of tests is presented in Table I. A summary of the tests completed to date is given in Table II and a summary of the threshold data is presented in Table III. It can be seen from Table III that, with the exception of the weld metal tested in air, after correction for crack closure, the effective threshold stress intensity range falls in the range 3.5 to 5.0 Mpa m^{1/2}. The individual test data are discussed in Section 6.3.

5. EXPERIMENTAL PROCEDURES

5.1 Materials

The material used in this study was MIL S-24645 Class 3, E/F quality, supplied by Lukens Steels Co. Near-threshold crack propagation data for this steel are also compared with results from A710 (Armco Class 3) collected during a Sea Grant program held at the University of Southern California. The compositions of both steels are given in Table IV and the mechanical properties are compared in Table V. Welds were prepared by MSNW according to the procedures described earlier and were tested without a stress relief treatment.

5.2 Near-threshold Corrosion Fatigue Crack Propagation Tests

Near-threshold corrosion fatigue crack propagation tests were conducted on one half inch thick compact tension (CT) specimens. Samples were oriented in the TL direction (i.e., notch parallel to the rolling direction of the base plate or the longitudinal direction of the weld) so that the minimum plate properties were being evaluated. Oversized holes were machined and fitted with black delrin rings so that the specimen could be isolated from the pins for either DC potential drop measurements of crack length for tests conducted in air or cathodic protection in ASTM seawater.

The test equipment and software have been continually upgraded throughout the program. Two 20 ksi servohydraulic fatigue machines, a MTS 880 and a CGS Model 112-10A, were used for the project and computer equipment has recently been acquired to automate a third, 50 ksi MTS system. The MTS systems are equipped with 386 personal computers (PC) and the MATE (Material Analysis and Testing Environment) software developed by the University of Dayton and in use at Wright Patterson Air Force Base. The CGS system was upgraded with the Instron 8500 Dynamic Testing System electronics, a 386 PC and the Instron Advanced Fatigue Crack Propagation (AFCP) program. Both of the near-threshold corrosion fatigue crack propagation software programs have been developed in accordance with ASTM standard E647.

Constant amplitude near-threshold fatigue tests using a sine waveform were carried out at frequencies of 10, 2 and 0.2 Hz, all with a stress ratio, $R = K_{min}/K_{max} = 0.1$. The threshold was approached by load shedding according to ASTM standard E647. Tests have been conducted in air, ASTM seawater at the free corrosion potential, ASTM seawater with

cathodic potentials of -0.8V SCE and -1.0 V SCE, and ASTM seawater at 4 C. Laboratory seawater, made according to ASTM standard D1141-75, was used as the reference environment, due to the difficulties associated with the compositional variability and availability of natural seawater. Procedures for making the ASTM seawater are given in Table VI. After preliminary tests using a clamp-on cell, an environmental chamber was constructed to provide a much larger volume of seawater. The ASTM seawater was changed every three days during the long term tests. The grips, pins and specimen, apart from a narrow region along the crack path, were coated with M-coat J to prevent corrosion. For the tests at 4 C, a recirculating controlled temperature bath was modified so that fluid at 4 C could be circulated through a stainless steel coil placed around the specimen in the large environmental chamber.

Specimens were fatigue pre-cracked in air at 20 Hz. Before initiating the tests a compliance calibration was performed. For the specimens tested in seawater, fixtures were attached to the specimen to prevent the clip gage from being immersed in the seawater. The compliance calibration was carried out by: (a) slotting the 0.5 inch thick CT specimen and measuring the load (P) - displacement (X) curve for each crack length, a_i , determined using a travelling microscope. The compliance values, $C_i = X/P$, and normalized compliance values $U_i = 1/((BEC_i)^{1/2} + 1)$ were then determined, where B is the thickness of the CT specimen and E is Young's modulus of the material. The normalized compliance was plotted against a_i/W , where W is the width of the CT specimen, and a least squares polynomial fit was used to obtain the coefficients for the equation relating A_i/W to U_i . An example of such data is plotted in Fig. 1. The coefficients were then loaded into the MATE/AFCP programs and were shown to correctly report the crack lengths during a test. This calibration technique is more accurate than that based on the conventional BEC - (a/w) curve, shown in Fig. 2.

The following methods of crack length monitoring have been compared: (1) D.C. electrical potential drop method using a precise source of constant D.C. current (SORENSEN SRL 10 - 50 power supply) plus a Keithley 181 nanovoltmeter. The experimental arrangement is shown schematically in Fig. 3;¹⁴ (2) back face strain gage compliance method; (3) crack opening displacement (COD) gage compliance method; and (4) measurement of the crack length either optically with a travelling microscope or from scanning electron micrographs. The optical/SEM techniques were for calibration only since they cannot be conveniently monitored during a test. The D.C. potential drop method was limited to tests in air since inaccurate results may arise from the presence of a conducting electrolyte (seawater) in the crack tip. For tests in seawater, either the back face strain gage or COD gage technique could be used. The MATE and AFCP software were both automated to determine crack length using the COD method.

Crack closure measurements to determine $K_{closure}$ were initially monitored using the back-face strain gage, but were fully automated, using the unloading compliance method, after installation of the MATE and AFCP programs.

5.3 Microstructural Studies

After the threshold crack propagation rates (10^{-8} mm cycle⁻¹) had been reached, specimens were either unloaded or were rapidly fractured. Samples tested in sea water were immediately drained, gently immersed in alcohol and dried as quickly as possible. The fracture surfaces were coated with epoxy to seal them from the air, and the unbroken samples were carefully infiltrated with epoxy and sealed on the sides. Both the fractured and unbroken specimens were then sectioned through the midplane, polished and etched in 3% nital, so that the fracture path at the center of the specimen could be observed using either an optical microscope or the Cambridge SIV-10 scanning electron microscope.

5.4 Polarization Curves

Potentiodynamic polarization curves were determined by several methods, according to ASTM standard G5-82, for MIL S-24645 steel, ASTM A710, a 1018 low carbon steel, the weld metal and the HAZ. Data were obtained for 600 grit finish cylindrical (ASTM A710) and flat (MIL S-24645, weld and HAZ) samples in aerated and argon deaerated ASTM seawater, pH = 8.2, at 20 C. The specimens were immersed in solution at the free corrosion potential for 30 minutes before scanning positively from -1600 mV SCE at a rate of 0.17 mV s⁻¹. The free corrosion potentials, corrosion currents and polarization resistances were determined respectively. The effect of testing conditions on the polarization curves was investigated by holding the specimens in seawater for 1.5 hours to allow the free corrosion potential to stabilize before scanning either positively or negatively from E_{corr} at 0.17 mV s⁻¹.

Data were collected for flat specimens of the weld metal and the HAZ by cutting sections parallel to the crack plane (LT orientation) from the welded specimens.

5.5 Impedance Measurements

Electrochemical impedance measurements have been initiated using a Solartron 1286 Electrochemical interface, a HP 35660A Dynamic signal analyzer and a 386 PC equipped with GPIB board, National Instruments measure, and Lotus 123 for data acquisition. Impedance data were initially collected on a base metal sample cathodically protected with -1.0 V (SCE) by scanning the frequency from 60 kHz to 10⁻³ Hz. Nyquist plots (imaginary part of the impedance versus real part) and Bode plots (modulus and phase plotted as a function of frequency) were determined. The data were then interpreted in terms of the following models: (1) single time constant model; (2) crack corrosion impedance model; (3) painted surface corrosion impedance model; (4) pit corrosion impedance model; (5) two time constant corrosion impedance model.

5.6 Accelerated Test Procedures

5.6.1 Frequency Shifting

The effect of frequency shifting, i.e., propagating the crack close to threshold at 10 Hz and then dropping the frequency to 0.2 Hz (or vice-versa 0.2 Hz shifted to 10 Hz), has been investigated as a method of accelerating the collection of near-threshold data.

5.6.2 Partial Hydrogen Embrittlement

A novel method of accelerated testing, designed to avoid time periods of weeks and months required to obtain single data points near the threshold,¹⁵ particularly at a frequency of 0.2 Hz, has also been initiated. It is proposed that threshold values can be obtained more rapidly by developing a small plastic zone in front of a fast moving fatigue crack partially embrittled by hydrogen. Tests using partially embrittled specimens to determine crack arrest characteristics in an increasing K-field have been demonstrated for single edge notch specimens¹⁶ but have not previously been demonstrated for fatigue.

Tests were conducted on face grooved DCB specimens of MIL S-24645 base metal, as shown in Fig. 4. The specimens were placed in an environmental chamber which contained a hydrogen charging bath consisting of a 5N H₂SO₄ acid with 0.25 mg/l of arsenite (As₂O₃). Shims were placed in the electrospark discharge machined face-grooves and the entire specimen and grooves, apart from 5 mm of the groove which was directly ahead of the pre-crack, were sealed with M-coat J or silicon rubber to isolate the environment. Hence, hydrogen could enter the specimen only in a small region around the pre-crack tip. A current density of 50 ma cm⁻² was applied, with the working electrode being the specimen and the reference electrodes being carbon.

After charging for twelve hours, fatigue cracking at $\Delta K_{app} = 10 \text{ MPa m}^{1/2}$ (close to ΔK_{th}) was initiated and crack propagation rates (predicted to be two orders of magnitude faster than the unembrittled specimens) were monitored. Once a constant crack propagation rate had been established during hydrogen charging, the bath was drained and the fatigue crack growth rates monitored as the crack propagated in air. During this period the fatigue crack propagation rates decreased drastically as hydrogen diffused out of the specimen until a steady state value, characteristic of the threshold behavior for MIL S-24645 steel in air, was achieved. The experiment was then repeated using lower values of ΔK_{app} to establish the threshold. By using different starting values of ΔK_i it was expected that the ΔK_{th} could be determined with less scatter and in a shorter time than either conventional load shedding or "increasing R-ratio" techniques.

5.7 Alloy Design Study

During the transition of Dr. Todd's laboratory from the University of Southern California to the Illinois Institute of Technology, a limited amount of theoretical research on the interphase precipitation was undertaken as this represents an alternative method of

directly strengthening copper containing steels using a single cooling treatment, rather than by a two stage quenching and tempering treatment. The interphase precipitation reaction results in periodic precipitation of copper precipitates at the austenite/ferrite interphase boundary during the transformation of austenite to ferrite. The intersheet spacing and the sizes of the precipitates are well known to influence the strength and toughness of ferritic steels. An understanding of this reaction could lead to the optimization of the mechanical properties of this class of HSLA steels.

6. RESULTS

6.1 Fatigue Crack Propagation Data

6.1.1 MIL S-24645 Base Metal - 10 Hz

The near-threshold corrosion fatigue crack propagation data for MIL S-24645 base metal tested in air at 10 Hz, 22 C and $R = 0.1$ are presented in Figure 5. The closed squares represent the original data and the open squares represent data which have been corrected for crack closure. Threshold stress intensity ranges of $\Delta K_{th} = 7.5 \text{ MPa m}^{1/2}$ and $\Delta K_{eff,th} = 5.5 \text{ MPa m}^{1/2}$ were obtained. The improved automation installed at IIT permitted much more accurate data collection down to crack growth rates of 3×10^{-7} mm per cycle, where the threshold values could be clearly identified. Figure 6 shows a comparison between recent data collected for MIL S-24645 base metal in air and earlier results where, due to the difficulties of collecting data below crack propagation rates of approximately 2×10^{-6} mm/cycle, ΔK_{th} was interpreted as $10 \text{ MPa m}^{1/2}$.

Figure 7 shows the results for the tests at 10 Hz in air, seawater at the free corrosion potential and seawater with -1.0 V SCE cathodic protection. ΔK_{th} decreased from $7.5 \text{ MPa m}^{1/2}$ in air to $6.5 \text{ MPa m}^{1/2}$ in seawater. The application of -1.0 V SCE resulted in an increase of ΔK_{th} to $11.5 \text{ MPa m}^{1/2}$. This contrasts with data collected earlier which indicated very little difference between the threshold values ($6.5 \text{ MPa m}^{1/2}$) for tests in seawater at (a) the free corrosion potential; (b) -0.8 V SCE and (c) -1.0 V SCE , as shown in Fig. 8. Crack closure corrections for the tests in air and seawater at -1.0 V SCE (Fig. 9) gave similar values of $\Delta K_{eff,th} = 5.5 \text{ MPa m}^{1/2}$ (air) and $5.0 \text{ MPa m}^{1/2}$ (-1.0 V SCE). Closure corrections are not yet available for the data collected in seawater at the free corrosion potential.

6.1.2 ASTM A710 Base Metal - 2 Hz

Tests at 2 Hz were conducted on ASTM A710, $R = 0.1$. Figure 10 compares data collected in air and also in ASTM seawater at the free corrosion potential before and after correction for crack closure. Values of $\Delta K_{th} = 6.0$ and $7.0 \text{ MPa m}^{1/2}$ were obtained for the tests in air and seawater, respectively. After correction for crack closure, $\Delta K_{eff,th}$ was found to be $4.5 \text{ MPa m}^{1/2}$. Figure 11 shows near-threshold data for tests conducted in ASTM seawater at the free corrosion potential, -0.8 V SCE and -1.0 V SCE . The application of cathodic potential increased ΔK_{th} to approximately $11.0 \text{ MPa m}^{1/2}$ in both cases. Further

studies at 2 Hz were discontinued as the effect of frequency appeared to be significantly greater when the frequency was reduced to 0.2 Hz.

6.1.3 MIL S-24645 Base Metal - 0.2 Hz

Near-threshold data for MIL S-24645 base metal were not required. Three attempts were made to collect the 0.2 Hz data in ASTM seawater. The first two tests were conducted with the old MTS software in which the precrack was obtained by load shedding and then crack propagation data were obtained by load increasing. The third test was conducted by load shedding. Crack closure data were collected simultaneously for test #3 using (a) a front face COD gage to measure crack mouth opening displacement, and (b) a back face strain gage sealed on the specimen using M coat-J. The value of the effective closure load given by these two methods was very close, hence the average value was used in calculating the effective delta K.

For specimen #1 (\blacktriangle in Fig. 12), crack growth initiated at 8×10^{-6} mm/cycle and a stress intensity range of $9 \text{ MPa m}^{1/2}$. Within a few days there was an emergency water shut-down, which stopped the test ($da/dN = 1.5 \times 10^{-5}$ mm/cycle) and the specimen remained in the sea water for two days. On resuming the test a slightly higher stress intensity range was required and the crack growth rate decreased to 1.3×10^{-5} mm/cycle. As it was not known (a) whether any overload occurred at the time of the shutdown and (b) whether significant corrosion products developed within the crack during this time, it was decided to repeat the test.

Specimen #2 (\blacktriangledown in Fig. 12) was pre-cracked and tested in a similar manner to specimen #1, but the test was initiated at a crack propagation rate of 9×10^{-7} mm/cycle. Unlike sample #1, this specimen, including the sides of the specimen ahead of the growing crack, was coated with M coat-J, a polymer paint, to prevent excessive corrosion. It was assumed that this paint film would break as the crack propagated. It became apparent during the test that the polymer film did not rupture, but acted as a flexible membrane across the specimen surface. Consequently access of the environment into the crack was restricted along the sides of the crack, occurring only through the mouth of the crack. No closure was observed in this test.

Data for specimen #3, tested by load shedding down to threshold, are shown as circles in Fig. 12. A higher threshold than for specimen #2 was observed at crack growth rates below approximately 2×10^{-6} mm/cycle. ΔK_{th} was initially found to be $8.5 \text{ MPa m}^{1/2}$ and the crack stopped growing at $da/dN = 7 \times 10^{-7}$ mm/cycle (cessation of crack growth being defined as no measurable crack growth in one week). The load was increased by 10% and crack growth resumed but immediately stopped. After one week, the load was then increased by another 10% and load shedding resumed. The crack stopped at a final value of $\Delta K_{th} = 9.5 \text{ MPa m}^{1/2}$ and a closure corrected $\Delta K_{eff,th} = 4.5 \text{ MPa m}^{1/2}$ (Fig. 13). It is interesting to note that after correction for closure, the plot of ΔK_{eff} versus da/dN closely parallels the ΔK_{eff} versus da/dN curves collected at 10 Hz.

The effect of prior history and frequency switching was evaluated using the same specimen, which had been tested for approximately 2 months at 0.2 Hz. After reaching the threshold at 0.2 Hz, the load was increased to give a crack growth rate of approximately 2×10^{-5} mm/cycle and the frequency was increased to 2 Hz. Load shedding to threshold was then repeated at 2 Hz. These data are shown as the squares, labelled test 6, in Fig. 14 and overlap previous results collected for ASTM A710, labelled Test 4 in Figure 15. The agreement between the two sets of data suggests that there is no prior history effect resulting from the test at 0.2 Hz. The results also suggest that frequency shifting from a low to higher frequency may be an effective method for collecting threshold data at more than one frequency from a single specimen.

6.1.4 Frequency Effect

Figure 15 shows a comparison between the data for 10 Hz, 2 Hz and 0.2 Hz indicating that the threshold stress intensity range increases from $6.5 \text{ MPa m}^{1/2}$ for 10 Hz to $7 \text{ MPa m}^{1/2}$ at 2 Hz and $10 \text{ MPa m}^{1/2}$ at 0.2 Hz. The largest increase occurred between 2 Hz and 0.2 Hz. After correction for crack closure, similar values of $\Delta K_{\text{eff,th}} = 4.5$ and $5.0 \text{ MPa m}^{1/2}$ were obtained for $\nu = 2$ and 0.2 Hz.

6.1.5 Weld Metal

Data for the weld metal tested in air at 10 Hz, before and after correction for crack closure, are presented in Fig. 16. Values of $\Delta K_{\text{th}} = 14 \text{ MPa m}^{1/2}$ and $\Delta K_{\text{eff,th}} = 9 \text{ MPa m}^{1/2}$ were obtained. When the weld metal was tested in ASTM seawater at the free corrosion potential (Fig. 17) and ASTM seawater at -0.8V SCE (Fig. 18), similar threshold values were observed. ΔK_{th} was found to be $11 \text{ MPa m}^{1/2}$ at the free corrosion potential and $12.8 \text{ MPa m}^{1/2}$ (-0.8V SCE) with $\Delta K_{\text{eff,th}} = 4 \text{ MPa m}^{1/2}$ (free corrosion potential) and $3.5 \text{ MPa m}^{1/2}$ (-0.8V SCE). Three attempts were made to test the weld metal in ASTM seawater at -1.0 V SCE . Data from the successfully completed test (test #2), which gave $\Delta K_{\text{th}} = 14.5 \text{ MPa m}^{1/2}$ and $\Delta K_{\text{eff,th}} = 4.5 \text{ MPa m}^{1/2}$, are presented in Fig. 19. [It should be noted that the initial test failed in the pre-crack when the crack deviated out of plane and no longer complied with ASTM standard E647. This proved to be a common problem for both the weld metal and HAZ specimens.]

The second attempt to test the weld in ASTM seawater at -1.0 V SCE , labelled test 1 in Figure 20, was conducted on a specimen which was being used to collect impedance data. Unfortunately the sign convention used for the Solartron 1286 electrochemical interface was the reverse of that used in the U.S. Hence, the application of -1.0 V SCE cathodic protection was, in fact, $+1.0 \text{ V SCE}$ anodic polarization. Significant corrosion of the specimen occurred for approximately 10 minutes before this error was corrected. The test was continued and the results proved interesting. Data for the successful test (#2) and the corroded specimen (#1) are compared in Fig. 20. The apparent threshold value increased to $18 \text{ MPa m}^{1/2}$ in test #1 and was attributed to the extensive initial corrosion. However, when the effects of crack closure were subtracted, $\Delta K_{\text{eff,th}}$ for test #1 was $5.5 \text{ MPa m}^{1/2}$, very close to the value of $4.5 \text{ MPa m}^{1/2}$ for the successful test (#2).

Data collected for the weld metal in ASTM seawater at -0.8V SCE and -1.0 V SCE, before and after correction for closure, are shown in Fig. 21. It can be seen that although similar threshold values are obtained in both cases, the near-threshold propagation rates below approximately 6×10^{-5} mm/cycle are slightly slower in the specimen tested at -0.8V SCE than at -1.0 V SCE. This is possibly attributable to hydrogen effects and confirms the same observation made for ASTM A710 tested in ASTM seawater at -0.8V SCE and -1.0 V SCE but at a lower frequency of 2 Hz.

The 10 Hz data for the weld metal tested in air, ASTM seawater at the free corrosion potential, -0.8V SCE and -1.0 V SCE are compared before and after correction for crack closure in Fig. 22. With the exception of the test conducted in air, which appeared not to have reached a steady threshold value at $da/dN = 6 \times 10^{-7}$ mm/cycle, the values of $\Delta K_{\text{eff,th}}$ were all in the range 3.5 to 5.5 MPa $m^{1/2}$.

6.1.6 Comparison Between MIL S-24645 Base and Weld Metals

Before correction for closure, the apparent crack propagation data for the weld metal in both air and seawater were significantly slower than for MIL S-24645 base metal as shown in Fig. 23. After correction for closure, the data for the weld metal in ASTM seawater and base metal in air were similar, with only the weld metal tested in air exhibiting a higher $\Delta K_{\text{eff,th}}$ and slower growth rates (Fig. 23). Data, before and after correction for crack closure, for the base and weld metal tested in ASTM seawater at -0.8V SCE and -1.0 V SCE are shown in Fig. 24. Again, the apparent threshold values are higher for the weld metal than MIL S-24645 base plate. However, after correction for closure the values for $\Delta K_{\text{eff,th}}$ are comparable.

6.1.7 MIL S-24645 HAZ

The HAZ microstructures proved extremely difficult to test, with many specimens either failing during precracking or becoming invalid according to ASTM standard E647. After an extensive study it was found that although the HAZ appeared to be straight on both sides of the compact tension specimen, the center of the HAZ was higher on one side than the other, giving a sloping HAZ for most specimens and making it impossible to conduct a valid test. Careful metallography revealed that the HAZ had curved as the last one or two weld beads were deposited. Consequently the compact tension blanks had to be reground to 9.5 mm thickness in order to achieve a straight HAZ oriented 90° to the applied load.

The data reported in this section are for specimens supplied to us as being notched in the HAZ. However, the data should be interpreted with caution as subsequent metallographic examination indicated that the cracks did not keep a constant path in the HAZ.

Figure 25 shows data, before and after correction for closure, for the HAZ tested in air at 10 Hz. ΔK_{th} was found to be 10 MPa $m^{1/2}$ and $\Delta K_{\text{eff,th}}$ was 4.5 MPa $m^{1/2}$. Data

collected in ASTM seawater at the free corrosion potential are given in Fig. 26 and for ASTM seawater at -1.0 V SCE in Fig. 27. A high value of $\Delta K_{th} = 19.5 \text{ MPa m}^{1/2}$ was obtained at the free corrosion potential compared to $11.5 \text{ MPa m}^{1/2}$ at -1.0 V SCE. The values of $\Delta K_{eff,th}$ were $4.0 \text{ MPa m}^{1/2}$ (free corrosion potential) and $3.5 \text{ MPa m}^{1/2}$ (-1.0 V SCE). However, it should be noted that for the test at -1.0 V SCE, it was subsequently observed that the crack path had deviated beyond the requirements of ASTM standard E647. A compilation of the data collected for the HAZ in air, seawater at the free corrosion potential and seawater at -1.0 V SCE is presented in Fig. 28. While the scatter in the apparent data reflects the difficulties of testing HAZ microstructures, it is interesting to note that the closure corrected data appear to approach the same apparent threshold.

6.2 Microstructural Studies

6.2.1 MIL S-24645 and ASTM A710 Base Metals

Scanning electron micrographs of polished MIL S-24645 are shown in Figs. 29a - 29c for the L-T orientation and Figs. 29d, 29e for the L-W orientation. An acicular ferritic microstructure containing large non-metallic inclusions is observed in Fig. 29a. At higher magnification and using the backscattered electron detector for atomic number contrast, regions of lighter contrast resembling precipitates were observed within the grains and at grain boundaries (Figs 29b, 29c). The lighter contrast suggests that these regions may be copper or copper-rich. Little difference was observed between the L-T and L-W orientations (Figs. 29d, 29e).

Similar acicular ferrite microstructures were observed for ASTM A710 (Fig. 30a). Transmission electron microscopy of ASTM A710 revealed inclusions (Fig. 30b), and copper precipitation on dislocations in the matrix shown in bright field (Fig. 30c) and dark field (Fig. 30d). Copper precipitates will also be observed in MIL S-24645 but may be slightly larger due to the longer tempering time (60 minutes vs 30 minutes in A710) at a higher tempering temperature (627 vs 598 C).

Fracture surfaces of both MIL S-24645 and ASTM A710 tested in air showed characteristic oxide markings, shown for ASTM A710 in Fig. 31a. Figure 31b is a fracture surface of the weld metal in ASTM A710, which has a flatter fracture appearance.

6.2.2 ASTM A710 Tested at 2 Hz

Figures 32a and 32b show the fracture surface of ASTM A710 tested in ASTM seawater at 2 Hz and reveal extensive corrosion product formation and a rough fracture surface. In contrast the sample cathodically protected at -0.8V showed virtually no surface films and a smoother fracture surface (Figs. 33a, 33b - note that these surfaces are protected by a layer of epoxy resin containing air bubbles). However, when the cathodic protection was increased to -1.0 V, there appeared to be extensive damage accumulation ahead of the crack tip and crack branching in the crack wake (Figs. 34a - 34f). These micrographs may be interpreted with the aid of Fig. 35. It is proposed that at 2 Hz frequency and -1.0 V

cathodic protection, hydrogen damage accumulated in the highly stressed region ahead of the crack tip. As the crack propagated, one of these damaged regions began to open up as a branch - compare Figs. 34c and 35b where the lower branch is the crack path. With continued cycling the upper crack branch opened and damage continued to accumulate in the region between the two branches (compare Fig. 35c with Figs. 34c, 34e). As the lower crack branch propagated, a grain or region of metal became detached and was able to rotate into the crack forming a wedge of metal, which could then contribute to crack closure (compare Figs. 34e, 34f, and 35d). This result is important since it indicates that although significant damage may be accumulating in the material, the crack was propagating slower than for the sample tested in air. A sudden overload, however, could lead to rapid propagation of the crack through the damaged region.^{17,18}

6.2.3 MIL S-24645 Base Metal

Microstructural observations of the specimens tested with increasing load at 0.2 Hz in ASTM seawater at the free corrosion potential are presented in Figures 36-39. Figure 36 shows the crack tip region along the centerline of test specimen #2. Higher magnification photographs of the same region are presented in Figures 37a-37c. Crack branching becomes extensive in tests #1 and #2 at a crack growth rate of approximately 10^{-4} mm/cycle. Crack propagation occurs around grain boundaries, with blunting and stopping of branches observed in some of the regions where extensive corrosion has occurred. Higher magnification photographs of specimen #1 are presented in Figures 38 and 39, clearly showing the formation of corrosion debris in the region at the crack tip. In both specimens the branch lengths increased towards the crack tip, showing that branching became more extensive as the load and crack velocity increased. In specimen #2 there appeared to be a correlation between the average branch length and the angle of the branch. For example, branches with angles between 10 to 30 degrees from the main crack were longer, with an average length of 0.17 mm compared to 0.03 mm for cracks with angles of 40 to 45 degrees from the main crack. Significantly less branching was observed for test #3, conducted at 0.2 Hz at the free corrosion potential by load shedding down to threshold, as shown in Figs. 40-42.

Optical micrographs of the fracture path of MIL S-24645 base metal tested at -1.0 V (SCE) in seawater, sectioned through the midplane, polished and etched with 5% Nital, near the notch and near the crack tip are shown in Figures 43a and 43b, respectively. Figures 44a and 44b show higher magnification views of the crack tip region. SEM micrographs of the fracture path near the crack tip are shown in Figure 45. Crack propagation around grain boundaries was observed but no corrosion products could be detected.

6.2.4 MIL S-24645 Weld Metal

Crack profiles for the weld metal tested in air at 10 Hz are presented in Figs. 46-48. They can be compared with crack profiles for the weld metal tested in ASTM seawater at the free corrosion potential at 10 Hz (Figs. 49-51) and for the weld tested in ASTM

seawater at -1.0 V (SCE) (Figs. 52-55) at 10 Hz. In all three cases the crack paths are straight and voids were observed opening up at non-metallic inclusions, some of which were less than 1 μm in size. Energy dispersive X-ray analysis showed that the inclusions were predominantly manganese aluminosilicates (Fig. 56) incorporated from the flux. After completion of the test in ASTM seawater at -1.0 V SCE, the specimen fracture surface was shiny and no corrosion products were observed. Figures 52a and 52b show optical micrographs of the fracture path of the specimen tested at -1.0 V (SCE) in seawater, sectioned through the midplane, polished and etched with 5% Nital, near the notch and near the crack tip, respectively. The fracture path near the crack tip is shown in the SEM micrographs in Figures 53a and 53b. The overall fracture path was smooth. Cracking around grain boundaries was observed and a large number of particles could be seen within the crack as shown in the SEM micrograph in Figure 54. Figure 55a shows an SEM micrograph of cracking around grain boundaries at a higher magnification in the region close to the crack tip. Figure 55b shows a higher magnification view of particles observed in the mid-region of the crack. These particles were observed at many places along the crack length and were found to be metal pieces, approximately 5 - 10 μm in size, rather than corrosion products. No calcareous deposits were identified by energy dispersive spectroscopy.

6.2.5 MIL S-24645 "HAZ"

The fracture path at the center of a specimen, supplied to us as notched in the HAZ, after testing at 10 Hz in ASTM seawater at the free corrosion potential is shown in Figures 57a (near the notch) and 57b (near the crack tip). The weld metal, HAZ and base metal are clearly visible and the crack path was found to be straight. Figures 58a-d show the microstructures of the base metal, the HAZ, the weld and the transition region between the weld and HAZ. The base plate consisted of ferrite grains, approximately 5 μm in size with what appear to be very fine pearlitic regions at the grain boundaries. A bainitic microstructure with a grain size of approximately 50 μm is observed in the HAZ and adjacent to the weld.

Microhardness readings taken on the specimen corresponding to Figure 57a (near the notch) and Figure 57b (near the crack tip) are given in Tables VIIa and VIIb. These data are plotted in Figures 59a and 59b. The hardness values in the base plate, HAZ and weld regions were found to be approximately the same along the length of the specimen.

It is clear from Figures 57a and 57b that the fracture path of this specimen did not lie in the HAZ. This was true for both sides of the specimen. Consequently, the remaining specimens supplied to us as notched in the HAZ were polished and etched and it was found that the notches in these specimens were also not exactly in the HAZ. It is, therefore, essential to polish and etch the specimen blanks prior to machining so that the notch can be accurately positioned in the HAZ.

For the test reported above, the width of the HAZ varied slightly along the length of the specimen and its distance from the fracture path was greater near the crack tip. A

schematic of the width of the HAZ and its distance from the fracture path (near the notch and near the crack tip) as obtained from the microhardness data is given in Figs. 60a and 60b, respectively.

Figure 61 shows SEM micrographs of the fracture path and a large number of particles could be seen within the crack. These particles were less than $5 \mu\text{m}$ in size and did not charge under the electron beam, suggesting that they may be metal grains rather than corrosion products. Higher magnification SEM micrographs from the area near the crack tip are shown in Figures 62a-c.

6.3 Polarization Curves

6.3.1 Test Series I

Potentiodynamic polarization data were collected according to ASTM standard G5-82 for ASTM A710, MIL S-24645 and a 1018 steel in the first series of tests. A second series of tests was later performed using MIL S-24645 base metal, weld metal and the HAZ region. Figure 63a shows the polarization curves for ASTM A710 (cylindrical sample) and MIL S-24645 (flat sample) steels in aerated ASTM seawater, $\text{pH} = 8.2$, at 20°C . These data were obtained from a single specimen, by scanning positively from -1600 mV at a rate of 0.17 mV s^{-1} . The free corrosion potentials, corrosion currents and polarization resistances were determined respectively as: -560 mV (MIL S-24645) and -460 mV (ASTM A710); $5.0 \mu\text{A cm}^{-2}$ (MIL S-24645) and $12.7 \mu\text{A cm}^{-2}$ (ASTM A710); $8.83 \text{ k ohms cm}^{-2}$ (MIL S-24645) and $1.9 \text{ K ohms cm}^{-2}$ (ASTM A710). Figure 63b compares the behavior of MIL S-24645 and ASTM A710 in deaerated ASTM seawater, collected under the same conditions as Fig. 63a. The free corrosion potential is now reduced to -736 mV (MIL S-24645) and -763 mV (ASTM A710). Since it is highly probable that the environment at the crack tip may become deaerated, then a potential more negative than -763 V is required to adequately protect these steels.

Additional tests were conducted on ASTM A710 and 1018 steels to investigate the effect of testing conditions on the polarization curves. Figure 63c shows data collected using two cylindrical specimens, where the specimens were held in seawater for 1.5 hours to allow the free corrosion potential to stabilize, then scanned either positively or negatively from E_{corr} at 0.17 mV s^{-1} . Under these conditions the free corrosion potential for ASTM A710 in seawater is reduced to -680 mV and is slightly more positive than that for 1018 carbon steel. Data for all the polarization curves is summarized in Table VIII.

The effect of oxygen in the seawater is shown for ASTM A710 in Fig. 63d. At potentials more positive than the free corrosion potential, the anodic reaction $\text{Fe} = \text{Fe}^{2+} + 2\text{e}$ occurs in both aerated and deaerated seawater. For cathodic potentials, oxygen diffusion control by the reaction $\text{O}_2 + 2\text{H}_2\text{O} + 4\text{e}^- = 4\text{OH}^-$ occurs in the range E_{corr} to approximately -1000 mV , below which hydrogen evolution, $2\text{H}_2\text{O} + 2\text{e}^- = \text{H}_2 + 2\text{OH}^-$ is the dominant mechanism. When tests are carried out in deaerated seawater, oxygen is no longer available for diffusion and hydrogen evolution will occur at all cathodic potentials.

The presence of hydrogen and hydroxyl ions at cathodic potentials can result in two mechanisms influencing corrosion fatigue crack propagation in seawater: (1) hydrogen embrittlement due to interaction of the hydrogen with the stress field at the tip of the crack, and (2) calcareous deposit formation, contributing to crack closure, by the build-up of $Mg(OH)_2$ and $CaCO_3$ deposits in the crack. It should be noted that calcareous deposits have not yet been identified in the corrosion fatigue specimens tested in ASTM seawater at -1.0 V (SCE) cathodic protection.

6.3.2 Test Series II

Polarization curves for MIL S-24645 base, weld and HAZ regions collected for an air saturated solution by holding the metal at the open circuit potential (OCP) for 30 minutes prior to scanning positively at 1 mV s^{-1} from 250 mV SCE below the corrosion potential are shown in Fig. 64. Corrosion potentials of -928 mV SCE (base), -793 mV SCE (weld) and -567 mV SCE (HAZ) were determined, clearly showing that the HAZ microstructure is most susceptible to corrosion. Data for the base, weld and HAZ collected in argon deaerated ASTM seawater with a 30 minute hold at the open circuit potential are shown in Figure 65. Similar values for the corrosion potential were obtained for the base metal (-792 mV SCE), weld metal (-798 mV SCE) and HAZ (-779 mV SCE). Figure 66 presents data for the weld and HAZ metals collected in argon deaerated ASTM seawater with a 10 minute reduction at -1500 mV SCE prior to scanning positively at 1 mV s^{-1} . In this case the corrosion potential for the weld was -891 mV SCE and for the HAZ was -907 mV SCE. Figures 67-69 compare data in air and argon saturated solutions with a 30 minute hold at the open circuit potential for base metal, weld metal and HAZ, respectively. A summary of the corrosion data, which includes the corrosion potential, corrosion current and polarization resistance, is presented in Table VIII.

6.4 Impedance Measurements

Preliminary AC impedance data have been collected from the weld metal tested at 10 Hz in ASTM seawater at -1.0 V SCE as a function of crack growth. The application of impedance methods to cracked structures is complex, in its infancy, and interpretation of the data is expected to be a controversial and challenging field. It appears, from the changes in impedance between the beginning and the end of the test, that the models required to interpret the data collected at the initial and final crack lengths may be different. The models currently being considered include (1) a single time constant corrosion impedance model; (2) a crack corrosion impedance model; (3) a painted surface corrosion impedance model; (4) a pit corrosion impedance model; and (5) a two time constant impedance model. The equations and methodologies show that several of these models do not fit the data well and it appears that models incorporating two or more time constants will be necessary to interpret our data. At this stage we have only collected sufficient exploratory data to indicate that the impedance method merits further investigation. Our data have been collected in collaboration with Dr. John Fildes of the Basic Industry Research Laboratory (BIRL), Northwestern University, who is assisting us with our model development and interpretation.

6.5 Accelerated Test Procedures

6.5.1 Frequency Shifting

An interesting result emerged from the tests conducted at 10 Hz, 2 Hz and 0.2 Hz on MIL S-24645 and ASTM A710 base metals. Although decreasing the frequency of the tests conducted in ASTM seawater at the free corrosion potential appeared to shift ΔK_{th} to higher values (6.5 MPa m^{1/2} - 10 Hz; 7.0 MPa m^{1/2} - 2 Hz; and 8.5 MPa m^{1/2} - 0.2 Hz), after correction for closure the $\Delta K_{eff,th}$ values were very similar (4.5 MPa m^{1/2}). This suggested that if design criteria were based on the values of $\Delta K_{eff,th}$, it may be possible to collect appropriate design data from tests at 10 Hz. However, more data collection is required at 0.2 Hz, particularly for the weld and HAZ materials, to confirm this hypothesis.

Shifting the frequency by load shedding at 0.2 Hz to threshold, then increasing the load and load shedding to threshold at 2 Hz has been shown to satisfactorily reproduce data collected at 2 Hz. Frequency shifting when accompanied by a load increase, therefore, appeared to be a promising method for accelerating the collection of near-threshold corrosion fatigue crack propagation data.

Further tests were conducted on MIL S-24645 base metal tested in ASTM seawater at -1.0 V (SCE). Figure 70 shows the first experiment in which the load was shed at 0.2 Hz giving threshold values of $\Delta K_{th} = 16$ MPa m^{1/2} and $\Delta K_{eff} = 5.6$ MPa m^{1/2} for da/dN = 10⁻⁶ mm/cycle. These values can be compared with $\Delta K_{th} = 11.5$ MPa m^{1/2} and $\Delta K_{eff} = 5.0$ MPa m^{1/2} for the test conducted at 10 Hz and -1.0 V (SCE). Hence, the apparent threshold has again shifted to higher values at the lower frequency (0.2 Hz) but the effective threshold values are similar. Once the threshold had been reached, closure built up very rapidly and negative crack growth rates were recorded. At this point the frequency was shifted to 10 Hz with no change in load. Figure 71 shows that the crack growth rate immediately increased to 10⁻⁵ mm/cycle and then load shedding proceeded to threshold values of $\Delta K_{th} = 16$ MPa m^{1/2} and $\Delta K_{eff} = 12$ MPa m^{1/2} at da/dN = 10⁻⁸ mm/cycle. It is interesting to note that a much higher effective stress intensity range ($\Delta K_{eff} = 12$ MPa m^{1/2}) was recorded than that ($\Delta K_{eff} = 5$ MPa m^{1/2}) for the test conducted at 10 Hz and -1.0 V (SCE) with no frequency shifting.

At this point the frequency was shifted to 0.2 Hz (experiment #3), but the crack appeared to fill and the program gave negative crack growth rates. To collect additional data the load was then increased by 10% and shed to threshold at 0.2 Hz. Figure 72 shows that the applied ΔK_{th} now increased to 19 MPa m^{1/2} giving an initial crack growth rate of 10⁻⁴ mm/cycle. The effective threshold decreased to 10 MPa m^{1/2}, when the closure load overlapped the reference window. When this problem had been corrected the effective stress intensity range decreased to 5.5 MPa m^{1/2} at da/dN = 2.5 x 10⁻⁷ mm/cycle, agreeing with the value of ΔK_{eff} obtained in the first experiment at 0.2 Hz. A comparison of experiments #1 and #3 is presented in Fig. 73 showing that despite the differences in ΔK_{th} and the experimental problems, similar values of ΔK_{eff} were ultimately obtained, but that lower values of da/dN were achieved in experiment #3.

The frequency was again shifted to 10 Hz with no change in load and the crack growth rate immediately increased to 10^{-5} mm/cycle as in experiment #2 (Fig. 74). Threshold values of $\Delta K_{th} = 18 \text{ MPa m}^{1/2}$ and $\Delta K_{eff} = 10 \text{ MPa m}^{1/2}$ were obtained at $da/dN = 10^{-7}$ mm/cycle. It is interesting to note that ΔK_{eff} was initially $5.5 \text{ MPa m}^{1/2}$ and then increased to $9.8 \text{ MPa m}^{1/2}$ as the crack propagation rate decreased. This is lower than the value of $12 \text{ MPa m}^{1/2}$ obtained the first time the frequency was shifted from 0.2 to 10 Hz in experiment #2. Experiments #2 and #4 are compared in Fig. 75, where it can be seen that ΔK_{th} increased and ΔK_{eff} decreased.

For experiments #1 through #4, the tests were first conducted at 0.2 Hz and then the frequency was shifted to 10 Hz. Experiments #5 and #6 were, therefore, conducted initially at 10 Hz and then switched to 0.2 Hz at threshold with no change in the load. Figure 76 shows experiment #5 in which the load was increased then shed to threshold. Figure 77 shows that experiment #5 directly reproduced the threshold data collected at 10 Hz in experiment #4. After reaching the threshold at 10 Hz, the frequency was then shifted to 0.2 Hz with no change in load. The crack growth rate again increased to 2×10^{-4} mm/cycle, as shown in Fig. 78, and threshold values of $\Delta K_{th} = 16 \text{ MPa m}^{1/2}$ and $\Delta K_{eff} = 6.5 \text{ MPa m}^{1/2}$ were subsequently obtained at $da/dN = 8 \times 10^{-8}$ mm/cycle.

The results of these experiments indicate that frequency shifting appears to reproduce the results of tests conducted at a single frequency when the frequency is switched from a high value (10 Hz) to a lower value (0.2 Hz) at threshold without changing the applied load. However, when tests are conducted initially at the low frequency (0.2 Hz), switching to a higher frequency (10 Hz) at threshold with no increase in load gives values of both ΔK_{th} and ΔK_{eff} that are significantly higher than the values obtained in a single test conducted at 10 Hz and -1.0 V (SCE).

6.5.2 Partial Hydrogen Embrittlement

Preliminary data collected by the partial hydrogen embrittlement technique indicates that this is an extremely promising method for accelerating the collection of near-threshold corrosion fatigue crack propagation data. Figure 79 shows typical crack growth data collected for $\Delta K = 10$ and $9 \text{ MPa m}^{1/2}$. The initial portion of each curve represents the crack growth data collected while the specimen was being cathodically charged with hydrogen. As the DCB specimen is a constant K specimen, da/dN will reach a constant value for a given ΔK . Values of $da/dN = 1.82 \times 10^{-4}$ and 1.64×10^{-4} mm/cycle for $\Delta K = 10$ and $9 \text{ MPa m}^{1/2}$, respectively, were obtained under hydrogen charging. Once a constant value of da/dN had been established, the arsenite solution was drained from the chamber and the crack growth rate decreased as the hydrogen diffused out of the specimen and the crack propagated into unembrittled material. (Note: the specimen could be briefly heated with a hot air blower to accelerate this process if necessary.) Figure 79 clearly shows that as the crack length increased, the crack growth rate decreased to a constant value characteristic of the applied ΔK in air. These values were 3.33×10^{-6} and 4.25×10^{-6} mm/cycle for $\Delta K = 10$ and $9 \text{ MPa m}^{1/2}$, respectively. The data collected for $\Delta K = 9 \text{ MPa m}^{1/2}$ took approximately 6 hours with hydrogen charging being conducted overnight. Figure

80 compares the experimental crack propagation rates with those measured during a conventional load shedding test showing that excellent agreement was obtained considering that the test technique is far from optimized. Further data collection is in progress to collect threshold data at lower values of ΔK . It would appear from the above experiment that it should be possible to identify the threshold within 5 days at 10 Hz compared to 7 - 10 days in a conventional load shedding test. Significantly greater time savings are expected for the tests conducted at 0.2 Hz.

7. CONCLUSIONS

1. With the exception of the weld metal tested in air at 10 Hz, the effective threshold stress intensity range, $\Delta K_{\text{eff,th}}$, determined after correction for crack closure, lay in the range 3.5 to 5.5 MPa m^{1/2} for all the tests conducted to date, irrespective of frequency or test conditions.
2. Reducing the frequency was found to increase the apparent threshold stress intensity range, ΔK_{th} , for tests in seawater, from 6.5 MPa m^{1/2} at 10 Hz to 8.5 - 9.5 MPa M^{1/2} at 0.2 Hz.
3. The apparent stress intensity range, ΔK_{th} , also increased for the weld metal and HAZ, compared to MIL S-24645 base metal at 10 Hz. However, similar values of $\Delta K_{\text{eff,th}}$ were obtained.
4. These results suggest that, if design is based on a minimum value of $\Delta K_{\text{eff,th}}$, it may be possible to collect data at 10 Hz, rather than by long term tests at 0.2 Hz.
5. Further tests are required at 0.2 Hz to substantiate this hypothesis.
6. The experimental program has shown that crack growth rates approaching 10⁻⁷ mm/cycle are required for an adequate determination of the threshold stress intensity range.
7. The application of -1.0 V SCE cathodic protection resulted in metal wedges, approximately one to two grains in size, being produced in the wake of the crack and contributing to crack closure. The damage mechanism was attributed to hydrogen embrittlement.
8. Calcareous deposits have not been detected in specimens tested with -1.0 V SCE.
9. Comparable threshold stress intensity ranges but slightly slower near-threshold crack propagation rates were observed in specimens tested at -0.8 V SCE compared to those tested at -1.0 V SCE.

10. Extensive corrosion of the specimen prior to test (by anodic polarization) significantly increased the apparent threshold stress intensity range, but gave only a small change in the effective threshold stress intensity range.
11. Shifting the frequency from 0.2 to 2 Hz with an accompanying increase in load at threshold adequately reproduced data collected at 2 Hz for the base metal in seawater.
12. Frequency shifting in the threshold regime is dependent on prior history. Load shedding to threshold at 10 Hz and then shifting the frequency to 0.2 Hz with no accompanying load change adequately reproduced data from individual tests at 10 and 0.2 Hz. Conversely, load shedding to threshold at 0.2 Hz and then shifting the frequency to 10 Hz with no accompanying load change gave higher values of ΔK_{th} and ΔK_{eff} than observed in an individual test at 10 Hz.
13. A new method, partial hydrogen embrittlement, has been identified as a potential method for accelerating the collection of threshold data by at least a factor of two, compared to both conventional load shedding and "increasing R-ratio" tests.
14. Polarization data have been collected for MIL S-24645 base metal, weld metal and HAZ and for ASTM A710 and the corrosion potentials, corrosion currents and polarization resistances identified for specific experimental conditions.
15. Base metal, weld metal and HAZ microstructures have been characterized and fracture paths/surfaces observed after threshold has been reached. Corrosion products contribute to closure in samples tested at the free corrosion potential, metal wedges in the specimens tested at -1.0 V SCE. Cracks, associated with the fine distribution of inclusions, were observed in the weld metal.
16. Testing the weld and HAZ microstructures has proved to be difficult due to the presence of residual stresses in the non-stress relieved welds. Accurately positioning the notches in the HAZ was found to be extremely difficult until it was recognized that the HAZ's supplied were not straight. Thinner specimen geometries were machined to correct this problem.
17. A system for collection of impedance data during crack propagation has been established, data is currently being collected and impedance models are being tested.
18. Seventy-five percent of the original corrosion fatigue crack propagation test matrix has been completed. In addition, polarization data has been collected for base metal, weld metal and HAZ microstructures. The microstructures of the test specimens have been characterized and an exploratory impedance system has been established. Additional tests are now urgently needed to support the accelerated test methodologies described above.

8. FUTURE RESEARCH

The most significant result to arise from this program, once the base-line near-threshold crack propagation data had been collected, was the development of the partial hydrogen embrittlement method to accelerate the collection of near-threshold data. This method merits immediate exploration as a generic method applicable to base metal, weld and HAZ structures in air, ASTM seawater at the free corrosion potential and ASTM seawater with cathodic protection. Investigation of different environments presents no problem as the hydrogen charging bath can be removed, the specimen heated if necessary and then the test continued in the environment of choice. Once demonstrated, this method will have wider application than ferrous materials and could be proposed for development as an ASTM standard.

9. REFERENCES

1. G. S. Booth and J. G. Wylde, Metals Science, 1977, 11, p. 308.
2. P. W. Marshall, Welding Res. Council Bull., April 1974, No. 193.
3. P. W. Marshall, Proc. National Water Resources Ocean Engineering Convention, ASCE, San Diego, CA, April 1976.
4. T. G. Gooch and G. S. Booth, "Corrosion Fatigue of Offshore Structures," Metal Science, 1979, 13, 7, pp. 402-410.
5. J. W. Cochera, J. P. Tralmer and P. W. Marshall, "Fatigue of Structural Steels for Offshore Platforms," Paper OTC 2604, 1976 Offshore Technology Conference, Houston, May 1969.
6. F. E. Havens and D. M. Bench, "Fatigue Strength of Quenched and Tempered Carbon Steel Plates and Welded Joints in Sea Water," Paper OTC 1046, 1969, Offshore Technology Conference, Houston, May 1969.
7. K. J. Marsh, T. Martin and J. McGregor, "The Effect of Random Loading and Corrosive Environment on the Fatigue Strength of Fillet-Welded Lap Joints," NEL Report 587, National Engineering Laboratory, East Kilbride, Glasgow, Feb. 1975.
8. J. C. Walter, E. Olbjorn, O. Allstad and G. Elde, "Safety Against Corrosion Fatigue Offshore," Publication No. 94, Det Norske Ventas, Horik, Norway, April 1976.
9. C. E. Jaske, D. Broek, J. E. Slater and W. E. Anderson, "Corrosion Fatigue of Structural Steels in Seawater and for Offshore Application," Corrosion Fatigue Technology, ASTM STP 642, 1978, pp. 19-47.
10. "Corrosion Fatigue of Welded Steel in Seawater," Florida Sea Grant Program, 1984.

11. D. J. Duquette, "Environmental Effects I. General Fatigue Resistance and Crack Nucleation in Metals and Alloys," Fatigue and Microstructure, ASM, 1978, pp. 335-363.
12. H. C. Marcus, "Environmental Effects II. Fatigue Crack Growth in Metals and Alloys," Fatigue and Microstructure, ASM, pp. 365-383.
13. R. W. Staehle, "A Point of View Concerning Mechanisms of Environment Sensitive Cracking of Engineering Materials," in Mechanisms of Environment Sensitive Cracking of Materials, Eds. P. R. Swann, F. P. Ford, A. R. C. Westwood, 1977, pp. 574-601.
14. R. O. Ritchie, private communication, Dept. Materials Science and Mineral Engineering, U. C. Berkeley, Berkeley, CA 94720.
15. R. O. Ritchie, Intl. Metals Reviews, 1979, Nos. 5 and 6.
16. P. B. Crosley and E. J. Ripling, "Crack Arrest in an Increasing K-field," Proc. 3rd Intl. Conf. on Pressure Vessel Tech., Part II, Materials Fabrication and Inspection, 1973.
17. J. A. Todd, P. Li, G. Liu and V. Raman, "Microstructural Studies of Corrosion Fatigue Cracks in ASTM A710," in Environmental Degradation of Engineering Materials, III, Eds. M. R. Louthan, R. P. McNitt and R. D. Sisson, Jr., 1987, pp. 533-541.
18. J. A. Todd, P. Li, G. Liu and V. Raman, "A New Mechanism of Crack Closure in Cathodically Protected ASTM A710 Steel," Scripta Metallurgica, 1988, 22, pp. 745-750.

WORK PLAN

TABLE I: Matrix of Proposed Tests

Specimen	frequency	air	seawater	seawater -1.0 V -0.8V	4 C	4 C -1.0
V	(HZ)	SCE				
MIL S-24645 .10	-	-	-	-	-	-
ASTM A710*	2	-	-	-	-	N
MIL S-24645 X	N	-	-	N	N	N
Weld Metal	10	-	-	-	N	N
Weld Metal	2 or X	-	-	-	N	N
HAZ	10	-	-	-	N	N
HAZ	2 or X	-	-	-	N	N
Base DH36	10	-	-	-	N	N
Base DH36	2 or X	O	O	O	N	N
Base Grade E	2 or X	O	O	O	N	N

* equivalent to MIL S-24645; X = 0.2 Hz; - = tests required; N = not required;
 O = optional, lower priority

WORK PLAN

TABLE II: Matrix of Completed Tests

Specimen	frequency (HZ)	air	seawater	seawater -1.0 V -0.8V	4 C	4 C -1.0
			SCE			
MIL S-24645 10		x	x	x	x	-
ASTM A710*	2		x	x	x	x
MIL S-24645 0.2		N	x3A	x	N	N
Weld Metal	10	x	x	x3A	x	N
Weld Metal	0.2	-	-	-	N	N
HAZ	10	x	x3A	x3A	N	N
HAZ	0.2	-	-	-	N	N
Base DH36	10	-	-	-	N	N
Base DH36	0.2	O	O	O	N	N
Base Grade E	0.2	O	O	O	N	N

* equivalent to MIL S-24645; x = tested; - = proposed test; N = not required;
O = optional, lower priority; A = test attempted (3A = 3 attempts)

TABLE III: Summary of Test Results

Specimen	Condition	Frequency (Hz)	ΔK_{th} Range (MPa m ^{1/2})	$\Delta K_{eff,th}$ (MPa m ^{1/2})	Comments Range
Mil-S 24645	Air	10	10.0	-	
Mil-S 24645	Air	10	7.5	5.5	
Mil-S 24645	Seawater	10	6.5	-	
Mil-S 24645	Seawater,-0.8V	10	6.5	-	
Mil-S 24645	Seawater,-1.0 V	10	6.5	-	
Mil-S 24645	Seawater,-1.0 V	10	11.5	5.0	
Mil-S 24645	Seawater,-1.0 V	10	16.0	12.0 ^{#2}	
Mil-S 24645	Seawater,-1.0 V	10	18.0	9.8 ^{#4,5}	
ASTM A710	Air	2.0	6.0	-	
ASTM A710	Seawater	2.0	7.0	4.5	
ASTM A710	Seawater,-0.8v	2.0	11.0	-	
ASTM A710	Seawater,-1.0v	2.0	11.0	-	
Mil-S 24645	Seawater	0.2	7.0	-	A
Mil-S 24645	Seawater	0.2	8.5	5.0	crack stopped
Mil-S 24645	Seawater	0.2	9.5	4.5	load increased
Mil-S 24645	Seawater,-1.0 V	0.2	16.0	5.6 ^{#1}	
Mil-S 24645	Seawater,-1.0 V	0.2	19.0	5.5 ^{#3}	
Mil-S 24645	Seawater,-1.0 V	0.2	16.0	6.5 ^{#6}	
Weld	Air	10	14.0	9.0	
Weld	Seawater	10	11.0	4.0	
Weld	Seawater,-0.8v	10	12.0	3.5	
Weld	Seawater,-1.0v	10	14.5	4.5	
Weld	Seawater,-1.0v	10	18.0	5.5	extensive corrosion before cathodic protection
HAZ	Air	10	10.0	4.5	
HAZ	Seawater	10	19.5	4.0	
HAZ	Seawater,-1.0v	10	11.5	3.5	crack path did not meet ASTM requirements

A --- load increasing test. All other tests load shedding. ^{#1}Frequency shifting experiment #1.

TABLE IV: Compositions of Steels

Material	C	Mn	P	S	Cu	Si	Ni	Cr	Mo	V	Ti	Al	Cb	Sb	As
MIL S-24645	.05	.50	.01	.002	1.17	.35	1.00	.72	.23	.003	.005	.018	.032	.003	.004
ASTM A710	.04	.58	.01	.004	1.18	.28	.76	.85	.21	-	-	-	.042	-	-

TABLE V: Mechanical Properties of Steels

Material	σ_Y (ksi)	σ_{UTS} (ksi)	%ϵ	%RA	Impact Properties	
					Type T(F) ft. lbs	
MIL S-24645* Class 3	TX 83	TX 92	36	67.8	TX 0	176
	BX 80	BX 89	26	81.0	BX 0	231
					TL 0	204
					BL 0	250
					TX -120	133
					BX -120	159
ASTM A710* Class 3	89	101	35	77.0	-80	50

*austenitized at 1660 F (904 C) for 108 minutes, water quenched, precipitation hardened at 1160 F (627 C) for 62 minutes and water quenched.

+austenitized at 1650 F (899 C) for 30 minutes, water quenched, precipitation hardened at 1100 F (598 C) for 30 minutes and furnace cooled.

**TABLE VI: SUBSTITUTE OCEAN WATER PREPARATION ACCORDING TO
ASTM STANDARD D1141-90**

Prepare Solution 1 and Solution 2 as follows:

Stock Solution 1:

MgCl ₂ ·6H ₂ O	555.6 g/l
CaCl ₂ (anhydrous)	57.9 g/l
SrCl ₂ ·6H ₂ O	2.1 g/l

Stock Solution 2:

KCl	69.5 g/l
NaHCO ₃	20.1 g/l
KBr	10.0 g/l
H ₃ BO ₃	2.7 g/l
NaF	0.3 g/l

Dissolve

NaCl	245.34 g/l
Na ₂ SO ₄ (anhydrous)	40.94 g/l

in 8-9 liters solution using deionized water. Then add slowly with vigorous stirring

200 ml of stock solution 1
100 ml of stock solution 2

Dilute to 10 liters. Adjust the pH value to 8.2 using 0.1N NaOH. Prepare the solution and adjust the pH immediately prior to use.

The final chemical composition of the substitute ocean water will be:

NaCl	24.53	g/l
MgCl ₂	5.20	g/l
Na ₂ SO ₄	4.09	g/l
CaCl ₂	1.16	g/l
KCl	0.695	g/l
NaHCO ₃	0.201	g/l
KBr	0.101	g/l
H ₃ BO ₃	0.027	g/l
SrCl ₂	0.025	g/l
NaF	0.003	g/l

Chlorinity = 19.38; pH = 8.2

Table VII. Microhardness Data of MIL S-24645 Steel Tested at 10 Hz in Seawater Near Notch and Crack Tip.

MICROHARDNESS DATA - NEAR NOTCH

Load - 50 kg		Mag: 40 X	
	Distance (mm)	HV	Avg.HV
BASE	0.00	161.00	
METAL	0.50	161.00	
	0.75	160.35	
	1.00	168.70	
CRACK	1.13		162.30
	1.25	161.40	
	1.50	165.10	
	2.00	160.30	
	2.50	160.50	
HAZ	2.70	188.95	
	2.75	184.10	
	2.85	215.40	192.55
	2.95	197.50	
	3.00	189.30	
	3.25	180.05	
WELD	3.50	159.65	
	3.75	169.50	
	4.00	173.80	172.10
	4.50	178.40	
	6.00	179.15	

MICROHARDNESS DATA - NEAR CRACK TIP

Load - 50 kg		Mag: 40 X	
	Distance (mm)	HV	Avg.HV
BASE	0.00	157.65	
METAL	0.50	159.70	
	0.75	165.15	
CRACK	1.00		159.70
	1.25	161.10	
	1.50	159.70	
	2.00	159.25	
	2.50	151.45	
	3.00	163.70	
HAZ	3.15	180.00	
	3.25	195.10	
	3.50	200.80	193.30
	3.60	201.60	
	3.70	188.95	
WELD	4.00	169.30	
	4.50	170.55	
	5.00	173.80	175.70
	5.50	181.70	
	6.00	183.15	

TABLE VIII: Summary of Data from the Polarization Curves

Specimen	Condition	Scan rate mV s ⁻¹	E _{corr} (mV)	I _{corr} (A)	R _p K Ω cm ⁻²
Test Series I					
MIL S-24645	Aerated flat	0.17*	-560	5.0	8.8
ASTM A710	Aerated cylinder	0.17*	-460	12.7	1.9
MIL S-24645	Deaerated flat	0.17*	-736	9.2	2.9
ASTM A710	Deaerated cylinder	0.17*	-763	-	-
ASTM A710	Aerated cylinder	0.17**	-637	11.4	1.9
1018	Aerated cylinder	0.17**	-738	11.5	3.0
ASTM A710	Deaerated cylinder	0.17**	-739	4.0	7.0
Test Series II					
<u>Aerated with 30 minute hold OCP</u>					
MIL S-24645	Base Metal flat	1.0	-928	14.0	4.4
MIL S-24645	Weld Metal flat	1.0	-793	17.0	1.2
MIL S-24645	HAZ flat	1.0	-567	20.1	1.3
<u>Argon Deaerated with 30 minute hold OCP</u>					
MIL S-24645	Base Metal flat	1.0	-792	4.1	6.3
MIL S-24645	Weld Metal flat	1.0	-798	4.4	5.8
MIL S-24645	HAZ flat	1.0	-779	4.1	6.6
<u>Argon Deaerated with 10 minute reduction at -1500 mV SCE</u>					
MIL S-24645	Weld Metal flat	1.0	-891	13.9	2.9
MIL S-24645	HAZ flat	1.0	-907	22.6	2.7

*Scanned positively from -1500 mV; **Held for 1.5 h in seawater prior to scan.

FIGURES

Figure 1. Plot of a/W versus normalized compliance.

Figure 2. Plot of BEC versus a/W .

Figure 3. Schematic diagram of DC electrical potential crack monitoring system.

Figure 4. DCB specimen geometry.

Figure 5. A comparison of near-threshold crack propagation rates in MIL-S24645 base metal tested in air at 22 C, $R = 0.1$, before and after correcting for crack closure.

Figure 6. A comparison of near-threshold crack propagation rates in MIL-S24645 base metal tested in air at 22 C, $R = 0.1$.

Figure 7. A comparison of near-threshold crack propagation data for MIL S-24645 tested at 10 Hz, $R = 0.1$, in air, seawater at the free corrosion potential and seawater at -1.0 V SCE.

Figure 8. A comparison of the near-threshold regime for MIL S-24645 tested at 10 Hz, $R = 0.1$, in seawater at the free corrosion potential, -0.8V SCE and -1.0 V SCE cathodic protection.

Figure 9. Near-threshold corrosion fatigue crack propagation data, before (closed symbols) and after (open symbols) correction for crack closure for MIL S-24645 base metal tested in air and seawater at -1.0 V SCE.

Figure 10. Near-threshold corrosion fatigue crack propagation data for ASTM A710 steel in air, and in ASTM seawater at the free corrosion potential, before and after correction for crack closure. 2 Hz, 25 C, $R = 0.1$.

Figure 11. A comparison of the near-threshold fatigue crack propagation data for ASTM A710 in ASTM seawater at the free corrosion potential before and after correction for crack closure; and in ASTM seawater at cathodic protection levels of -0.8V SCE and -1.0 V SCE before correction for crack closure.

Figure 12. Near-threshold corrosion fatigue crack propagation data collected in air, 22 C, $R = 0.1$, $\nu = 0.2$ Hz. Tests 1 and 2 load increasing, test 3 load shedding.

Figure 13. Near-threshold corrosion fatigue crack propagation data, before and after correction for crack closure, for MIL S-24645 tested in ASTM seawater at the free corrosion potential, $R = 0.1$, 22 C, $\nu = 0.2$ Hz. (Test #3)

Figure 14. Effect of increasing ΔK to 15 Mpa m^{1/2} and ν to 2.0 Hz then load shedding to threshold (test #6) after completing test #3 at 0.2 Hz on the same specimen. ASTM seawater at the free corrosion potential, R = 0.1, 22 C.

Figure 15. A comparison of the near-threshold corrosion fatigue data for MIL S-24645 tested in ASTM seawater at the free corrosion potential and frequencies of 10, 2 and 0.2 Hz.
R = 0.1, 22 C.

Figure 16. Near-threshold fatigue crack propagation data, before and after correction for closure, for the weld metal tested in air, ν = 10 Hz, R = 0.1, 22 C.

Figure 17. Near-threshold fatigue crack propagation data, before and after correction for closure, for the weld metal tested in ASTM seawater, 10 Hz, R = 0.1, 22 C.

Figure 18. Near-threshold fatigue crack propagation data, before and after correction for closure, for the weld metal tested in ASTM seawater at -0.8V SCE, 10 Hz, R = 0.1, 22 C.

Figure 19. Near threshold fatigue crack propagation data, before and after correction for closure, for the weld metal tested in ASTM seawater at -1.0 V SCE, 10 Hz, R = 0.1, 22 C.

Figure 20. A comparison of near-threshold propagation data between test #1, weld metal anodically polarized to +1.0 V SCE for 10 minutes prior to testing at -1.0 V SCE, and test #2, weld metal protected with -1.0 V SCE, in ASTM seawater, before and after correction for crack closure. 10 Hz, R = 0.1, 22 C.

Figure 21. Comparison between the near-threshold fatigue crack propagation data, before and after correction for closure, for the weld metal tested in ASTM seawater at -0.8V SCE and -1.0 V SCE. 10 Hz, R = 0.1, 22 C.

Figure 22. Comparison between the near-threshold fatigue crack propagation data, before and after correction for closure, for the weld metal tested in air, ASTM seawater at the free corrosion potential, and ASTM seawater at -0.8V SCE and -1.0 V SCE. 10 Hz, R = 0.1, 22 C.

Figure 23. Comparison between the near-threshold crack propagation data, before and after correction for closure for MIL S-24645 base and weld metals in air and ASTM seawater at the free corrosion potential. 10 Hz, R = 0.1, 22 C.

Figure 24. Comparison between the near-threshold crack propagation data, before and after correction for closure for MIL S-24645 base and weld metals in ASTM seawater at -0.8V SCE and -1.0 V SCE. 10 Hz, R = 0.1, 22 C.

Figure 25. Near-threshold fatigue crack propagation data, before and after correction for closure, for MIL S-24645 "HAZ" tested in air, ν = 10 Hz, R = 0.1, 22 C.

Figure 26. Near-threshold fatigue crack propagation data, before and after correction for closure, for the MIL S-24645 "HAZ" tested in ASTM seawater, 10 Hz, R = 0.1, 22 C.

Figure 27. Near threshold fatigue crack propagation data, before and after correction for closure, for MIL S-24645 "HAZ" tested in ASTM seawater at -1.0 V SCE, 10 Hz, R = 0.1, 22 C.

Figure 28. Comparison between the near-threshold fatigue crack propagation data, before and after correction for closure, for MIL S-24645 "HAZ" tested in air, ASTM seawater at the free corrosion potential, and ASTM seawater at -1.0 V SCE. 10 Hz, R = 0.1, 22 C.

Figures 29a-29c. Scanning electron micrographs for the LT orientation of polished MIL S-24645.

Figures 29d, 29e. Scanning electron micrographs for the LW orientation of polished MIL S-24645.

Figure 30. ASTM A710

- (a) optical micrograph showing acicular ferrite microstructure
- (b)-(d) transmission electron micrographs showing (b) inclusion;
- (c) copper precipitation on dislocations (bright field)
- (d) copper precipitation on dislocations (dark field)

Figure 31. Fracture surfaces of ASTM A710 (left) and ASTM A710 weld metal (right) tested in air.

Figures 32a, 32b. SEM micrographs of fracture surfaces of ASTM A710 tested in ASTM seawater at 2 Hz showing extensive corrosion product and a rough fracture surface.

Figures 33a, 33b. SEM micrographs of ASTM A710 tested in ASTM seawater at -0.8V SCE showing no corrosion product and smooth fracture surface. Note: the specimen surface is covered with a layer of epoxy containing air bubbles.

Figures 34a-34f. SEM micrographs of ASTM A710 tested in seawater at -1.0 V SCE.

- (a) crack profile
- (b) damage ahead of crack tip
- (c) crack branch
- (d) cracks opening up around grain boundaries
- (e) metal grain in crack tip
- (f) metal wedges in the crack wake.

Figure 35. Schematic representation of crack propagation in ASTM A710 tested in ASTM seawater at -1.0 V SCE.

- (a) damage accumulation ahead of crack tip
- (b) development of upper crack (A) and main branch (B) by cracking along grain boundaries
- (c) extension of both cracks (A,B), movement of metal wedge and damage accumulation at C
- (d) crack extension at C and metal wedge contributing to crack closure.

Figure 36. Crack profile of MIL S-24645 Base metal tested in ASTM seawater at the free corrosion potential at 0.2 Hz under load increasing conditions (test #2).

Figure 37. Higher magnification views of MIL S-24645 tested in ASTM seawater at the free corrosion potential at 0.2 Hz under load increasing conditions (test #2).

Figure 37 continued. Higher magnification views of MIL S-24645 tested in ASTM seawater at the free corrosion potential at 0.2 Hz under load increasing conditions (test #2).

Figure 38. MIL S-24645 tested in ASTM seawater at the free corrosion potential at 0.2 Hz under load increasing conditions (test #1).

Figure 39. MIL S-24645 tested in ASTM seawater at the free corrosion potential at 0.2 Hz under load increasing conditions (test #1).

Figure 40. MIL S-24645 tested in ASTM seawater at the free corrosion potential at 0.2 Hz under load shedding conditions (test #3).

Figure 41. Higher magnification views of MIL S-24645 tested in ASTM seawater at the free corrosion potential at 0.2 Hz under load shedding conditions (test #3).

Figure 42. Higher magnification views of MIL S-24645 tested in ASTM seawater at the free corrosion potential at 0.2 Hz under load shedding conditions (test #3).

Figure 43a. Optical Micrographs of the Fracture Path (Near Notch) of MIL-S24645 Steel Base Metal Tested at 10 Hz at -1.0 V in ASTM Seawater.

Figure 43b. Optical Micrographs of the Fracture Path (Near Crack Tip) of MIL-S24645 Steel Base Metal Tested at 10 Hz at -1.0 V in ASTM Seawater.

Figure 44. Optical Micrographs of the Fracture Path (Near Crack Tip) of MIL-S24645 Steel Base Metal tested at 10 Hz at -1.0 V in ASTM Seawater (a) 400 X, 5% Nital; (b) 1000 X, 5% Nital.

Figure 45. SEM Micrographs of the Fracture Path of MIL-S24645 Steel Base Metal Tested at 10 Hz in Seawater at -1.0 V (SCE).

Figure 46. Crack profile for MIL S-24645 Weld metal tested in air at 10 Hz.

Figure 47. Higher magnification views of the crack profile for MIL S-24645 Weld metal tested in air at 10 Hz.

Figure 48. Higher magnification views of the crack profile for MIL S-24645 Weld metal tested in air at 10 Hz.

Figure 49. Crack profile for MIL S-24645 weld metal tested in ASTM seawater at the free corrosion potential.

Figure 50. Higher magnification views of the crack profile for MIL S-24645 weld metal tested in ASTM seawater at the free corrosion potential, showing small non-metallic inclusions.

Figure 51. Higher magnification views of the crack profile for MIL S-24645 weld metal tested in ASTM seawater at the free corrosion potential, showing small non-metallic inclusions.

Figure 52a. Optical Micrographs of the Fracture Path (Near Notch) of MIL-S24645 Steel in the Weld Tested at 10 Hz at -1.0 V in Seawater.

Figure 52b. Optical Micrographs of the Fracture Path (Near Crack Tip) of MIL-S24645 Steel in the Weld Tested at 10 Hz at -1.0 V in Seawater.

Figure 53. SEM Micrographs of the Fracture Path (Near Crack Tip) of MIL-S24645 Steel in the Weld Tested at 10 Hz at -1.0 V in Seawater (a) 750 X, 5% Nital; (b) 1500 X, Unetched.

Figure 54. SEM Micrographs of the Fracture Path with Crack Branching and Damage Accumulation of MIL-S24645 Steel in the Weld Tested at 10 Hz at -1.0 V in Seawater.

Figure 55. SEM Micrographs of the Fracture Path with Crack Branching and Damage Accumulation of MIL-S24645 Steel in the Weld Tested at 10 Hz at -1.0 V in Seawater (a) Behind Crack Tip (b) In the Middle Region.

Figure 56. Typical Energy dispersive X-ray analysis of inclusions observed in the weld metal.

Figure 57a. Optical Micrographs of the Fracture Path (Near Notch) of MIL-S24645 "HAZ" Tested at 10 Hz in Seawater.

Figure 57b. Optical Micrographs of the Fracture Path (Near Crack Tip) of MIL-S24645 "HAZ" Tested at 10 Hz in Seawater.

Figure 58. Optical Micrographs of the Different Regions of MIL-S24645 Steel Tested at 10 Hz in Seawater (a) Base Metal; (b) HAZ; (c) Weld; (d) Transition between Weld and HAZ.

Figure 59a. Hardness Distribution in the Vicinity of the Weld. MIL S-24645 "HAZ" CT sample near the notch.

Figure 59b. Hardness Distribution in the Vicinity of the Weld. MIL S-24645 "HAZ" CT sample near the crack tip.

Figure 60. Schematic of the Width of the HAZ and its Distance from the Crack:
(a) Near Notch; (b) Near Crack Tip.

Figure 61. SEM Micrograph of the Fracture Path of MIL-S24645 "HAZ" Tested at 10 Hz in ASTM Seawater.

Figure 62. SEM Micrograph at High Magnifications of the Fracture Path near the Crack Tip of MIL-S24645 Steel Tested at 10 Hz in Seawater: (a) 10,000 X; (b) 35,000 X; (c) 50,000 X.

Figure 63. Potentiodynamic polarization curves:

- (a) Comparison of data for ASTM A710 (cylindrical) and MIL S-24645 (flat) steels in aerated ASTM seawater, pH = 8.2, 22 C.
- (b) Comparison of data for ASTM A710 (cylindrical) and MIL S-24645 (flat) steels in deaerated ASTM seawater, pH = 8.2, 22 C.
- (c) ASTM A710 and 1018 steel held in ASTM seawater for 1.5 hours prior to scanning positively or negatively from the free corrosion potential.
- (d) Comparison of data for ASTM A710 held in aerated and deaerated ASTM seawater for 1.5 hours prior to scanning positively or negatively from the free corrosion potential.

Figure 64. Polarization Curves for MIL S-24645 Base, Weld and HAZ microstructures in air saturated ASTM seawater, pH = 8.2, 22 C, with a 30 minute hold at the open circuit potential (OCP) prior to scanning positively from 250 Mv below the corrosion potential.

Figure 65. Polarization Curves for MIL S-24645 Base, Weld and HAZ microstructures in argon saturated ASTM seawater, Ph = 8.2, 22 C, with a 30 minute hold at the open circuit potential (OCP) prior to scanning positively from 250 Mv below the corrosion potential.

Figure 66. Polarization Curves for MIL S-24645 Base, Weld and HAZ microstructures in argon saturated ASTM seawater, Ph = 8.2, 22 C, with a 10 minute reduction at -1500 Mv SCE prior to scanning positively from 250 Mv below the corrosion potential.

Figure 67. Comparison of the polarization curves for MIL S-24645 Base metal collected in air and argon saturated ASTM seawater, Ph = 8.2, 22 C, with a 30 minute hold at the open circuit potential (OCP) prior to scanning positively from 250 Mv below the corrosion potential.

Figure 68. Comparison of the polarization curves for MIL S-24645 Weld metal collected in air and argon saturated ASTM seawater, pH = 8.2, 22 C, with a 30 minute hold at the open circuit potential (OCP) prior to scanning positively from 250 mV below the corrosion potential.

Figure 69. Comparison of the polarization curves for MIL S-24645 HAZ collected in air and argon saturated ASTM seawater, pH = 8.2, 22 C, with a 30 minute hold at the open circuit potential (OCP) prior to scanning positively from 250 mV below the corrosion potential.

Figure 70. A comparison of near-threshold crack propagation data, before and after correction for crack closure, for MIL S-24645 base metal tested in ASTM seawater at -1.0 V (SCE) and at 0.2 Hz, R = 0.1, 22 C.

Figure 71. A comparison of near-threshold crack propagation data, before and after correction for crack closure, for MIL S-24645 base metal tested in ASTM seawater at -1.0 V (SCE) and at 10.0 Hz, following the test at 0.2 Hz in Fig. 70. R = 0.1, 22 C.

Figure 72. A comparison of near-threshold crack propagation data, before and after correction for crack closure, for MIL S-24645 base metal tested in ASTM seawater at -1.0 V (SCE) and at 10.0 Hz, R = 0.1, 22 C. Frequency was shifted to 0.2 Hz accompanied by a load increase following the 10 Hz test shown in Fig. 71.

Figure 73. A comparison of near-threshold crack propagation data, before and after correction for crack closure, for MIL S-24645 base metal tested in ASTM seawater at -1.0 V (SCE) and at 10.0 Hz, R = 0.1, 22 C. Test #1 conducted initially at 0.2 Hz and test #3, conducted at 0.2 Hz following the 10 Hz test shown in Fig. 71.

Figure 74. A comparison of near-threshold crack propagation data, before and after correction for crack closure, for MIL S-24645 base metal tested in ASTM seawater at -1.0 V (SCE) and at 10.0 Hz, following test #3 at 0.2 Hz as shown in Fig. 72. R = 0.1, 22 C.

Figure 75. A comparison of the near-threshold crack propagation data for tests #2 and 4, before and after correction for crack closure, for MIL S-24645 base metal tested in ASTM seawater at -1.0 V (SCE) and at 10.0 Hz, following prior tests at 0.2 Hz. R = 0.1, 22 C.

Figure 76. A comparison of near-threshold crack propagation data, before and after correction for crack closure, for MIL S-24645 base metal test #5 in ASTM seawater at -1.0 V (SCE) and at 10.0 Hz. The load was increased and then shed to threshold at 10 Hz following test #4 at 10 Hz (shown in Fig. 75). R = 0.1, 22 C.

Figure 77. A comparison of the near-threshold crack propagation data for tests #4 and #5, before and after correction for crack closure, for MIL S-24645 base metal tested in ASTM seawater at -1.0 V (SCE) and at 10.0 Hz. $R = 0.1$, 22 C.

Figure 78. A comparison of near-threshold crack propagation data, before and after correction for crack closure, for MIL S-24645 base metal tested in ASTM seawater at -1.0 V (SCE) and at 10.0 Hz, $R = 0.1$, 22 C. Test #5 conducted at 10 Hz and test #6, conducted at 0.2 Hz with no increase in load following the 10 Hz test shown in Fig. 77.

Figure 79. The effect of hydrogen charging on the crack growth rate for MIL-S24645 base metal tested at 10 Hz, $R = 0.1$, with 5N H_2SO_4 + 0.25 mg/liter As_2O_3 solution and in air.

Figure 80. A comparison of the near-threshold crack propagation data for MIL-S 24645 base metal tested at 10 Hz, $R = 0.1$, in air and in 5N H_2SO_4 + 0.25 mg/liter As_2O_3 solution with an applied current density of 50 mA cm^{-2} .

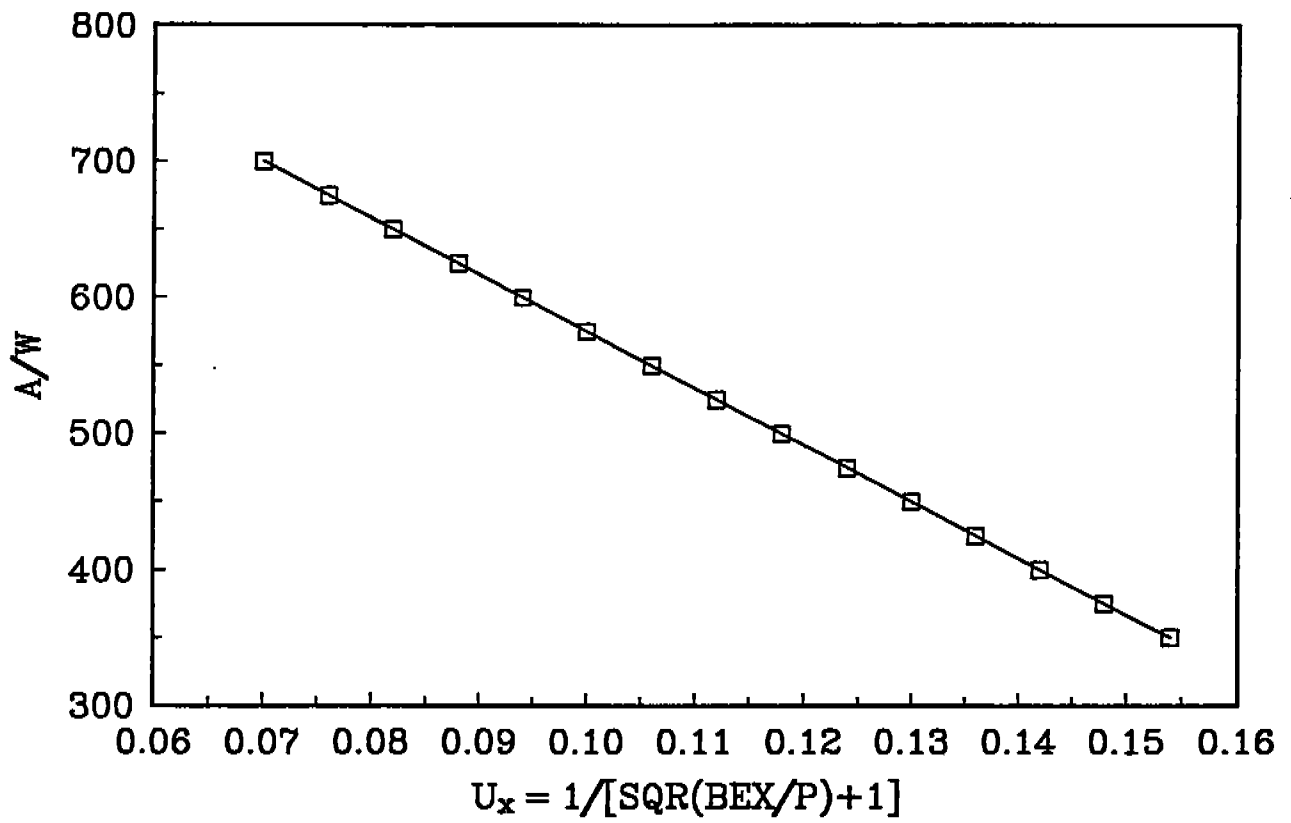


Figure 1. Plot of a_i/W versus normalized compliance.

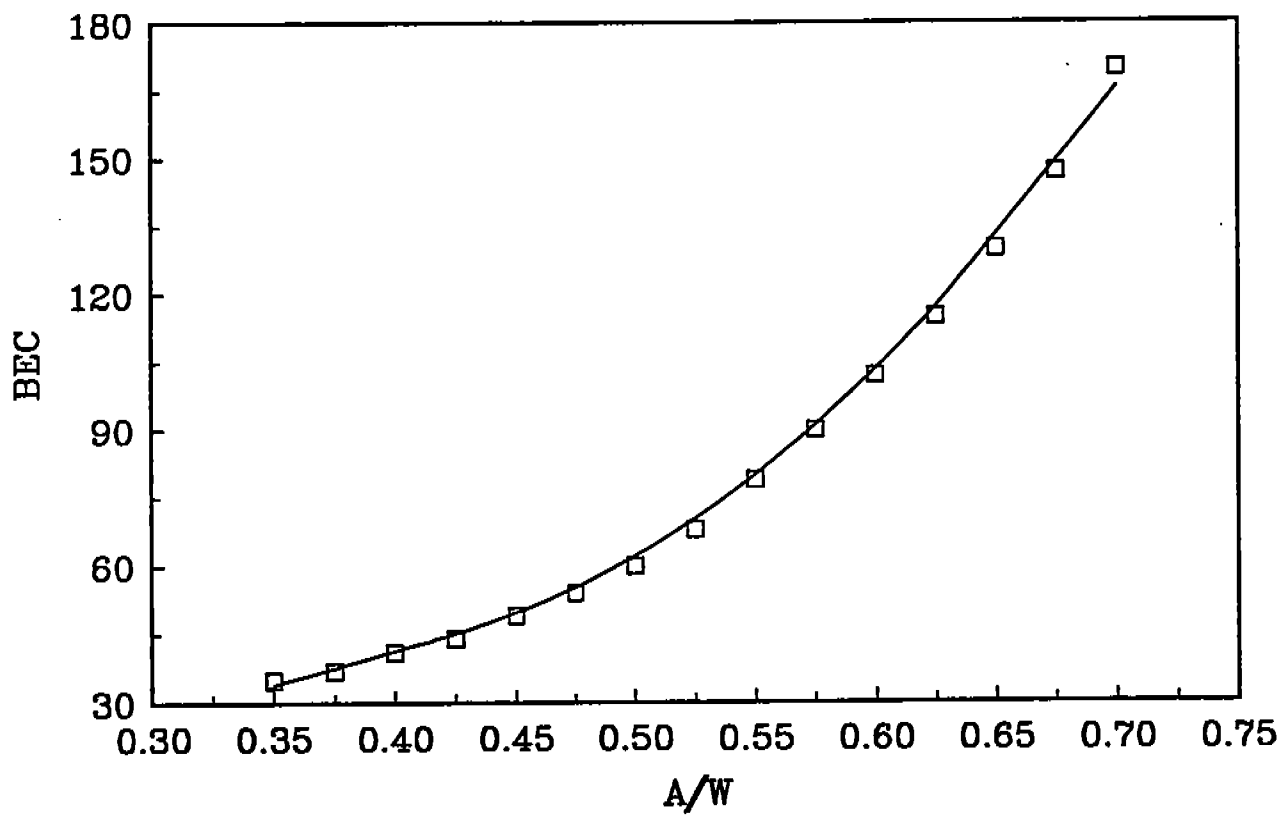


Figure 2. Plot of BEC versus a_i/W .

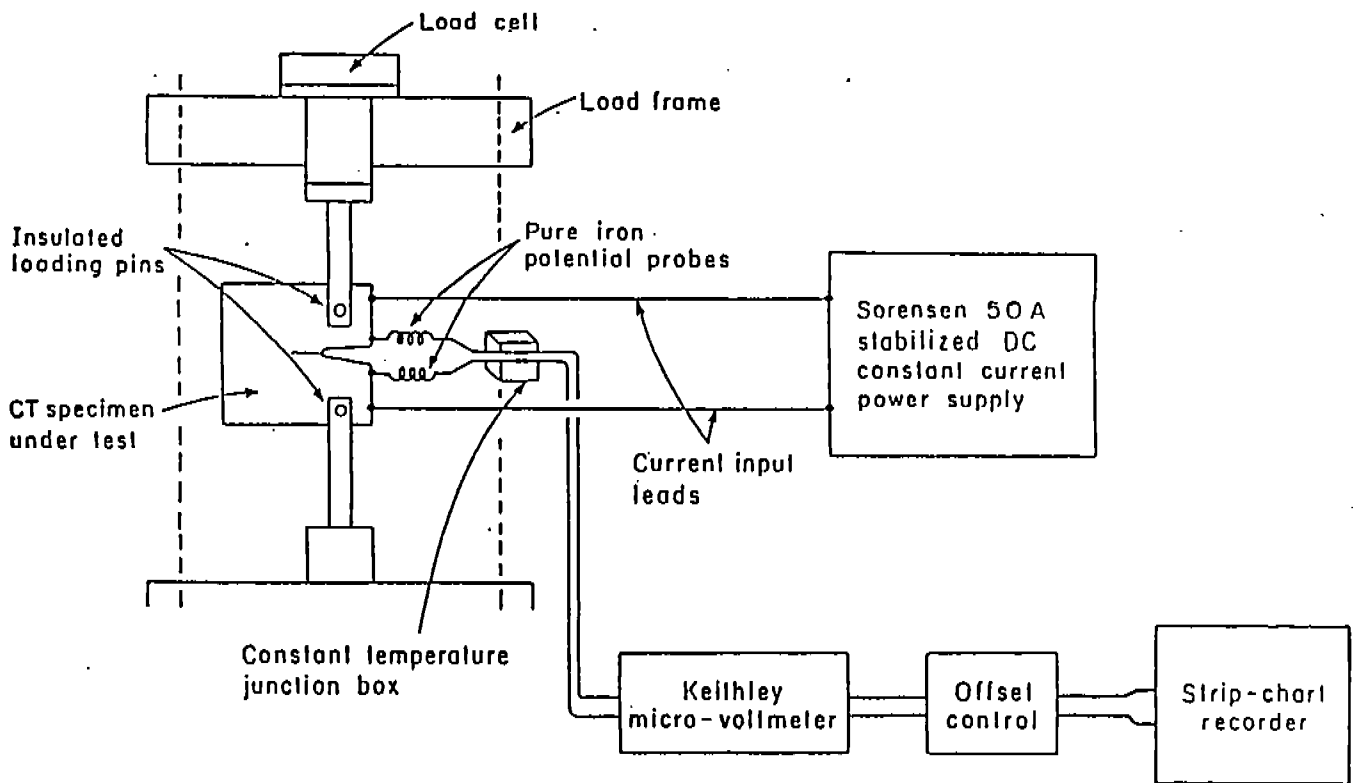


Figure 3. Schematic diagram of D.C. electrical potential crack monitoring system.

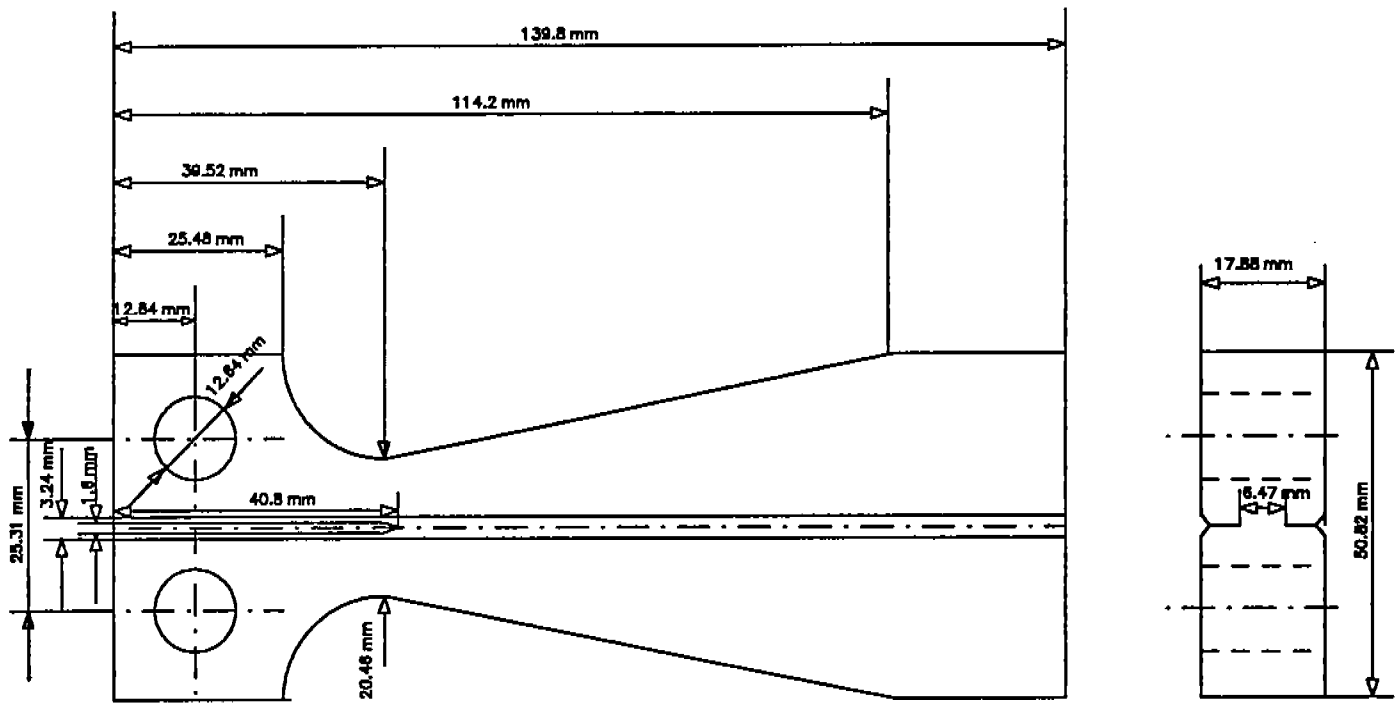


Figure 4. DCB specimen geometry.

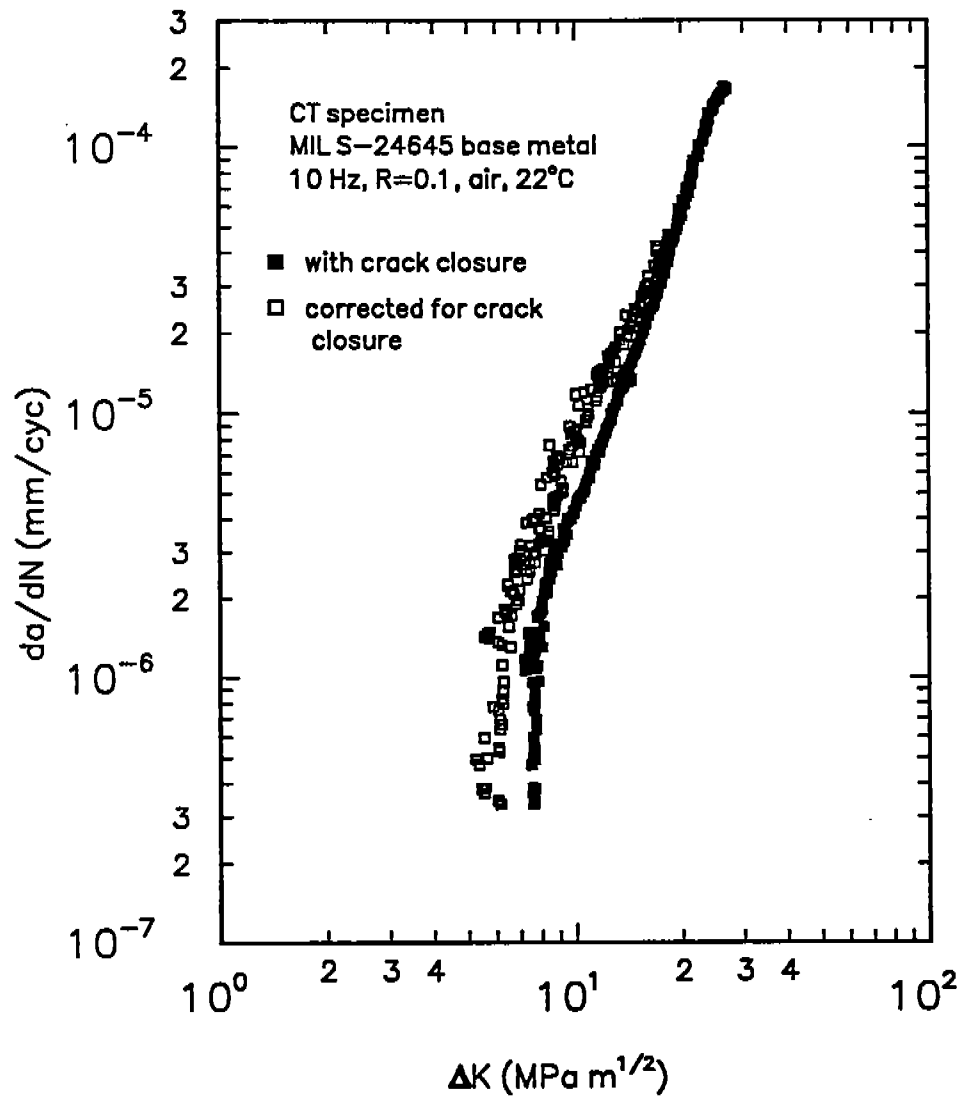


Figure 5. A comparison of near-threshold crack propagation rates in MIL S-24645 base metal tested in air at 10 Hz, 22 C, R = 0.1, before and after correcting for crack closure.

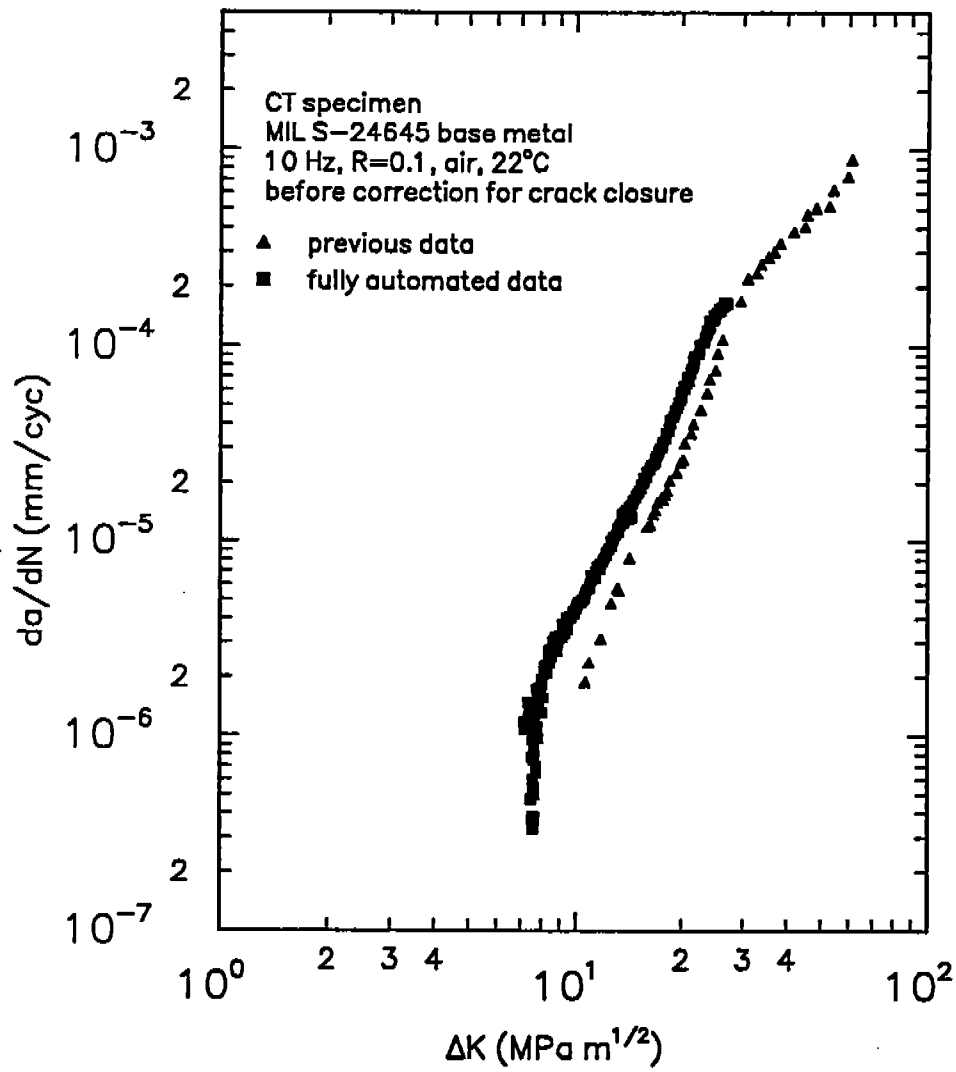


Figure 6. A comparison of near-threshold crack propagation rates in MIL S-24645 base metal tested in air at 10 Hz, 22 C, R = 0.1.

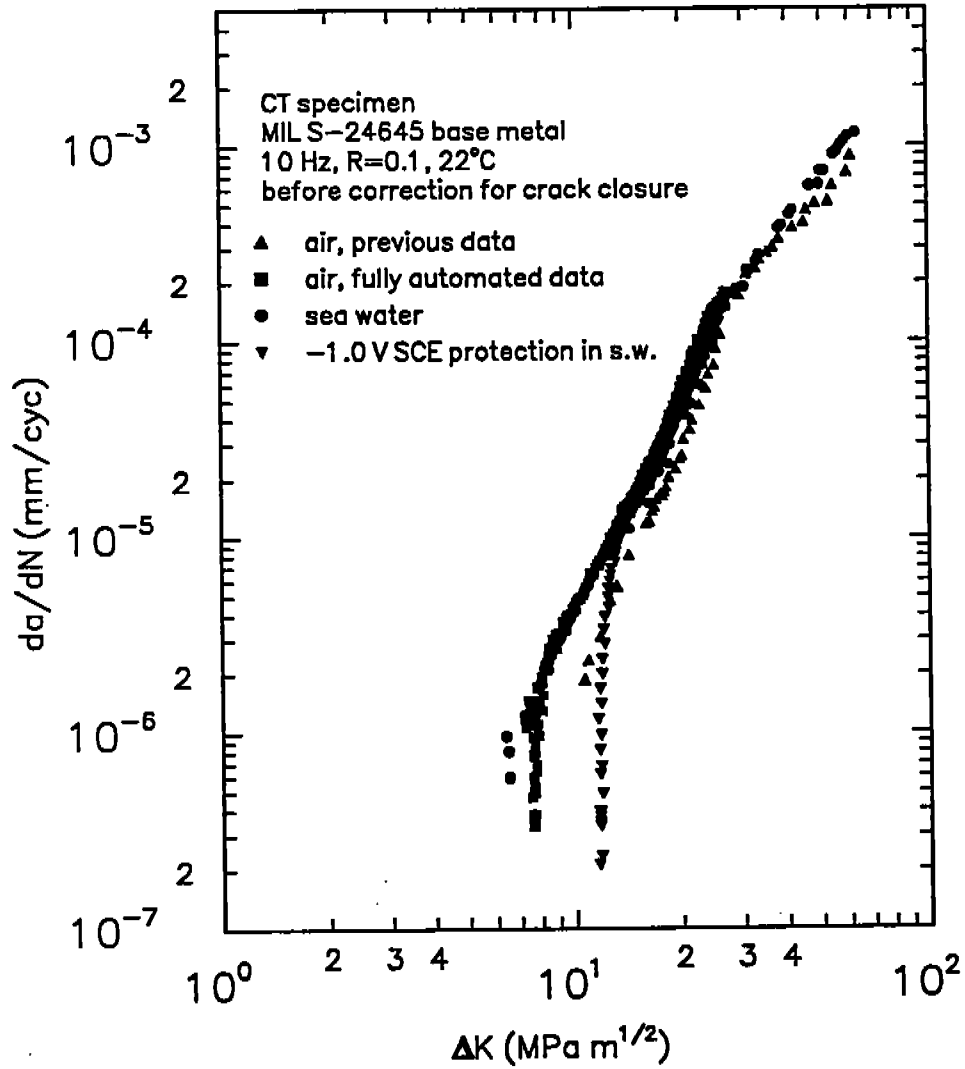


Figure 7. A comparison of near-threshold crack propagation rates in MIL S-24645 base metal tested at 10 Hz, R = 0.1 in air, seawater at the free corrosion potential and seawater at -1.0V SCE.

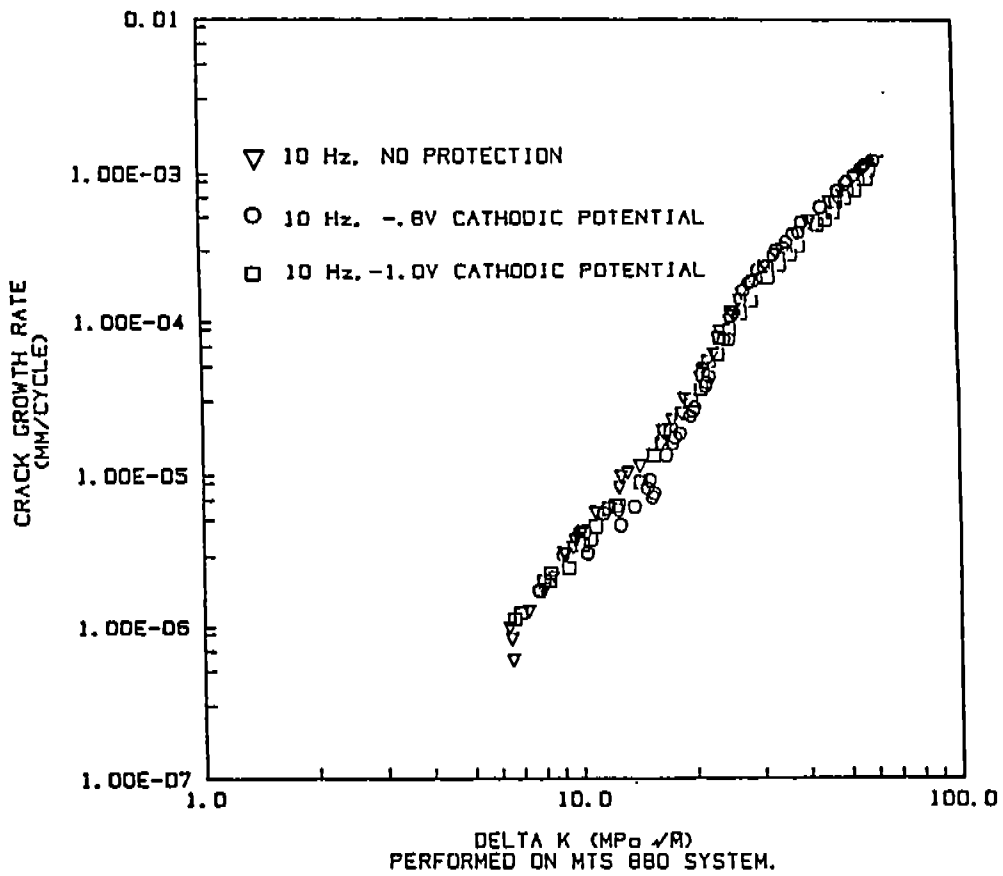


Figure 8. A comparison of the near-threshold regime for MIL S-24645 tested at 10 Hz, R = 0.1 in seawater at the free corrosion potential, -0.8V SCE and -1.0V SCE cathodic protection.

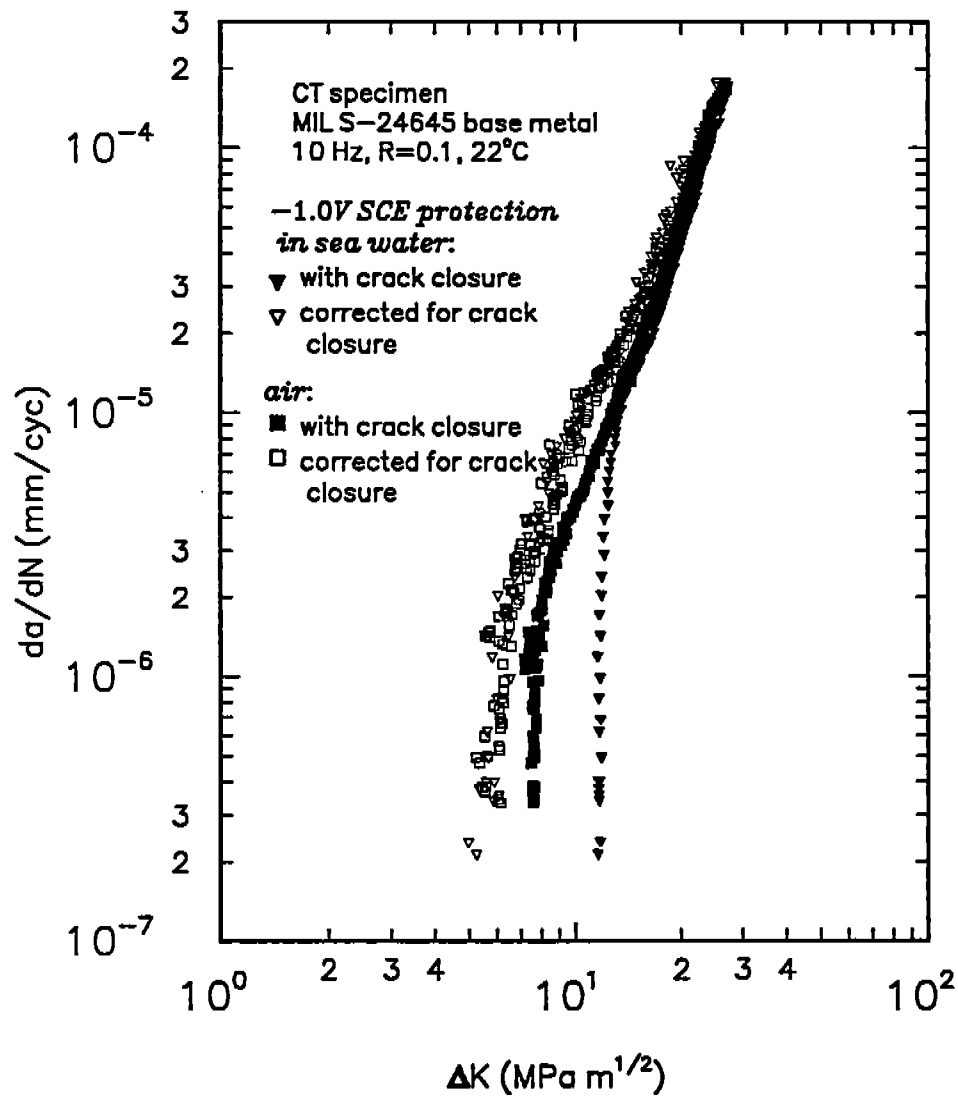


Figure 9. Near-threshold corrosion fatigue crack propagation data, before (closed symbols) and after (open symbols) correction for crack closure, for MIL S-24645 base metal tested in air and seawater at -1.0V SCE.

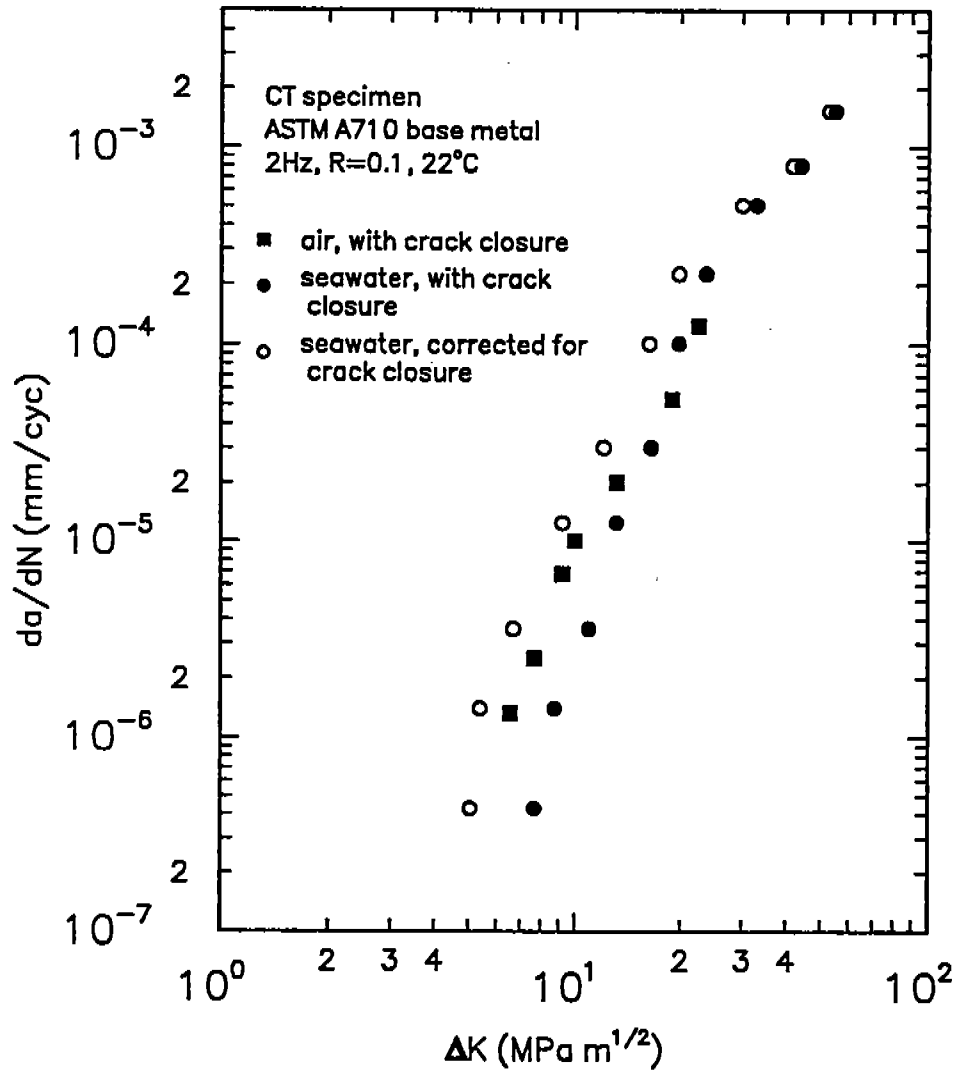


Figure 10. Near-threshold corrosion fatigue crack propagation data for ASTM A710 base metal in air and in ASTM seawater at the free corrosion potential, before and after correction for crack closure. 2 Hz, 22 C, R = 0.1.

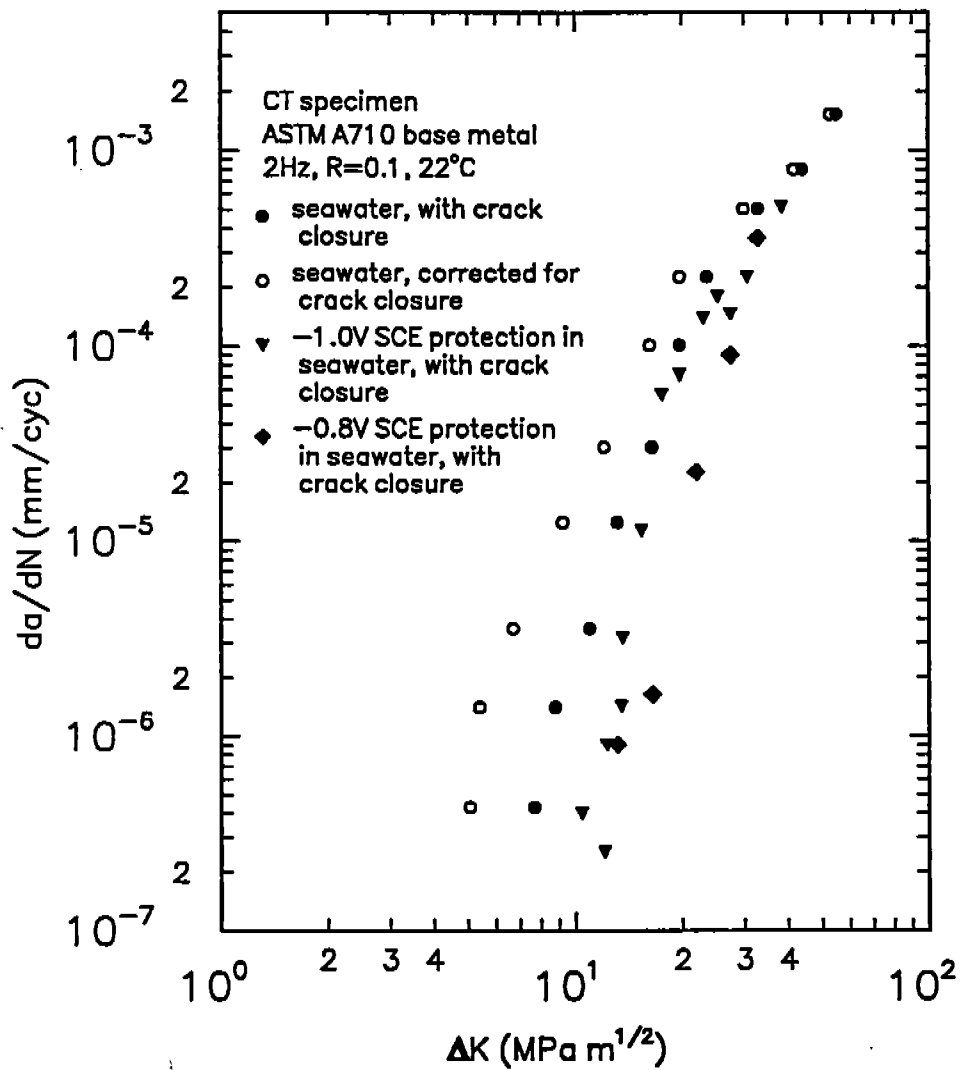


Figure 11. A comparison of the near-threshold fatigue crack propagation data for ASTM A710 in ASTM seawater at the free corrosion potential before and after correction for crack closure and in ASTM seawater at cathodic protection levels of -0.8V SCE and -1.0V SCE before correction for crack closure. 2 Hz, 22 C, R = 0.1.

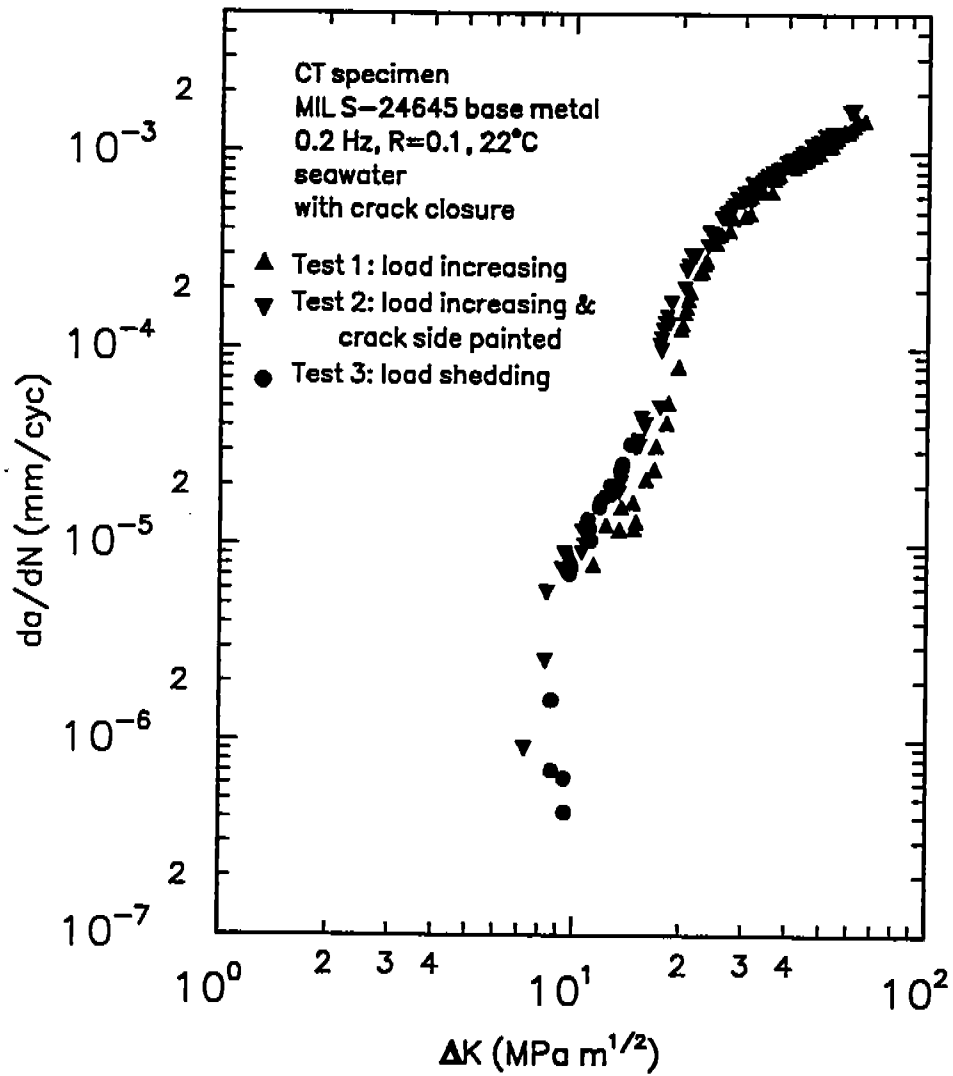


Figure 12. Near-threshold corrosion fatigue crack propagation data collected in air at 0.2 Hz, 22 C, R = 0.1, Tests #1 and #2 load increasing, test #3 load shedding.

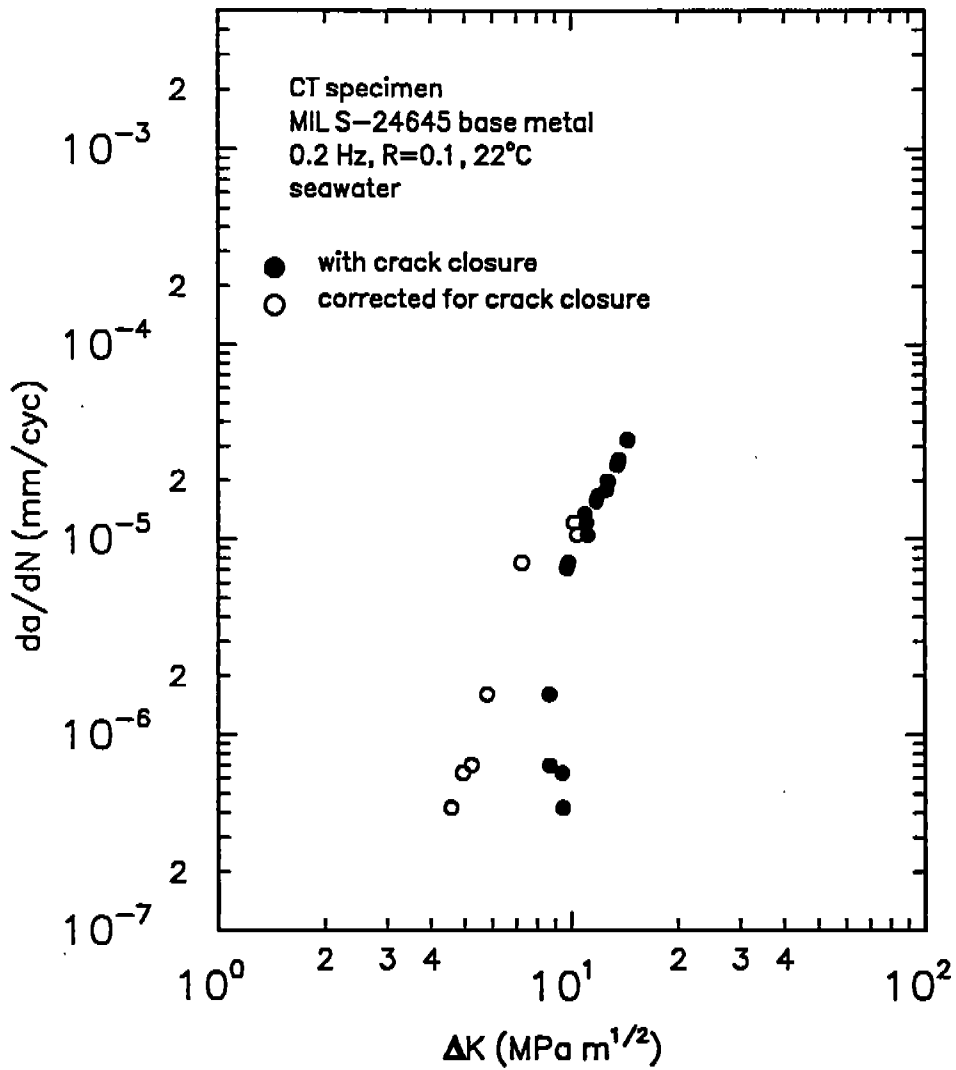


Figure 13. Near-threshold corrosion fatigue crack propagation data, before and after correction for crack closure, for MIL S-24645 base metal tested in ASTM seawater at the free corrosion potential, 0.2 Hz, 22 C, R = 0.1. (Test #3)

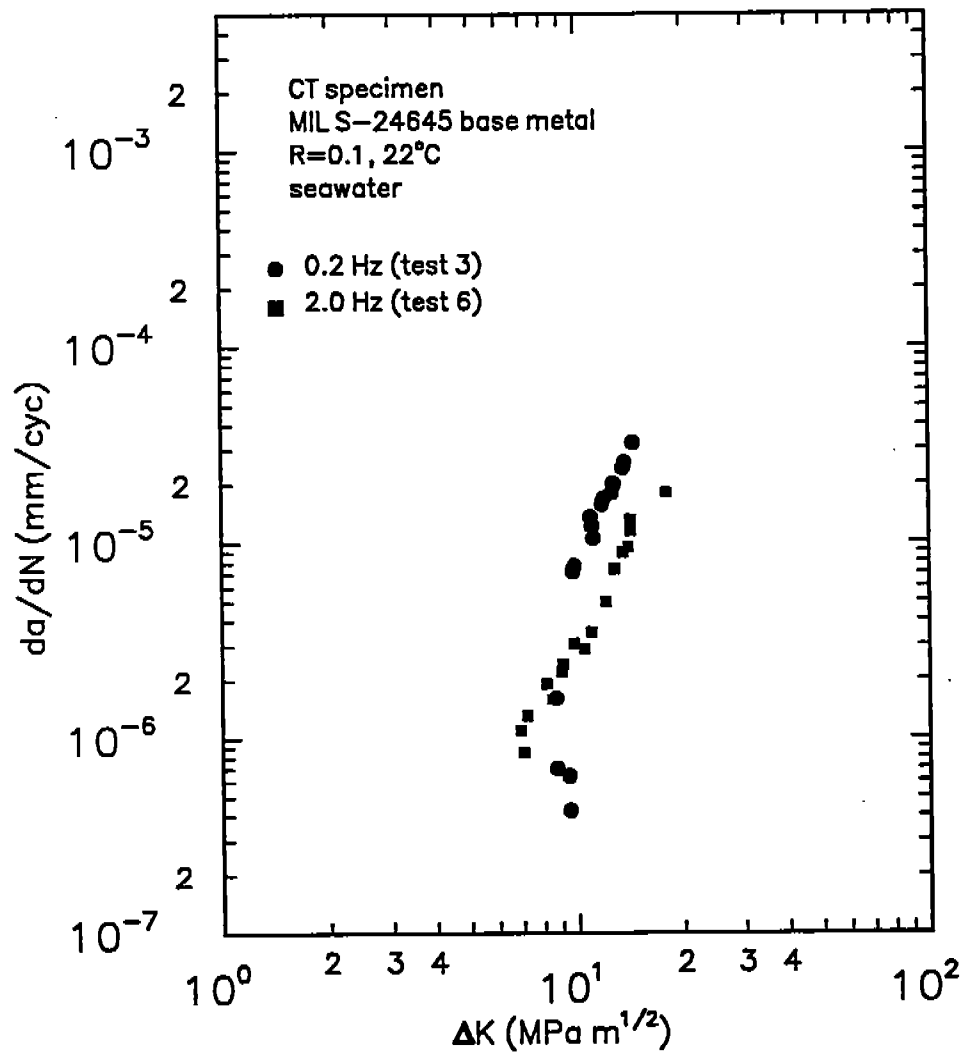


Figure 14. Effect of increasing ΔK to 15 MPa $m^{1/2}$ and ν to 2.0 Hz, then load shedding to threshold (test #6) after completing test #3 at 0.2 Hz on the same specimen. ASTM seawater at the free corrosion potential, R = 0.1, 22 C.

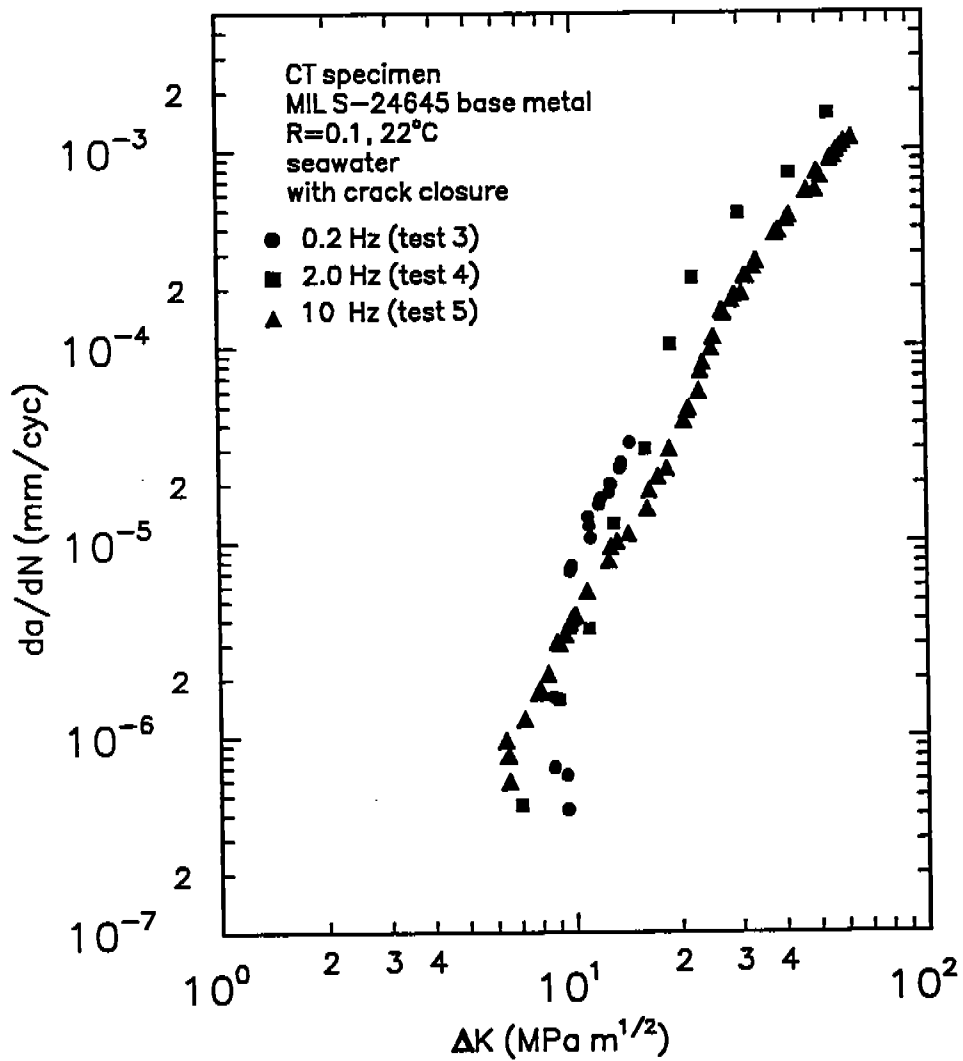


Figure 15. A comparison of the near-threshold corrosion fatigue data for MIL S-24645 base metal tested in ASTM seawater at the free corrosion potential and frequencies of 10, 2 and 0.2 Hz. 22 C, R = 0.1.

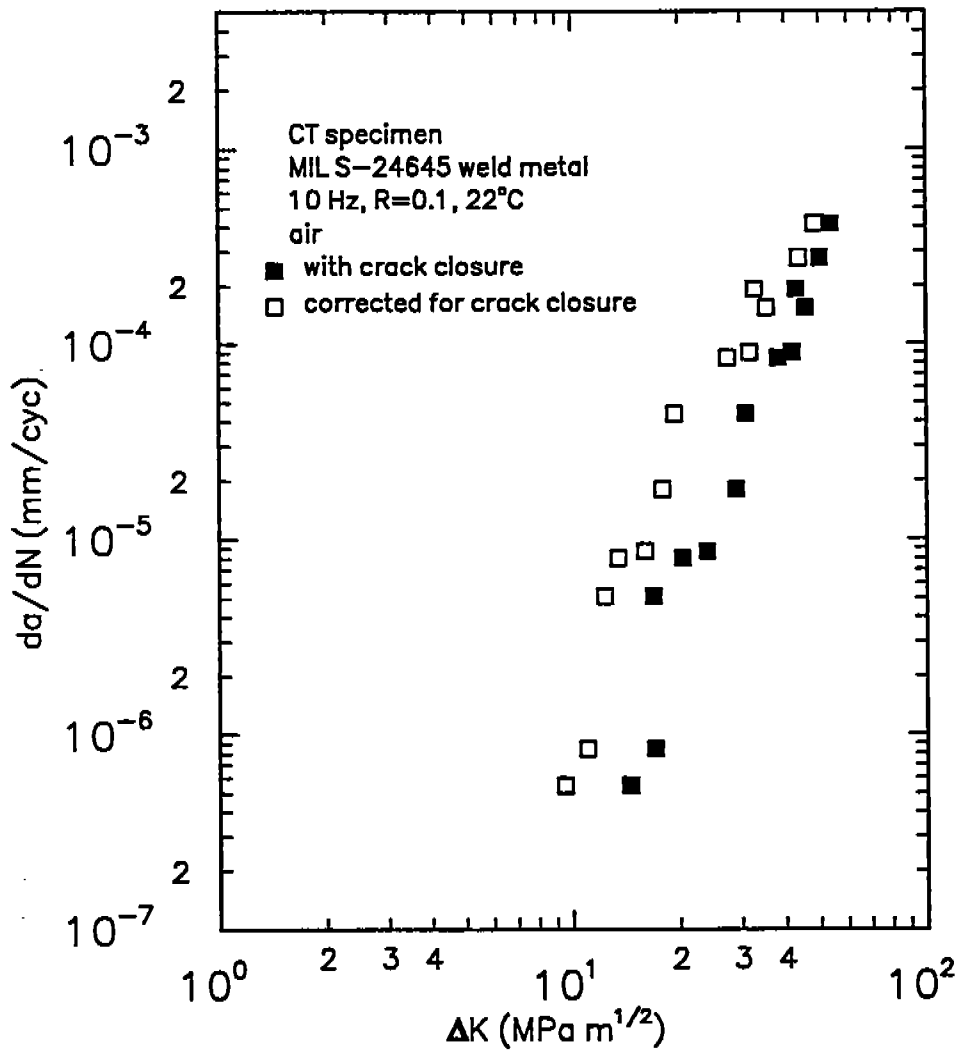


Figure 16. Near-threshold fatigue crack propagation data, before and after correction for closure, for MIL S-24645 weld metal tested in air at 10 Hz, R = 0.1, 22 C.

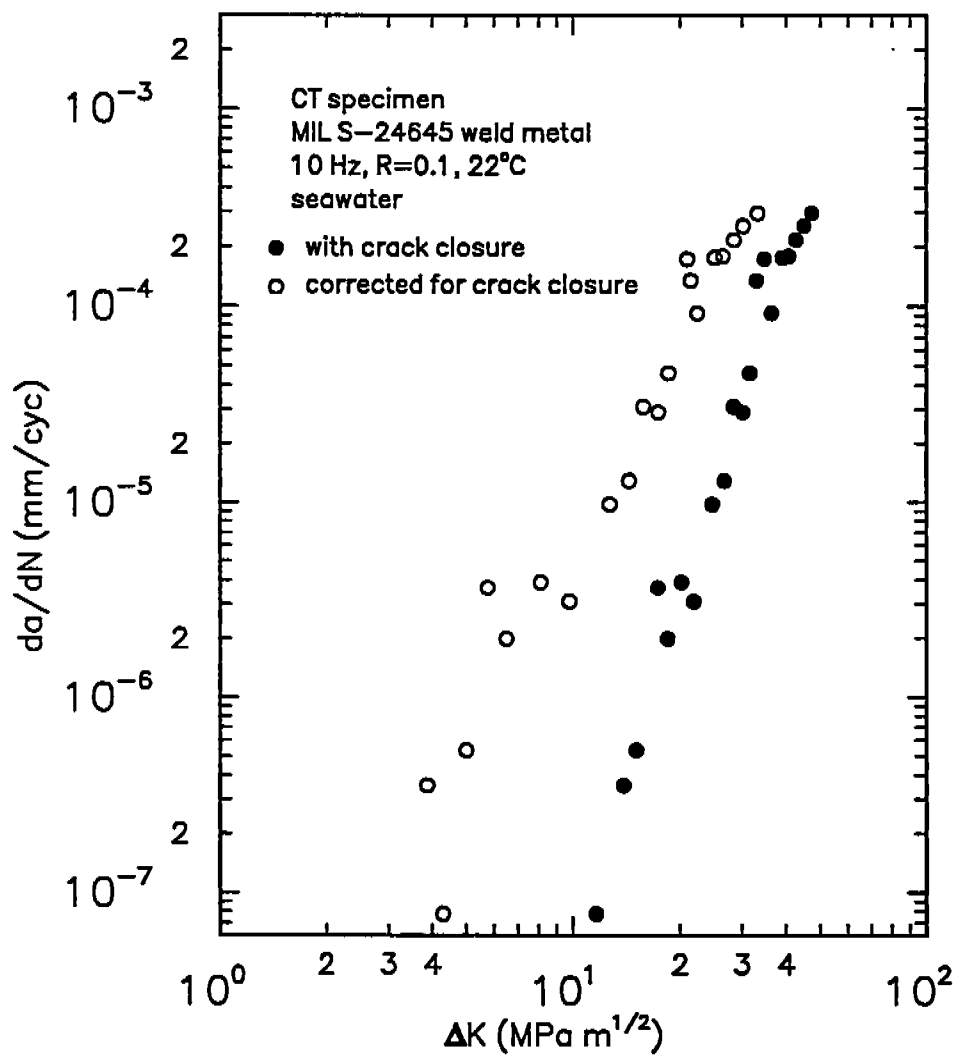


Figure 17. Near-threshold fatigue crack propagation data, before and after correction for closure, for MIL S-24645 weld metal tested in ASTM seawater, 10 Hz, R = 0.1, 22 C.

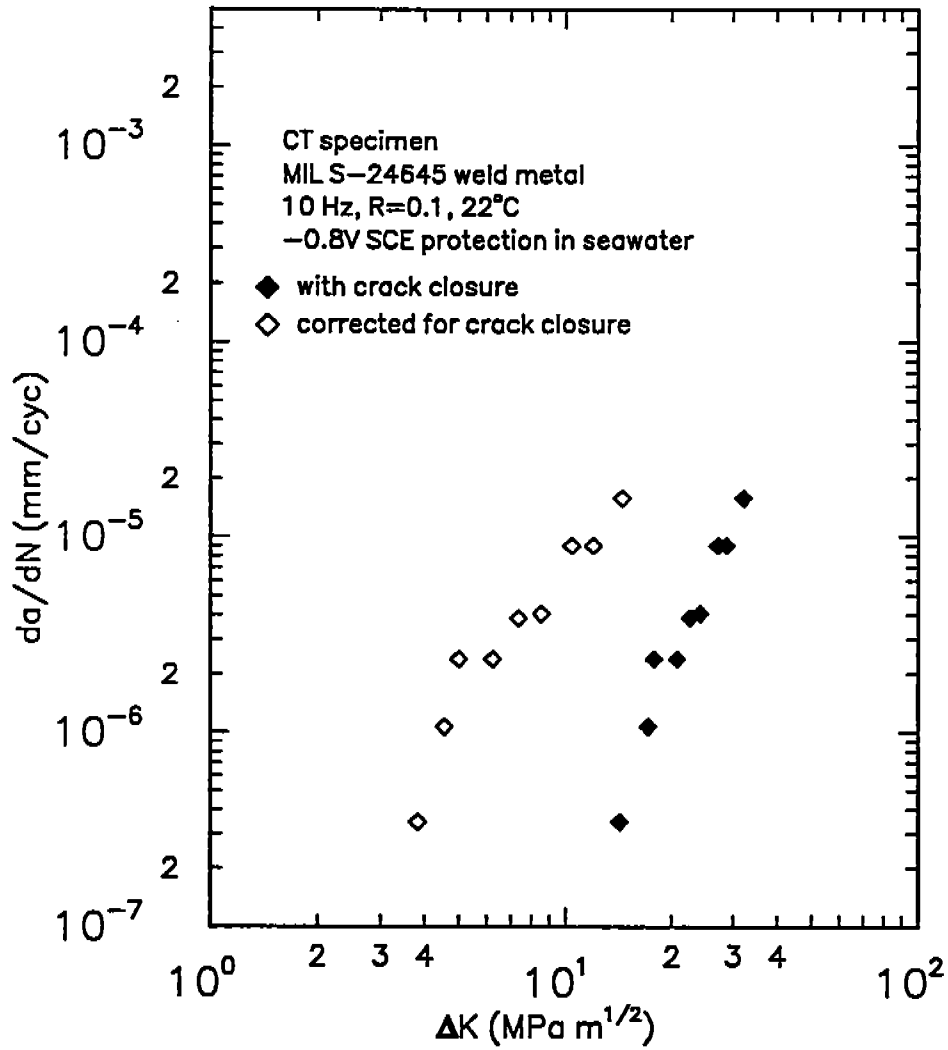


Figure 18. Near-threshold fatigue crack propagation data, before and after correction for closure, for MIL S-24645 weld metal tested in ASTM seawater at -0.8V SCE, 10 Hz, R = 0.1, 22 C.

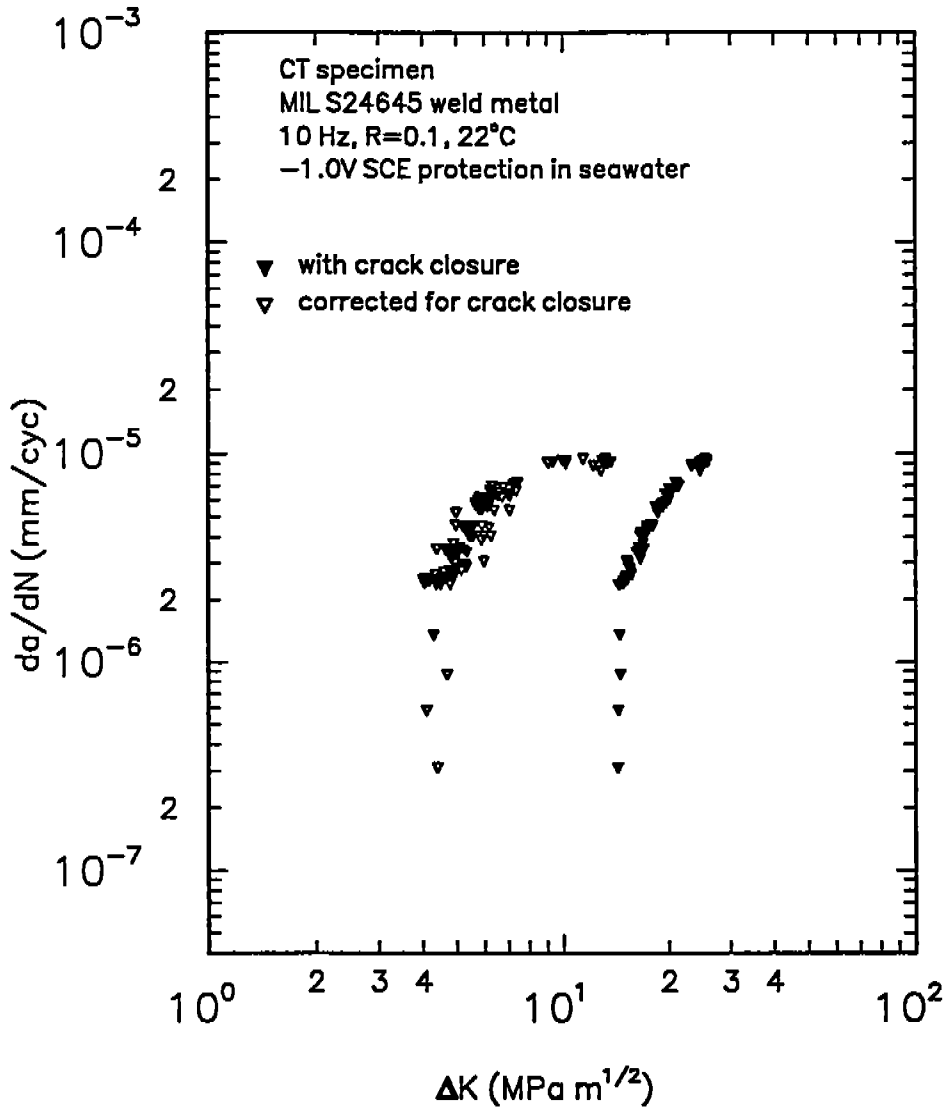


Figure 19. Near-threshold fatigue crack propagation data, before and after correction for closure, for MIL S-24645 weld metal tested in ASTM seawater at -1.0V SCE, 10 Hz, R = 0.1, 22 C.

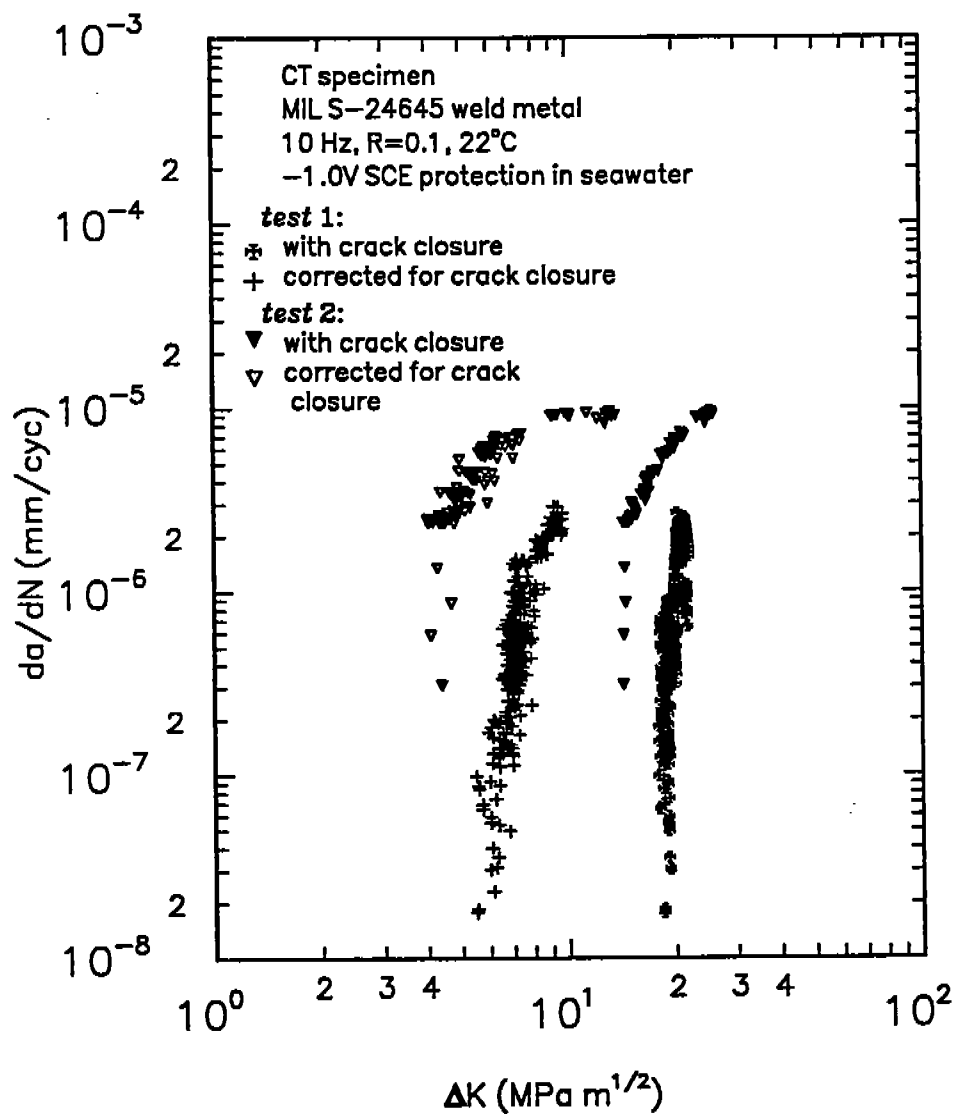


Figure 20. A comparison of near-threshold propagation data from test #1, weld metal anodically polarized to +1.0V SCE for 10 minutes prior to testing at -1.0V SCE, and test #2, weld metal protected with -1.0V SCE, in ASTM seawater, before and after correction for crack closure. 10 Hz, R = 0.1, 22 C.

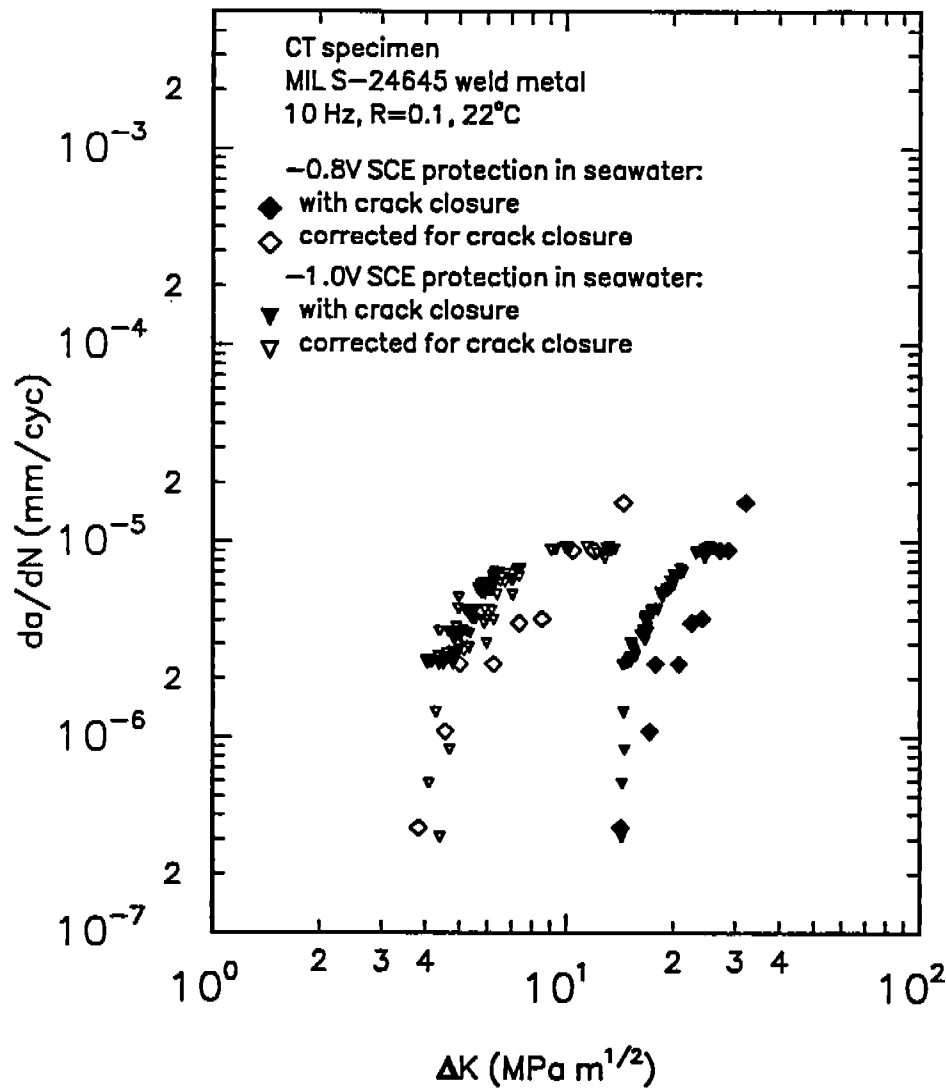


Figure 21. Comparison between the near-threshold fatigue crack propagation data, before and after correction for closure, for MIL S-24645 weld metal tested in ASTM seawater at -0.8V SCE and -1.0V SCE. 10 Hz, R = 0.1, 22 C.

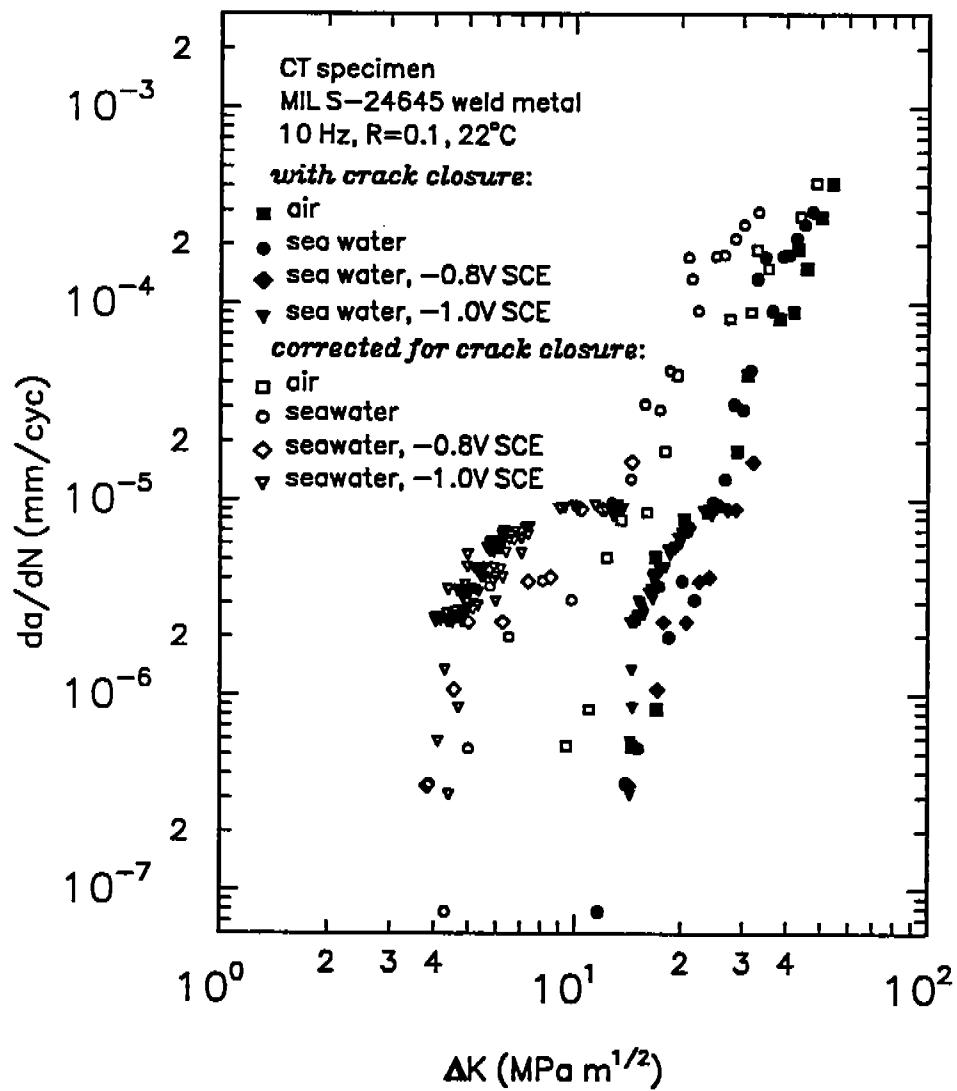


Figure 22. Comparison between the near-threshold fatigue crack propagation data, before and after correction for closure, for MIL S-24645 weld metal tested in air, ASTM seawater at the free corrosion potential and ASTM seawater at -0.8V SCE and -1.0V SCE. 10 Hz, R = 0.1, 22 C.

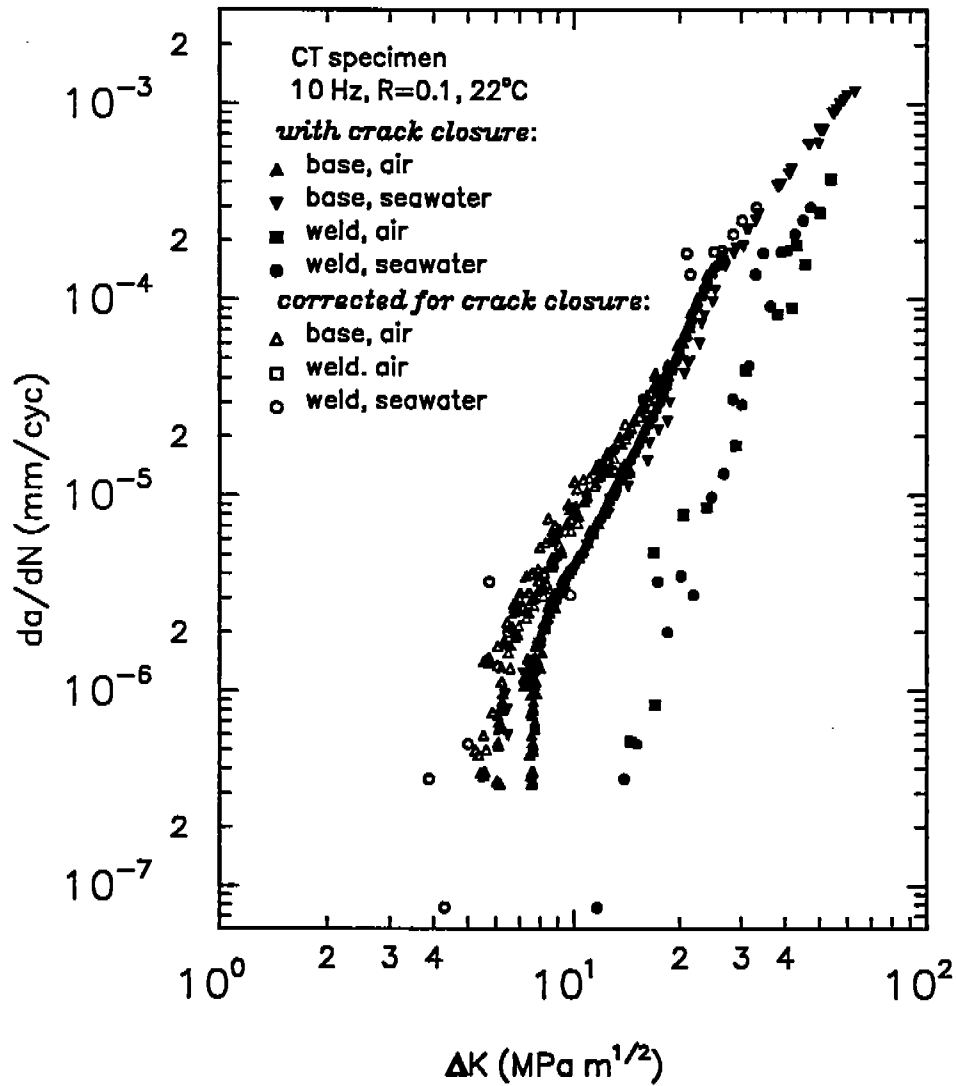


Figure 23. Comparison between the near-threshold crack propagation data, before and after correction for closure, for MIL S-24645 base and weld metals in air and ASTM seawater at the free corrosion potential. 10 Hz, R = 0.1, 22 C.

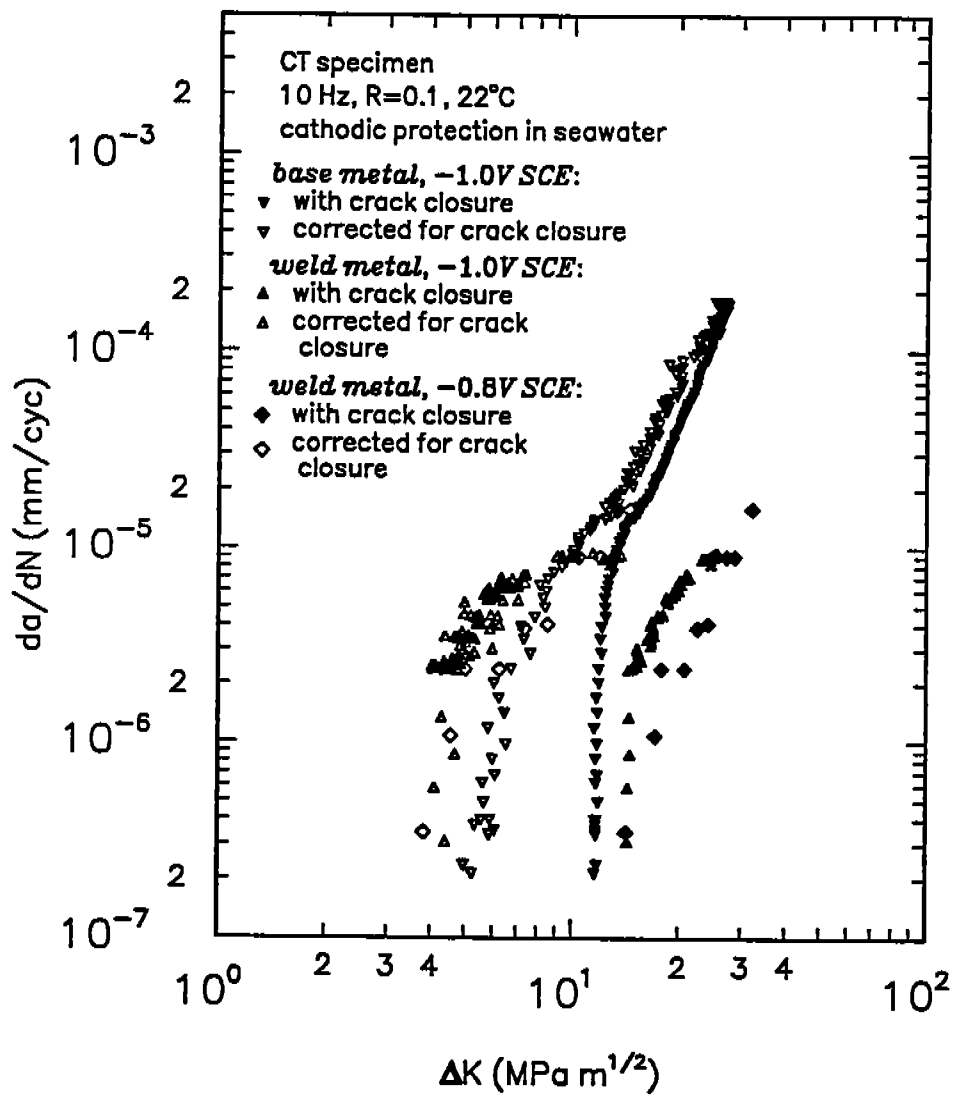


Figure 24. Comparison between the near-threshold crack propagation data, before and after correction for closure, for MIL S-24645 base and weld metals in ASTM seawater at -0.8V SCE and -1.0V SCE. 10 Hz, R = 0.1, 22 C.

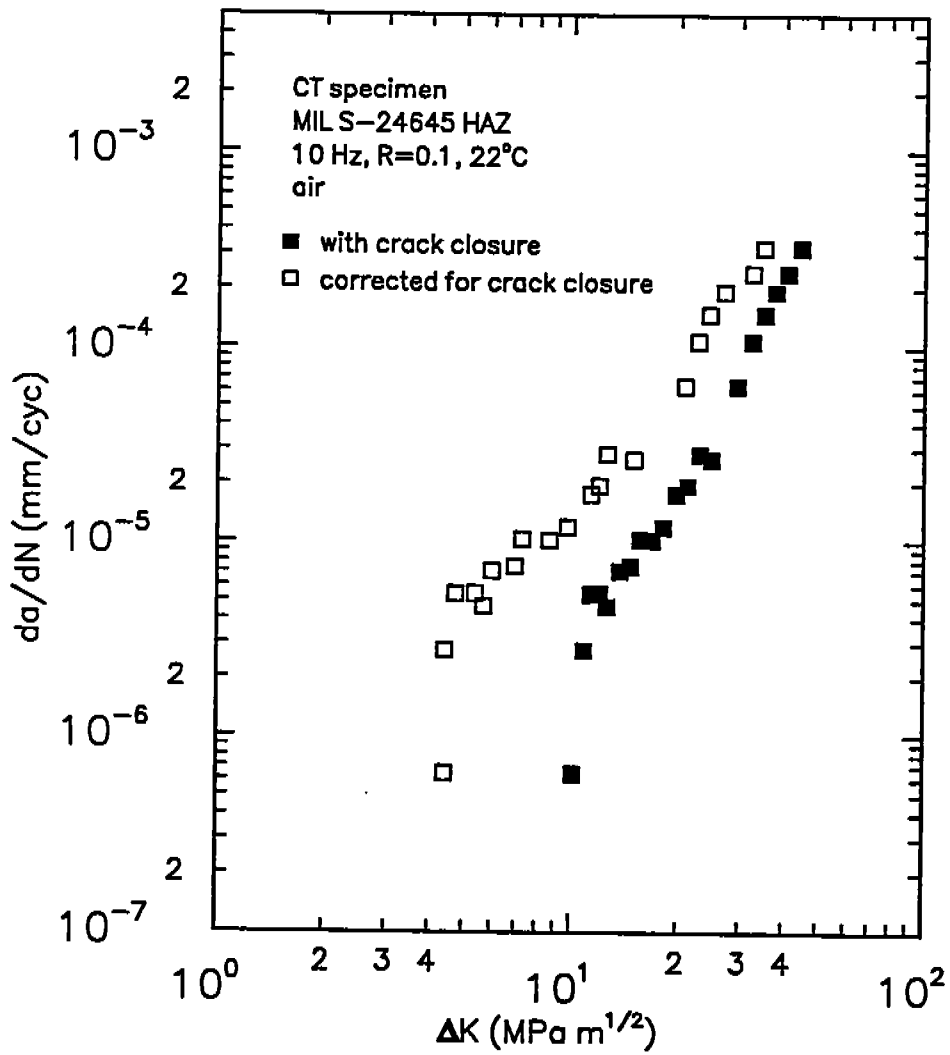


Figure 25. Near-threshold fatigue crack propagation data, before and after correction for closure, for MIL S-24645 HAZ tested in air at 10 Hz, R = 0.1, 22 C.

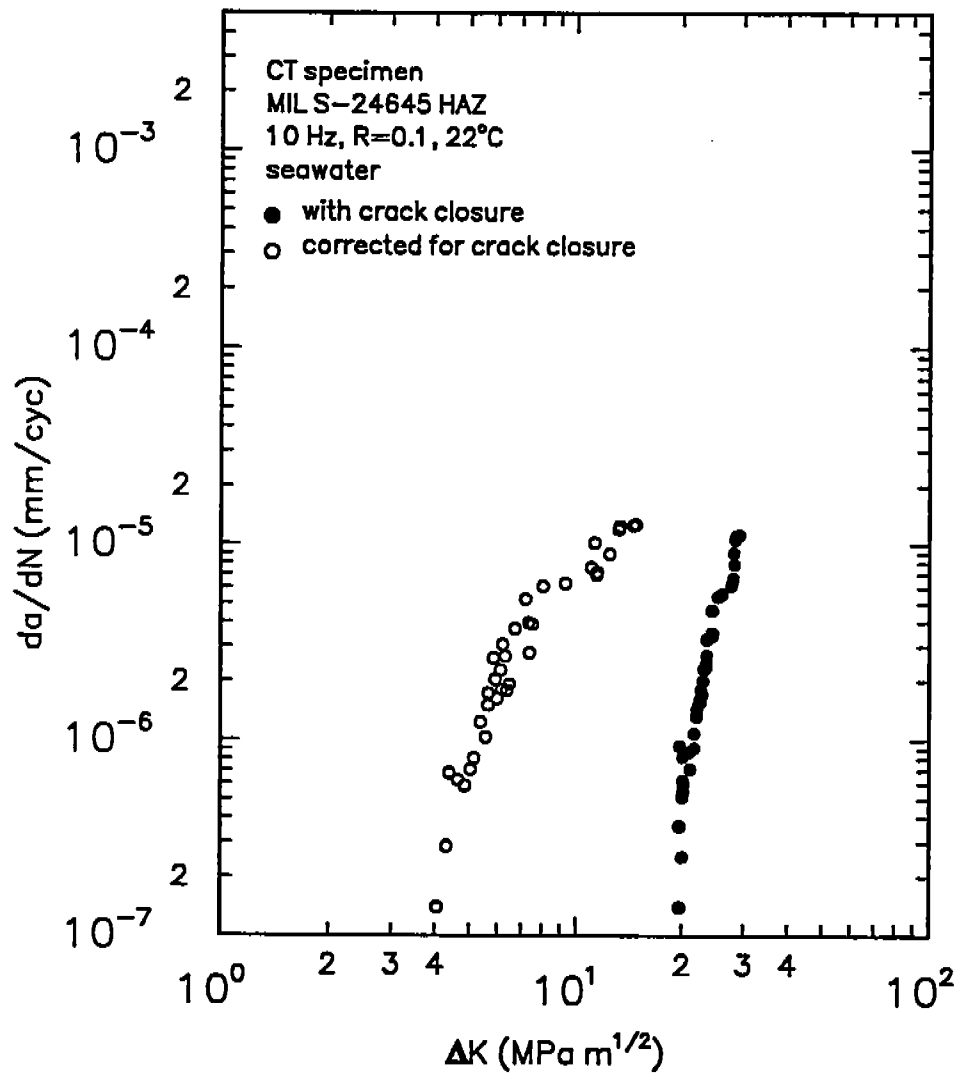


Figure 26. Near-threshold fatigue crack propagation data, before and after correction for closure, for MIL S-24645 HAZ tested in ASTM seawater at 10 Hz, R = 0.1, 22 C.

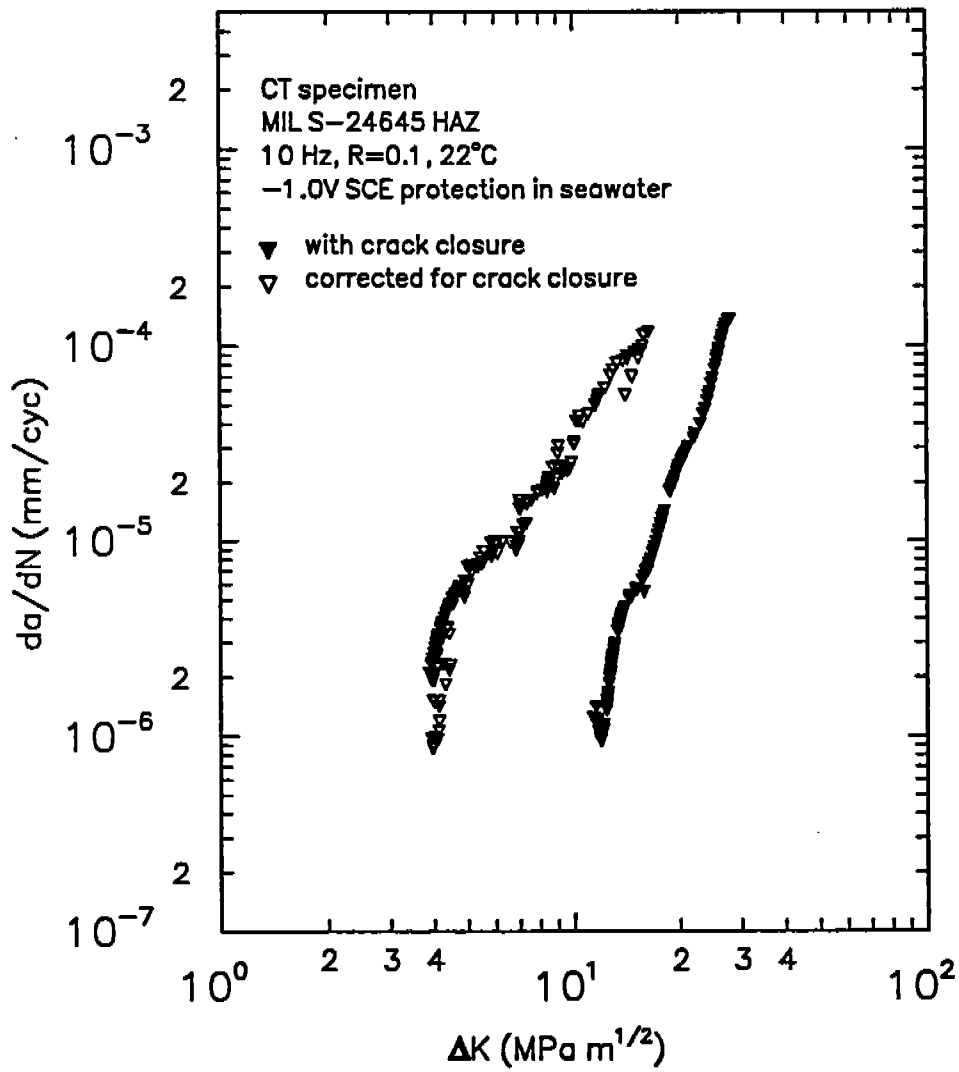


Figure 27. Near-threshold fatigue crack propagation data, before and after correction for closure, for MIL S-24645 HAZ tested in ASTM seawater at -1.0V SCE, 10 Hz, R = 0.1, 22 C.

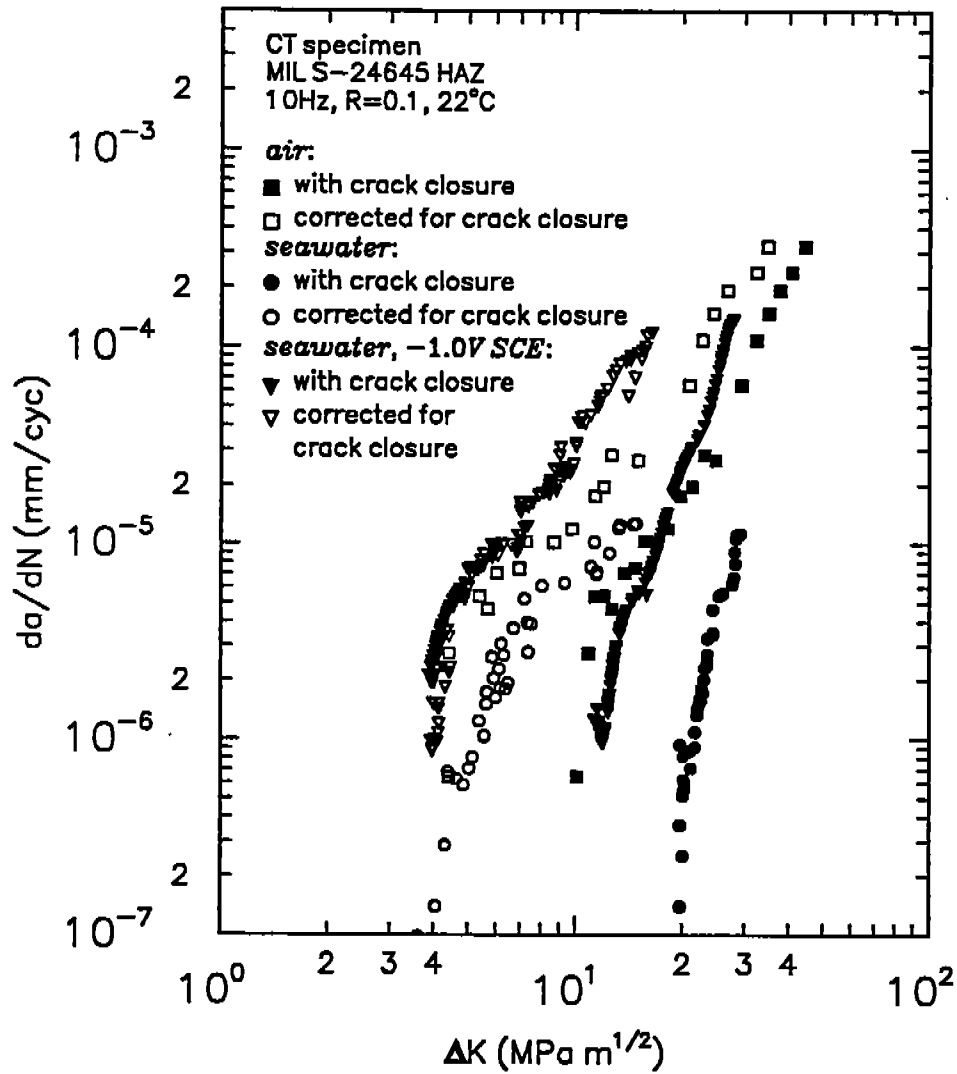
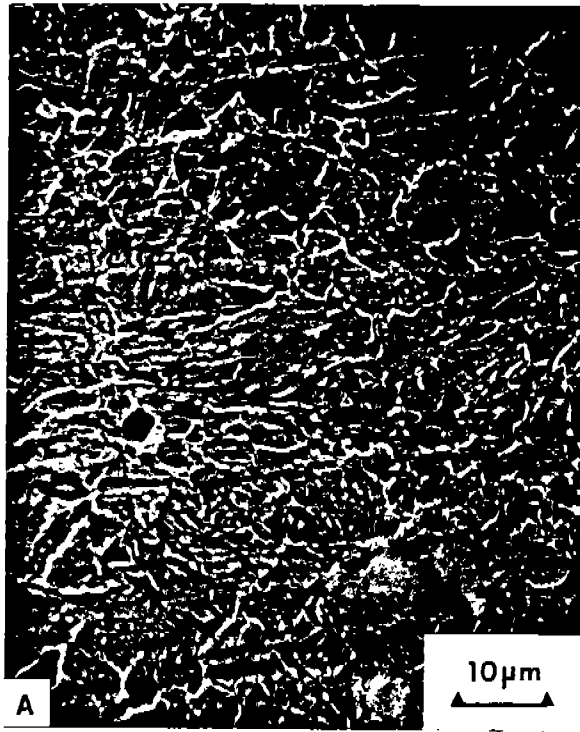
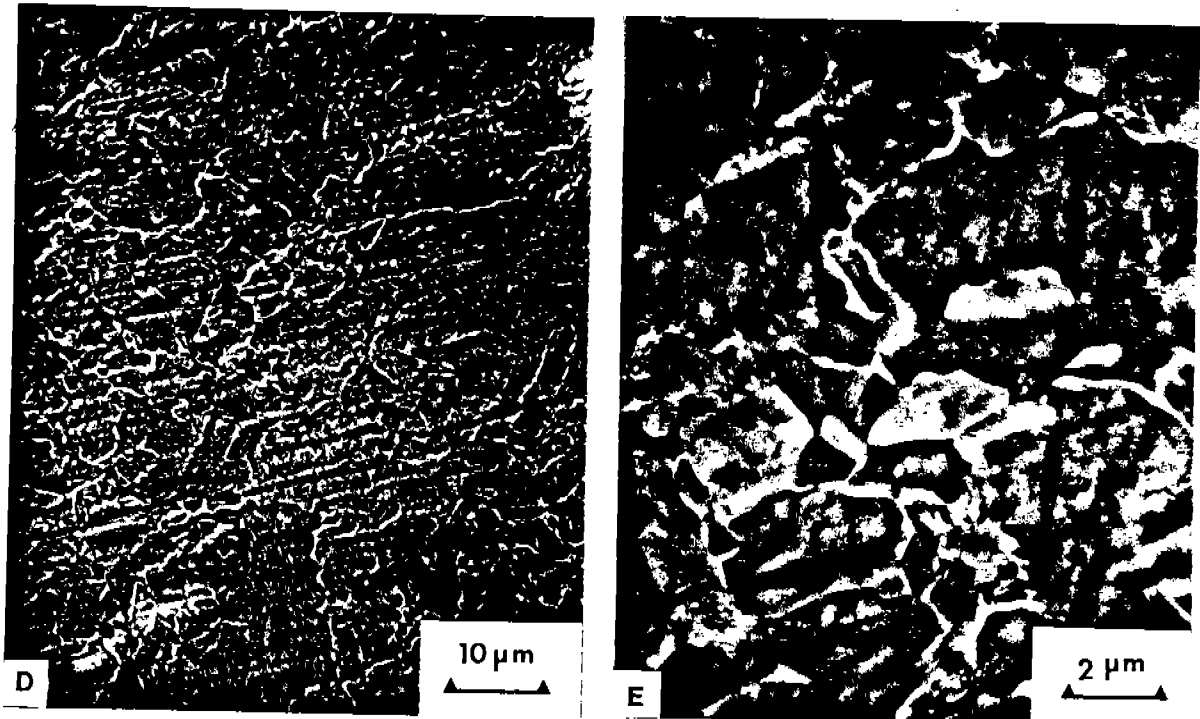


Figure 28. Comparison between the near-threshold fatigue crack propagation data, before and after correction for closure, for MIL S-24645 HAZ tested in air, ASTM seawater at the free corrosion potential and ASTM seawater at -1.0V SCE. 10 Hz, R = 0.1, 22 C.



Figures 29a-29c. Scanning electron micrographs for the LT orientation of polished MIL S-24645.



Figures 29d, 29e. Scanning electron micrographs for the LW orientation of polished MIL S-24645.

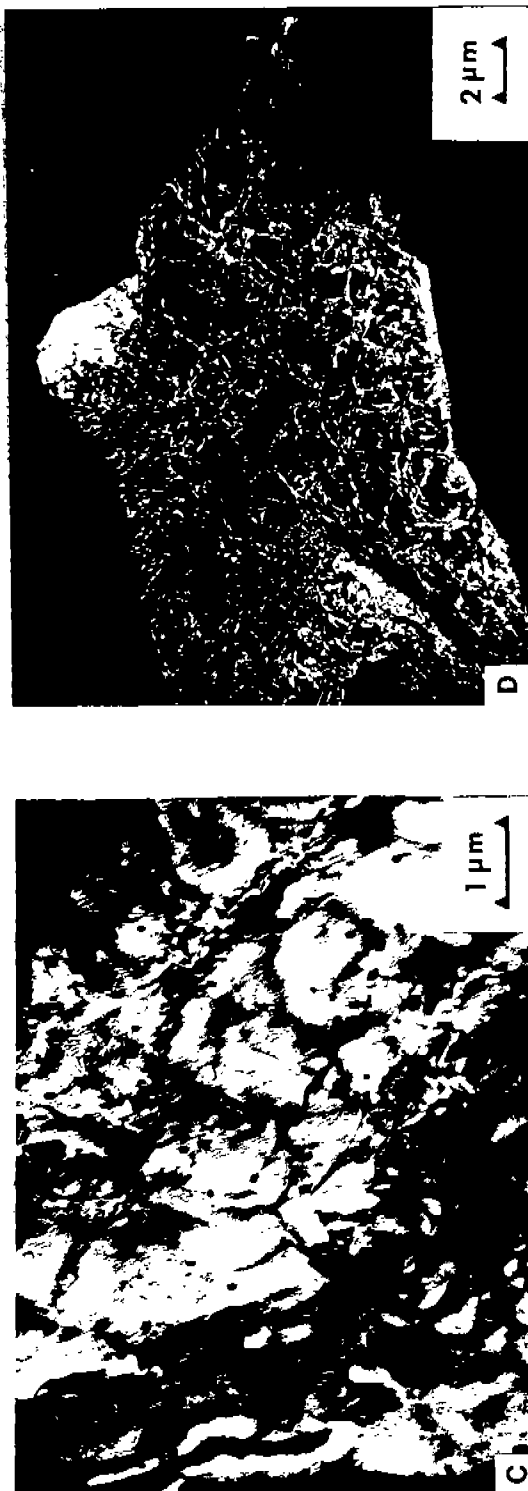
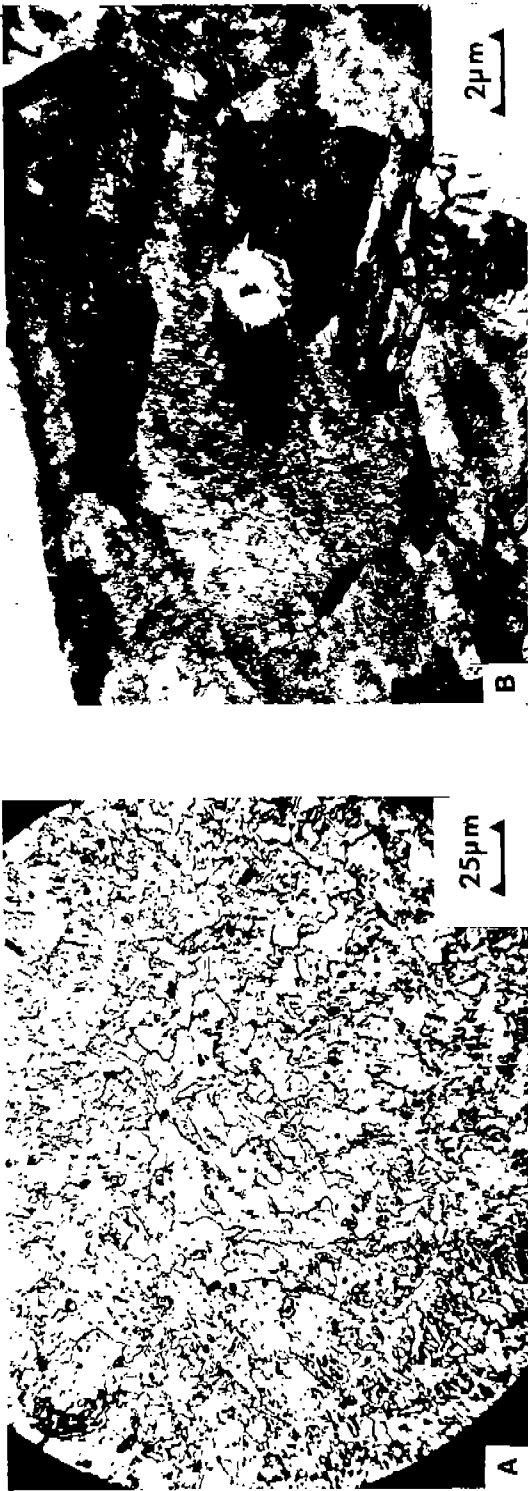


Figure 30. ASTM A710: (a) optical micrograph showing acicular ferrite microstructure; (b)-(d) transmission electron micrographs showing (b) inclusion, (c) copper precipitation on dislocations (bright field), (d) copper precipitation on dislocations (dark field).

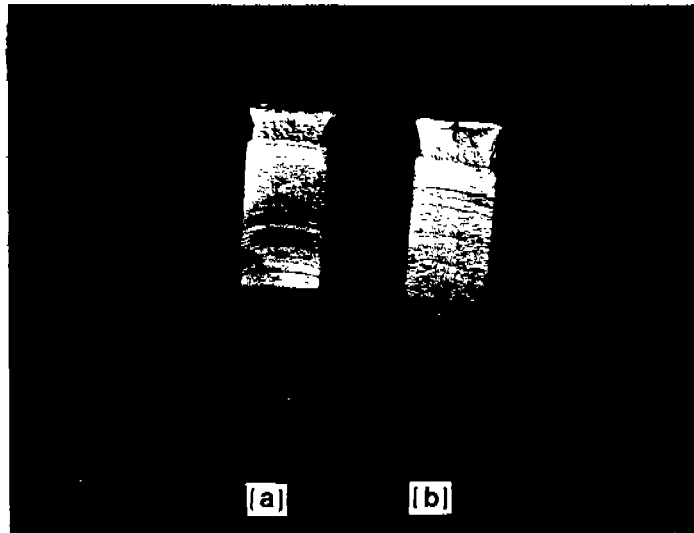
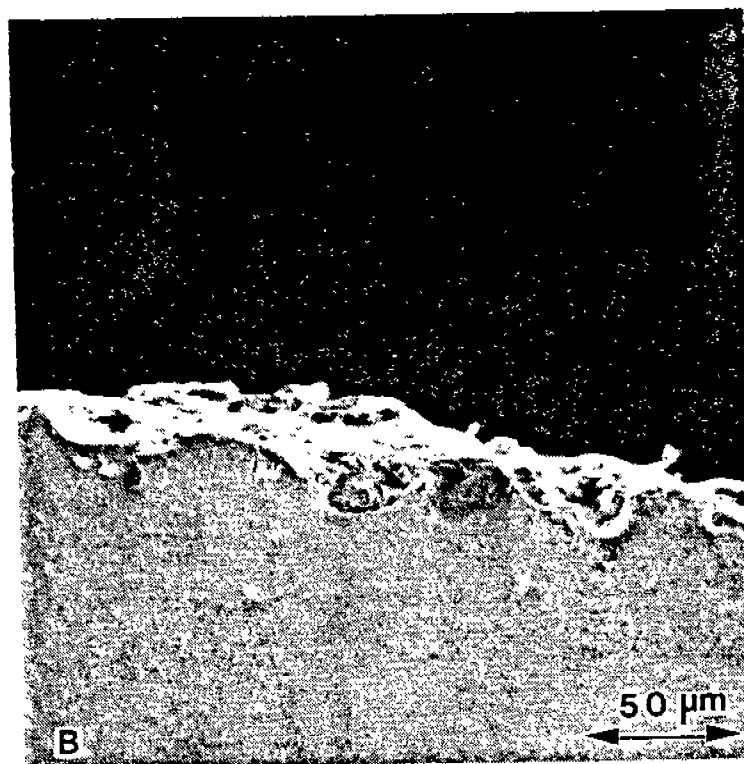
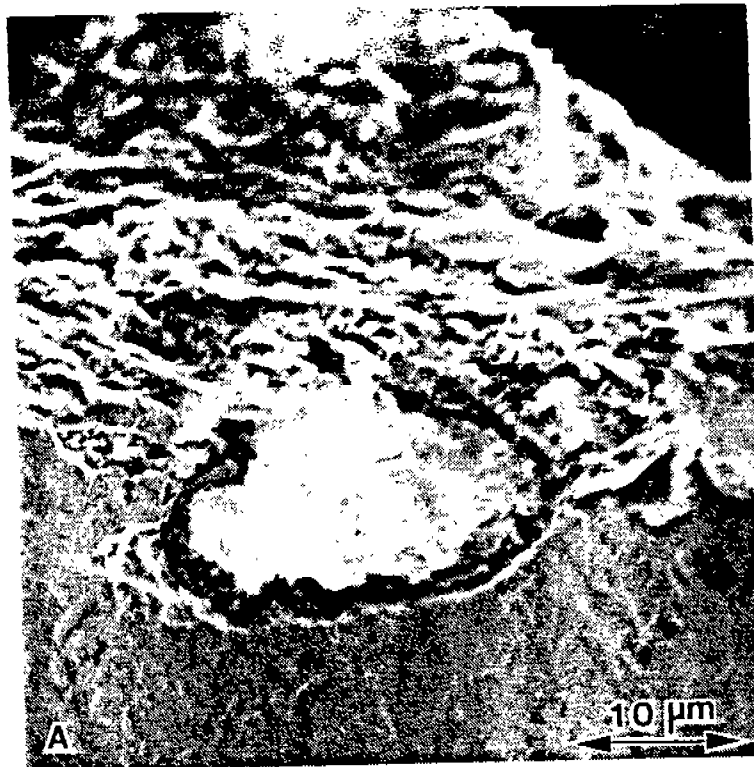
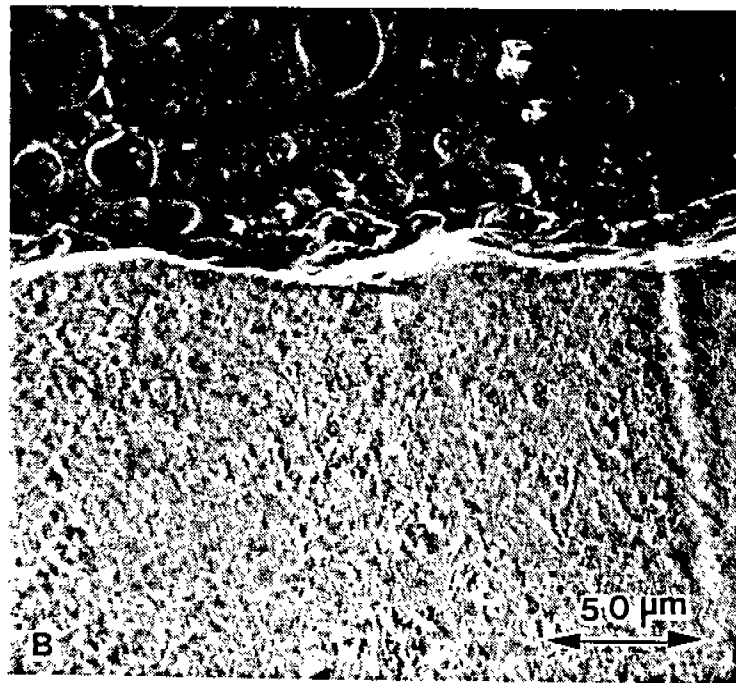


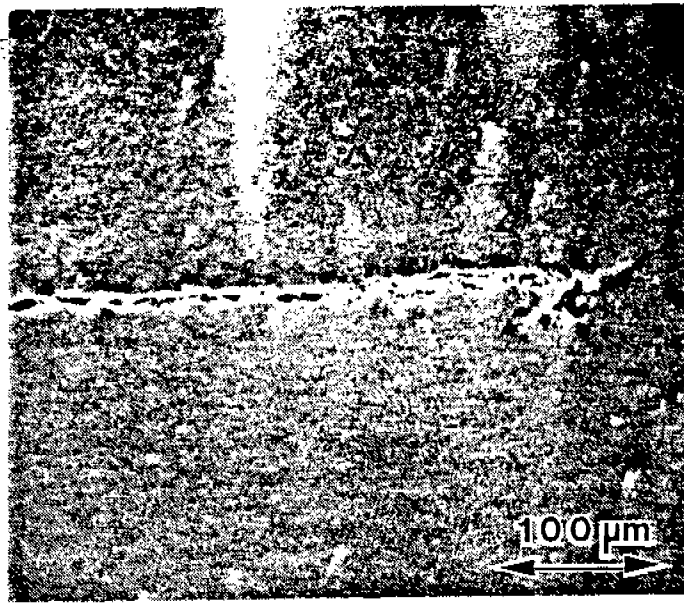
Figure 31. Fracture surfaces of ASTM A710 (a) and ASTM A710 weld metal (b) tested in air.



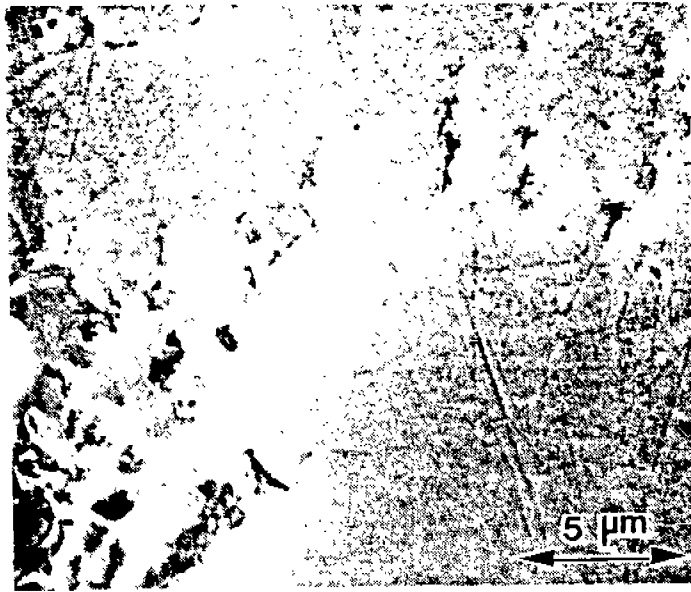
Figures 32a, 32b. SEM micrographs of fracture surfaces of ASTM A710 tested in ASTM seawater at 2 Hz showing extensive corrosion product and a rough fracture surface.



Figures 33a, 33b. SEM micrographs of ASTM A710 tested in ASTM seawater at -0.8V SCE showing no corrosion product and smooth fracture surface. Note: the specimen surface is covered with a layer of epoxy containing air bubbles.

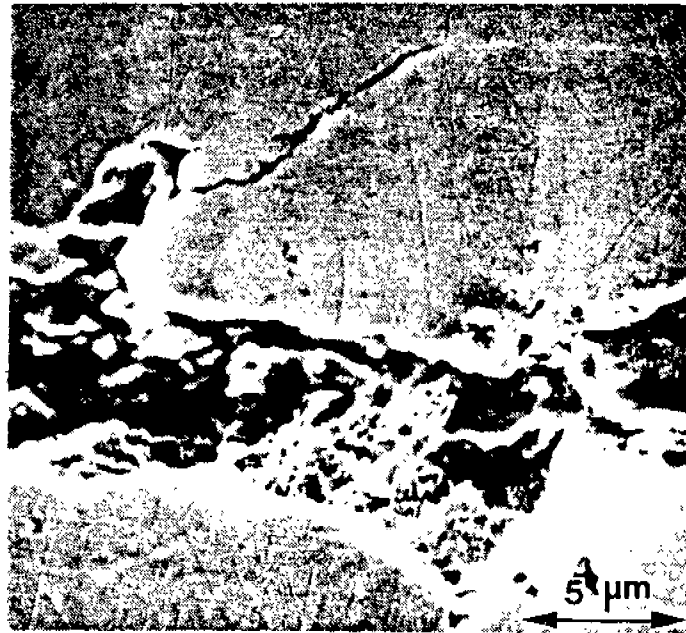


A



B

Figure 34. SEM micrographs of ASTM A710 tested in seawater at -1.0V SCE: (a) crack profile, (b) damage ahead of crack tip,

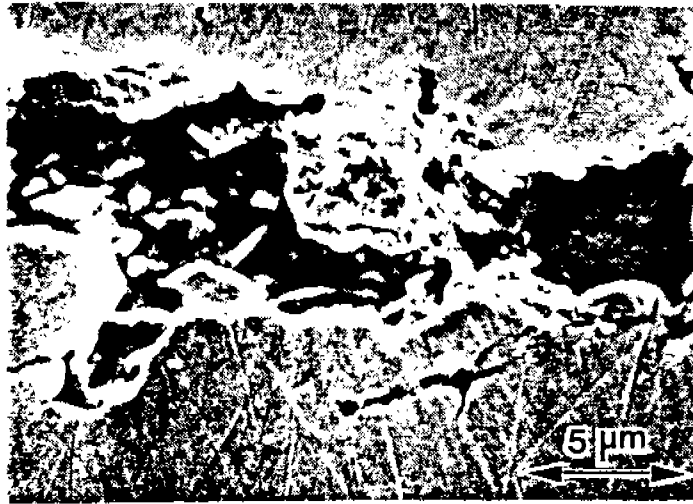


C



D

Figure 34. SEM micrographs of ASTM A710 tested in seawater at -1.0V SCE: (c) crack branch, (d) cracks opening up around grain boundaries.



E



F

Figure 34. SEM micrographs of ASTM A710 tested in seawater at $-1.0V$ SCE: (e) metal grain in crack tip, (f) metal wedges in the crack wake.

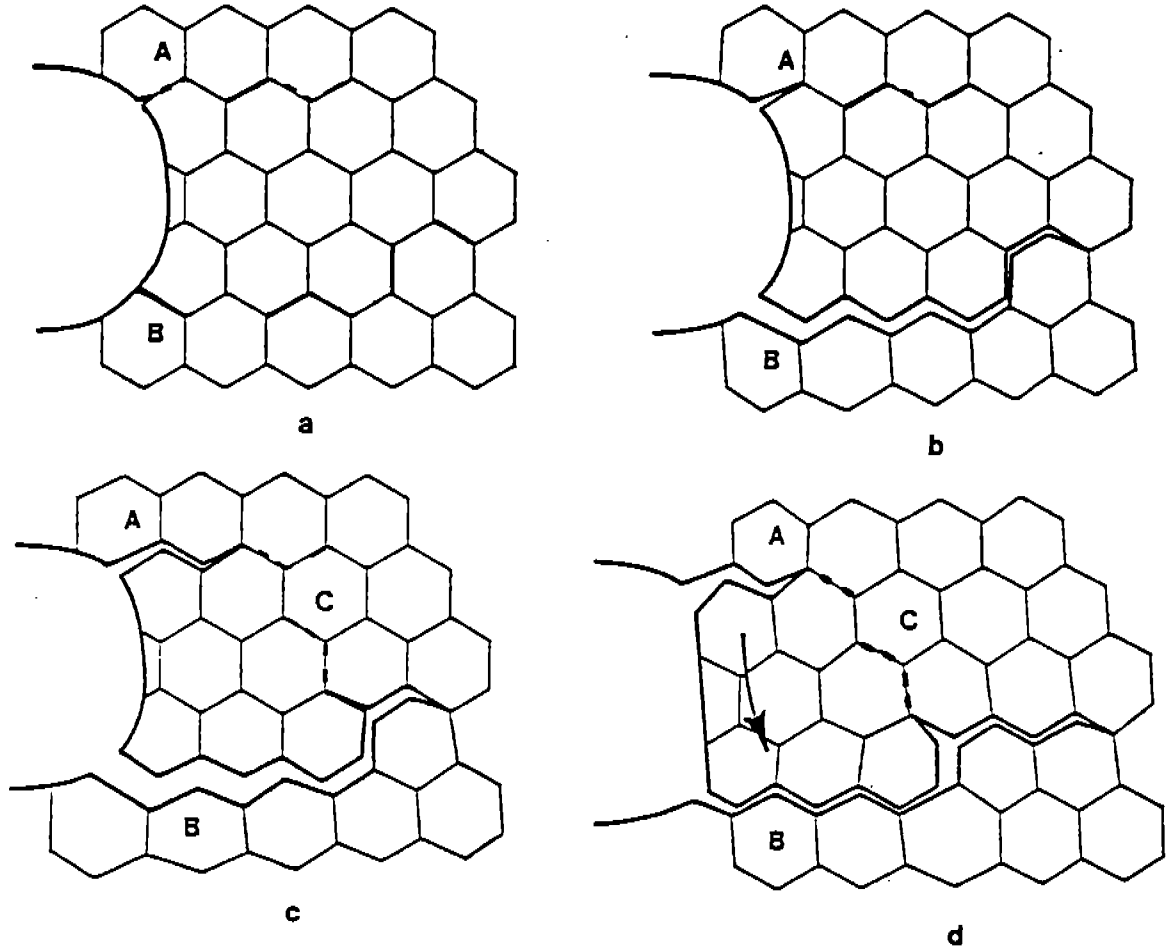
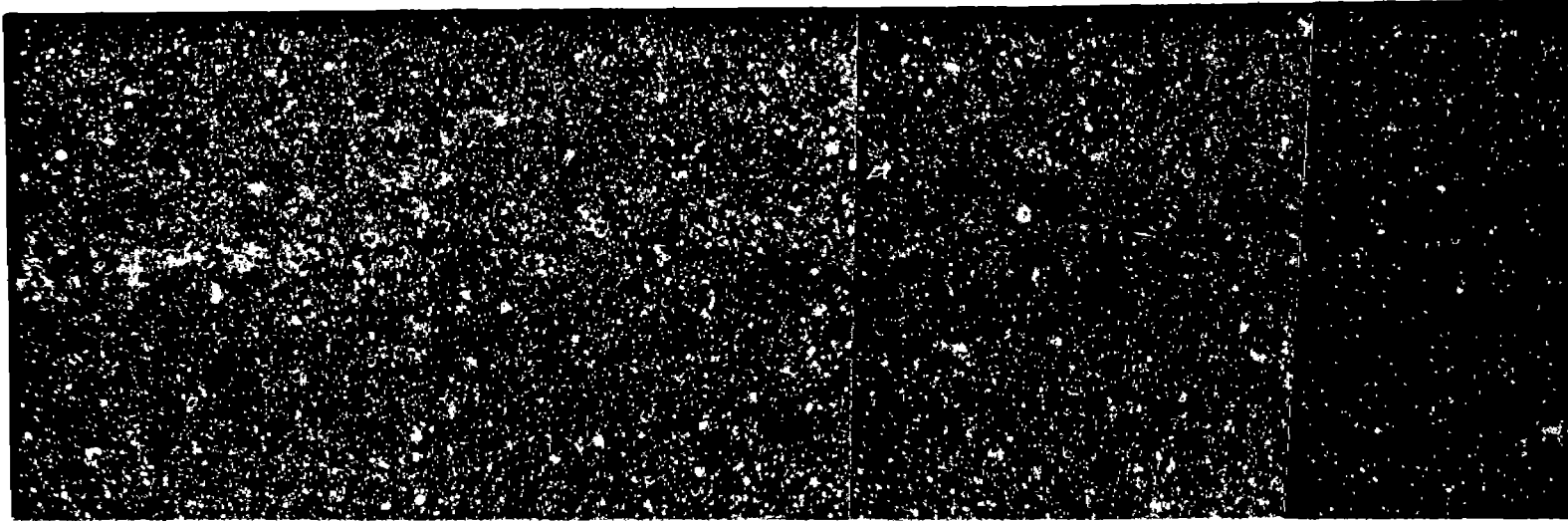


Figure 35. Schematic representation of crack propagation in ASTM A710 tested in ASTM seawater at $-1.0V$ SCE: (a) damage accumulation ahead of crack tip; (b) development of upper crack (A) and main branch (B) by cracking along grain boundaries; (c) extension of both cracks (A,B), movement of metal wedge and damage accumulation at C; (d) crack extension at C and metal wedge contributing to crack closure.



A-79

Figure 36. Crack profile of MIL S-24645 base metal tested in ASTM seawater at corrosion potential at 0.2 Hz under load increasing conditions (test #

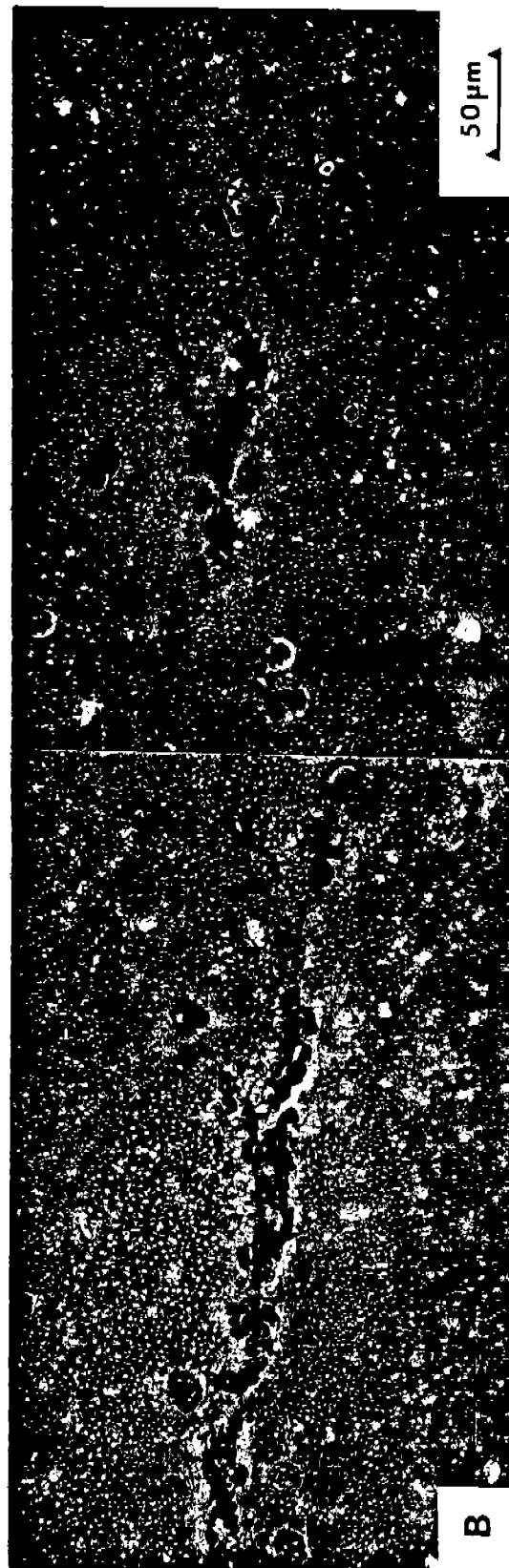
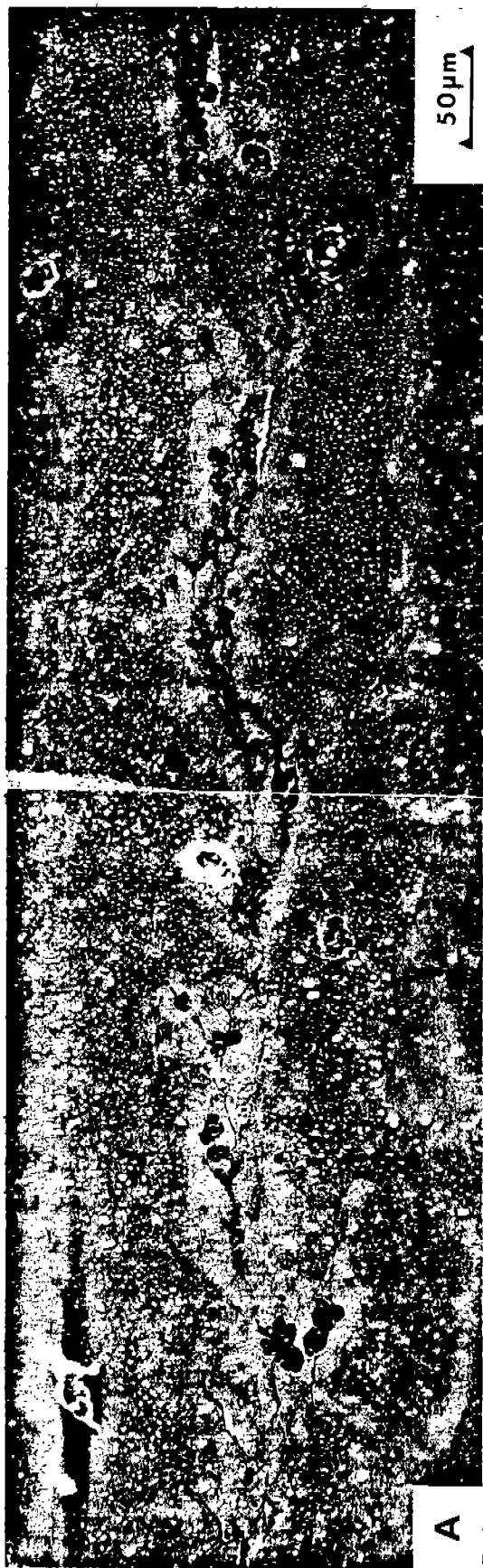


Figure 37. Higher magnification views of MIL S-24645 base metal tested in ASTM seawater at the free corrosion potential at 0.2 Hz under load increasing conditions (test #2).



Figure 37. Continued

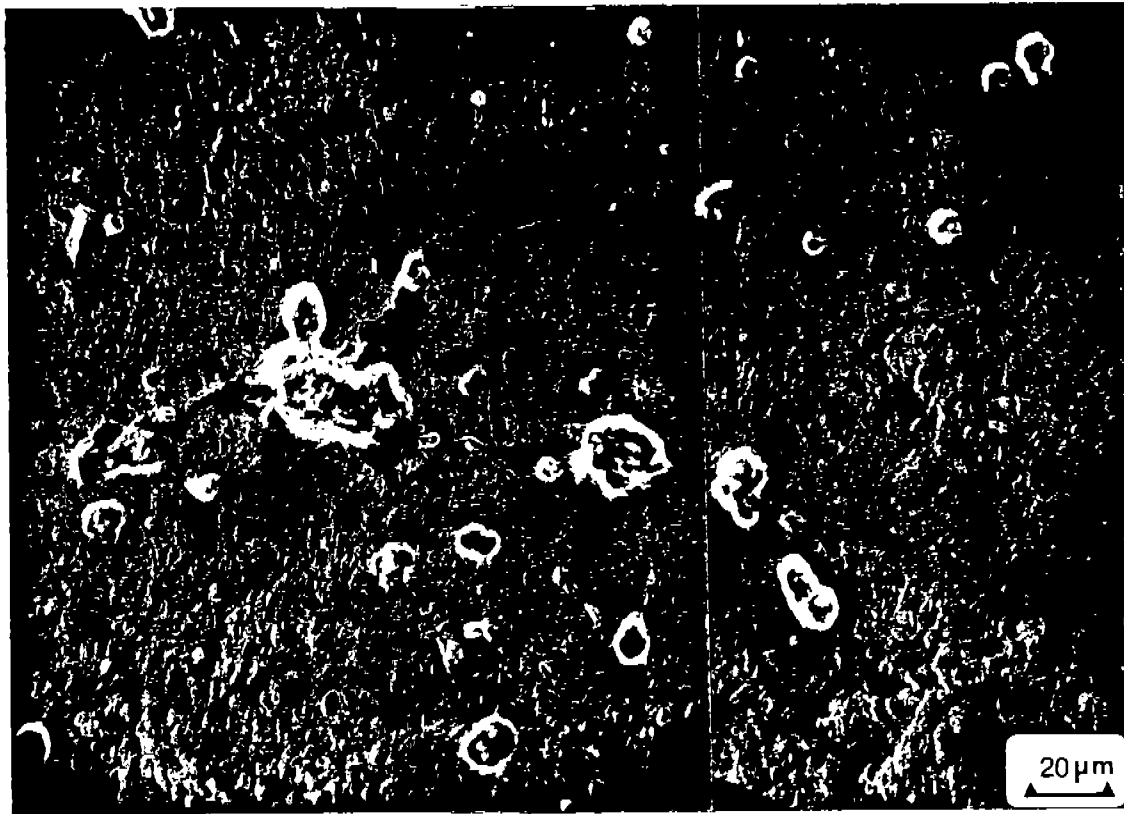


Figure 38. MIL S-24645 base metal tested in ASTM seawater at the free corrosion potential at 0.2 Hz under load increasing conditions (test #1).

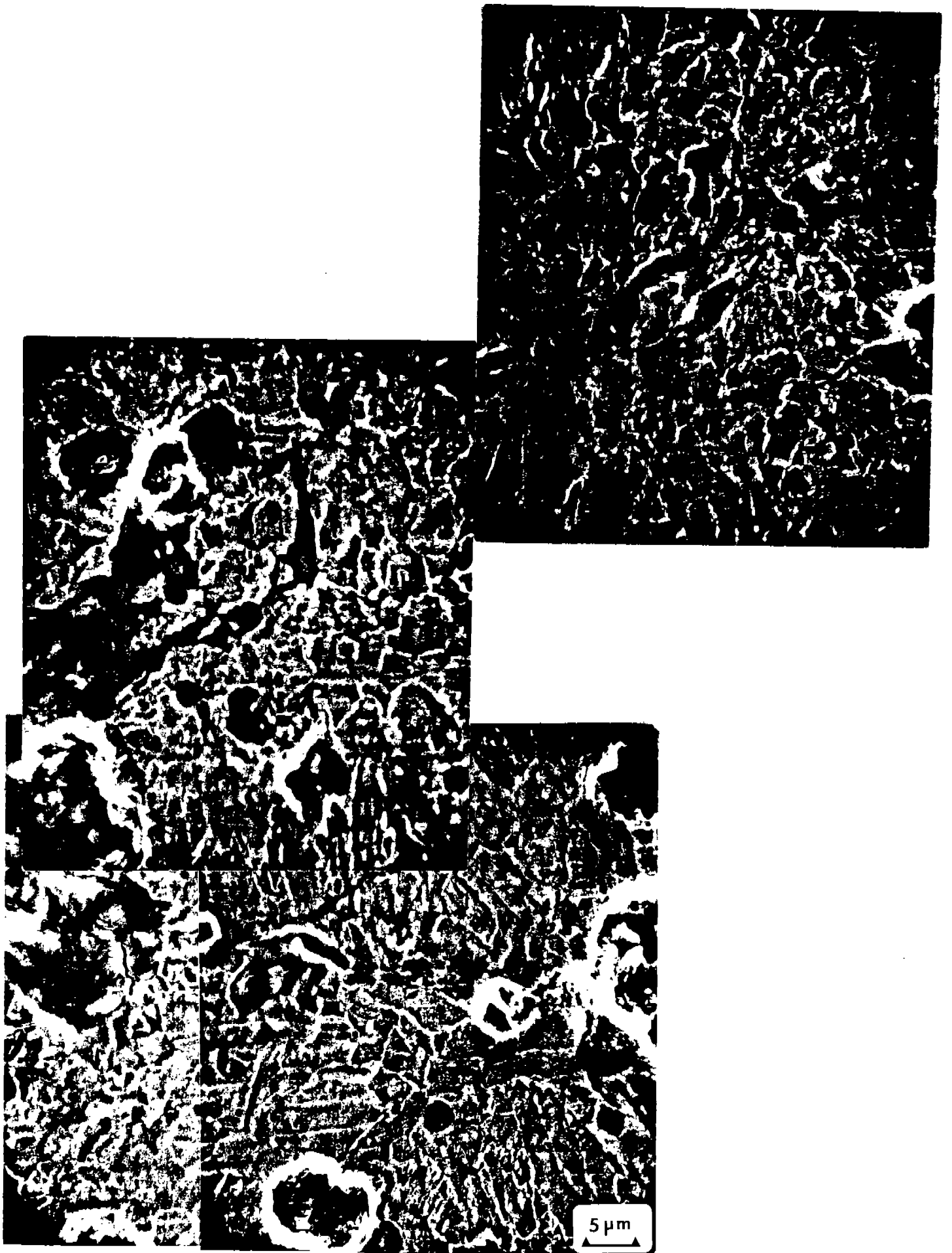


Figure 39. MIL S-24645 base metal tested in ASTM seawater at the free corrosion potential at 0.2 Hz under load increasing conditions (test #1).

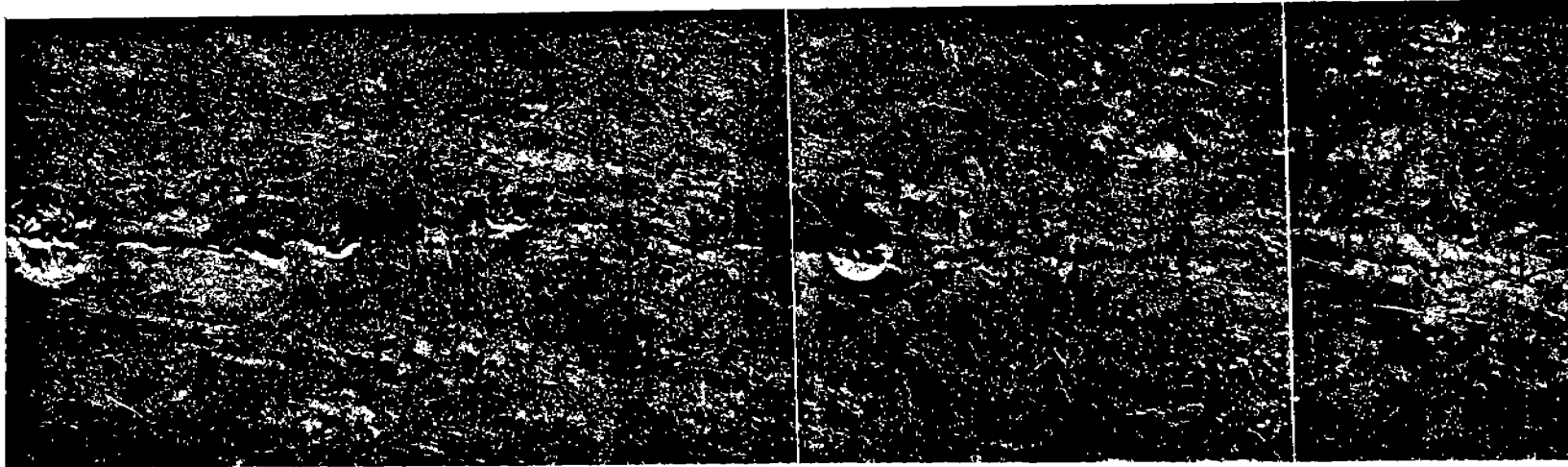


Figure 40. MIL S-24645 base metal tested in ASTM seawater at the free c potential at 0.2 Hz under load shedding conditions (test #3).

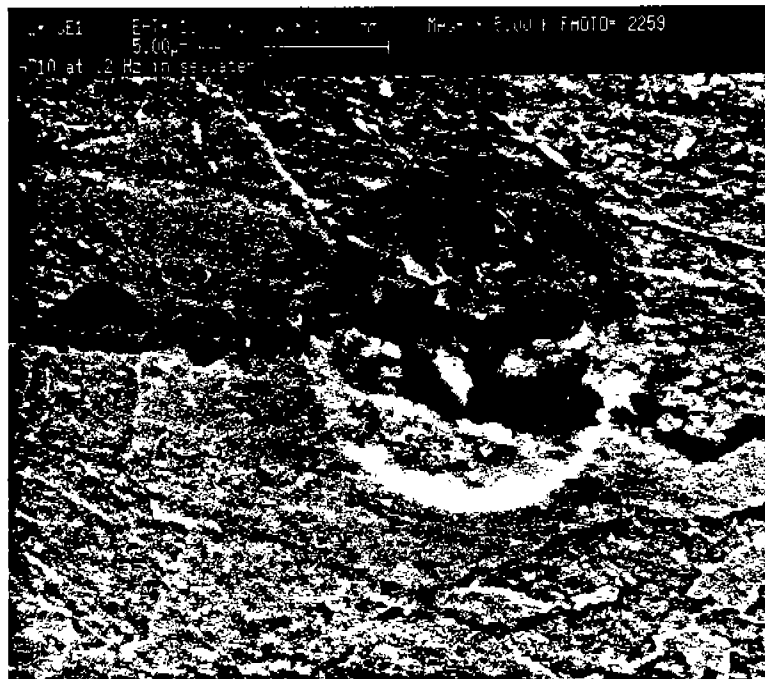
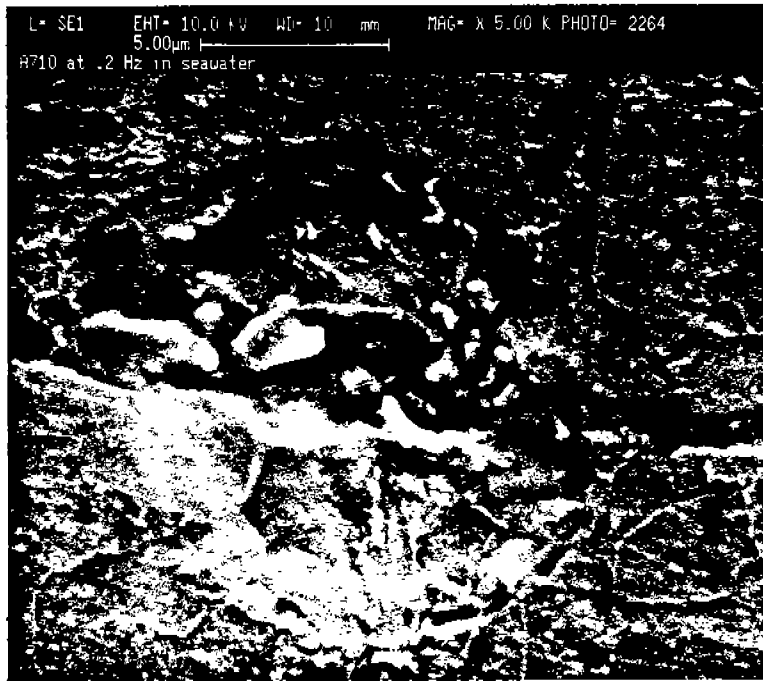


Figure 41. Higher magnification views of MIL S-24645 base metal tested in ASTM seawater at the free corrosion potential at 0.2 Hz under load shedding conditions (test #3).

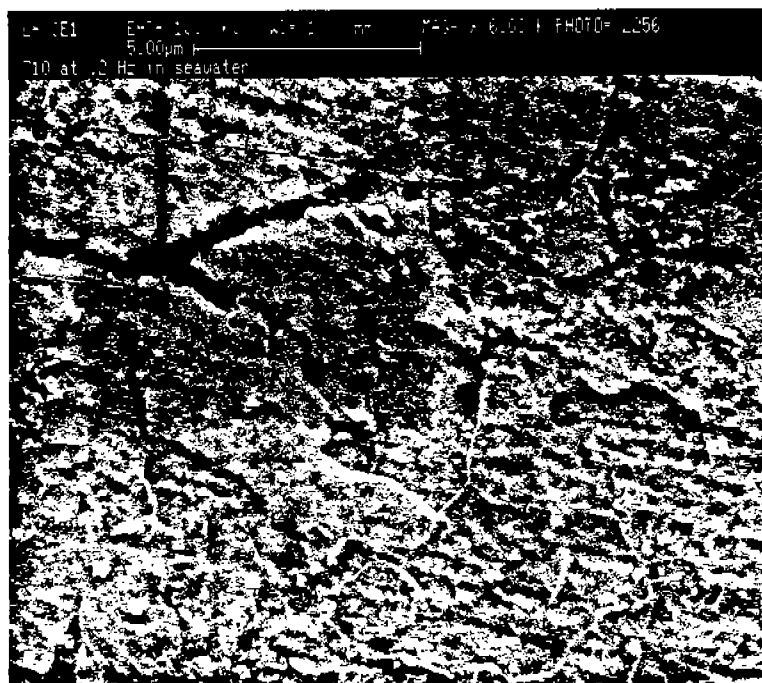
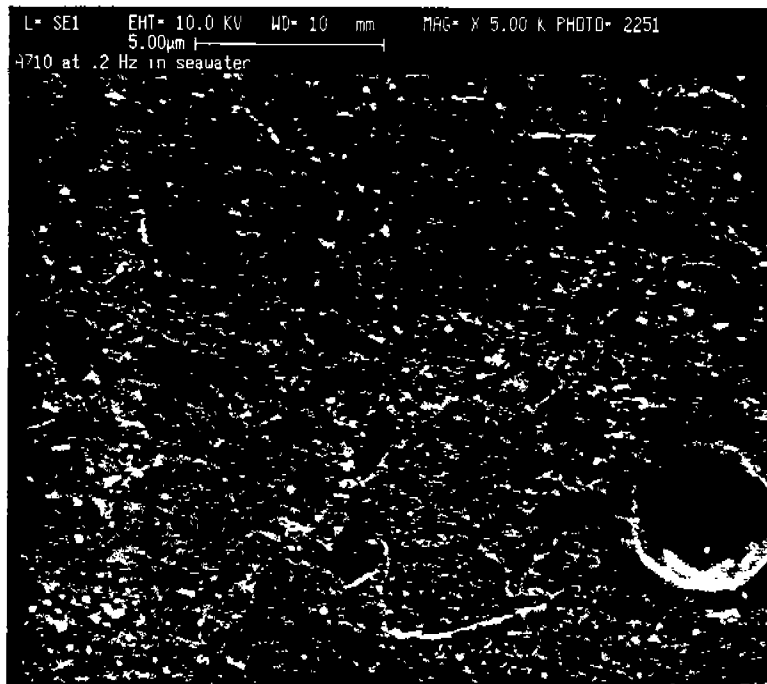


Figure 42. Higher magnification views of MIL S-24645 base metal tested in ASTM seawater at the free corrosion potential at 0.2 Hz under load shedding conditions (test #3).

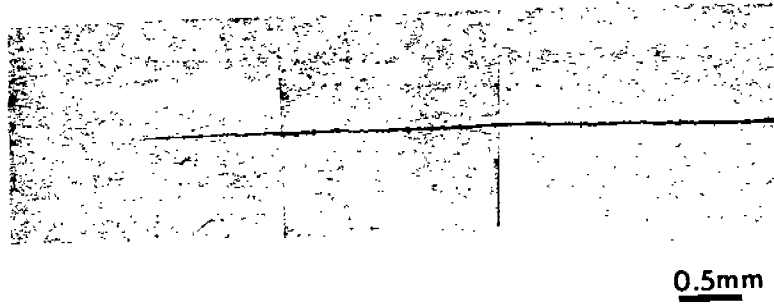
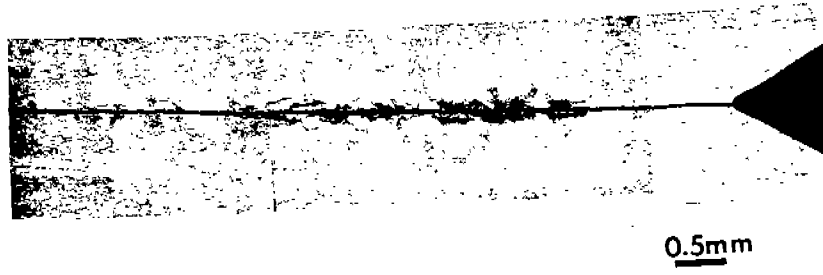


Figure 43. Optical micrographs of the fracture path of MIL S-24645 base metal tested at 10 Hz at -1.0 V in ASTM seawater: (a) near notch, (b) near crack tip.

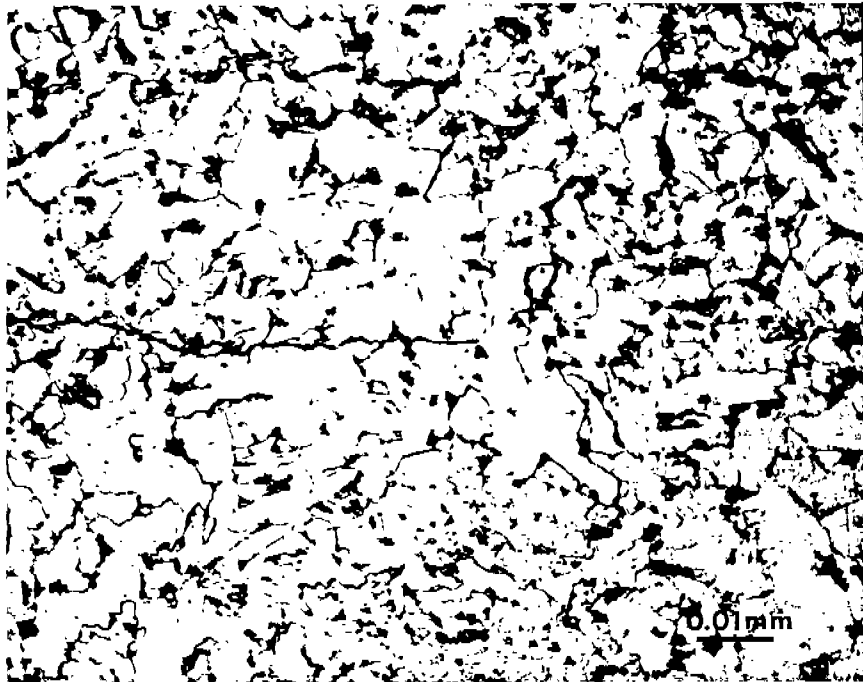
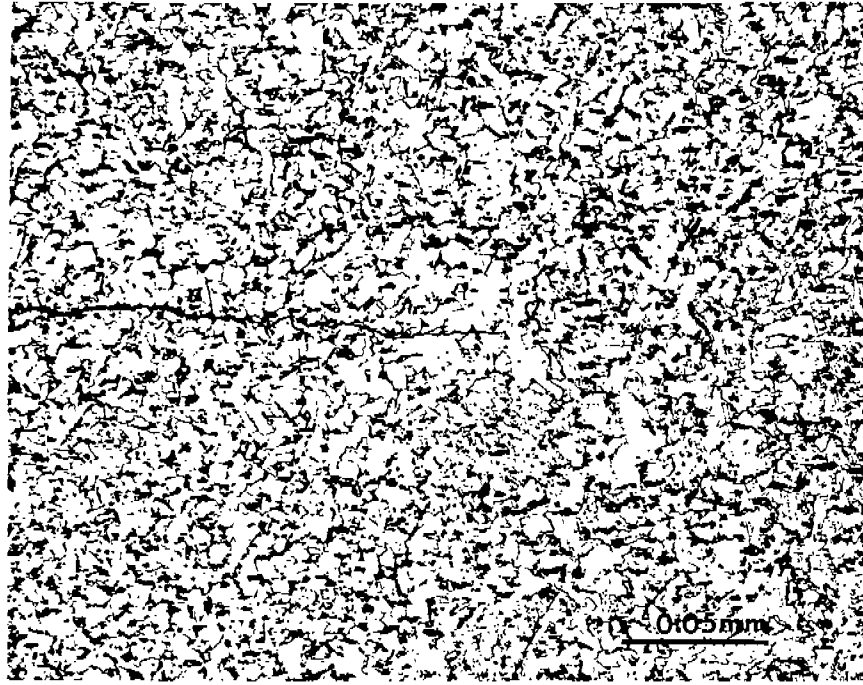


Figure 44. Optical micrographs of the fracture path (near crack tip) of MIL S-24645 base metal tested at 10 Hz at -1.0 V in ASTM seawater: (a) 400 X, 5% Nital; (b) 1000 X, 5% Nital.

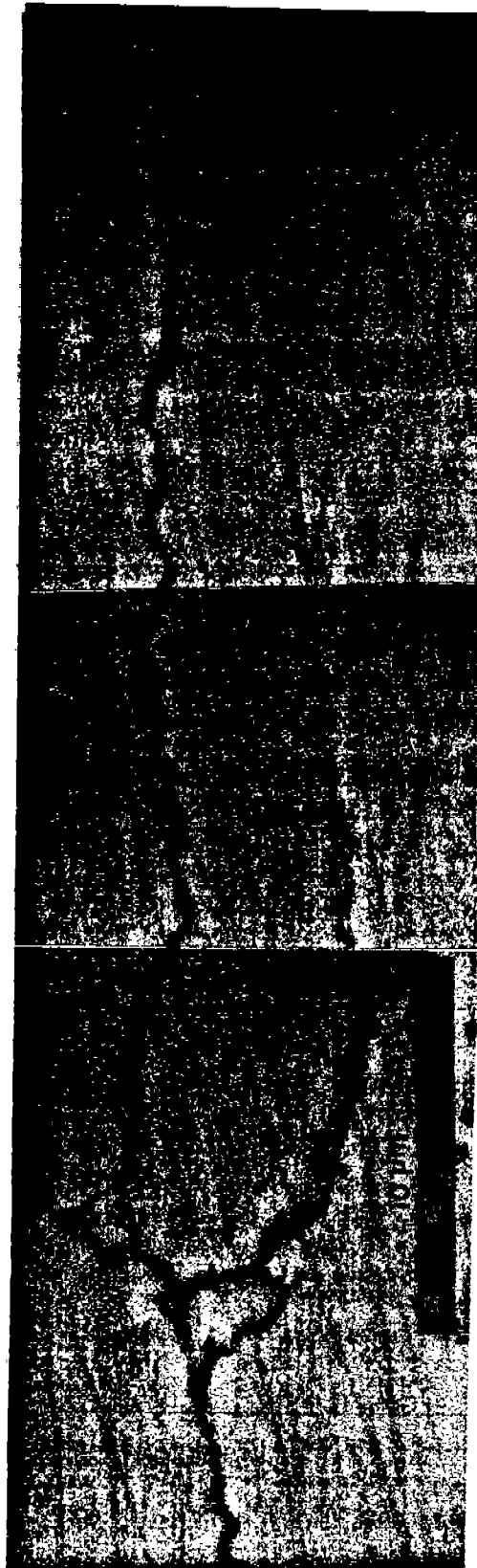


Figure 45. SEM micrographs of the fracture path of MIL S-24645 base metal tested at 10 Hz in seawater at -1.0 V (SCE).

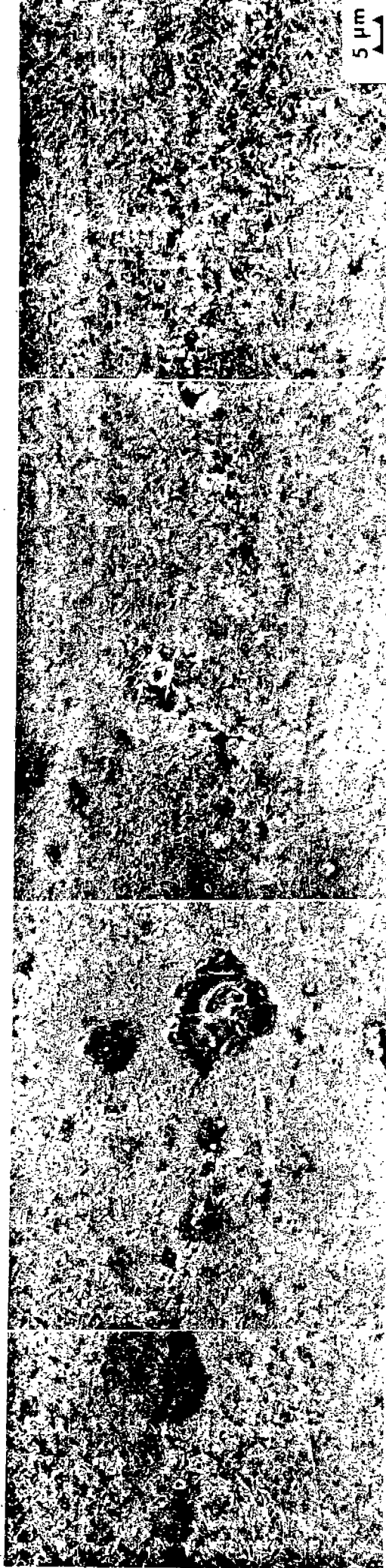


Figure 46. Crack profile for MIL S-24645 weld metal tested in air at 10 Hz.

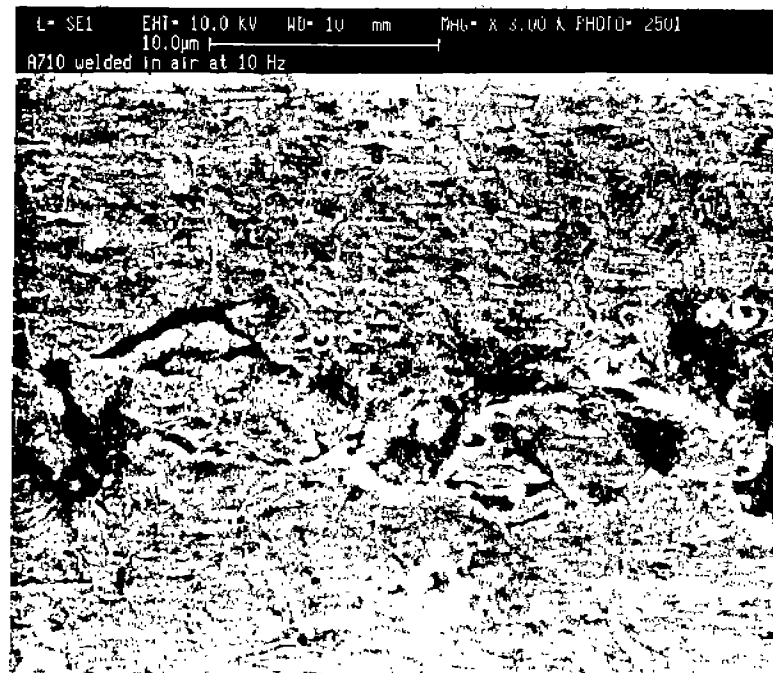
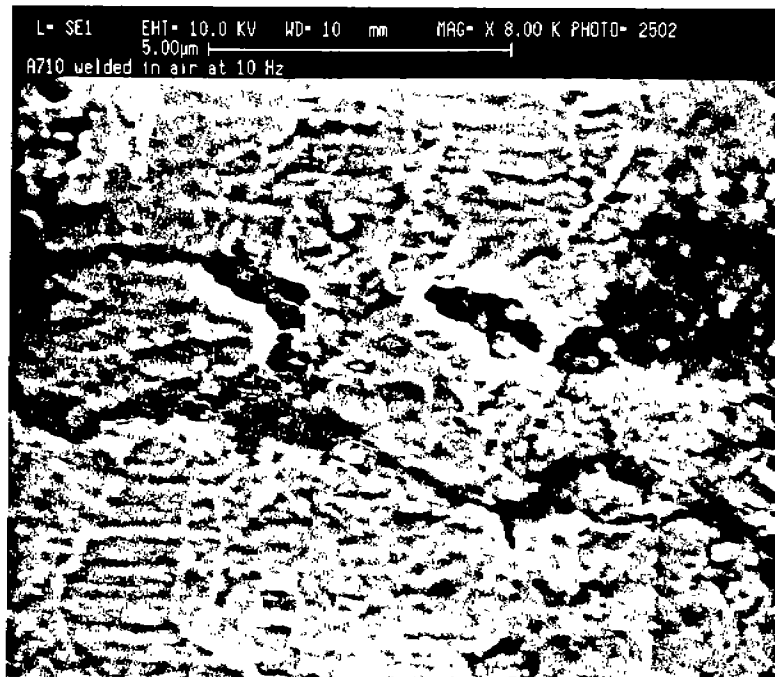


Figure 47. Higher magnification views of the crack profile for MIL S-24645 weld metal tested in air at 10 Hz.

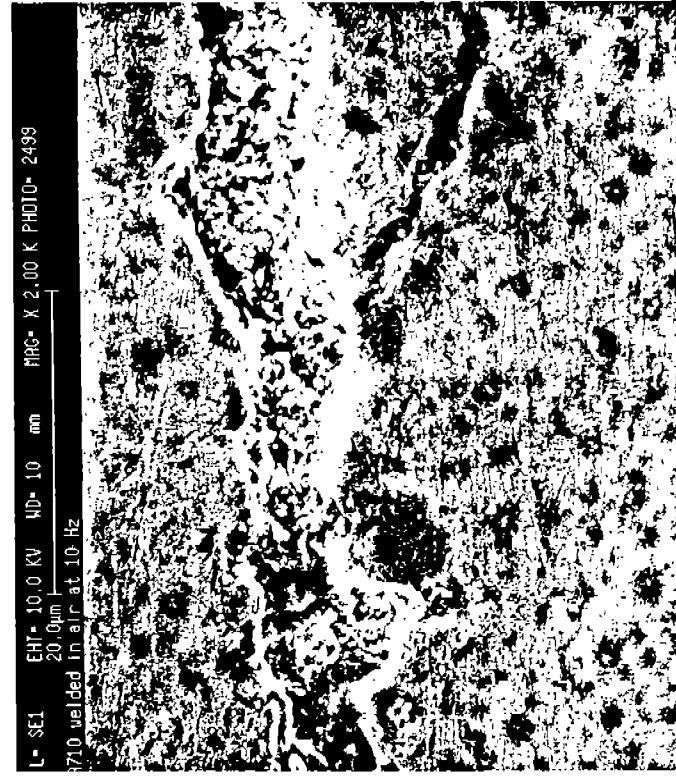
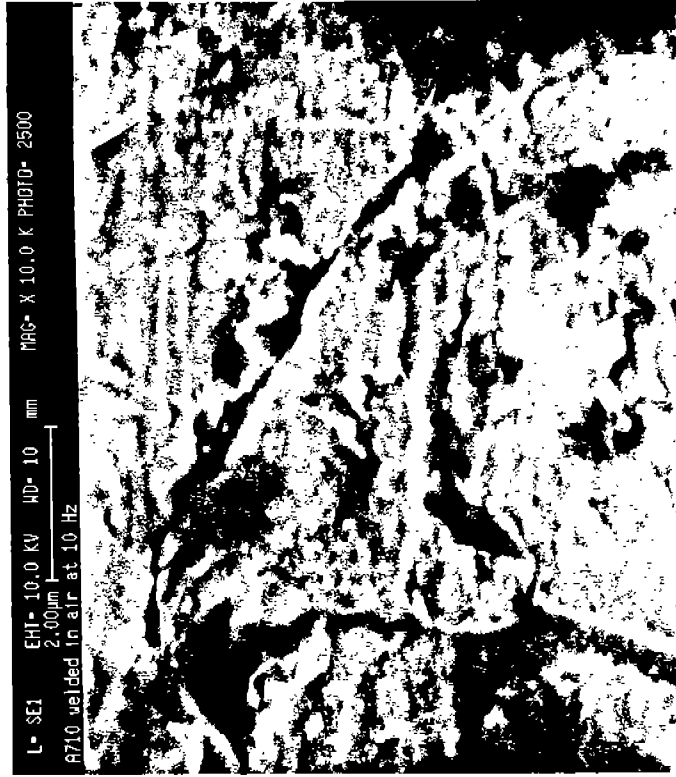
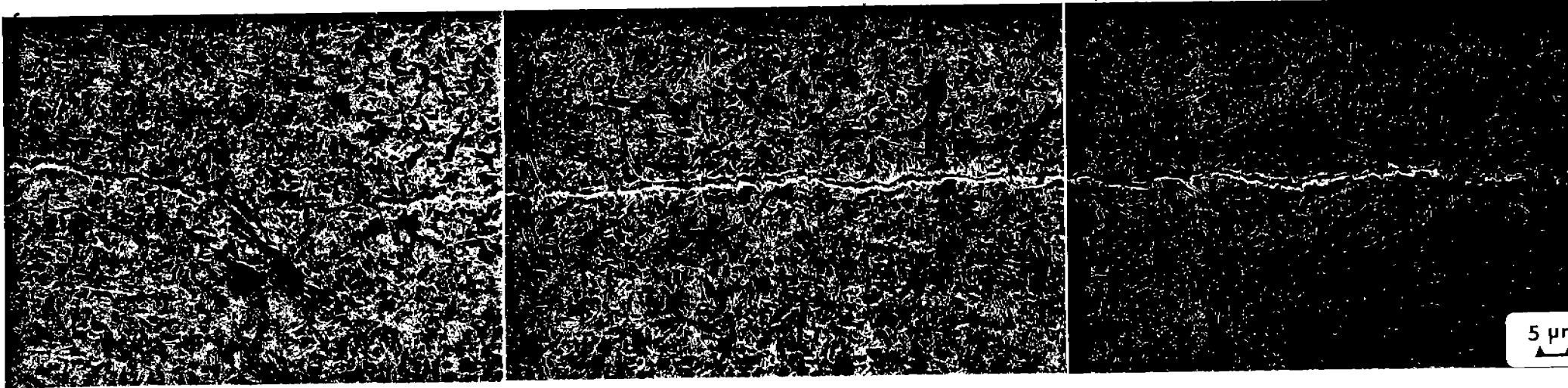


Figure 48. Higher magnification views of the crack profile for MIL S-24645 weld metal tested in air at 10 Hz.



A-93

Figure 49. Crack profile for MIL S-24645 weld metal tested in ASTM seawater at the free corrosion potential.

A-94

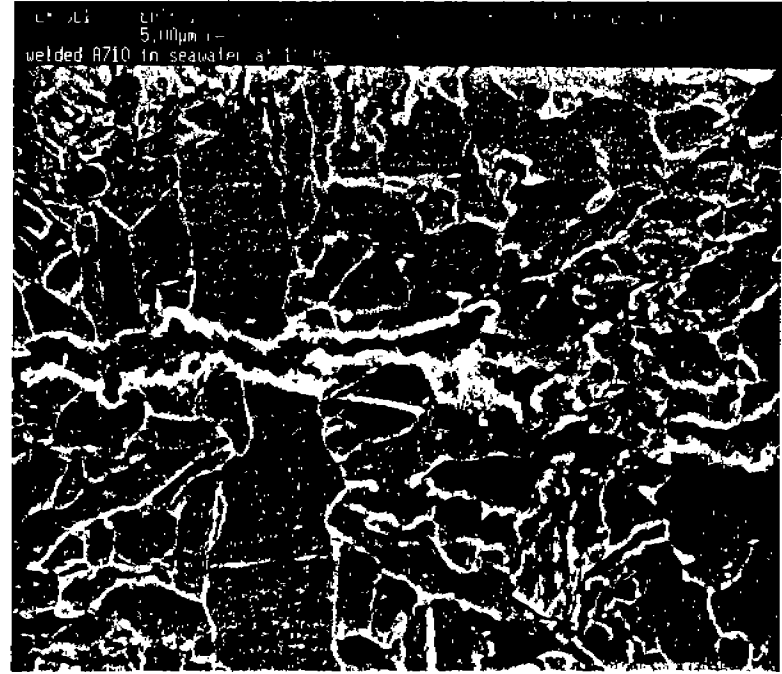
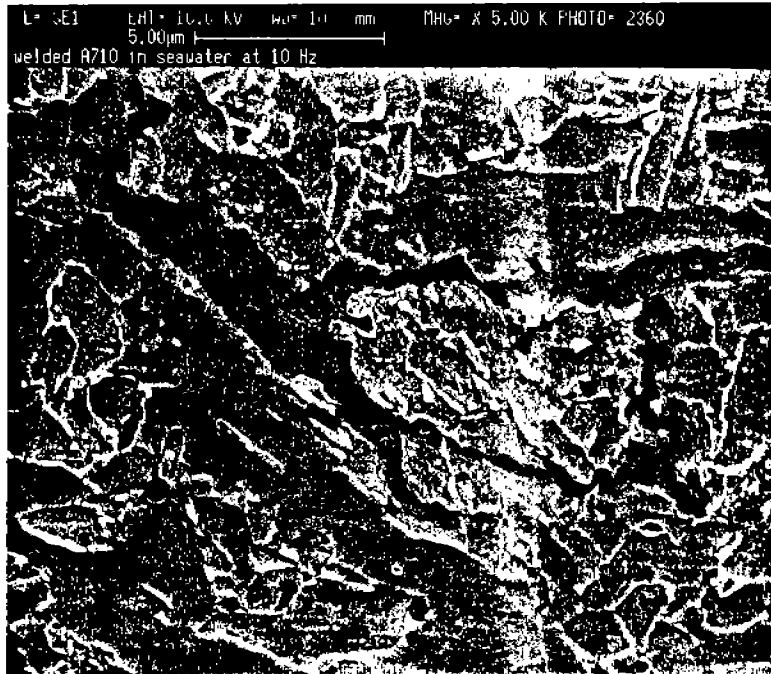


Figure 50. Higher magnification views of the crack profile for MIL S-24645 weld metal tested in ASTM seawater at the free corrosion potential, showing small non-metallic inclusions.

A-95

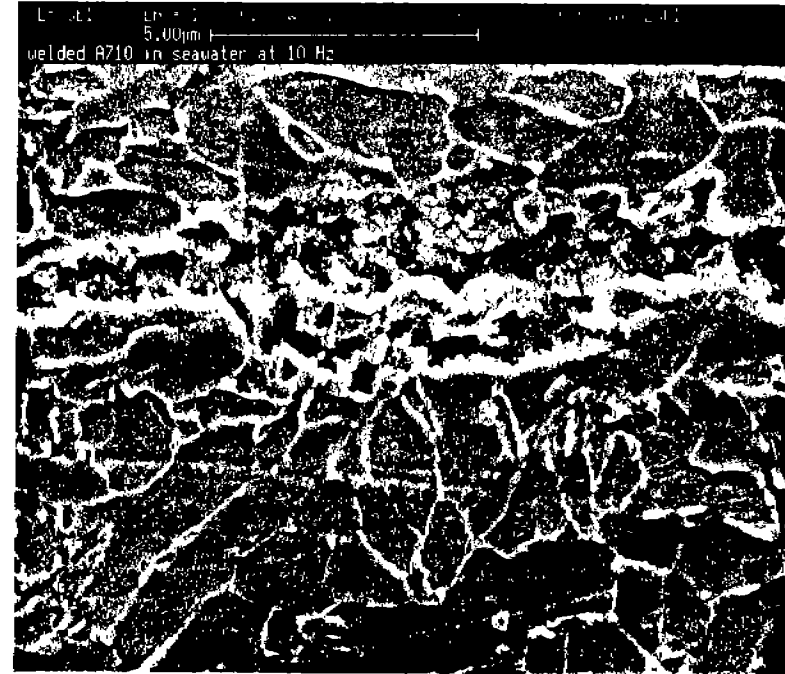
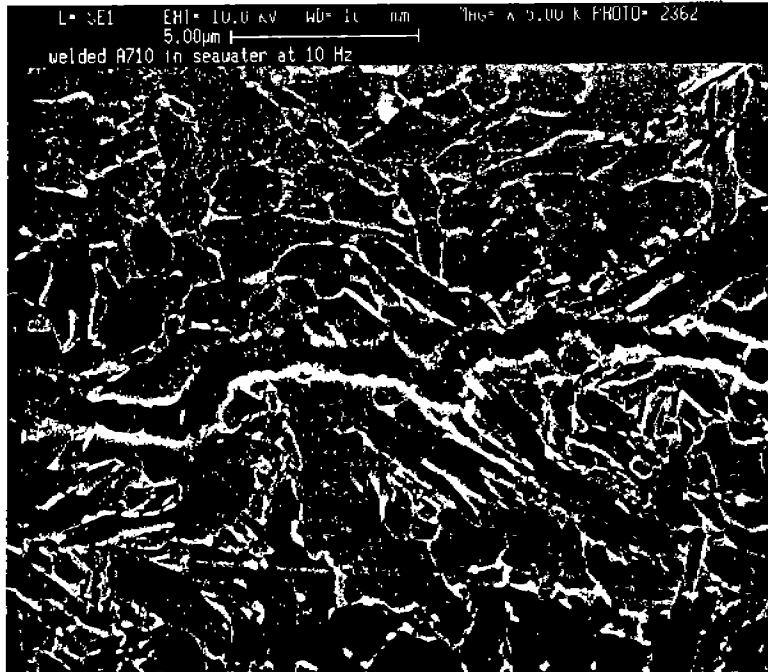


Figure 51. Higher magnification views of the crack profile for MIL S-24645 weld metal tested in ASTM seawater at the free corrosion potential, showing small non-metallic inclusions.

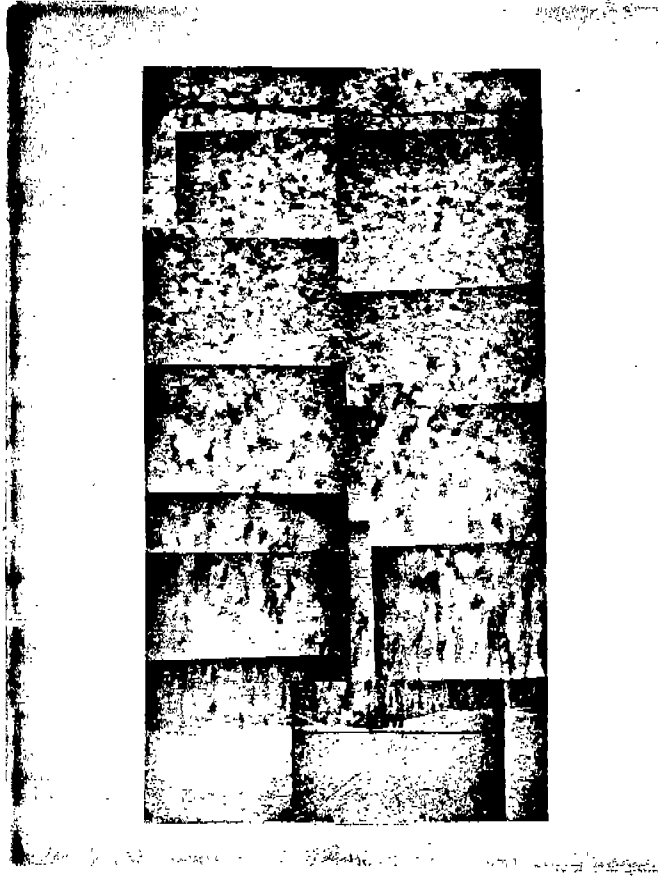


Figure 52a. Optical micrographs of the fracture path (near notch) of MIL S-24645 steel in the weld tested at 10 Hz at -1.0 V in seawater.



Figure 52b. Optical micrographs of the fracture path (near crack tip) of MIL S-24645 steel in the weld tested at 10 Hz at -1.0 V in seawater.

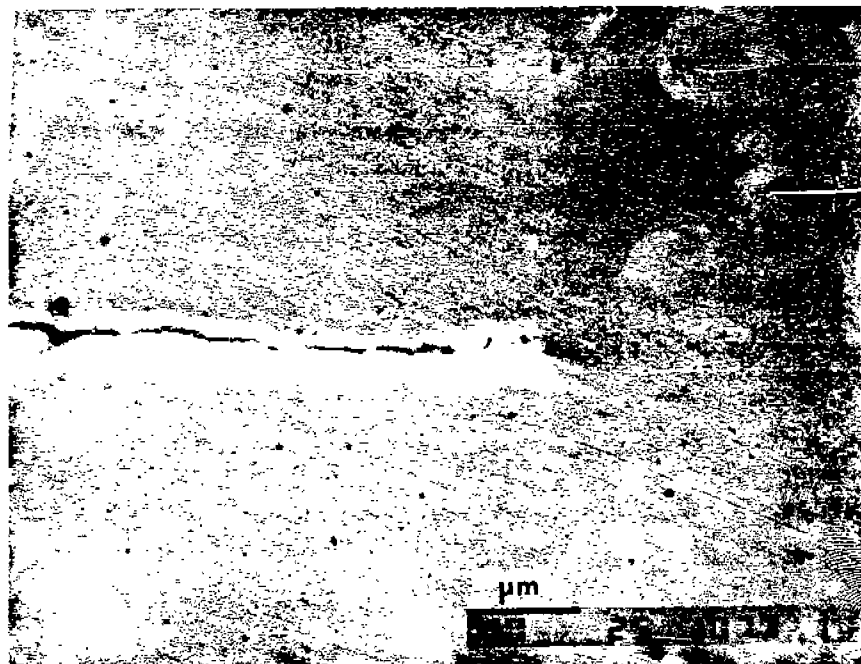


Figure 53. SEM micrographs of the fracture path (near crack tip) of MIL S-24645 steel in the weld tested at 10 Hz at -1.0V in seawater: (a) 750 X, 5% Nital; (b) 1500 X, unetched.

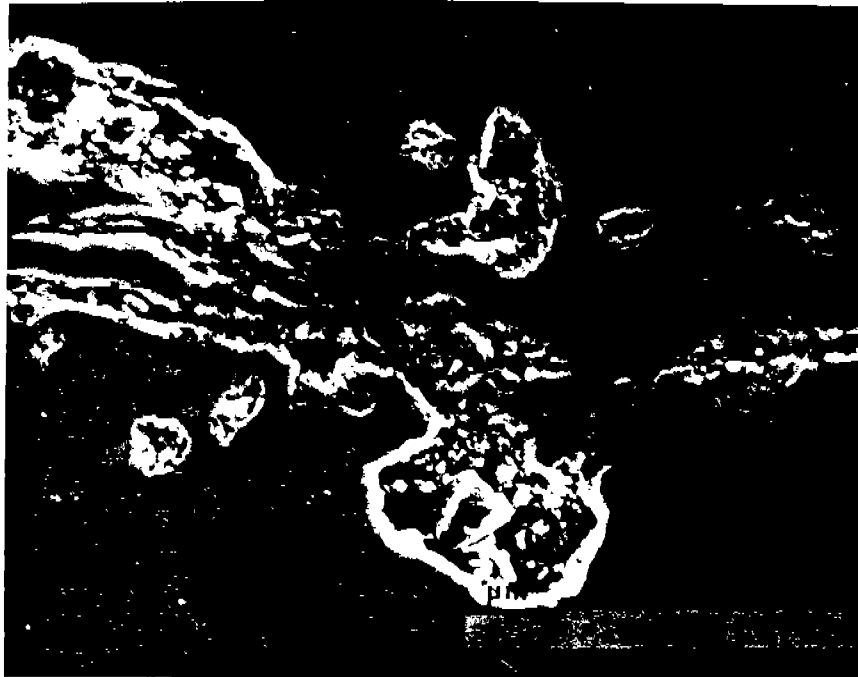


Figure 54. SEM micrograph of the fracture path with crack branching and damage accumulation of MIL S-24645 steel in the weld tested at 10 Hz at -1.0V in seawater.

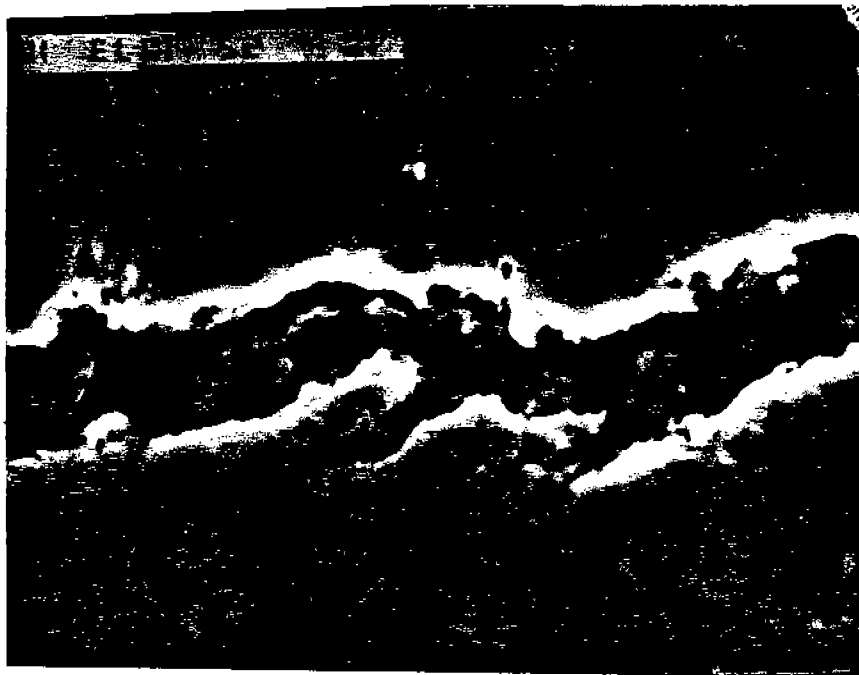
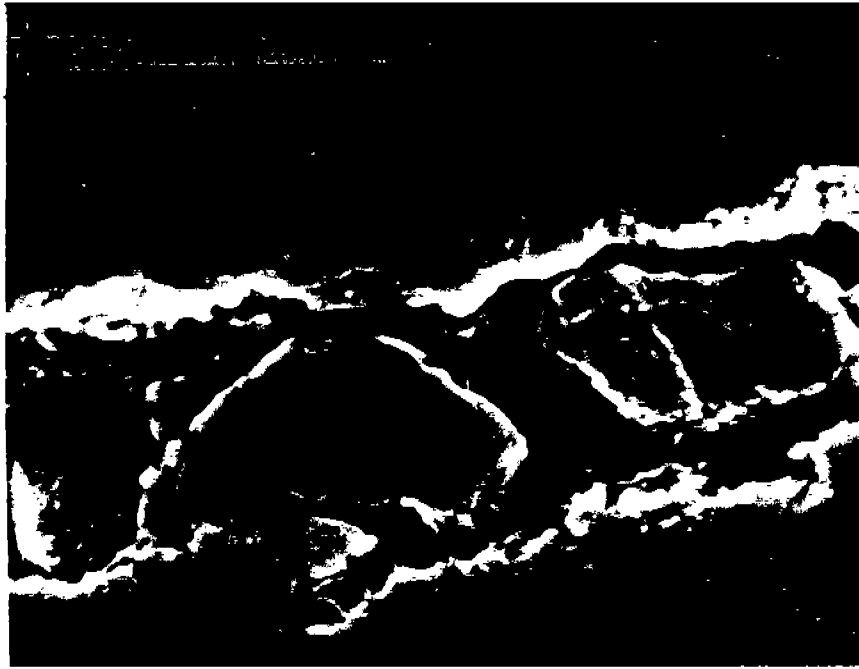


Figure 55. SEM micrographs of the fracture path with crack branching and damage accumulation of MIL S-24645 steel in the weld tested at 10 Hz at -1.0V in seawater: (a) behind crack tip; (b) in the middle region.

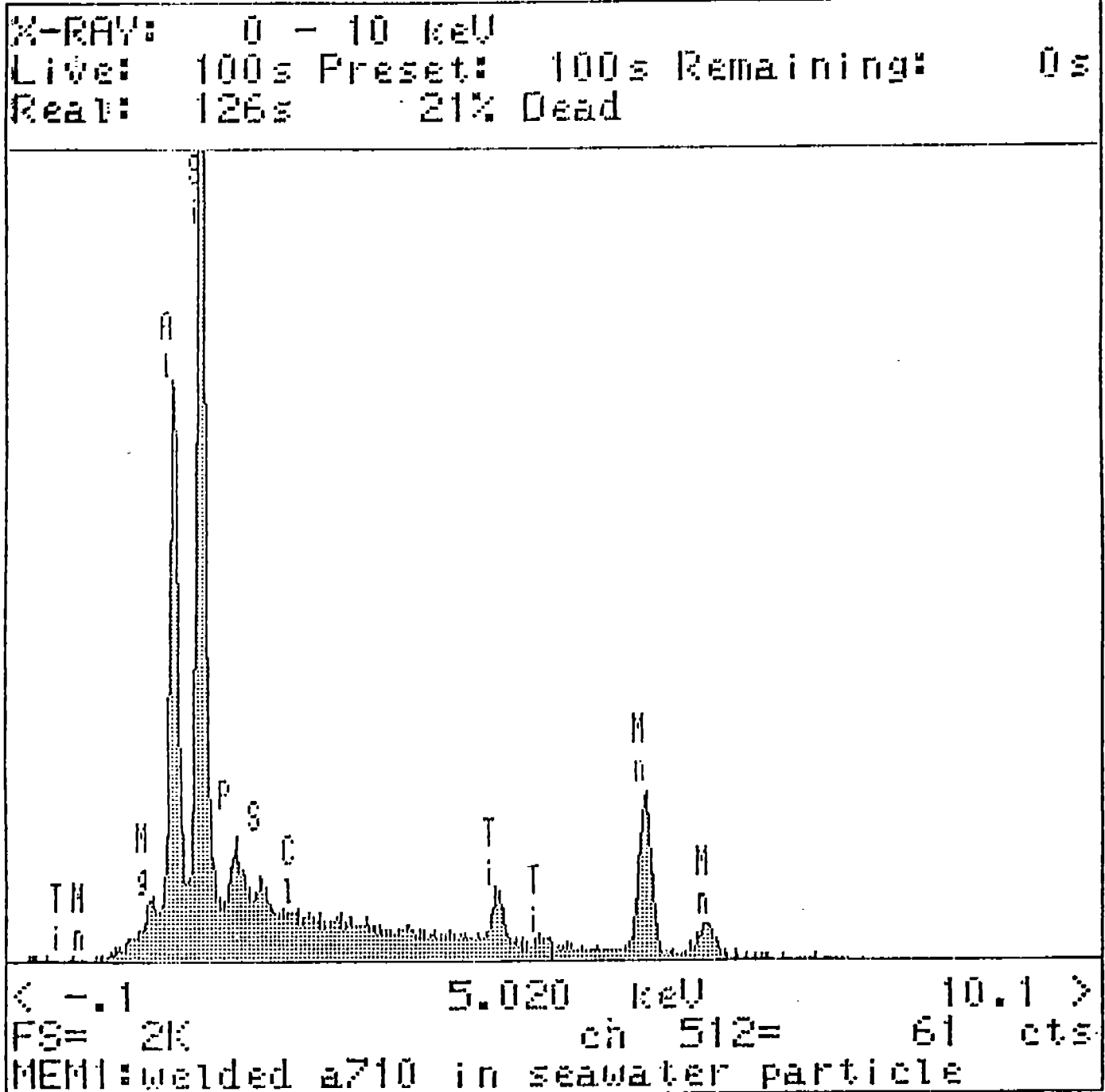


Figure 56. Typical energy dispersive x-ray analysis of inclusions observed in MIL S-24645 weld metal.

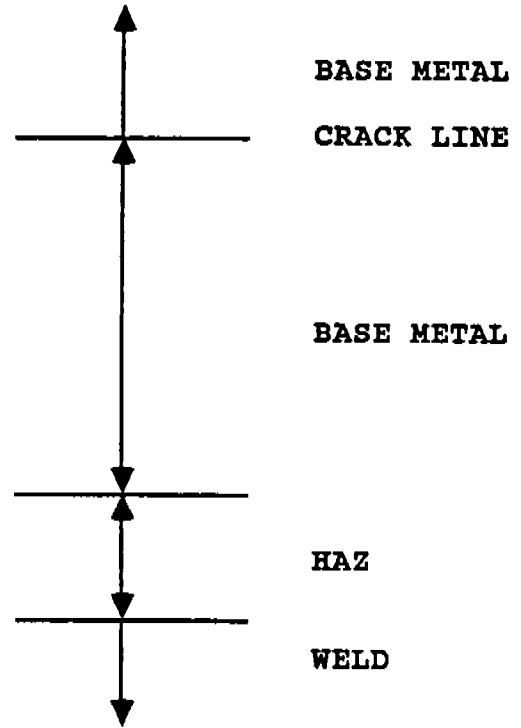
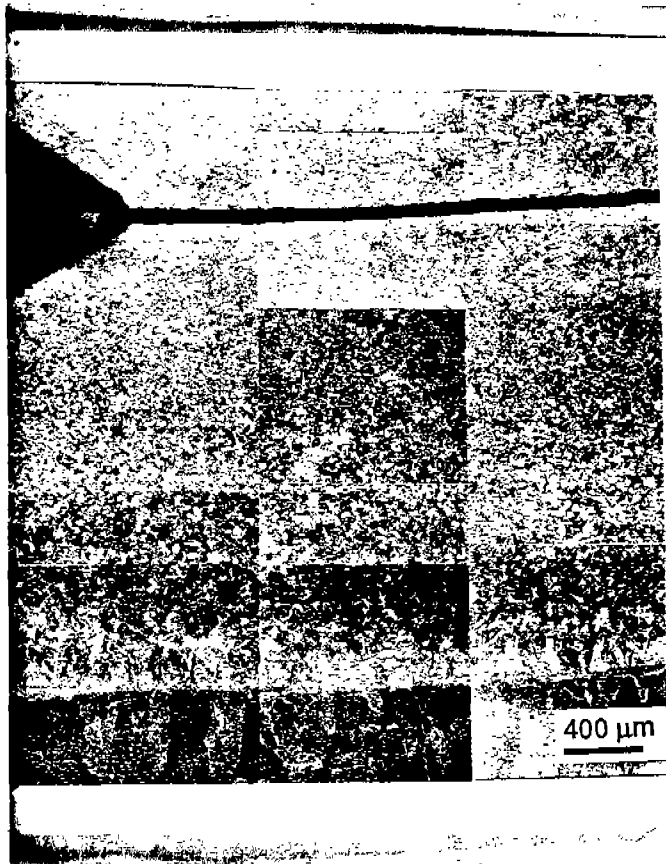


Figure 57a. Optical micrographs of the fracture path (near notch) of MIL S-24645 HAZ tested at 10 Hz in seawater.

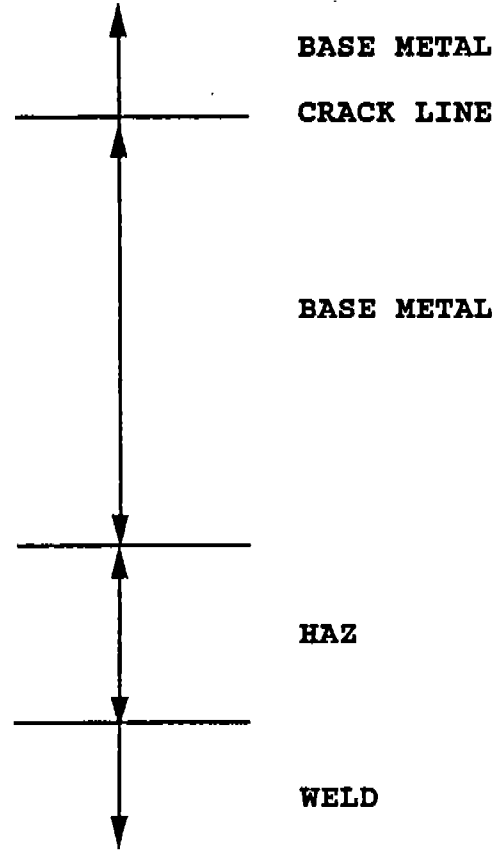
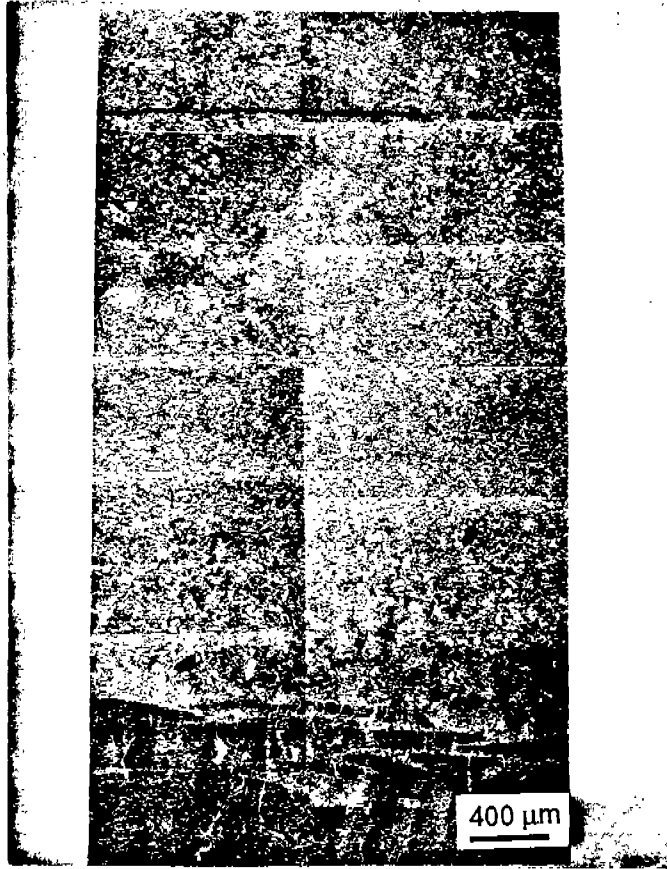
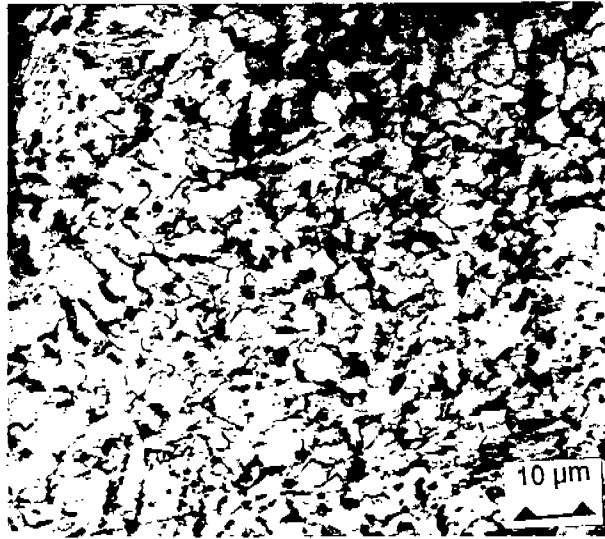
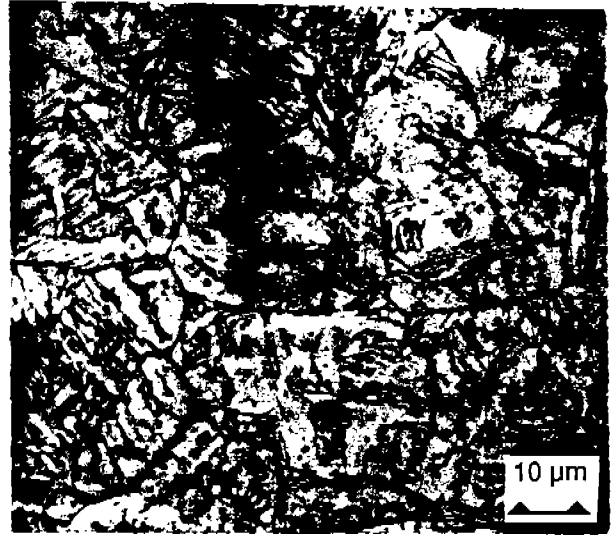


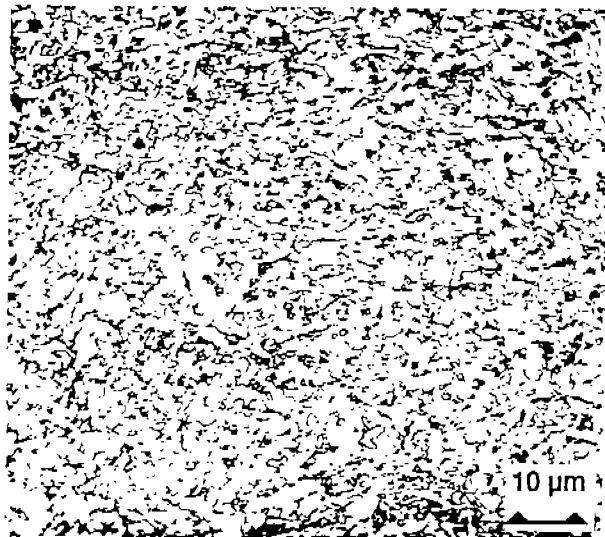
Figure 57b. Optical micrographs of the fracture path (near crack tip) of MIL S-24645 HAZ tested at 10 Hz in aeawater.



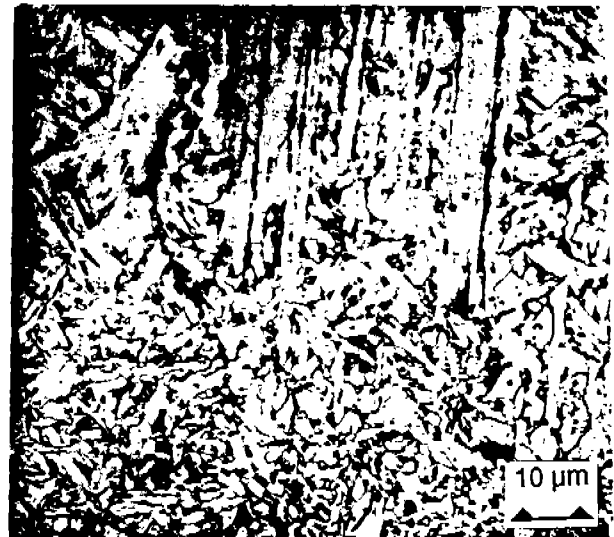
(a)



(b)



(c)



(d)

Figure 58. Optical micrographs of the different regions of MIL S-24645 steel tested at 10 Hz in seawater: (a) base metal; (b) HAZ; (c) weld; (d) transition between weld and HAZ.

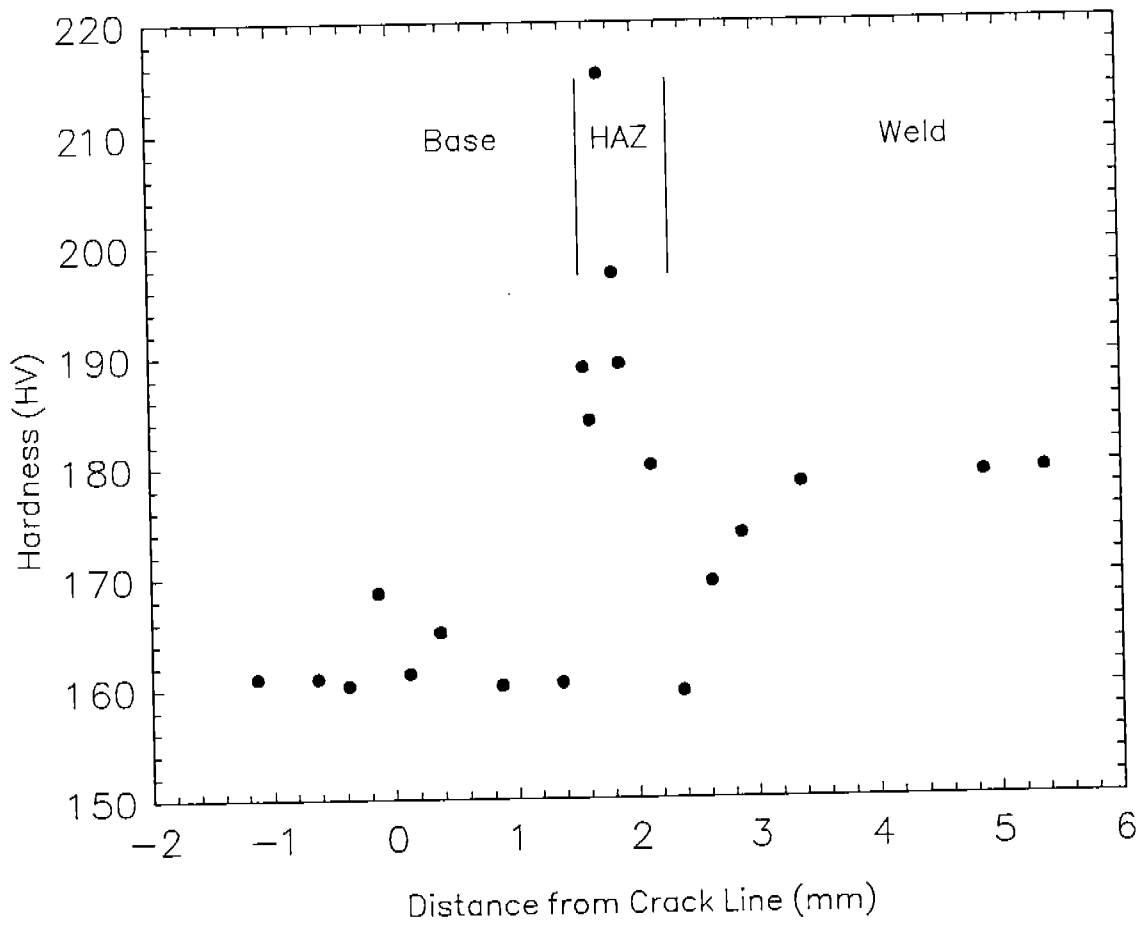


Figure 59a. Hardness distribution in the vicinity of the weld in MIL S-24645 HAZ CT sample near the notch.

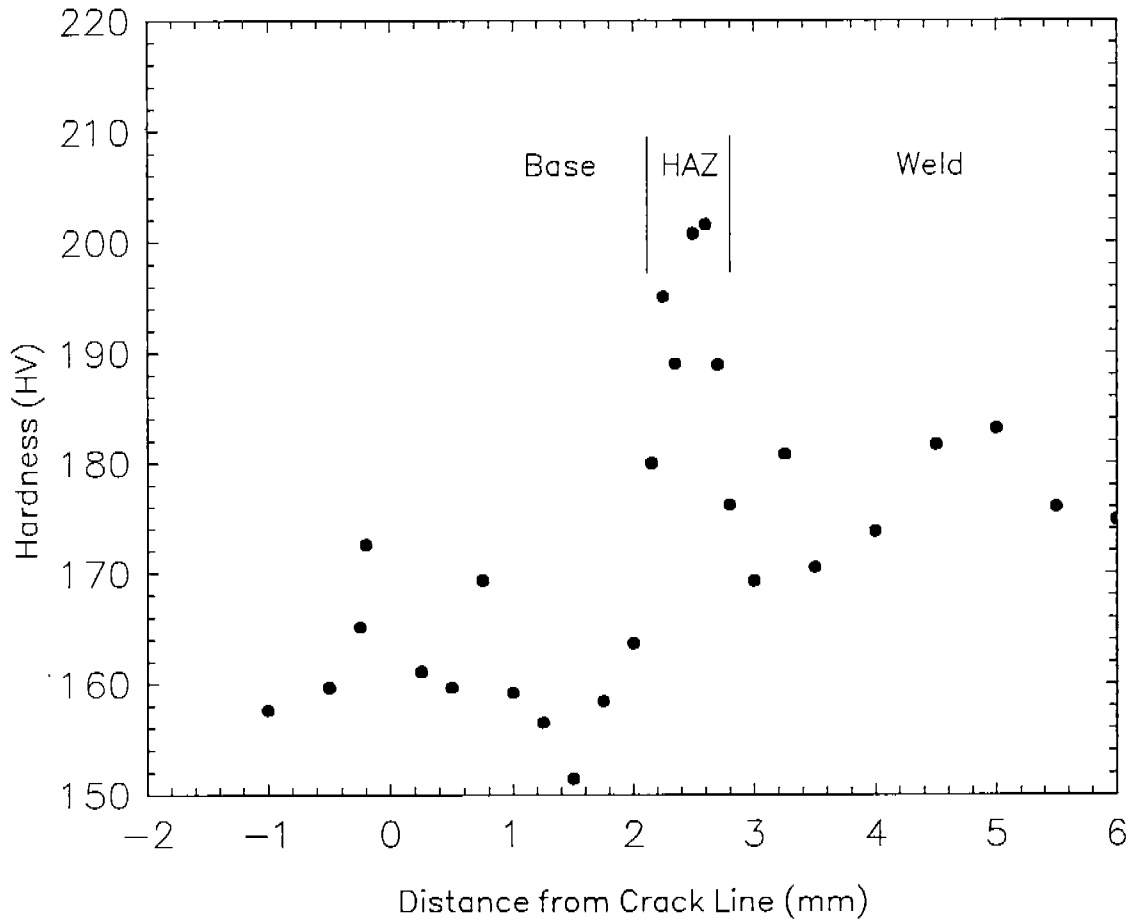


Figure 59b. Hardness distribution in the vicinity of the weld in MIL S-24645 HAZ CT sample near the crack tip.

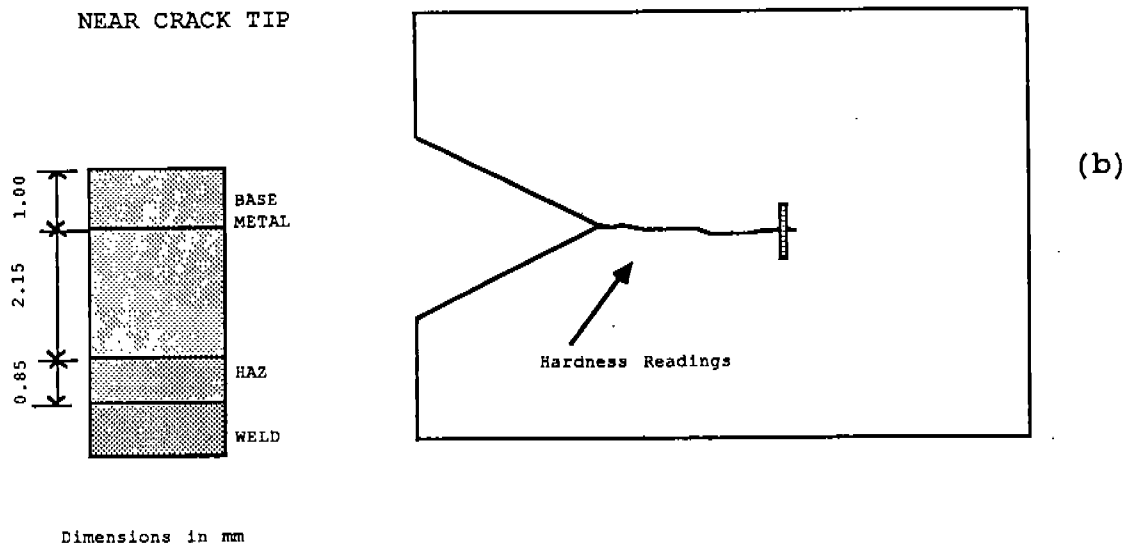
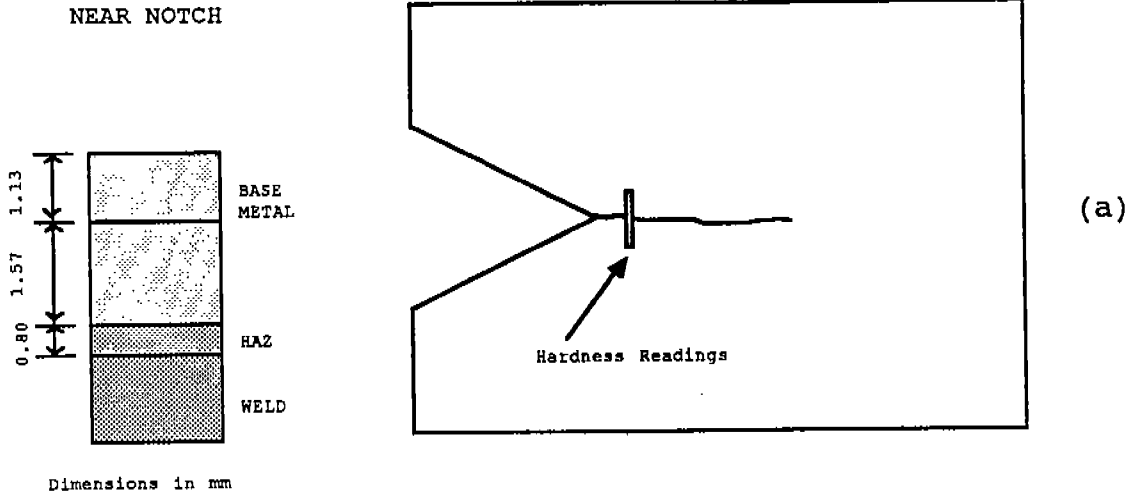


Figure 60. Schematic of the width of the HAZ and its distance from the crack: (a) near notch; (b) near crack tip.

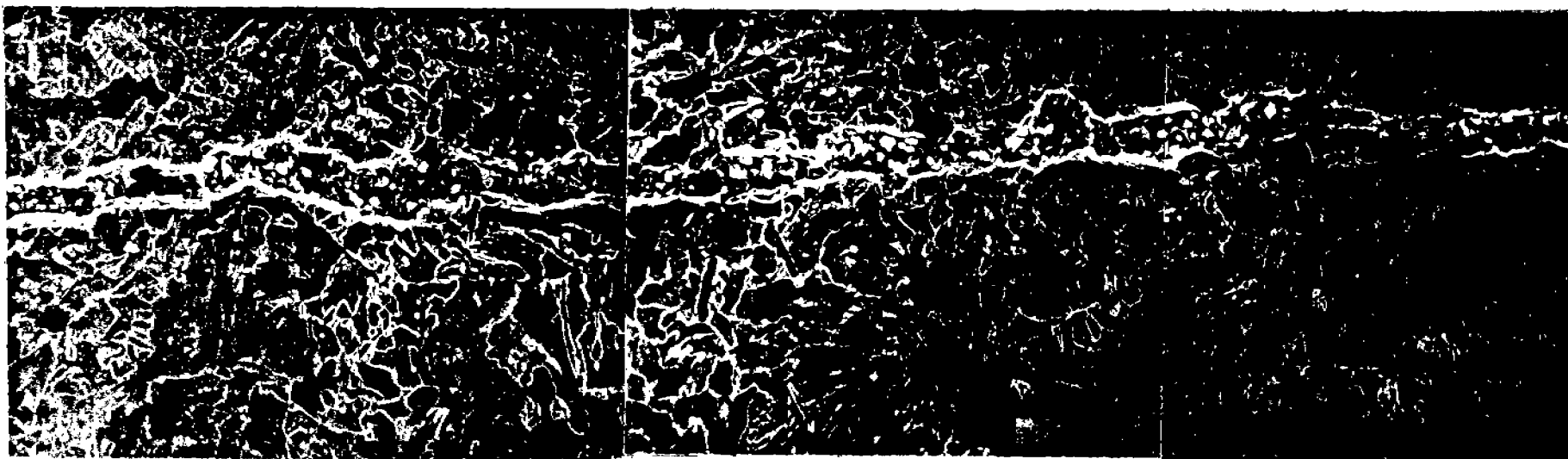
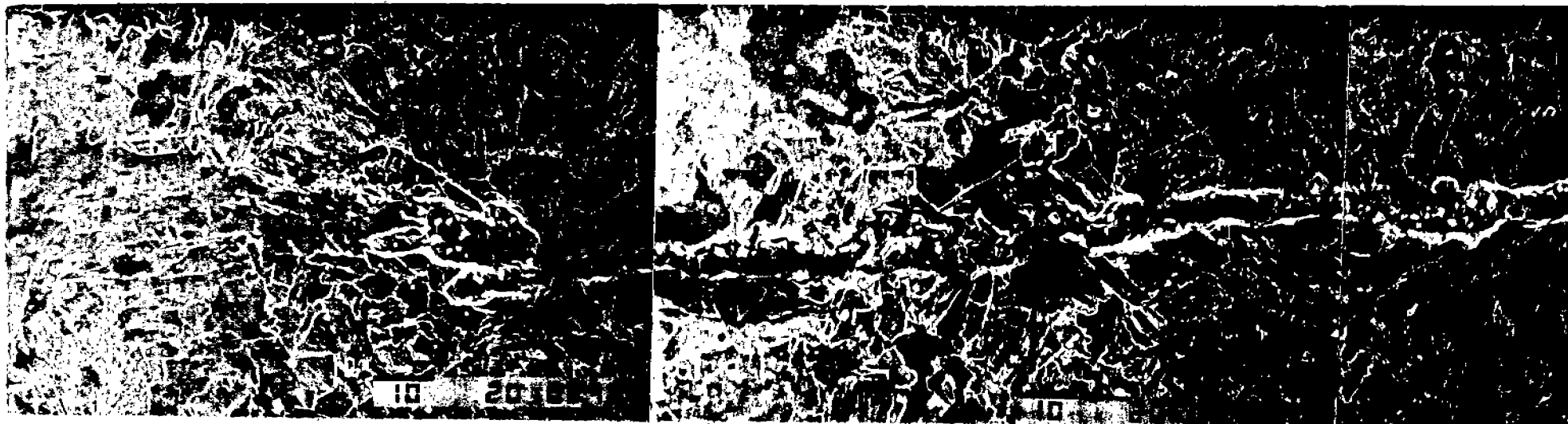
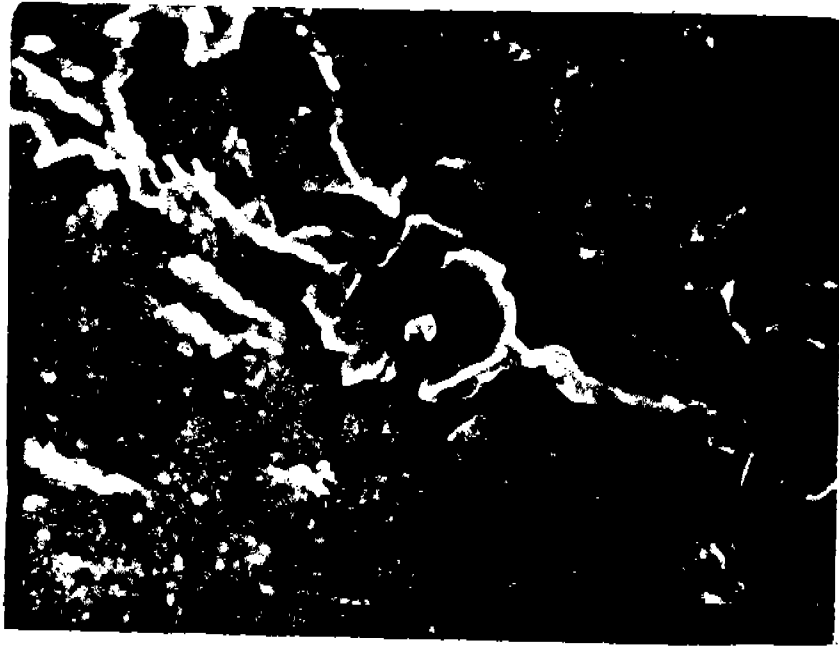
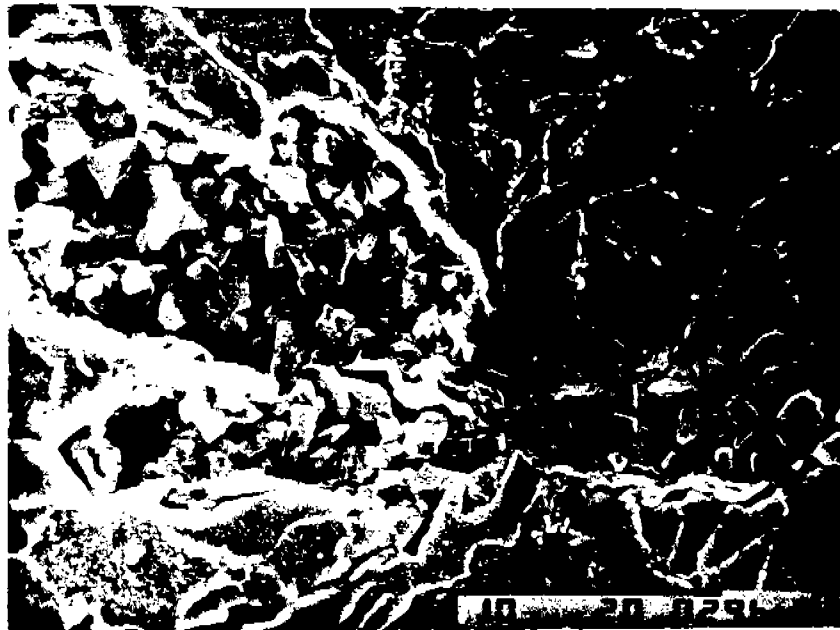


Figure 61. SEM micrographs of the fracture path of MIL S-24645 HAZ tested at 10 Hz in ASTM seawater.

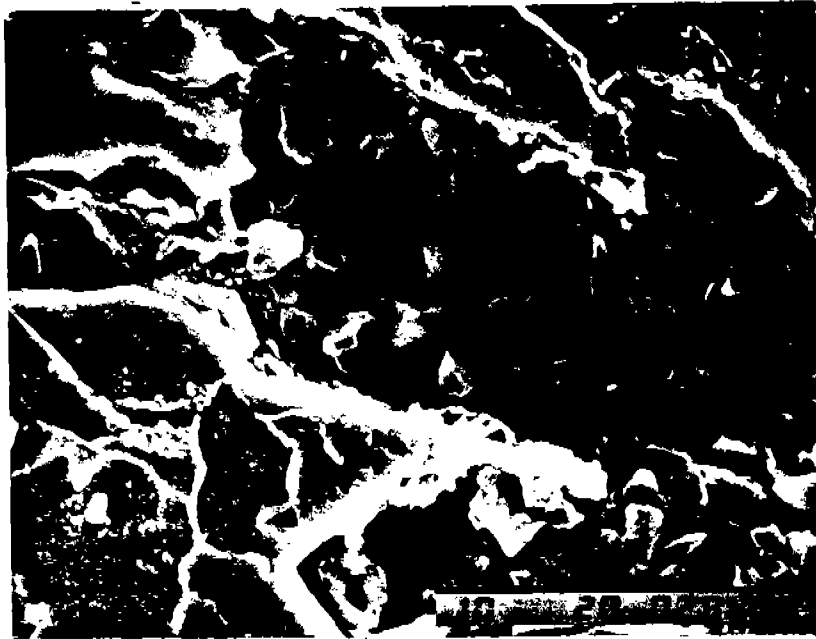


(a)



(b)

Figure 62. SEM micrograph at high magnifications of the fracture path near the crack tip of MIL S-24645 HAZ tested at 10 Hz in seawater: (a) 10,000 X; (b) 35,000 X.



(c)

Figure 62. SEM micrograph at high magnifications of the fracture path near the crack tip of MIL S-24645 HAZ tested at 10 Hz in seawater: (c) 50,000 X.

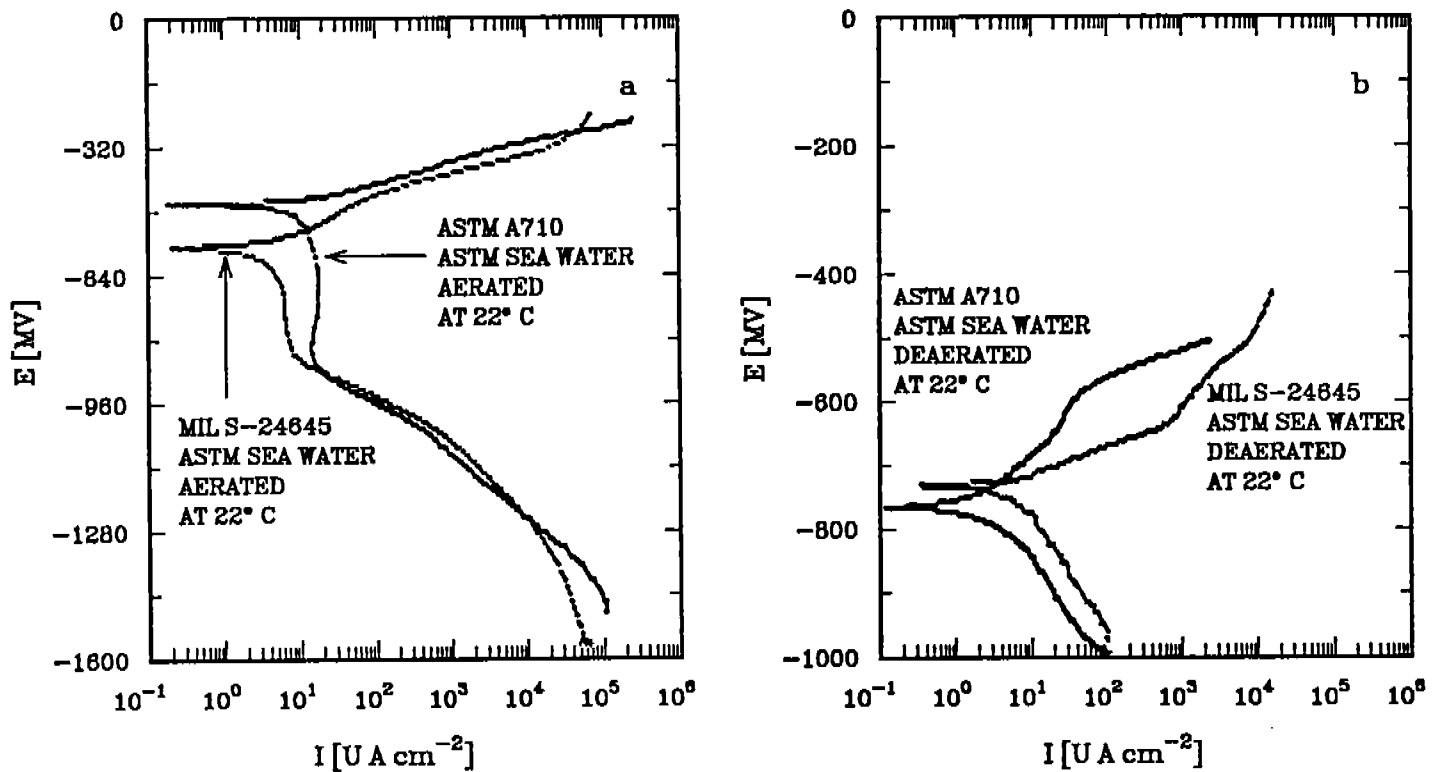


Figure 63. Potentiodynamic polarization curves: (a) comparison of data for ASTM A710 (cylindrical) and MIL S-24645 (flat) steels in aerated ASTM seawater, pH = 8.2, 22 C; (b) comparison of data for ASTM A710 (cylindrical) and MIL S-24645 (flat) steels in deaerated ASTM seawater, pH = 8.2, 22 C.

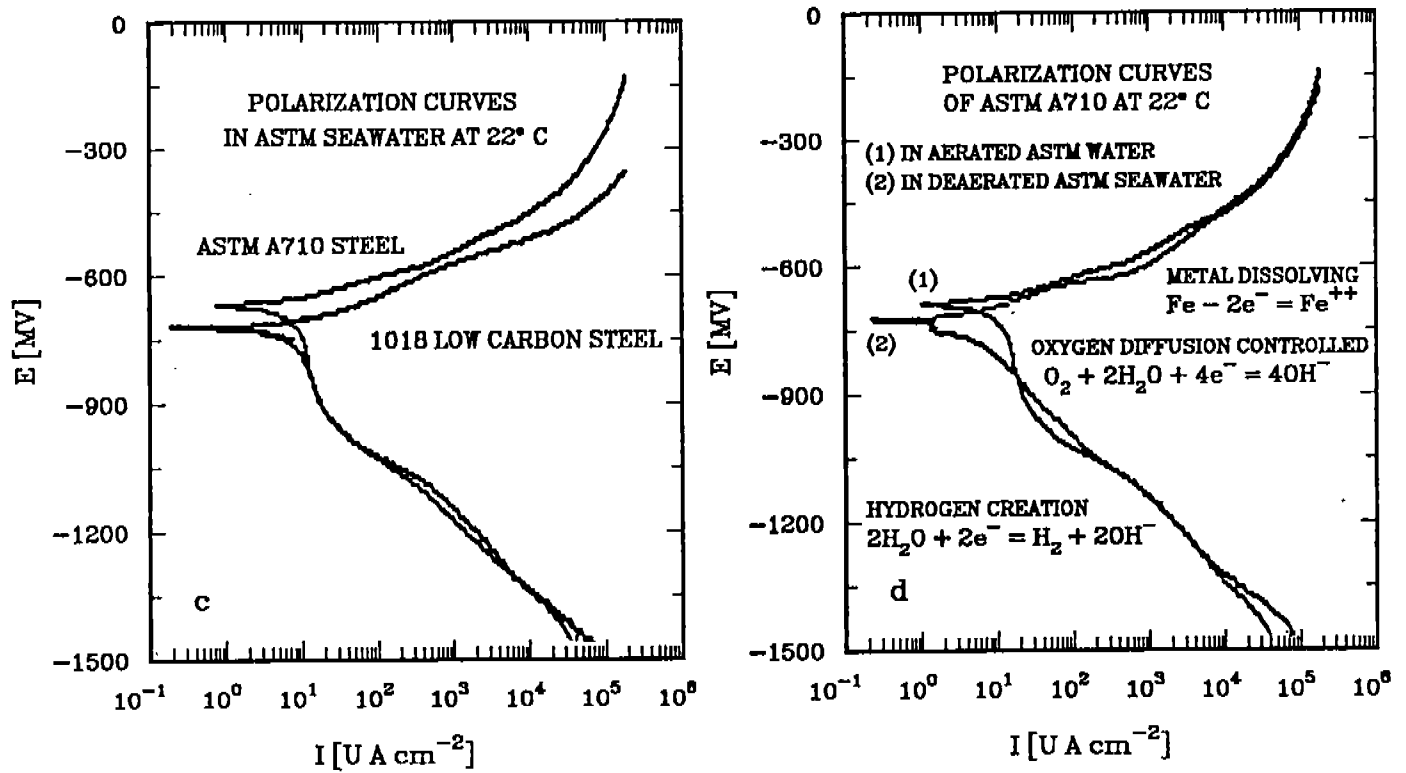


Figure 63. Potentiodynamic polarization curves: (c) ASTM A710 and 1018 steel held in ASTM seawater for 1.5 hours prior to scanning positively or negatively from the free corrosion potential; (d) comparison of data for ASTM A710 held in aerated and deaerated ASTM seawater for 1.5 hours prior to scanning positively or negatively from the free corrosion potential.

File : 08029101

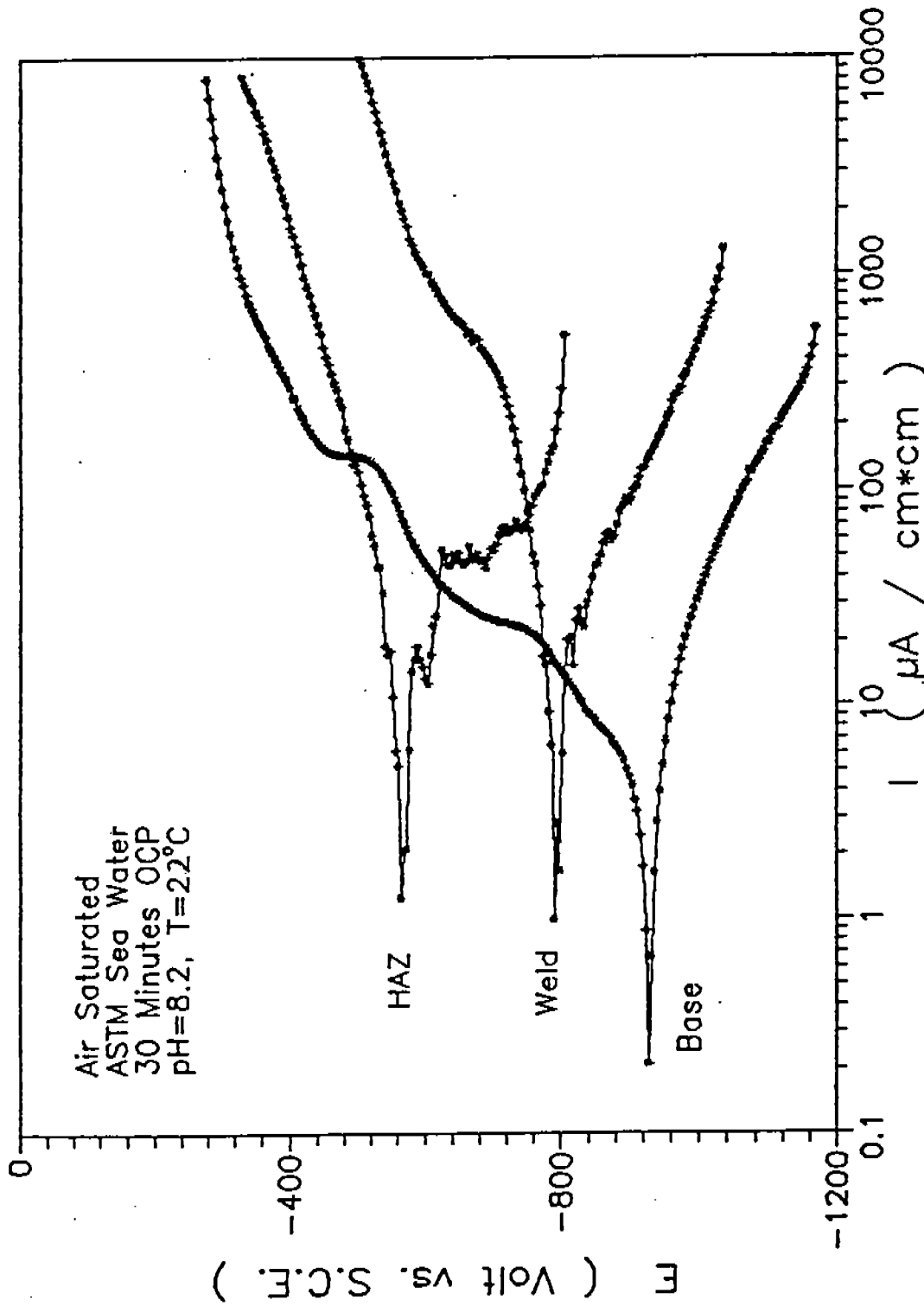


Figure 64. Polarization curves for MIL S-24645 base, weld and HAZ microstructures in air saturated ASTM seawater, pH = 8.2, 22 C, with a 30 minute hold at the open circuit potential (OCP) prior to scanning positively from 250 mV below the corrosion potential.

File : 08029102

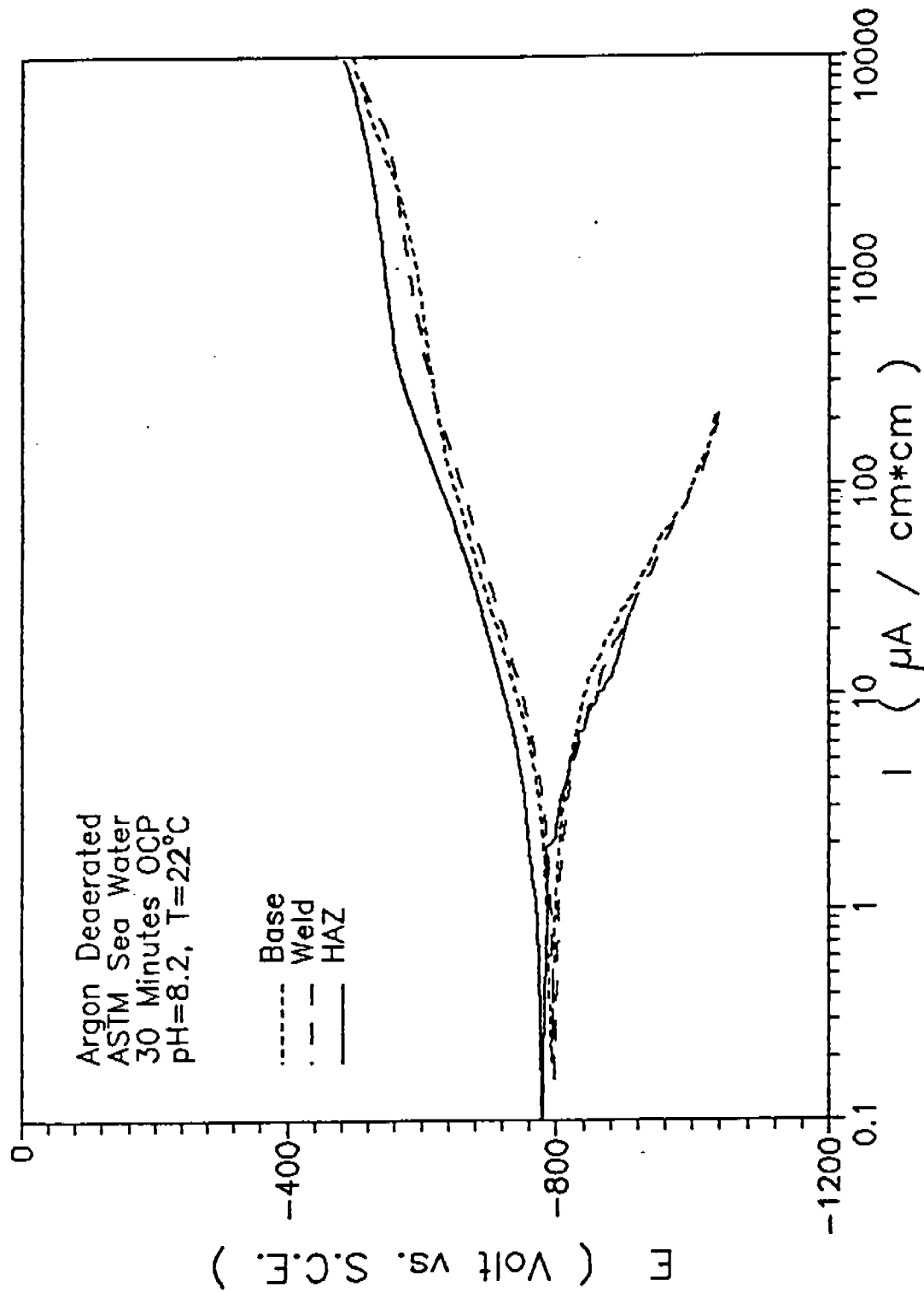


Figure 65. Polarization curves for MIL S-24645 base, weld and HAZ microstructures in argon saturated ASTM seawater, pH = 8.2, 22 C, with a 30 minute hold at the open circuit potential (OCP) prior to scanning positively from 250 mV below the corrosion potential.

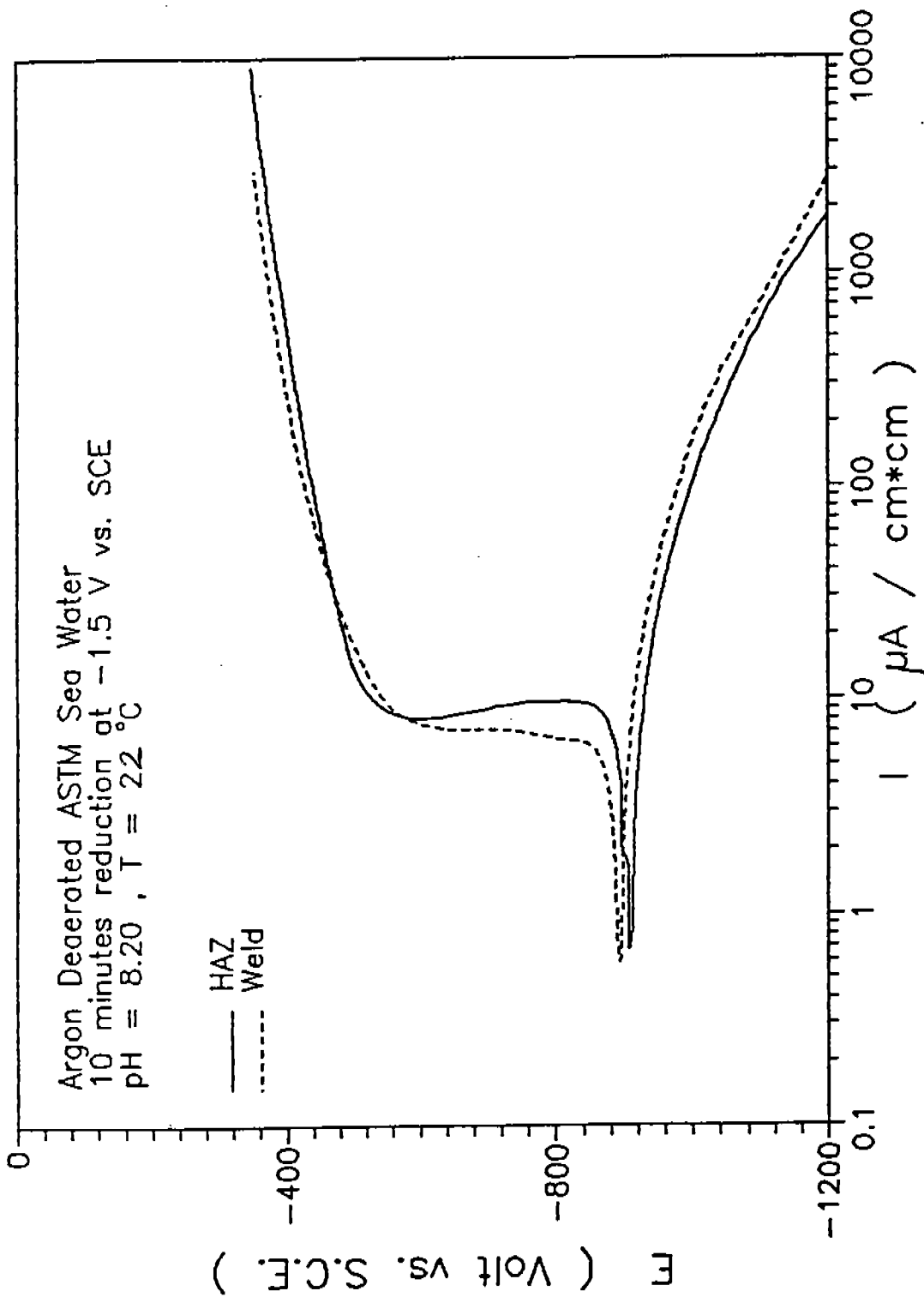


Figure 66. Polarization curves for MIL S-24645 base, weld and HAZ microstructures in argon saturated ASTM seawater, pH = 8.2, 22 C, with a 10 minute reduction at -1500 mV SCE prior to scanning positively from 250 mV below the corrosion potential.

File : 08029103

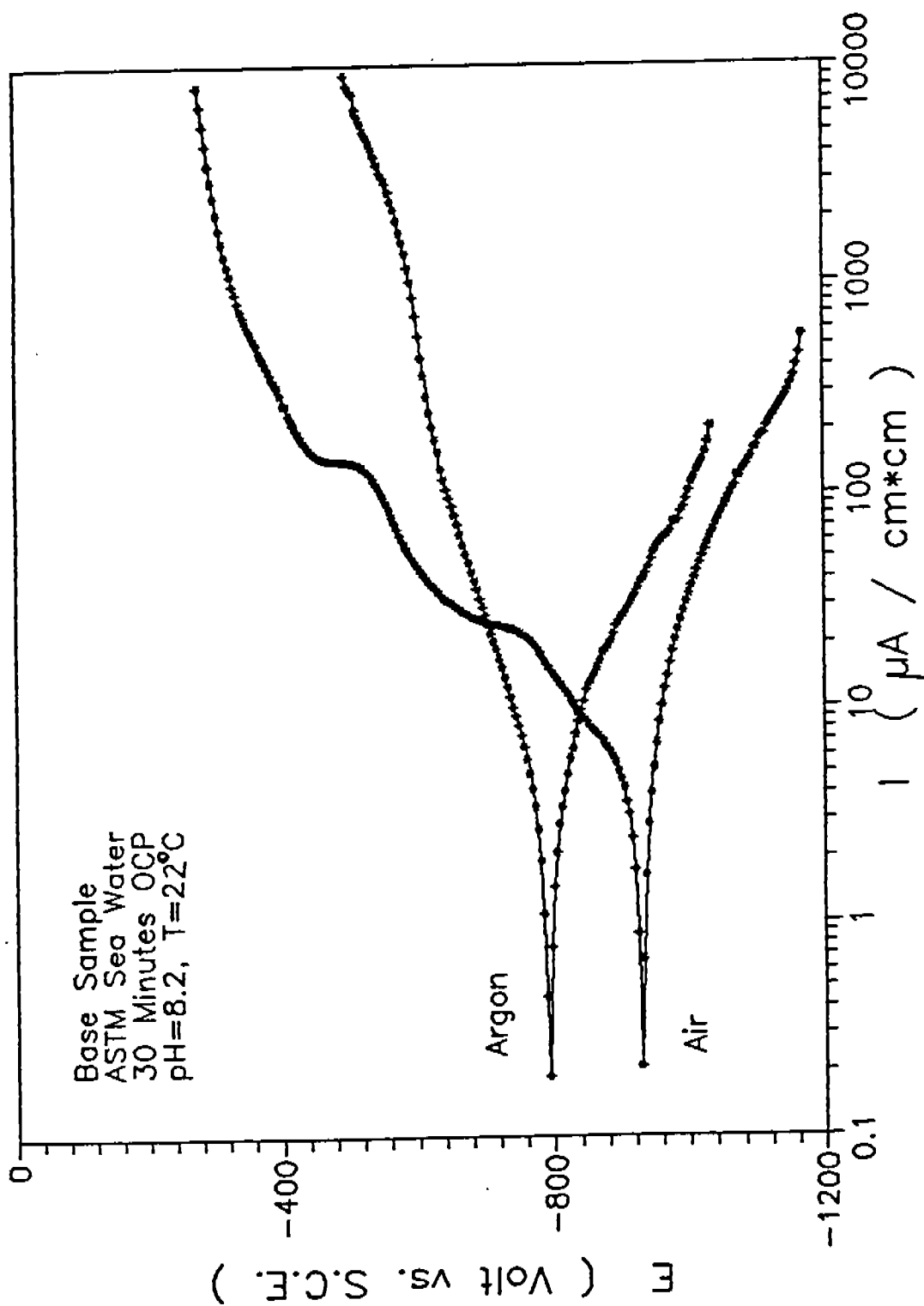


Figure 67. Comparison of the polarization curves for MIL S-24645 base metal in air and argon saturated ASTM seawater, pH = 8.2, 22 C, with a 30 minute hold at the open circuit potential (OCP) prior to scanning positively from 250 mV below the corrosion potential.

A-117

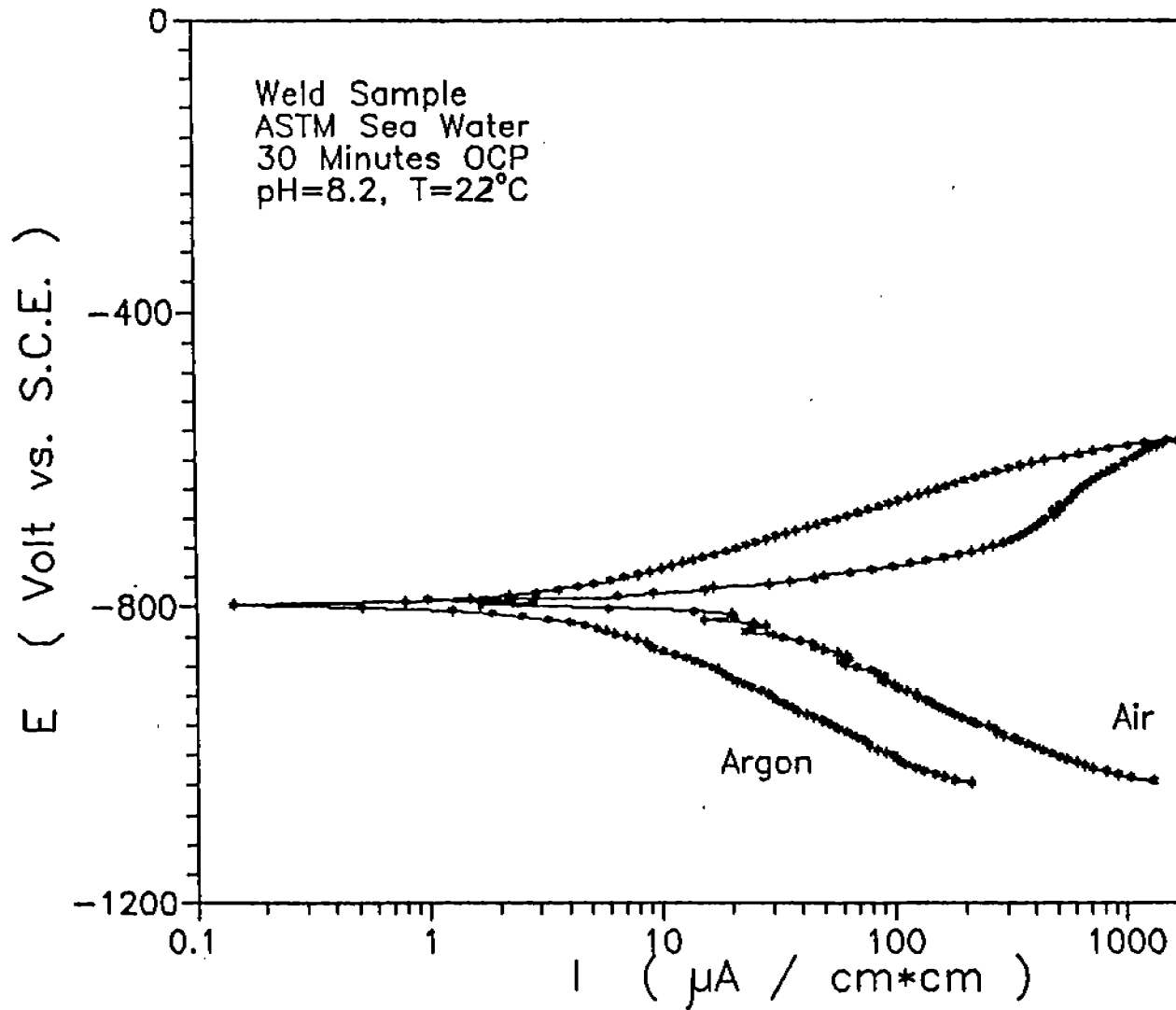


Figure 68. Comparison of the polarization curves for MIL S-24645 weld metal in argon saturated ASTM seawater, pH = 8.2, 22 C, with a 30 minute hold at open circuit potential (OCP) prior to scanning positively from 250 mV below corrosion potential.

File : 08029105

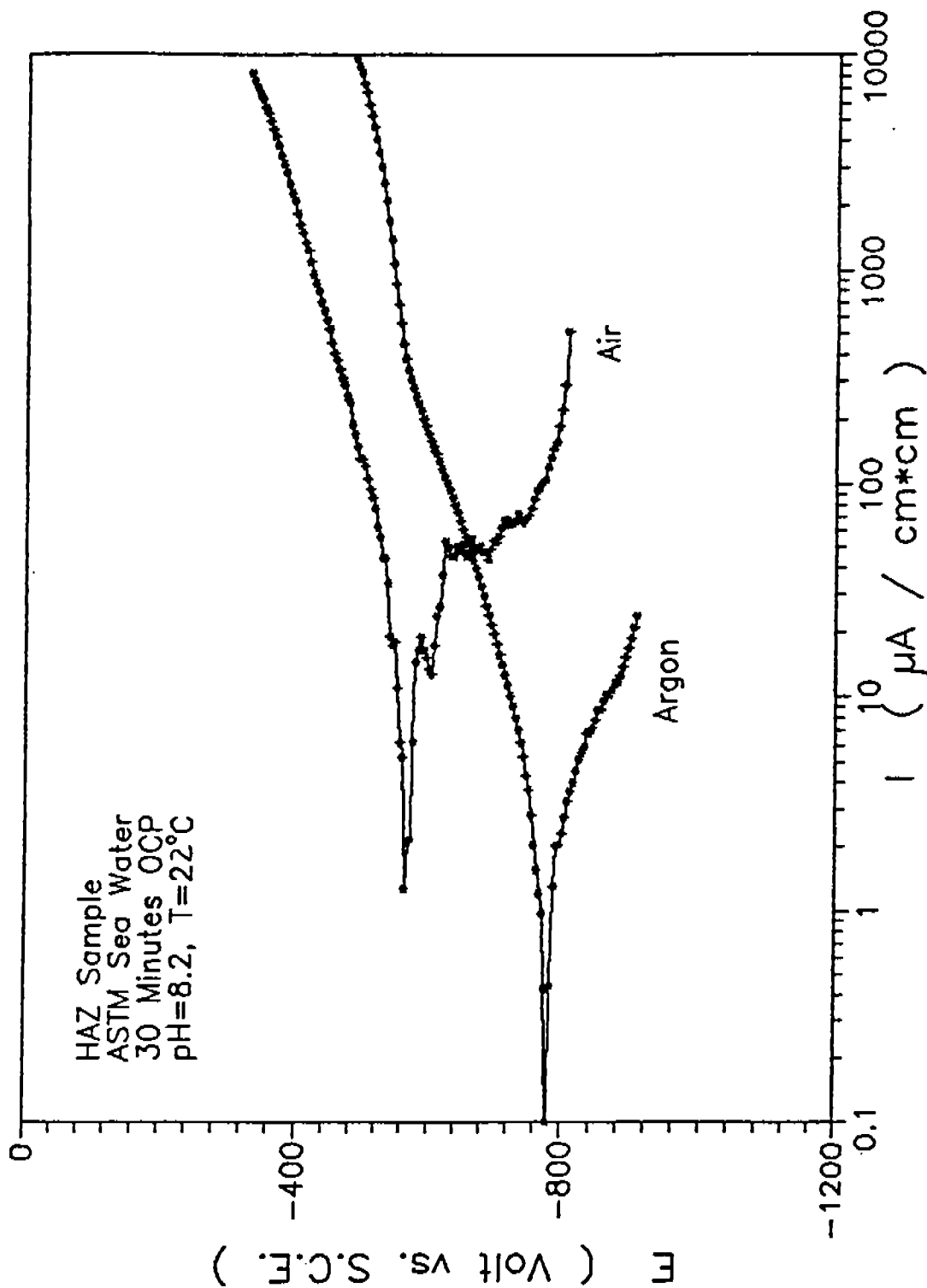


Figure 69. Comparison of the polarization curves for MIL S-24645 HAZ in air and argon saturated ASTM seawater, pH = 8.2, 22 C, with a 30 minute hold at the open circuit potential (OCP) prior to scanning positively from 250 mV below the corrosion potential.

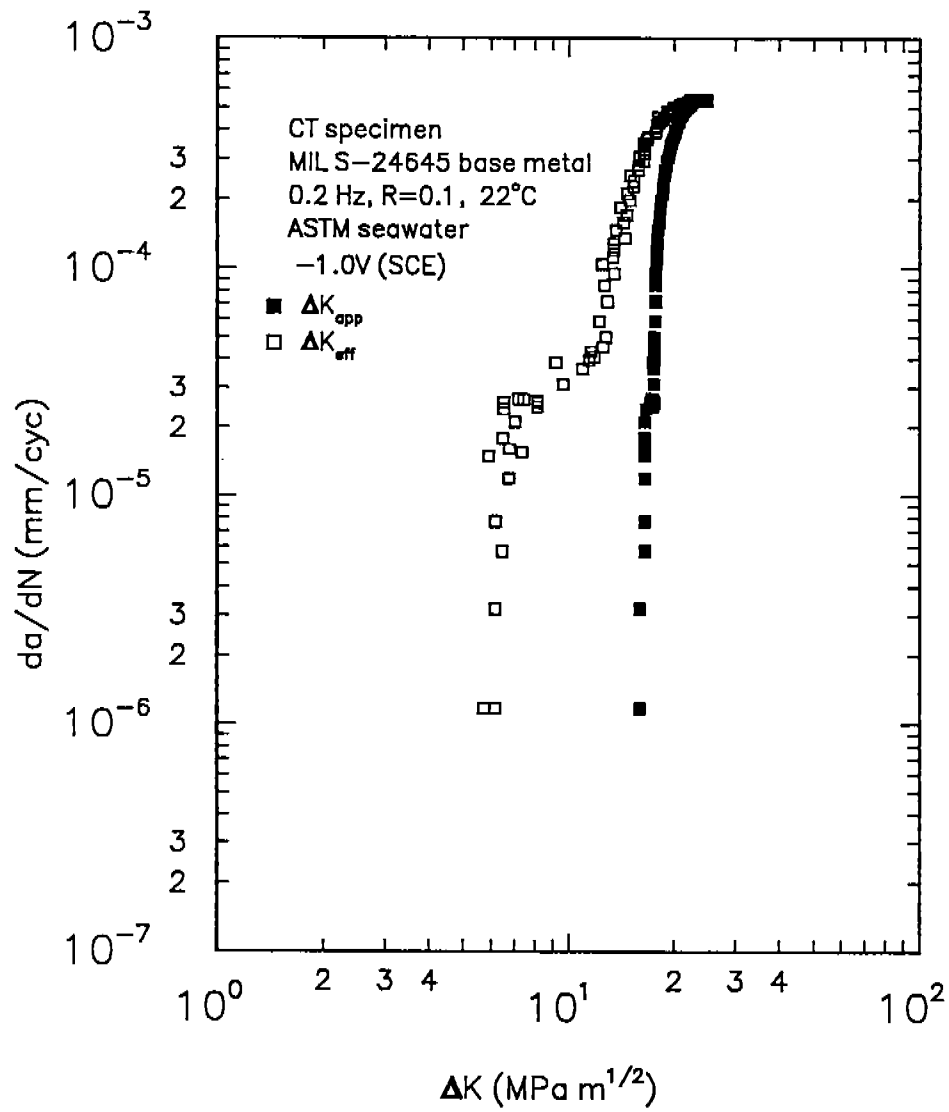


Figure 70. A comparison of near-threshold crack propagation data, before and after correction for crack closure, for MIL S-24645 base metal tested in ASTM seawater at -1.0 V (SCE) and at 0.2 Hz, R = 0.1, 22 C.

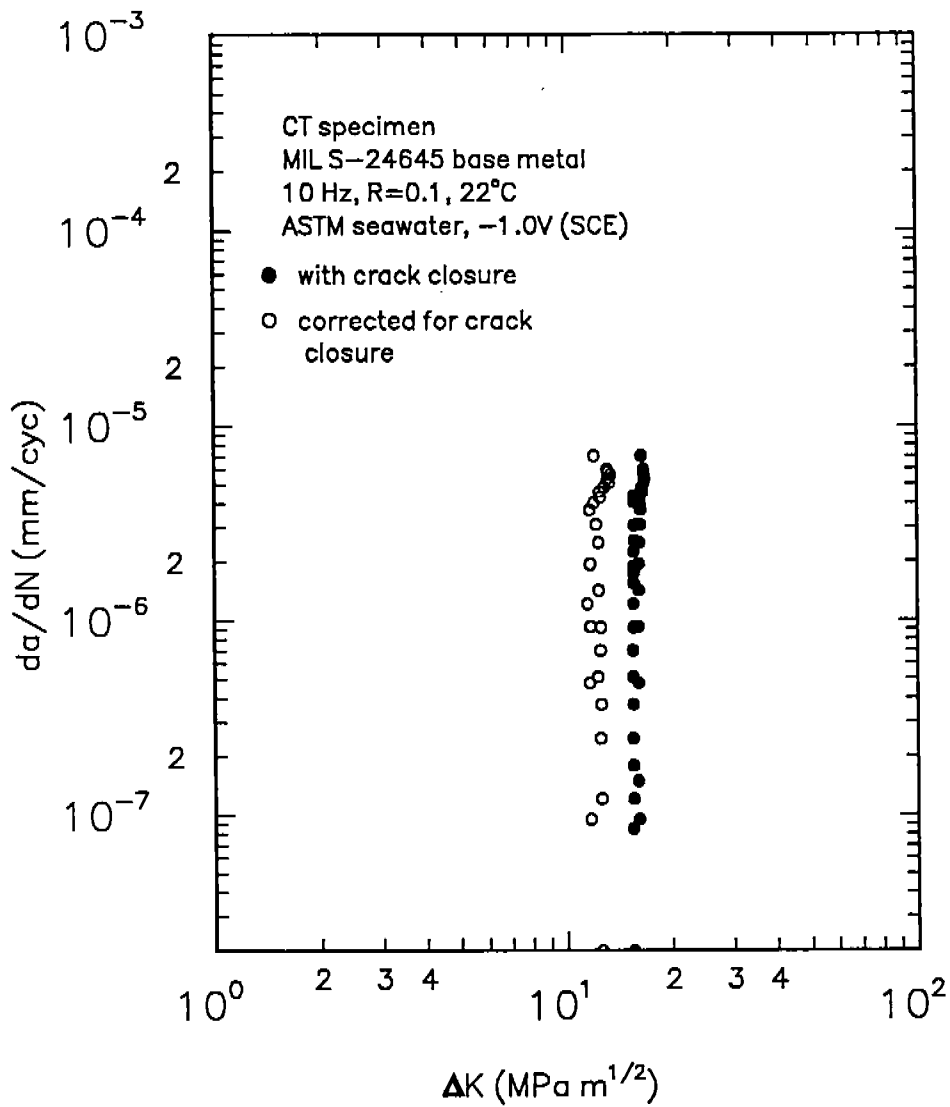


Figure 71. A comparison of near-threshold crack propagation data, before and after correction for crack closure, for MIL S-24645 base metal tested in ASTM seawater at -1.0 V (SCE) and at 10.0 Hz, following the test at 0.2 Hz in Fig. 70. R = 0.1, 22 C.

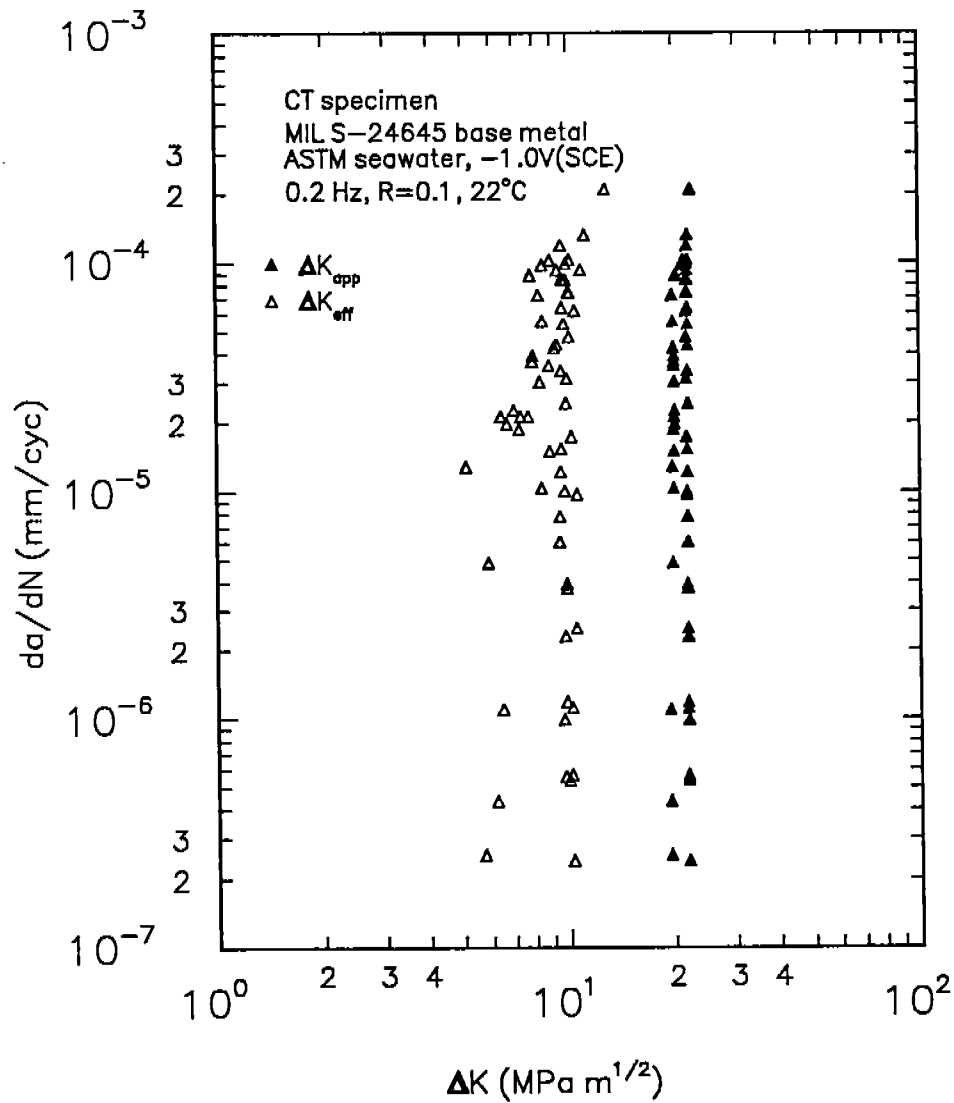


Figure 72. A comparison of near-threshold crack propagation data, before and after correction for crack closure, for MIL S-24645 base metal tested in ASTM seawater at -1.0 V (SCE) and at 10.0 Hz, R = 0.1, 22 C. Frequency was shifted to 0.2 Hz accompanied by a load increase following the 10 Hz test shown in Fig. 71.

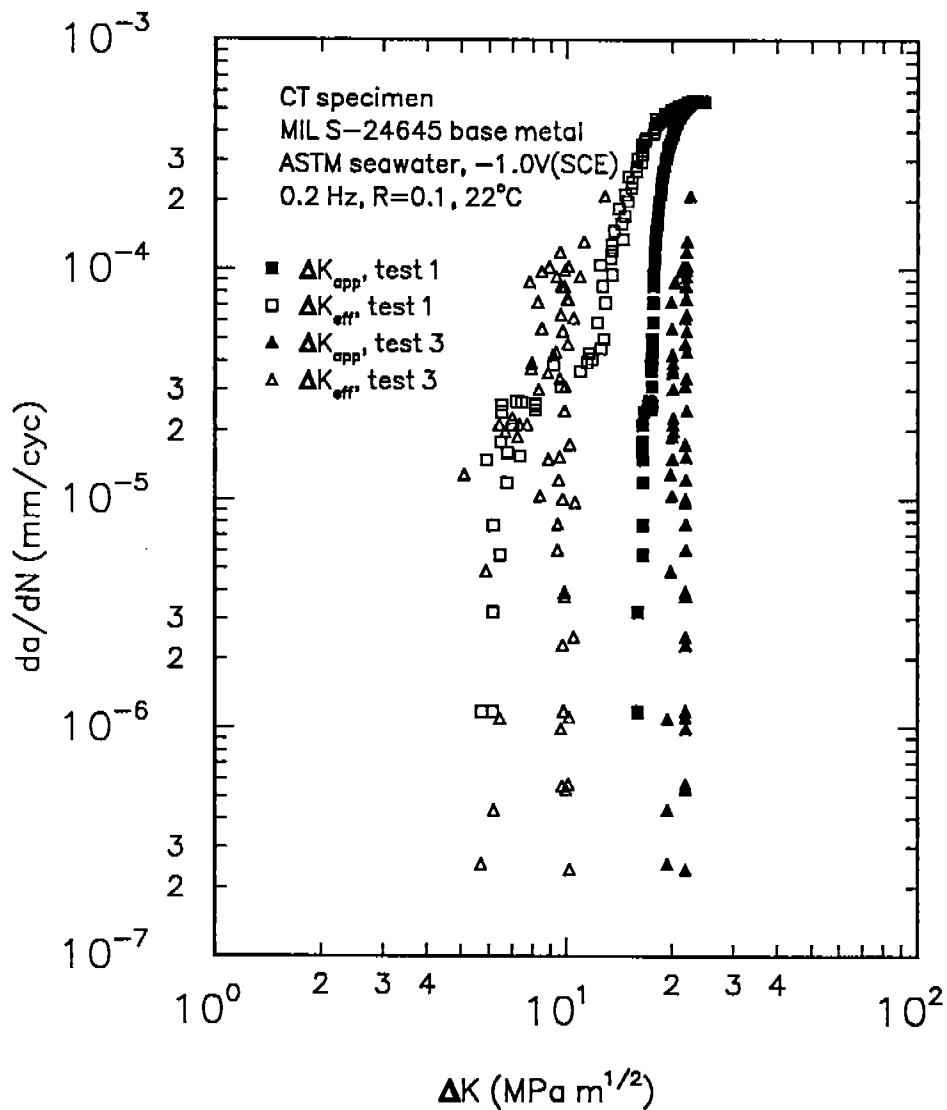


Figure 73. A comparison of near-threshold crack propagation data, before and after correction for crack closure, for MIL S-24645 base metal tested in ASTM seawater at -1.0 V (SCE) and at 10.0 Hz, R = 0.1, 22 C. Test #1 conducted initially at 0.2 Hz and test #3, conducted at 0.2 Hz following the 10 Hz test shown in Fig. 71.

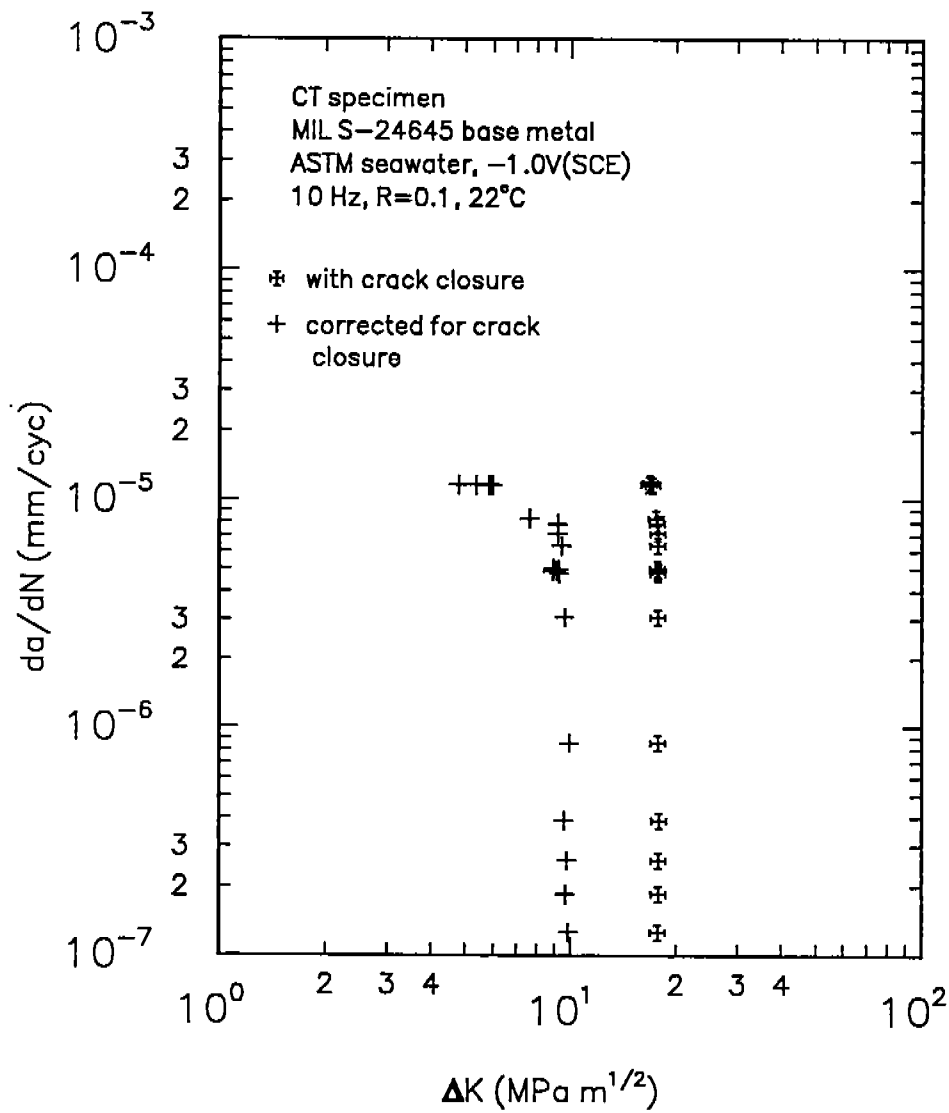


Figure 74. A comparison of near-threshold crack propagation data, before and after correction for crack closure, for MIL S-24645 base metal tested in ASTM seawater at -1.0 V (SCE) and at 10.0 Hz, following test #3 at 0.2 Hz as shown in Fig. 72. R = 0.1, 22 C.

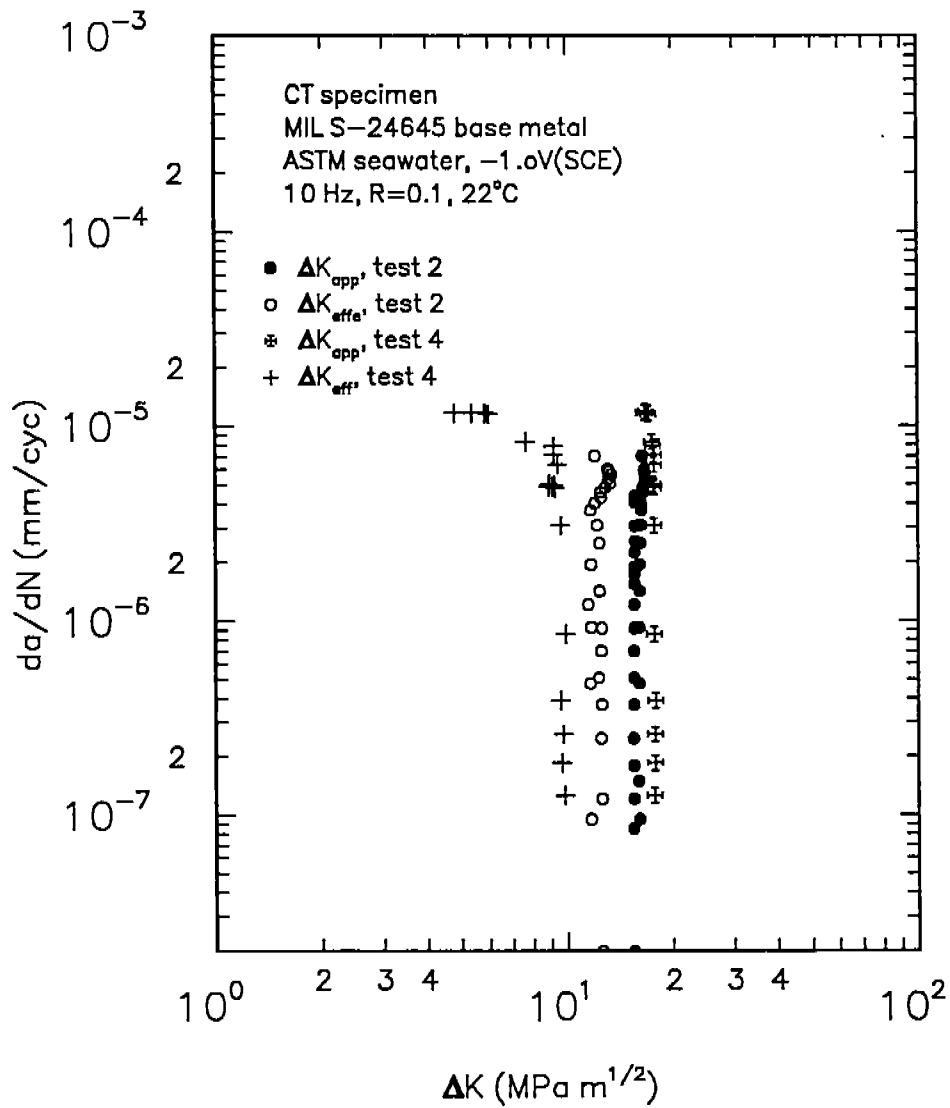


Figure 75. A comparison of the near-threshold crack propagation data for tests #2 and 4, before and after correction for crack closure, for MIL S-24645 base metal tested in ASTM seawater at -1.0 V (SCE) and at 10.0 Hz, following prior tests at 0.2 Hz. R = 0.1, 22 C.

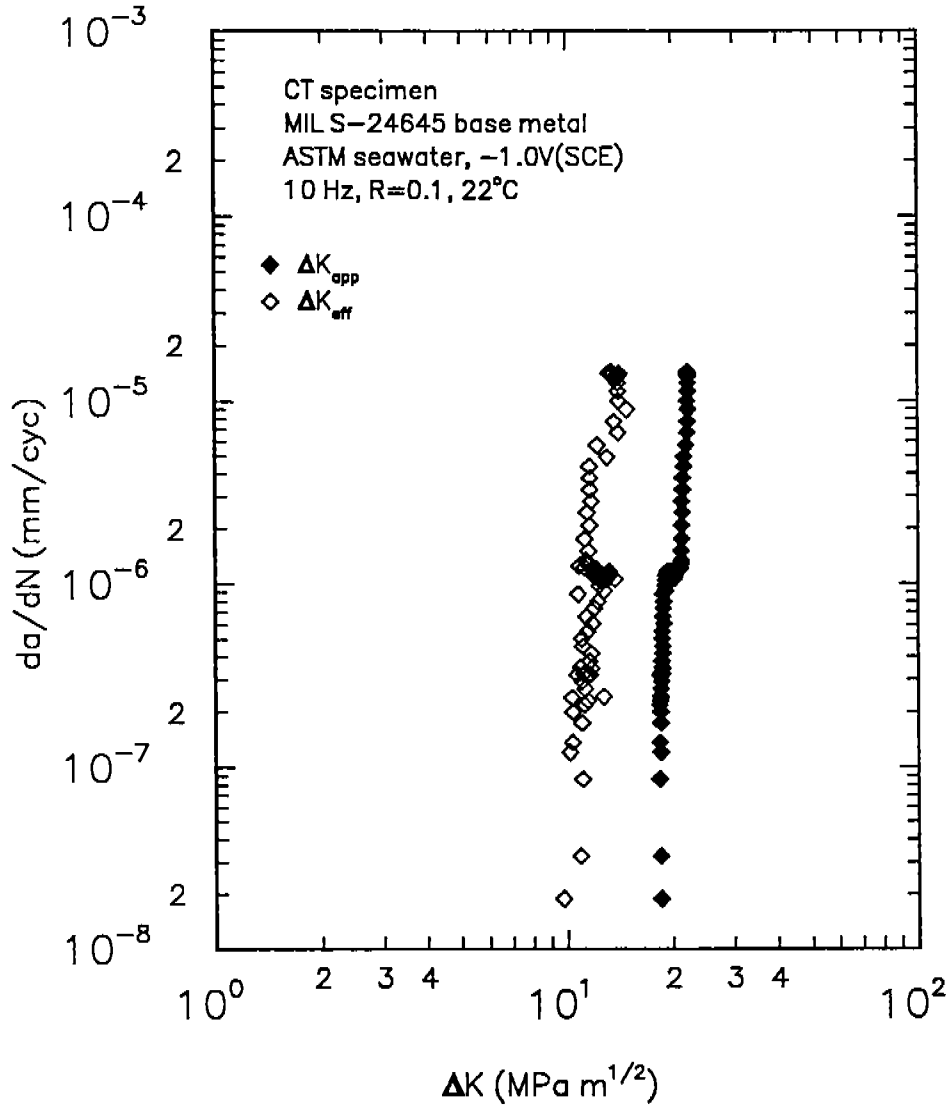


Figure 76. A comparison of near-threshold crack propagation data, before and after correction for crack closure, for MIL S-24645 base metal test #5 in ASTM seawater at -1.0 V (SCE) and at 10.0 Hz. The load was increased and then shed to threshold at 10 Hz following test #4 at 10 Hz (shown in Fig. 75). R = 0.1, 22 C.

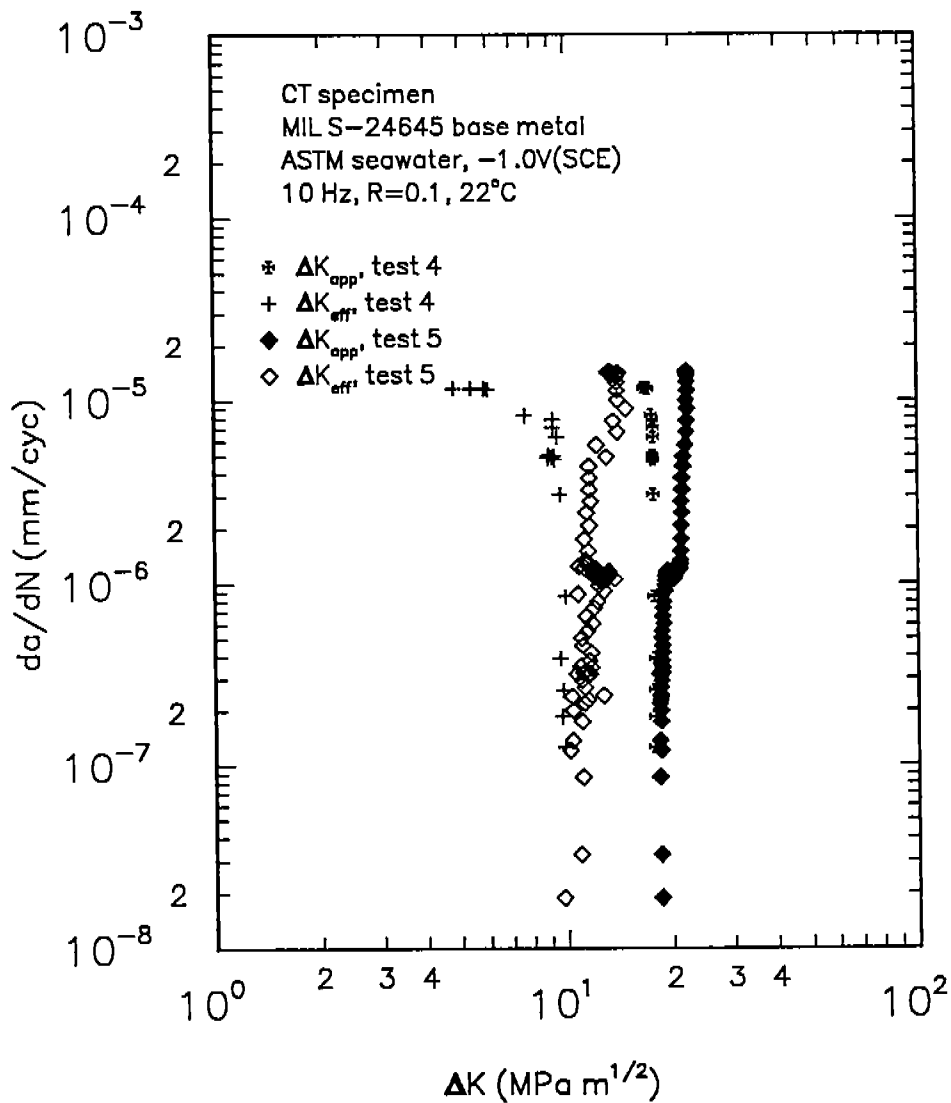


Figure 77. A comparison of the near-threshold crack propagation data for tests #4 and #5, before and after correction for crack closure, for MIL S-24645 base metal tested in ASTM seawater at -1.0 V (SCE) and at 10.0 Hz. R = 0.1, 22.

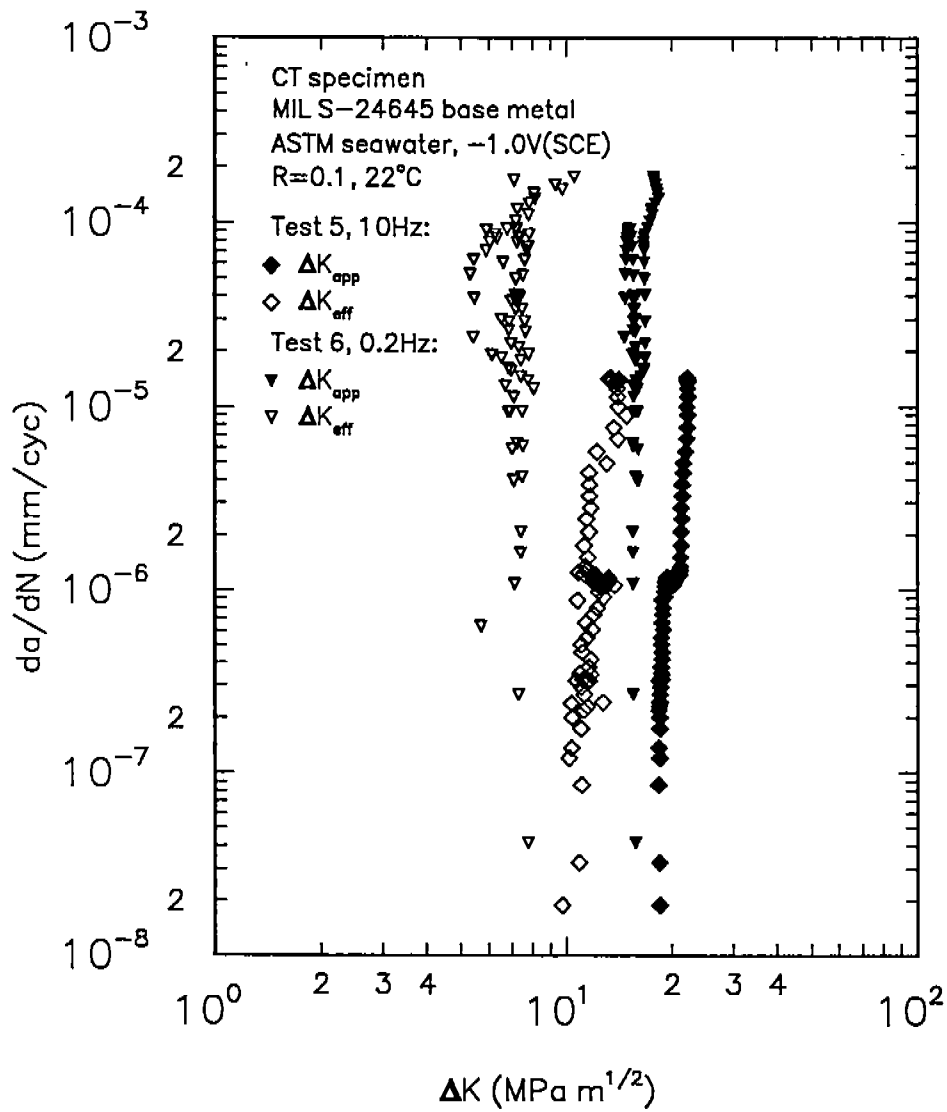


Figure 78. A comparison of near-threshold crack propagation data, before and after correction for crack closure, for MIL S-24645 base metal tested in ASTM seawater at -1.0 V (SCE) and at 10.0 Hz, R = 0.1, 22 C. Test #5 conducted at 10 Hz and test #6, conducted at 0.2 Hz with no increase in load following the 10 Hz test shown in Fig. 77.

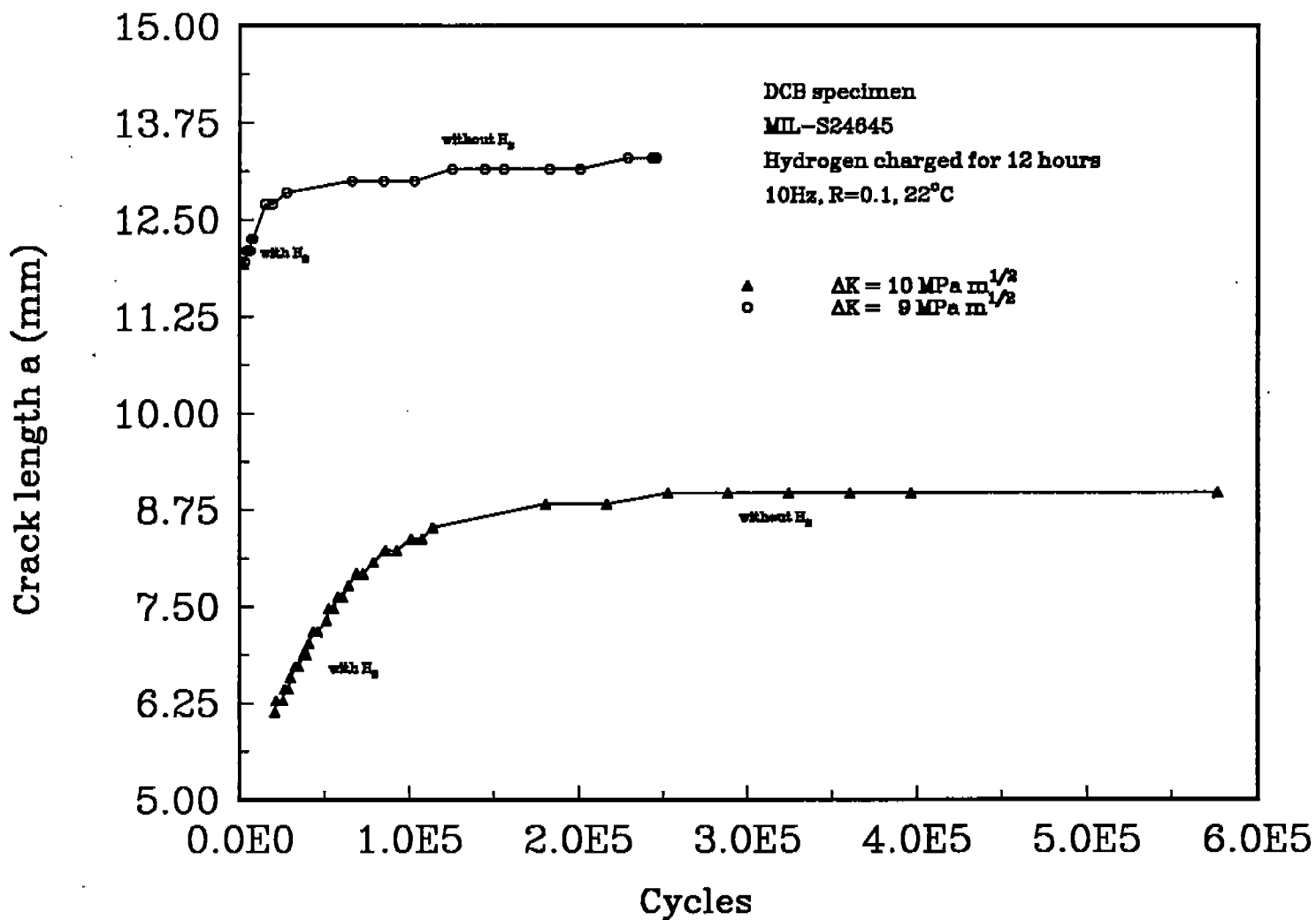


Figure 79. The effect of hydrogen charging on the crack growth rate for MIL-S24645 base metal tested at 10 Hz, R = 0.1, with 5N H₂SO₄ + 0.25 mg/liter As₂O₃ solution and in air.

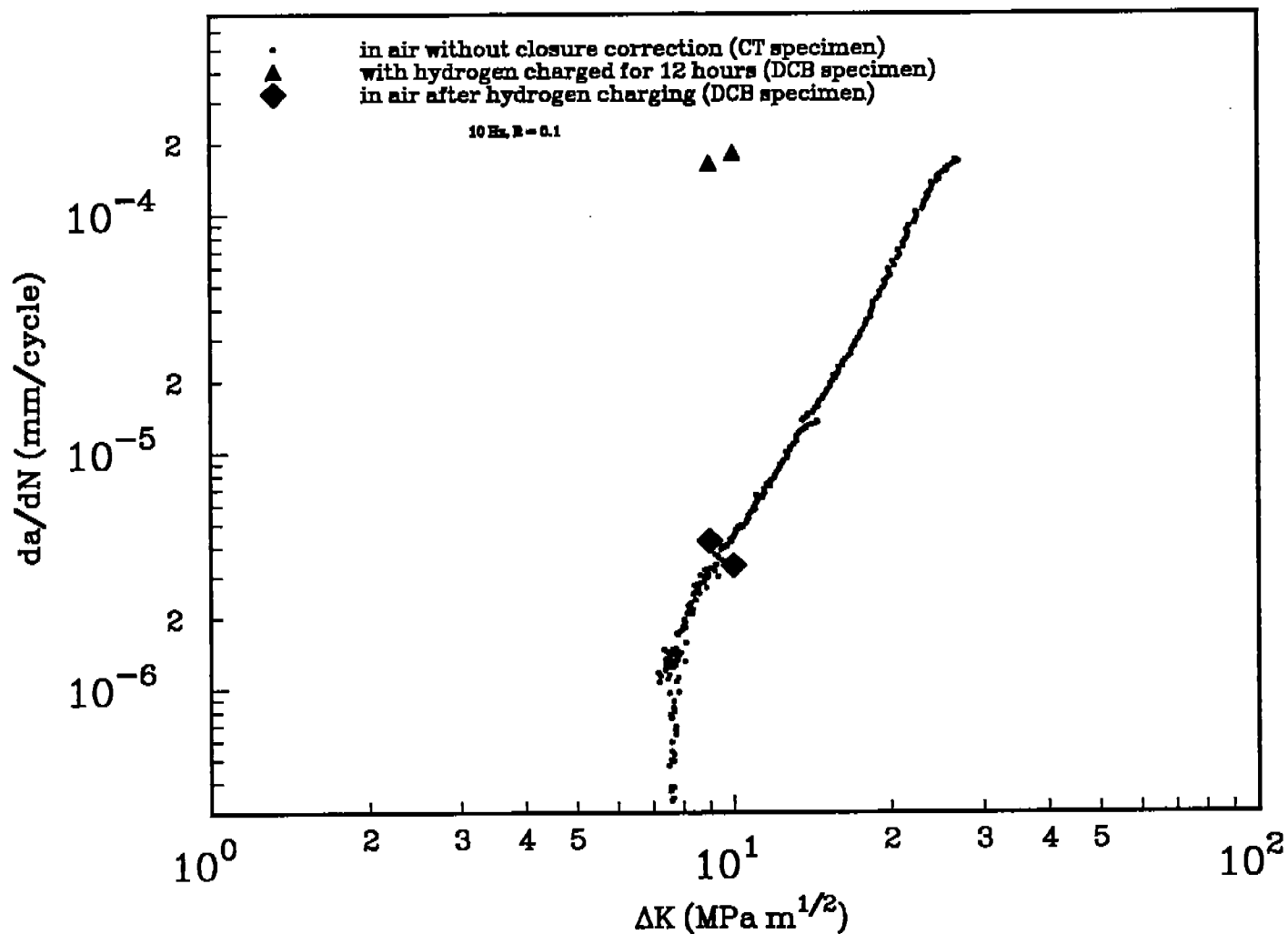


Figure 80. A comparison of the near-threshold crack propagation data for MIL-S 24645 base metal tested at 10 Hz, R = 0.1, in air and in 5N H₂SO₄ + 0.25 mg/liter As₂O₃ solution with an applied current density of 50 mA cm⁻².

APPENDIX I

A-130

A COMPARISON OF THE NEAR-THRESHOLD CORROSION FATIGUE CRACK PROPAGATION RATES IN MIL-S24645 HSLA STEEL AND ITS WELD METAL

J. A. Todd, L. Chen, H. Tao*, E. Y. Yankov and G. H. Reynolds⁺

Department of Metallurgical and Materials Engineering, Illinois Institute of Technology, Chicago, IL 60616, USA

* Atlas Testing Laboratories, Inc., 6929 E. Slauson Ave., Los Angeles, CA 90040, USA

+ MSNW, Inc., P. O. Box 865, San Marcos, CA 92069

ABSTRACT

Near-threshold corrosion fatigue crack propagation studies have been conducted using compact tension specimens of Mil-S24645 HSLA steel and a compatible weld metal in air, ASTM seawater at the free corrosion potential, and ASTM seawater with -1.0V (SCE) cathodic protection. Tests were conducted at 10 Hz and a stress ratio, $R = 0.1$. The weld metal exhibited slower crack growth rates and higher threshold stress intensity ranges in both air and seawater than the base metal. However, the weld metal itself exhibited similar behavior in air, seawater and under cathodic protection, giving a threshold stress intensity range of 11 to 14 MPa $m^{1/2}$. With the exception of the weld metal tested in air, after correction for crack closure, the effective threshold stress intensity range was reduced to 3.5 to 5.5 MPa $m^{1/2}$. Metal wedges, approximately 5 to 10 μm (1-2 grain sizes), which developed during the tests, were observed to contribute to crack closure in the -1.0V (SCE) cathodically protected specimens.

1.

INTRODUCTION

Precipitation strengthened, Cu-containing, high strength low alloy (HSLA) steels are currently being evaluated for ship plate and marine structural applications. These low carbon (0.05 w/o) steels are inexpensive, have corrosion behavior equivalent to or better than 1010 steel, are easily weldable and may not require a stress-relief treatment. In this paper MIL S-24645 base and weld metals are compared in order to determine whether the non-stress relieved condition is detrimental to the near-threshold corrosion fatigue crack propagation behavior.

Despite recent advances in our understanding of near-threshold behavior¹⁻⁴, relatively few studies have addressed the problem of crack closure in HSLA steels and welds exposed to marine environments at the free corrosion potential and with cathodic protection⁵⁻²¹. Due to the difficulties of testing in natural seawater, the majority of laboratory studies have used aqueous NaCl environments, where corrosion deposits may contribute to closure at the free corrosion potential. However, unlike the aqueous chloride environment, when a cathodic potential is applied in the marine environment two competing mechanisms may operate: (1) the formation of calcareous deposits (CaCO_3 and $\text{Mg}(\text{OH})_2$) which may retard near-threshold growth, and (2) hydrogen embrittlement which accelerates crack growth.²²⁻²⁷ For the welds there may be additional contributions to closure arising from residual stresses and/or microstructural changes.

This paper presents near-threshold corrosion fatigue crack propagation data for MIL-S24645 HSLA steel and a compatible strength weld metal tested in air, ASTM seawater at the free corrosion potential and ASTM seawater with -1.0V cathodic protection in order to compare the magnitudes of their near-threshold closure contributions and determine their effective stress intensity ranges.

2.

EXPERIMENTAL PROCEDURES

The materials tested in this study were MIL S-24645, Class 3, E/F quality, and ASTM A710 HSLA steels and a C-Mn-Ni weld metal. Their compositions and mechanical properties are listed in Tables I and II, respectively. Submerged arc welds (SAW) were prepared in plates of MIL S-24645 steel, 0.76 m in length and 0.019 m in thickness, according to the procedures listed in Table III. No stress relief treatment was given.

Near-threshold corrosion fatigue crack propagation tests were conducted on 12.7 mm thick compact tension (CT) specimens in the TL orientation using a MTS 880 servohydraulic test system equipped with a personal computer and Materials Analysis and Testing Environment (MATE)²⁸ software, developed in accordance with ASTM standard E647. Load shedding tests were performed under load control, at frequencies of 10 Hz and 0.2 Hz (sine wave), stress ratio, $R = 0.1$, in air, ASTM seawater at the free corrosion potential and ASTM seawater at $-0.8V$ and $-1.0V$ cathodic protection referenced to a saturated calomel electrode (SCE). The substitute seawater was prepared in accordance with ASTM standard D1141-90 with the composition given in Table IV, and was changed every three days for tests conducted with cathodic polarization and every day for tests at the free corrosion potential.

Specimens were fatigue pre-cracked in air at 20 Hz. Crack lengths were monitored by the compliance method, with extension arms supporting the clip gage above the liquid level for the tests in seawater, as described in reference 20. Crack closure loads were obtained from unloading data by comparing the average displacement deviations for a series of secondary windows with reference data collected from a region of the hysteresis loop where the data

displayed linear behavior. The closure load was taken as the load where the deviation error became greater than 0.25% of the displacement deviation range.

After reaching the threshold, the specimens tested in seawater were immediately removed, gently immersed in alcohol, dried and then placed in a vacuum. The cracks were then carefully infiltrated with epoxy and sealed on the sides. The samples were sectioned through the midplane, polished and etched with 3% nital, in order to observe the fracture path at the center of the specimen by optical and scanning electron microscopy (SEM).

3.

RESULTS

Figure 1 compares data for the base plate tested at 10 Hz in air, ASTM seawater at the free corrosion potential, and ASTM seawater with -1.0V (SCE) cathodic protection. The base plate exhibited higher crack growth rates in seawater than in air and a lower threshold stress intensity range, ΔK_{th} , of 6.5 MPa m^{1/2} compared to a value of 7.5 MPa m^{1/2} for the test in air. The application of -1.0V (SCE) resulted in an increase of ΔK_{th} to 11.5 MPa m^{1/2}. However, when the contributions due to crack closure were subtracted, Figure 2 shows that the effective stress intensity ranges, ($\Delta K_{eff,th}$), gave similar values of $\Delta K_{eff,th} = 5.5$ MPa m^{1/2} in air and 5.0 MPa m^{1/2} in seawater at -1.0V (SCE).

Figure 3 presents data for the weld metal tested in air, ASTM seawater at the free corrosion potential, -0.8V (SCE) and -1.0V (SCE). ΔK_{th} was found to be 11 MPa m^{1/2} at the free corrosion potential, 12.8 MPa m^{1/2} in ASTM seawater at -0.8V (SCE) and 14-14.5 MPa m^{1/2} in air and -1.0V (SCE) in seawater. After correction for crack closure the values of $\Delta K_{eff,th}$ were in the range 3.5 to 5.5 MPa m^{1/2}, with the exception of the test conducted in air, which gave a value of 9 MPa M^{1/2} and appeared not to have reached a steady threshold value at da/dN = 6

$\times 10^{-7}$ mm/cycle. Figure 4 compares the data for the base and weld metals in air and ASTM seawater and shows that, before correction for crack closure, the apparent crack propagation rates for the weld metal in both air and ASTM seawater were significantly slower than for the base metal. Similarly, the apparent crack propagation rates in the cathodically protected weld metal are slower than those for the base metal at -1.0V (SCE), as shown in Fig. 5. It is interesting to note that although similar apparent threshold values were observed for the weld metal at -0.8V and -1.0V (SCE) the near-threshold crack propagation rates were slightly slower in the -0.8V (SCE) cathodically protected specimen.

Figure 6 compares data for the base metal tested in seawater at frequencies of 10 Hz, 2 Hz and 0.2 Hz, respectively. The apparent ΔK_{th} range increased from 6.5 MPa $m^{1/2}$ at 10 Hz to 7 MPa $m^{1/2}$ at 2 Hz and to 8.5 MPa $m^{1/2}$ at 0.2 Hz, where the crack stopped at 7×10^{-7} mm/cycle. The load was then increased and crack propagation initially resumed and then stopped with the lowest growth rate of 4×10^{-7} mm/cycle being recorded at an apparent threshold value of 9.5 MPa $m^{1/2}$. After correction for crack closure, similar values of $\Delta K_{eff,th}$ (4.5 and 5.0 MPa $m^{1/2}$, respectively) were obtained for 2 Hz and 0.2 Hz.

A summary of the threshold data collected in this study is presented in Table V.

4.

DISCUSSION

Mechanisms contributing to near-threshold corrosion fatigue crack propagation in ferritic steels exposed to marine environments include: (1) the corrosion or dissolution of Fe; (2) hydrogen uptake from the corrosion process or cathodic protection; and (3) precipitation of heavy soluble compounds (corrosion products, calcareous deposits, etc.) in the crack.²⁹⁻³² The first two reactions accelerate crack growth while the latter retards crack growth. These reactions

depend on the crack tip electrochemistry; the externally applied potential; and mechanical variables such as the stress amplitude, ΔK , stress ratio and frequency. For the stress ratio, $R = 0.1$, used in this study, closure contributions from oxide films in air; corrosion products in the marine environment; calcareous deposits and/or metal particles under cathodic protection and weld residual stresses may also retard near-threshold growth. These contributions are discussed in further detail below.

Characteristic markings, arising from fretting oxidation, were observed on the fracture surfaces of the specimens tested in air, as reported by Ritchie³³. Such films have been shown by Suresh et al.³⁴ to produce a closure contribution to the near-threshold growth of pressure vessel steels tested in moist air, and they also account for the small shift in threshold stress intensity range, ($\Delta K_{th} - \Delta K_{eff,th} = 2 \text{ MPa m}^{1/2}$) observed for the base metal tests in air at 10 Hz.

Extensive corrosion products were observed on the fracture surfaces of both base plate and weld metal tested in ASTM seawater at the free corrosion potential. For both materials the apparent threshold stress intensity range was slightly lower ($\sim 1\text{-}3 \text{ MPa m}^{1/2}$) for the tests in seawater than those in air. After correction for closure, the threshold stress intensity ranges for the weld metal were reduced by $5 \text{ MPa m}^{1/2}$ and $7 \text{ MPa m}^{1/2}$ for the tests in air and seawater, respectively, indicating that the corrosion products gave a larger contribution to closure than the oxide films in air.

The contribution of corrosion products to crack closure is demonstrated further in Fig. 7. Test #2 shows near-threshold data collected for the weld metal in seawater at -1.0V (SCE). In test #1, the specimen was anodically polarized at $+1.0\text{V}$ (SCE) for 10 minutes, giving extensive corrosion at the beginning of the test, before the polarization was reversed to -1.0V

(SCE) and the test continued. The apparent threshold stress intensity, ΔK_{th} , increased from 15 MPa m^{1/2} for test #2 to 18 MPa m^{1/2} for test #1 (+1.0V SCE). After correction for closure, the threshold stress intensity ranges were reduced by 10.5 MPa m^{1/2} (test #2) and 12.5 MPa m^{1/2} (test #1) again indicating that corrosion products in the wake of the crack contribute significantly to crack closure. It should be noted that the effective threshold stress intensity ranges are very close, i.e. 5.5 MPa m^{1/2} and 4.5 MPa m^{1/2} for tests #1 and #2, respectively.

The contribution of corrosion products to crack closure is shown to be time dependent in Fig. 6, where a higher apparent threshold stress intensity is observed at 0.2 Hz than at 10 Hz. The shift in threshold stress intensity range ($\Delta K_{th} - \Delta K_{eff,th}$) increased from 2.5 MPa m^{1/2} to 3.5 MPa m^{1/2} as the frequency was decreased from 2 Hz to 0.2 Hz and then to 5 MPa m^{1/2} when the load was increased at 0.2 Hz. Closure built up very rapidly as the threshold was approached at 0.2 Hz and the crack stopped as it became wedged open.

When the specimens were tested at 2 Hz and -1.0V (SCE), Todd et al.²⁷ reported that metal wedges, induced by hydrogen embrittlement and approximately 5 to 10 μm in diameter (1-2 grain sizes), could be found along the crack wake. Similar observations were made in the present study at 10 Hz for both base and weld metals as shown in Figs. 8a and 8b for the base metal. Figure 8a shows the crack tip (observed along the specimen center line) for the base metal tested in ASTM seawater at -1.0V (SCE) and 10 Hz. The microstructure contains ferrite and pearlite and both intergranular and transgranular fracture can be observed. Figure 8b shows a higher magnification view of the region labelled A in Fig. 8a. It can be seen that the crack has propagated around the ferrite grain boundaries leaving metal grains, (3 to 8 μm in size) which are still cathodically protected to contribute to closure in the crack wake. The observed

grain size is well above the maximum pulsating crack tip opening displacement, calculated as $0.53 \mu\text{m}$ following the method used by Suresh et al.³⁴ Energy dispersive X-ray spectroscopy (EDS) was conducted on the crack surface but no evidence of calcareous deposit formation was found. As optical and scanning electron microscopy observations also produced no evidence of surface films, it was concluded that the metal wedges alone could account for the closure at -1.0V (SCE).

Neither metal wedges nor calcareous deposits were observed in the specimen tested at -0.8V (SCE) in ASTM seawater and, to date, no satisfactory explanation has been found for the slightly slower near-threshold corrosion fatigue crack propagation rates at -0.8V (SCE) compared to -1.0V (SCE).

The slower near-threshold corrosion fatigue crack propagation rates and greater degree of closure observed for the weld compared to the base metal specimens agrees well with data in the literature.^{7,8,35-38} For compact tension specimens of ASTM A710 HSLA-80 steel, notched in the heat affected zone and tested in air in the mid-growth regime at $R = 0.1$ and $\nu = 5$ Hz, Link³⁵ observed that closure loads were initially greater than 80% of the maximum load and decreased to 40% of P_{max} as the crack extended. These observations were found to be consistent with the presence of crack closure resulting from the redistribution of weldment residual stresses due to machining of the specimen notch and through crack propagation.^{36,39-41}

In the present near-threshold study, closure loads were also significantly higher in the weld metal than in the base metal at the beginning of the test. However, it is interesting to compare the data for base and weld metals tested in seawater at -1.0V SCE. $K_{\text{cl}}/K_{\text{max}}$ was initially 0.5 in the weld metal and increased to 0.75 at threshold as the load was shed, whereas

K_{cl}/K_{max} was initially 0.1 in the base metal and increased slowly at first and then rapidly to 0.6 as the threshold was approached. Despite these differences, after correction for crack closure, the values of $\Delta K_{eff,th}$ were similar: 5 MPa m^{1/2} for the base metal and 4.5 MPa m^{1/2} for the weld metal.

Several factors may contribute to closure in the weld metal specimens tested in ASTM seawater at -1.0V (SCE): microstructural changes, metal wedges and residual stresses. The strength levels and ferrite grain sizes (5 - 10 μ m) were similar for both weld and base metal and metal wedges were present in both samples. Tests are now in progress to determine whether a stress relief treatment will restore crack propagation rates and threshold values comparable to those of the base plate in the weld metal as demonstrated by Link³⁵ for the HSLA-80 steel in the mid-growth regime.

5. CONCLUSIONS

1. With the exception of the weld metal tested in air at 10 Hz, the effective threshold stress intensity range, $\Delta K_{eff,th}$, determined after correction for crack closure lies in the range of 3.5 to 5.5 MPa m^{1/2} for both base and weld metals, irrespective of frequency or test conditions.
2. Oxide films and corrosion products contributed to crack closure for the tests in air and seawater at the free corrosion potential, respectively.
3. The applied threshold stress intensity range, ΔK_{th} , increased with decreasing frequency in ASTM seawater at the free corrosion potential from 6.5 MPa m^{1/2} at 10 Hz to 8.5-9.5 MPa m^{1/2} at 0.2 Hz.

The application of cathodic protection resulted in the formation of metal bridges (approximately 100 micrometers in size) in the wake of the crack, contributing to crack closure in both base and weld metal.

5. The weld metal has a lower applied stress intensity range, ΔK_{th} , than, but similar values of effective stress intensity range, $\Delta K_{eff,th}$ to the base metal at 10 Hz and this is attributed to the presence of metal bridges.

ACKNOWLEDGEMENTS

This work was supported by the Naval Sea Systems Command under Contract No. N00012-88-C-1003 through a sub-contract from MSNW Inc. The authors gratefully acknowledge this support.

REFERENCES

1. R. P. Gangloff: "Corrosion Fatigue Crack Propagation in Metals", NASA Report 4301, 1990.
2. "Mechanics of Fatigue Crack Closure", eds. J. C. Newman, Jr and W. Elber, ASTM STP 982, ASTM, Philadelphia, PA, 1988.
3. "Current Research on Fatigue Cracks," eds. T. Tanaka, M. Jono and K. Komai, Current Japanese Materials Research, Vol. I, Elsevier, N.Y., 1987.
4. "Fracture Mechanics; Perspectives and Directions," eds. R. P. Wei and R. P. Gangloff, ASTM STP 1020, ASTM, Philadelphia, PA, 1989.
5. Y. Itoh, S. Suruga and H. Kashiwaya: "Prediction of Fatigue Crack Growth Rate in Welding Residual Stress Field," Engineering Fracture Mechanics, vol 33, 3, 1989, pp. 397-407.
6. H. -J. Spies, G. Pusch, C. Henkel and K. Roessler: "Theoretical and Applied Fracture Mechanics", Vol. 11, 2, 1989, pp. 121-5.
7. R. W. Chang, Y. G. Kweon and C. B. Lim: "Influence of the Welding Heat Input on Fatigue Crack Growth in Offshore Structural Steel Welds," in Proc. Eighth Internat. Conf. on Offshore Mechanics and Arctic Engineering, ASME, N.Y., pp.419-30.
8. L. R. Link, "Fatigue Crack Growth of Weldments," ASTM STP 1058, ASTM, Philadelphia, PA, 1990, pp. 16-33.
9. Ki J. Kang, Ji H. Song and Y. Youn: "Fatigue Crack Growth and Closure Behavior through a Compressive Residual Stress Field," Fatigue and Fracture of Engineering Materials and Structures, Vol. 13, 1, 1990, pp. 1-13.
10. G. S. Booth and J. G. Wylde. Metals Science. 1977, 11, 308.

11. P. W. Marshall. Welding Res. Council Bull., April 1974, No. 193.
12. P. W. Marshall. Proc. National Water Resources Ocean Engineering Convention. ASCE, San Diego, CA. April 1976.
13. T. G. Gooch and G. S. Booth: "Corrosion Fatigue of Offshore Structures", Metal Science, 1979, 13, 7, pp. 402-410.
14. J. W. Cochera, J. P. Tralmer and P. W. Marshall. Fatigue of Structural Steels for Offshore Platforms, Paper OTC 2604, 1976 Offshore Technology Conference. Houston, May 1969.
15. F. E. Havens and D. M. Bench, Fatigue Strength of Quenched and Tempered Carbon Steel Plates and Welded Joints in Sea Water. Paper OTC 1046, 1969, Offshore Technology Conference, Houston, May 1969.
16. K. J. Marsh, T. Martin and J. McGregor. The Effect of Random Loading and Corrosive Environment on the Fatigue Strength of Fillet-Welded Lap Joints. NEL Report 587, National Engineering Laboratory, East Kilbride, Glasgow, Feb. 1975.
17. J. C. Walter, E. Olbjorn, O. Allstad and G. Elde. Safety Against Corrosion Fatigue Offshore. Publication No;. 94;, Det Norske Ventas, Horik, Norway, April 1976.
18. C. E. Jaske, D. Broek, J. E. Slater, W. E. Anderson. Corrosion Fatigue of Structural Steels in Seawater and for Offshore Application. Corrosion Fatigue Technology. ASTM STP 642, 1978, pp. 19-47.
19. Corrosion Fatigue of Welded Steel in Seawater. Florida Sea Grant Program, 1984.
20. G. H. Reynolds and J. A. Todd: Threshold Corrosion Fatigue of Welded Shipbuilding Steels, Final Report-Phases I Program, US Navy Report, Contract No. N00024-88-C-5708, 1989.

21. K. Komai: "Corrosion-Fatigue Crack Growth Retardation and Enhancement in Structural Steels," in "Current Research on Fatigue Cracks," eds. T. Tanaka, M. Jono and K. Komai, Current Japanese Materials Research, Vol. I, Elsevier, N.Y., 1987, pp. 267-289.
22. R. P. Gangloff: "Inhibition of Aqueous Chlorides Corrosion Fatigue by Control of Crack Hydrogen Production," in Critical Issues in Reducing the Corrosion of Steels, H. Leidheiser Jr. and S. Haruyama, eds, JSPPS/NSF, Tokyo, 1985.
23. W. H. Hartt and W. Y. Mao: NACE Paper 317, Boston, March 25-29, 1985.
24. K. M. Kunjapur, W. H. Hartt and S. W. Smith Jr.: NACE Paper 316, Boston, March 25-29, 1985.
25. W. C. Hooper and W. H. Hartt, Corrosion Journal, 34, 1978, p. 320.
26. W. H. Hartt and W. C. Hooper: Corrosion Journal, 36, 107, 1980.
27. J. A. Todd, P. Li, G. Liu and V. Raman: Scripta Metall., 22, 745, 1988.
28. University of Dayton Research Institute, Dayton, Ohio.
29. E. Maahn: Crack Tip Chemistry under Cathodic Protection and its Influence on Fatigue Crack Growth, CANMET, Energy, Mines and Resources Canada, 555 Booth St., Ottawa, Canada, K1A 0G1, 1986.
30. D. J. Duquette. Environmental Effects I. General Fatigue Resistance and Crack Nucleation in Metals and Alloys. Fatigue and Microstructure. ASM 1978, pp. 335-363.
31. H. C. Marcus. Environmental Effects II. Fatigue Crack Growth in Metals and Alloys, Fatigue and Microstructure. ASM pp. 365-383.
32. R. W. Staehle. A Point of View Concerning Mechanisms of Environment Sensitive Cracking of Engineering Materials, in Mechanisms of Environment Sensitive Cracking of Materials, Eds. P. R. Swann, F. P. Ford, A. R. C. Westwood. 1977, pp. 574-601.

33. R. O. Ritchie: "Near-Threshold Fatigue Crack Propagation in Steels," *International Metals Reviews*, 5 and 6, 1979, pp. 205-30.
34. S. Suresh, G. F. Zamiski and R. O. Ritchie, *Metall. Trans. A*, 12A, 1981, p. 1435.
35. L. R. Link: Fatigue Crack Growth of 5456-H116 Aluminum and HSLA-80 Weldments, US Navy Report, DTRC/SME-88-39, 1988.
36. D. A. Davis and E. J. Czyryca: "Corrosion Fatigue Crack-Growth Behavior of HY-130 Steel and Weldments," *Trans. ASME*, 103, 314, 1981.
37. M. Beghini and L. Bertini: "Fatigue Crack Propagation Through Residual Stress Fields with Closure Phenomena," *Engineering Fracture mechanics*, 36, 3, 1990, pp. 379-87.
38. Y. W. Shi, B. Y. Chen and J. X. Zhang: "Effects of Welding Residual Stresses on Fatigue Crack Growth Behavior in Butt Welds of a Pipeline Steel," *Engineering Fracture mechanics*, 36, 6, 1990, pp. 893-902.
39. D. A. Davis and E. J. Czyryca: "Corrosion-Fatigue Crack Growth Characteristics of Several HY-100 Steel Weldments with Cathodic Protection," in *Corrosion Fatigue: Mechanics, Metallurgy, Electrochemistry and Engineering*, eds. T. W. Crooker and B. N. Leis, ASTM STP 801, 1983, pp. 175-96.
40. G. E. Nordmark, L. N. Muller and R. A. Kelsey: "Effect of Residual Stresses on Fatigue Crack Growth Rates in Weldments of Aluminum Alloy 5456 Plate," in *Residual Stress Effects in Fatigue*, ASTM STP 776, ASTM, 44, 1982.
41. J. H. Underwood, L. P. Pook and J. K. Sharples, "Fatigue-Crack Propagation Through a Measured Residual Stress Field in Alloy Steel,": in *Flaw Growth and Fracture*, ASTM STP 631, 1977, pp. 402-15.

TABLE I: Compositions of MIL S-24645 Steel and Weld Metal

Material	C	Mn	P	S	Cu	Si	Ni	Cr	Mo	V	Ti	Al	Cb	Sb	As
MIL S-24645	.05	.50	.010	.002	1.17	.35	1.00	.72	.23	.003	.005	.018	.032	.003	.004
ASTM A710	.04	.58	.010	.004	1.18	.28	.76	.85	.21	-	-	-	.042	-	-
Weld metal	.03	1.40	.013	.011	0.14	.39	1.74	.14	.33	-	-	-	-	-	-

TABLE II: Mechanical Properties of MIL S-24645 Steel and Weld Metal

Material	σ_Y (ksi)	σ_{UTS} (ksi)	% ϵ	%RA	Impact Properties (0 F) (J)
MIL S-24645*	TX 83	92	36	67.8	176
Class 3	BX 80	89	26	81.0	231
	TL				204
	BL				250
ASTM A710+					
Class 3	89	101	35	77.0	50 (-80F)
Weld Metal	TL 86	110	26	71.3	94

*austenitized at 1660 F (904 C) for 108 minutes, water quenched, precipitation hardened at 1160 F (627 C) for 62 minutes and water quenched.

+austenitized at 1650 F (899 C) for 30 minutes, water quenched, precipitation hardened at 1100 F (598 C) for 30 minutes and furnace cooled.

Table III: Submerged Arc Weld Procedures

Joint Configuration:

Weld Length:	0.66 m
Electrode:	2.36 x 10 ⁻³ m D., Linde 95 MIL 100S-1
Electrode Extension:	0.038 m
Flux:	Oerlikon OP 121TT
Flux Depth:	1.91 x 10 ⁻² m
Preheat:	None
Interpass Temperature:	93 C
Voltage:	33V DCRP
Amperage:	350 A
Travel Speed:	5.4 x 10 ⁻³ m s ⁻¹
Heat Input:	2110 KJ m ⁻¹
Number of passes:	10

Table IV: Chemical Composition of ASTM Substitute Seawater

NaCl	24.53	g/l
MgCl ₂	5.20	g/l
Na ₂ SO ₄	4.09	g/l
CaCl ₂	1.16	g/l
KCl	0.695	g/l
NaHCO ₃	0.201	g/l
KBr	0.101	g/l
H ₃ BO ₃	0.027	g/l
SrCl ₂	0.025	g/l
NaF	0.003	g/l

Chlorinity = 19.38; pH = 8.2

TABLE V: Summary of Test Results

Specimen	Condition	Frequency (Hz)	ΔK_{th} Range (MPa m ^{1/2})	$\Delta K_{eff,th}$ Range (MPa m ^{1/2})	Comments
Mil-S 24645	Air	10	10.0	-	
Mil-S 24645	Air	10	7.5	5.5	
Mil-S 24645	Seawater	10	6.5	-	
Mil-S 24645	Seawater, -0.8V	10	6.5	-	
Mil-S 24645	Seawater, -1.0V	10	6.5	-	
Mil-S 24645	Seawater, -1.0V	10	11.5	5.0	
ASTM A710	Seawater	2.0	7.0	4.5	
Mil-S 24645	Seawater	0.2	8.5	5.0	crack stopped
Mil-S 24645	Seawater	0.2	9.5	4.5	load increased
Weld	Air	10	14.0	9.0	
Weld	Seawater	10	11.0	4.0	
Weld	Seawater, -0.8V	10	12.8	3.5	
Weld	Seawater, -1.0V	10	14.5	4.5	
Weld	Seawater, -1.0V	10	18.0	5.5	+1.0V (SCE) extensive corrosion before cathodic protection

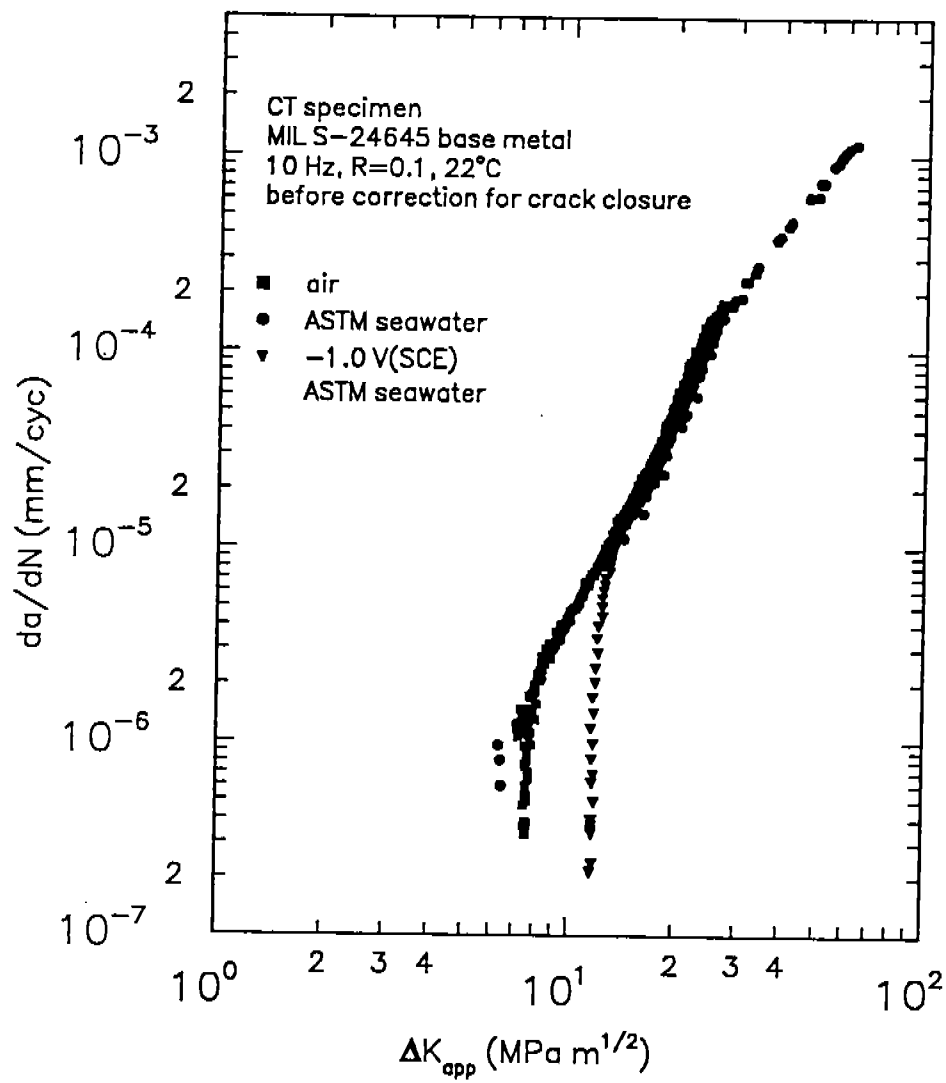


Figure 1. A comparison of near-threshold crack propagation data for MIL S-24645 base metal tested at 10Hz, R=0.1, in air, ASTM seawater at the free corrosion potential and at -1.0V (SCE).

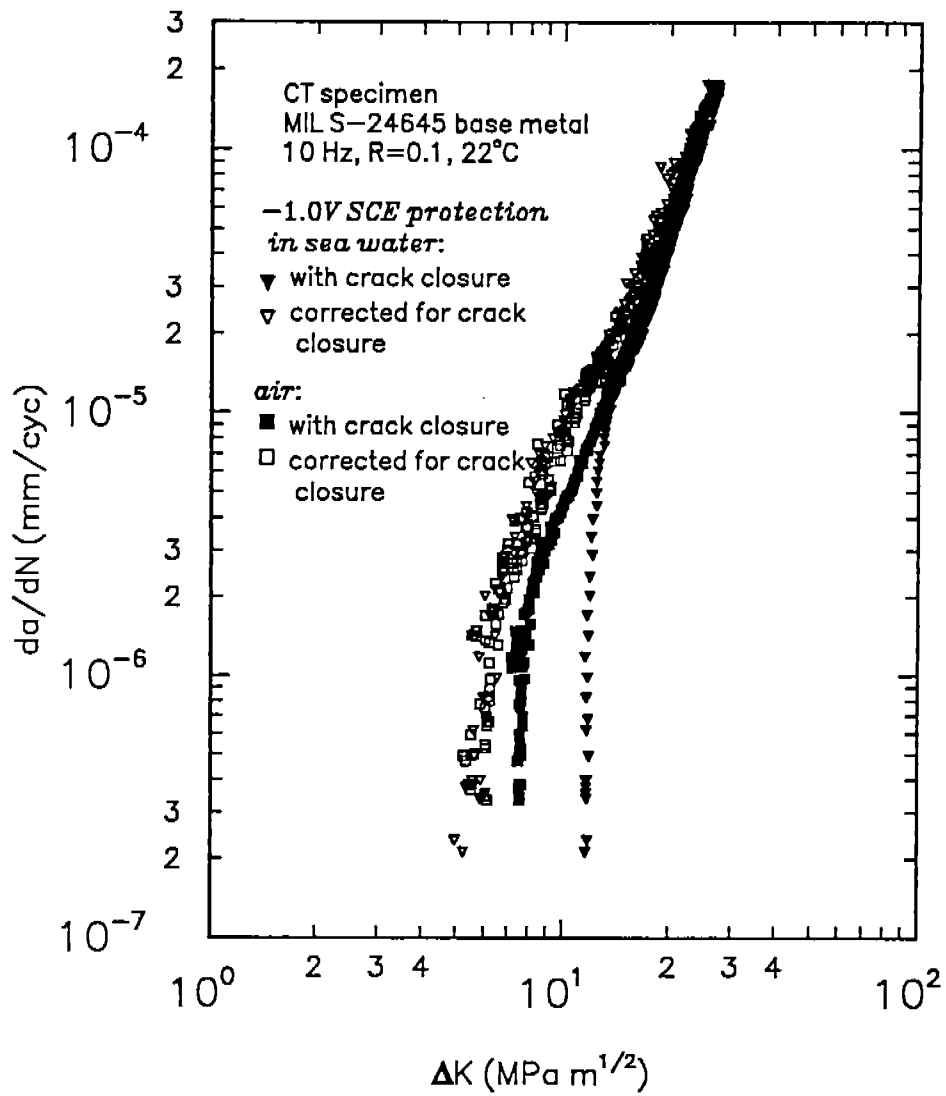


Figure 2. Near-threshold corrosion fatigue crack propagation data, before (closed symbols) and after (open symbols) correction for crack closure for MIL S-24645 base metal tested in air and seawater at -1.0V SCE.

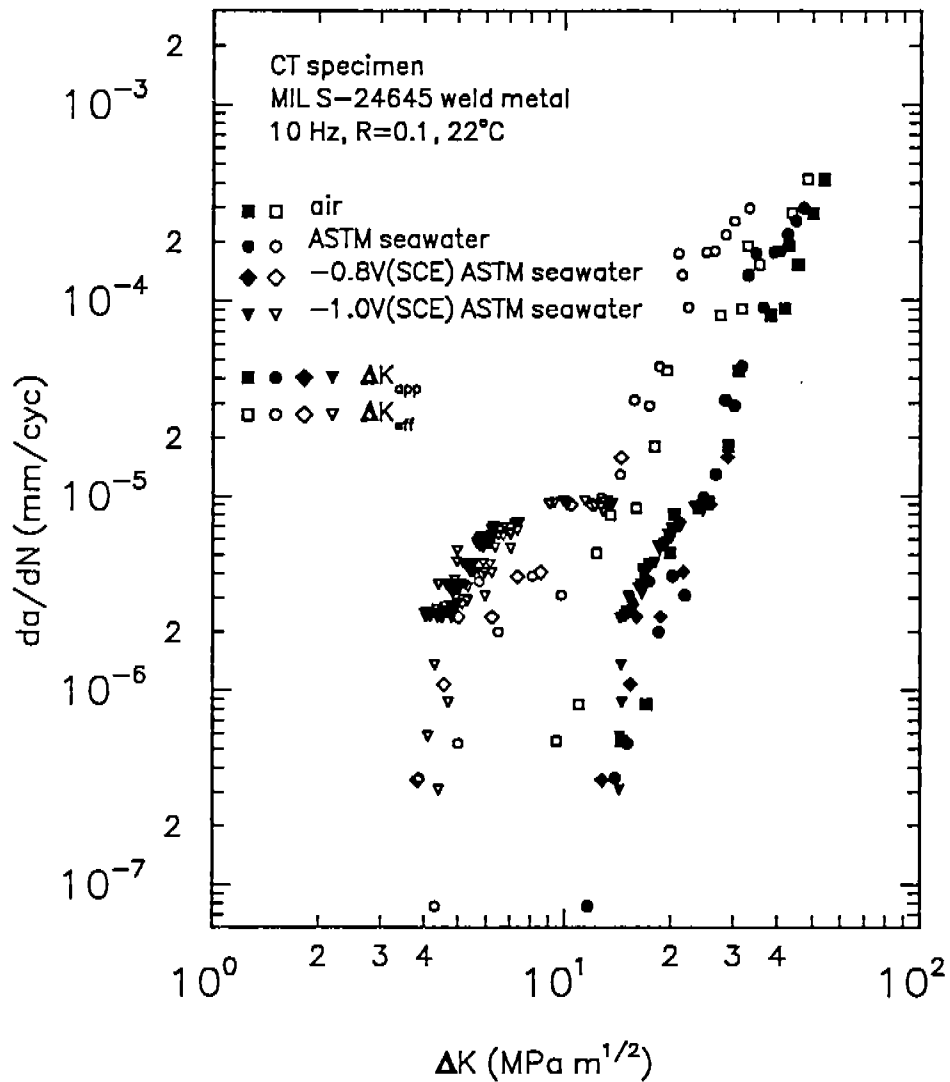


Figure 3. Comparison between the near-threshold crack propagation data, before and after correction for crack closure, for the weld metal tested in air, ASTM seawater at free corrosion potential, and ASTM seawater at -0.8V (SCE) and -1.0V (SCE). 10Hz, R=0.1, 22 C.

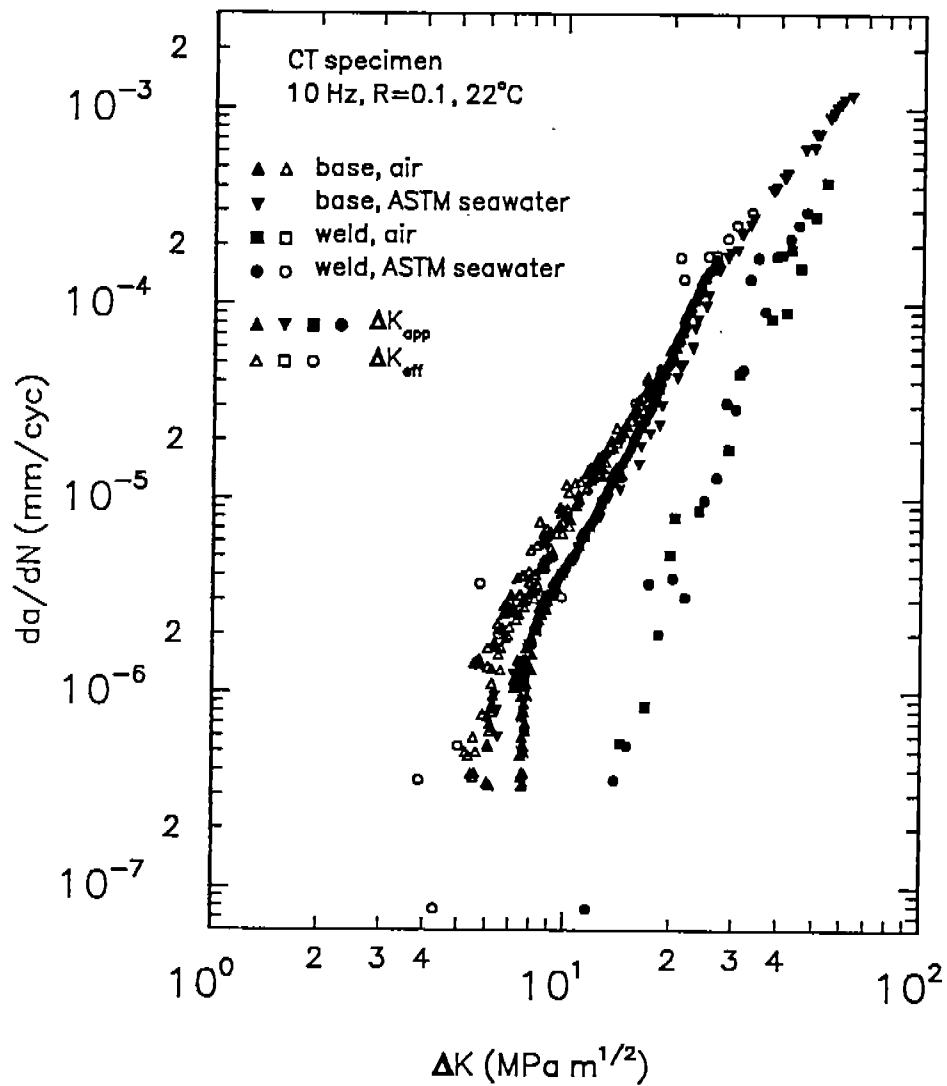


Figure 4. Comparison between the near-threshold crack propagation data, before and after correction for crack closure for MIL S-24645 base and weld metals in air and ASTM seawater at the free corrosion potential. 10Hz, R=0.1, 22 C.

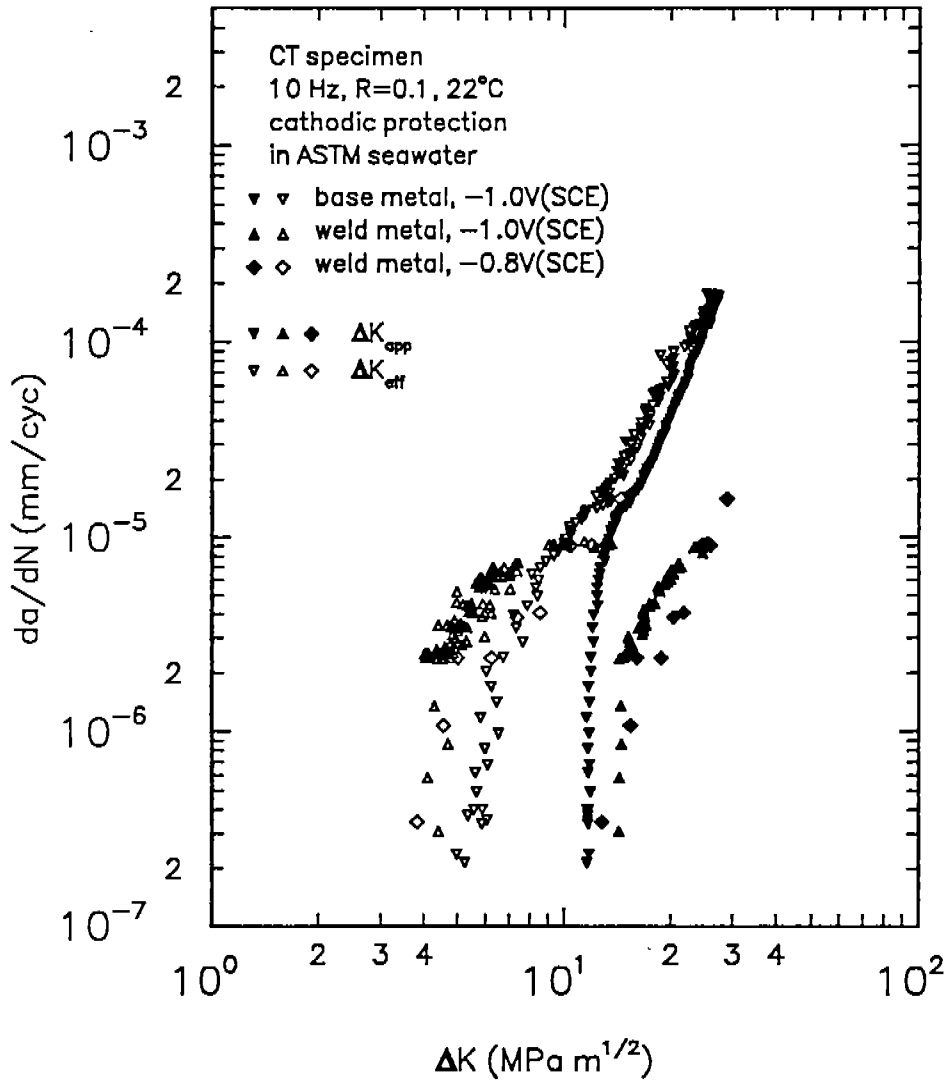


Figure 5. Comparison between the near-threshold fatigue crack propagation data, before and after correction for crack closure, for MIL S-24645 base and weld metals in ASTM seawater at -0.8V SCE and -1.0V SCE. 10Hz, R=0.1, 22 C

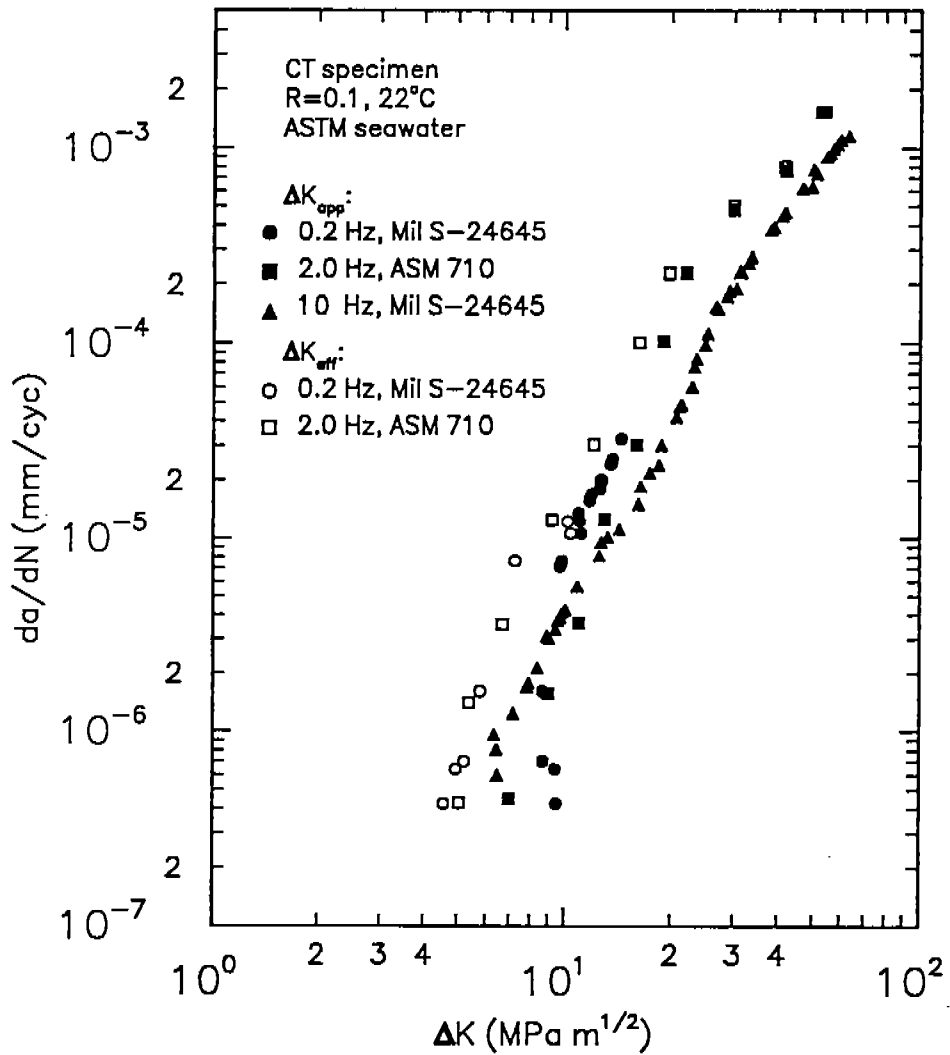


Figure 6. A comparison of the near-threshold corrosion fatigue crack propagation data for MIL S-24645 and ASM 710 base metals tested in ASTM seawater at the free corrosion potential and frequencies of 10, 2 and 0.2 Hz, R=0.1, 22 C

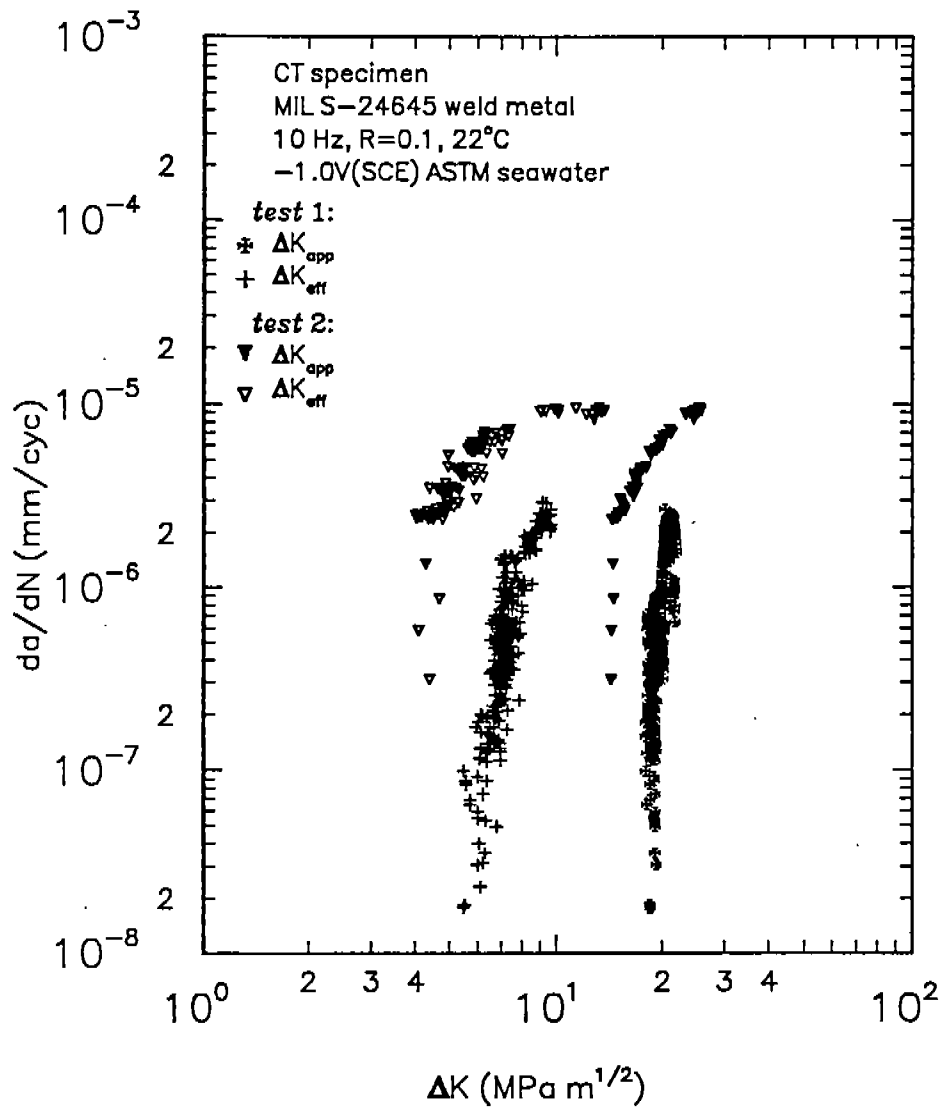


Figure 7. A comparison of near-threshold fatigue propagation data between test 1, weld metal anodically polarized to +1.0V (SCE) for 10 minutes prior to testing at -1.0V (SCE), and test 2, weld metal protected with -1.0V (SCE), in seawater, before and after correction for crack closure. 10Hz, R=0.1, 22 C.



Figure 8a. Optical micrograph of the crack tip in Mil S-24645 base metal tested in ASTM seawater with -1.0V (SCE) protection at 10Hz, R=0.1, etched in 3% Nital.

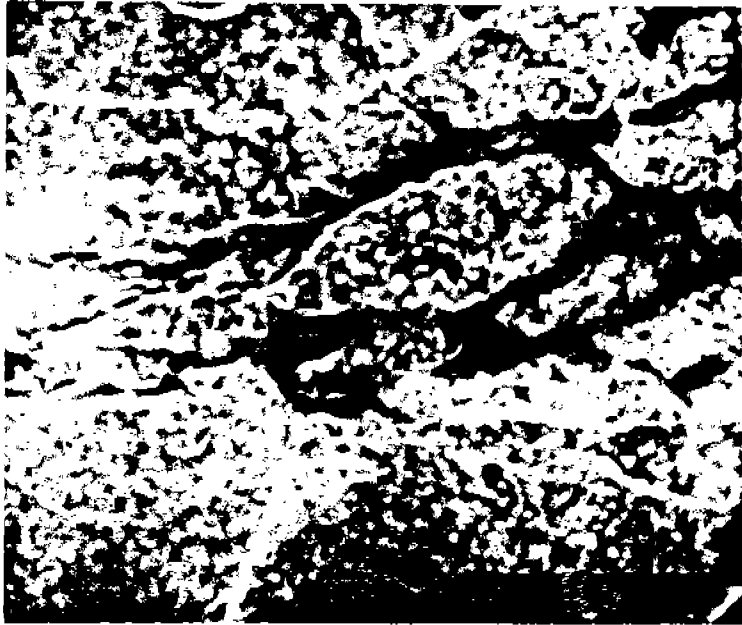


Figure 8b. SEM micrograph of Mil S-24645 base metal tested in seawater with -1.0V (SCE) protection at 10Hz, R=0.1, showing region A in Fig. 8a.

COMMITTEE ON MARINE STRUCTURES

Commission on Engineering and Technical Systems

National Academy of Sciences - National Research Council

The COMMITTEE ON MARINE STRUCTURES has technical cognizance over the interagency Ship Structure Committee's research program.

Peter M. Palermo (Chairman), Alexandria, VA
Mark Y. Berman, Amoco Production Company, Tulsa, OK
Peter A. Gale, John J. McMullin Associates, Arlington, VA
Rolf D. Glasfeld, General Dynamics Corporation, Groton, CT
William H. Hartt, Florida Atlantic University, Boca Raton, FL
Paul H. Wirsching, University of Arizona, Tucson, AZ
Alexander B. Stavovy, National Research Council, Washington, DC
Michael K. Parmelee, Ship Structure Committee, Washington, DC

LOADS WORK GROUP

Paul H. Wirsching (Chairman), University of Arizona, Tucson, AZ
Subrata K. Chakrabarti, Chicago Bridge and Iron Company, Plainfield, IL
Keith D. Hjelmstad, University of Illinois, Urbana, IL
Hsien Yun Jan, Martech Incorporated, Neshanic Station, NJ
Jack Y. K. Lou, Texas A & M University, College Station, TX
Naresh Maniar, M. Rosenblatt & Son, Incorporated, New York, NY
Solomon C. S. Yim, Oregon State University, Corvallis, OR

MATERIALS WORK GROUP

William H. Hartt (Chairman), Florida Atlantic University, Boca Raton, FL
Fereshteh Ebrahimi, University of Florida, Gainesville, FL
Santiago Ibarra, Jr., Amoco Corporation, Naperville, IL
Paul A. Lagace, Massachusetts Institute of Technology, Cambridge, MA
John Landes, University of Tennessee, Knoxville, TN
Mamdouh M. Salama, Conoco Incorporated, Ponca City, OK
James M. Sawhill, Jr., Newport News Shipbuilding, Newport News, VA

SHIP STRUCTURE COMMITTEE PUBLICATIONS

- SSC-350 Ship Vibration Design Guide by Edward F. Noonan 1989
- SSC-351 An Introduction to Structural Reliability Theory by Alaa E. Mansour 1990
- SSC-352 Marine Structural Steel Toughness Data Bank by J. G. Kaufman and M. Prager 1990
- SSC-353 Analysis of Wave Characteristics in Extreme Seas by William H. Buckley 1989
- SSC-354 Structural Redundancy for Discrete and Continuous Systems by P. K. Das and J. F. Garside 1990
- SSC-355 Relation of Inspection Findings to Fatigue Reliability by M. Shinozuka 1989
- SSC-356 Fatigue Performance Under Multiaxial Load by Karl A. Stambaugh, Paul R. Van Mater, Jr., and William H. Munse 1990
- SSC-357 Carbon Equivalence and Weldability of Microalloyed Steels by C. D. Lundin, T. P. S. Gill, C. Y. P. Qiao, Y. Wang, and K. K. Kang 1990
- SSC-358 Structural Behavior After Fatigue by Brian N. Leis 1987
- SSC-359 Hydrodynamic Hull Damping (Phase I) by V. Ankudinov 1987
- SSC-360 Use of Fiber Reinforced Plastic in Marine Structures by Eric Greene 1990
- SSC-361 Hull Strapping of Ships by Nedret S. Basar and Roderick B. Hulla 1990
- SSC-362 Shipboard Wave Height Sensor by R. Atwater 1990
- SSC-363 Uncertainties in Stress Analysis on Marine Structures by E. Nikolaidis and P. Kaplan 1991
- SSC-364 Inelastic Deformation of Plate Panels by Eric Jennings, Kim Grubbs, Charles Zanis, and Louis Raymond 1991
- SSC-365 Marine Structural Integrity Programs (MSIP) by Robert G. Bea 1992
- none Ship Structure Committee Publications - A Special Bibliography